

# **Nanomaterials, Nanoparticles, Nanodevices**

*EDITORS:*

**Maria Zaharescu, Horia Chiriac, Dan Dascalu**



**EDITURA ACADEMIEI ROMÂNE**

**București, 2016**

## CONTENTS

<b>FOREWORD</b> .....	
<b>PREPARATION OF Fe<sub>3</sub>O<sub>4</sub> MAGNETIC NANO AND MICRO-PARTICLES COATED WITH POLYMERS</b> <u>S. PERETZ</u> , D.F. ANGHEL, E.L. SIMION, M. RUSE, C. STOIAN, M. ELISA, I. FERARU.....	
<b>KEY PARAMETERS CONTROLLING THE STABILITY AND REACTIVITY OF MICRO AND NANOSTRUCTURED MATERIALS: ENERGETICS OF NANOMATERIALS</b> S. TANASESCU, F. MAXIM, A. NEACSU, F. TEODORESCU, A. MILEA .....	
<b>EXPERIMENTS WITH POSSIBLE APPLICATION TO THE HOMOGENOUS SOLUTIONS OF SOLID NANOSTRUCTURES WITH LIQUID SOLVENTS</b> M. TEODORESCU .....	
<b>FROM BIOLOGICAL CELLS TO SEMICONDUCTOR AND METALLIC NANOPARTICLES: THE SAME RECIPE WITH DIFFERENT FLAVORS</b> S. TITUS .....	
<b>NUMERICAL STUDY OF METALLIC NANOPARTICLES HANDLING IN ELECTRIC FIELD WITH APPLICATIONS IN CELL ELECTROPORATION</b> O.T. NEDELICU, G. BOLDEIU, R. CORMAN, O.L. CINTEZA, D. STAN .....	
<b>NANOELECTRONIC DEVICES BASED ON ATOMICALLY THIN MATERIALS</b> M. DRAGOMAN, A. DINESCU, D. DRAGOMAN, A. CISMARU, M. ALDRIGO, A. RADOI .....	
<b>EFFECT OF DIFFERENT SOLVENTS IN THE EXFOLIATED GRAPHITE NANOPLATELETS SYSTEMS AT (313.15 AND 318.15) K TEMPERATURES</b> F. SIRBU, A.C. ION, I. ION .....	
<b>DEVELOPMENT OF AN APTASENSOR FOR LYSOZYME BASED ON GRAPHENE OXIDE THROUGH THE LAYER-BY-LAYER METHOD</b> A. VASILESCU, A. VEZEANU, S. DAVID, S.GASPAR .....	
<b>TiO<sub>2</sub> ANATASE AND ZnO NANOPOWDERS ELECTROCHEMICALLY SYNTHESIZED INVOLVING CHOLINE CHLORIDE BASED IONIC LIQUIDS</b> L. ANICAL, S. COSTOVICI, M. ENACHESCU.....	

**ZINC OXIDE THIN FILMS FOR RADIATION HARDENED DEVICES BY MATERIALS ENGINEERING**

*R. PLUGARU, I. MIHALACHE, R. GAVRILA, A.I.DANCIU, G. BOLDEIU,  
O.T. NEDELICU, N. PLUGARU, V.A. MARALOIU, D. GHICA,  
M. STEFA, S.V. NISTOR .....*

**CURRENT AND FUTURE TRENDS TO ELABORATE NANOSTRUCTURED MATERIALS BY THE POWDER METALLURGY TECHNOLOGY. EDUCATION AND RESEARCH MANAGEMENT**

*O. GINGU, C. TEISANU, G. SIMA, D. COMAN, A. DIDU, M. MANGRA.....*

## Preparation of Fe<sub>3</sub>O<sub>4</sub> Magnetic Nano and Micro-Particles Coated With Polymers

Sandu PERETZ<sup>1</sup>, Dan Florin ANGHEL<sup>1</sup>, Elena Livia SIMION<sup>1</sup>,  
Mircea RUSE<sup>2</sup>, Cristina STOIAN<sup>3</sup>, Mihai ELISA<sup>4</sup> and Ionut FERARU<sup>4</sup>

<sup>1</sup>Institute of Physical Chemistry “Ilie Murgulescu”, Romanian Academy, Department of Colloids, 202 Spl. Independentei, 060021 Bucharest, Romania  
E-mail: sanduperetz@gmail.com

<sup>2</sup>Department of Chemistry and Petrochemistry, National Research and Development Institute for Chemistry and Petrochemistry – ICECHIM, 202 Spl. Independentei, 060021 Bucharest, Romania  
E-mail: mircearusel@yahoo.com

<sup>3</sup>University “Dunarea de Jos” of Galati, Faculty of Sciences and Environment, Department of Chemistry, 111 Domneasca St., 800201, Galati, Romania  
E-mail: stoianc@yahoo.com

<sup>4</sup> National Institute of Research and Development Optoelectronics - INOE 2000, 409 Atomistilor St., 77125, Magurele, Romania  
E-mail: astatin18@yahoo.com

**Abstract.** Nano and micro-particles have been synthesized through an original method by coating an iron oxide core with polymer layers formed by interaction between chitosan (Chi) and sodium alginate (Alg). The synthesis has two stages: In the first the magnetite (Fe<sub>3</sub>O<sub>4</sub>) nanoparticles having negatively charged surface were synthesized, and covered with cationic chitosan. In the second, the chitosan coated Fe<sub>3</sub>O<sub>4</sub> nanoparticles were introduced in a NaAlg solution, when complex layers were formed by the interaction between the two polymers, which led to an increase in size of the particles. The coated microparticles (CM) were morphologically and structurally characterized by SEM microscopy, FTIR spectroscopy, and their surface area and porosity was determined by BET method. The obtained microparticles have a quasi-spherical shape with a mean diameter of about 700 nm, and show a rough surface with pores in the form of scales. The saturation magnetization measured by using a vibrating sample magnetometer (VSM) showed good superparamagnetic properties for the CM. The adsorption capacity of CM was tested on two reactive dyes: Reactive Red 11 (RR11) and Reactive Red195 (RR195). The removal efficiency of dyes increases with the CM dose, and the amount of adsorbed dye increases with the initial pollutants concentration. The adsorption kinetic study shows that the process rapidly develops in the first 3 hours, then it slows down, and the equilibrium is reached. The kinetic

experiments proved that the adsorption of RR11 and RR195 obey the Langmuir model.

**Key words:** magnetite, microparticle, chitosan, alginate, adsorption, reactive dye.

## 1. Introduction

In the last decade the study of magnetic particles coated with polymers has expanded due to its theoretical importance, and because of many medical and industrial applications [1-3]. At the same time the use of polymeric matrices for dyes adsorption is one of the mostly used options to removing contaminants from polluted waters. Contamination of surface and groundwater by dyes resulted from industrial processes is a main and current environment problem. Residues from dyeing processes contribute to the water pollution, even if present in minute concentrations. The dyes released in water lead to changes in water transparency by coloring effect [4, 5].

The sunlight penetrates harder in dyes contaminated waters, entailing reduction of photosynthesis with direct effects on flora and fauna [6]. Some persistent dyes show resistance to biochemical degradation, which can cause allergies, skin irritation or even tumors [7].

Generally, a suitable adsorbent used for dyes sorption should meet several conditions: i) low cost; ii) readily available; iii) large capacity and rate of adsorption; iv) high selectivity for different concentrations; v) efficient at removing a wide variety of dyes [8]. A considerable advantage of polymeric matrices is the presence of a variety of functional groups, which are able to modulate their properties for desired applications [9].

Among the polymeric adsorbents, chitosan is a successfully used biopolymer for sorption of metals and organic substances from aqueous media [10]. The chitosan is obtained by partially deacetylation of chitin, and has the following formula poly(b-1-4)-2-amino-2-deoxy-dglucopyranose [11].

Chitosan nanocomposites which include iron oxide were used in recent years as adsorbents for removal of hazardous azo dyes, or as electrochemical sensor of nitric oxide [12, 13].

Magnetic particles with different compositions (hematite, magnetite or maghemite) were coated with synthetic polymers such as polyvinyl alcohol, polyacrylic acid [14, 15], or with natural polymers like dextran, proteins, or starch [16-18]. The polymer coated magnetic microparticles have the advantage that can be easily separated from the water [19].

In order to improve the properties of the chitosan-coated particles, in particular to increase their strength and stability in an acidic medium, the synthesis of the complex polymer layers containing alginate was attempted [20].

Sodium alginate (Alg), a water soluble salt of alginic acid, is a natural linear polysaccharide from marine brown algae composed of  $\beta$ -D-mannuronic and  $\alpha$ -L-guluronic acid residues arranged in a nonregular and blockwise fashion along

the chain [21].

A large amount of effluents discharged in water are acidic, therefore the use of the chitosan for their retention is not recommended, because it is soluble in this environment. On the other hand, the good solubility in water of these reactive dyes is the main reason why they are difficult to be removed from aqueous solutions. The research performed to date for chemical modification of chitosan led to the improvement of its stability at low pH and increased its adsorbent ability [22]. The complexation of chitosan with other polymer was necessary to stabilize the microparticles in acid medium as well as to grant the porosity and mechanical strength of the material necessary for the adsorption studies in these dynamic systems [23].

The purpose of this study is to synthesize and characterize magnetite nano- and micro-particles coated with a new type of chitosan-alginate complex layers. We intend also to use the coated microparticles for dyes removal from aqueous solutions, to investigate their adsorption efficiency and kinetic behavior.

We applied the particles for adsorption and removal of two commercial monochlorotriazinic dyes Reactive Red 11 (RR11), and Reactive Red 195 (RR195), which are routinely used for silk dyeing.

## **2. Materials and Methods**

### ***2.1. Materials***

Chitosan medium weight (Chi) and sodium alginate (Alg) was purchased from Fluka (Switzerland).  $\text{FeSO}_4 \times 7\text{H}_2\text{O}$  and  $\text{FeCl}_3 \times 6\text{H}_2\text{O}$  were purchased from Sigma-Aldrich (Germany). The dyes: Reactive Red 11 (RR11) and Reactive Red 195 (RR 195) were purchased from ACC Corporation (USA) having purity >95%. The water used in the experiments was Milli-Q water (MILLIPORE Simplicity UV Lab System - France).

### ***2.2. Preparation of the Particles***

The present study shows how to confer special properties to the magnetite particles by coating them with complex polymers layers which possess different functional groups.

#### ***2.2.1. Preparation of $\text{Fe}_3\text{O}_4$ nanoparticles***

Magnetite nanoparticles were prepared by co-precipitation reaction of a mixture of ferric/ferrous salts in a molar ratio of 2:1. In a round-bottom flask equipped with mechanical stirring  $\text{FeSO}_4 \times 7\text{H}_2\text{O}$  and  $\text{FeCl}_3 \times 6\text{H}_2\text{O}$  were dissolved in 200 mL of water. The solution was then purged with  $\text{N}_2$  to eliminate air. Then, over this solution, ammonium hydroxide (25% v/v) was added under vigorous stirring (at 400 rpm). The formed precipitate was treated with HCl, and

after 30 minutes a 0.2 M lactic acid solution was added. The mixture was heated to about 80°C for 1.5 hours under atmosphere of N<sub>2</sub>, then it was cooled at room temperature. The obtained particles were repeatedly washed with Millipore water (5-6 times with 100 mL of water), centrifuged and then decanted. Then the resulted particles were washed with ethanol 50% v/v (3-4 times with 100 mL), collected by magnetic separation, and vacuum-dried, to obtain homogeneous dry nanoparticle of magnetite powder.

### 2.2.2. Coating process of Fe<sub>3</sub>O<sub>4</sub> nanoparticles with polymers

The chitosan solution was prepared by dissolving 2g of chitosan in 100 mL of aqueous acetic acid solution 1 % (w/v) under stirring at 200 rpm, for 24h at room temperature. For coating with polymers the Fe<sub>3</sub>O<sub>4</sub> powder was dispersed (at 300 rpm) in 100 mL of 2% (w/v) solution of chitosan (in 1% v/v solution of acetic acid), at 40-45°C for 90 minutes, when magnetite particles were covered with thin shells of chitosan. After that, the Fe<sub>3</sub>O<sub>4</sub>-Chi nanoparticles were transferred in a flask over which an aqueous solution of sodium alginate 3% (w/v) it was added, under rapid stirring (200 rpm) that was mentained for 60 minutes, when the chitosan-alginate complex layers are formed. We assume that the positive charge of chitosan primary layers interacted with negatives charges of alginate, to form polyelectrolyte complex layers [9]. In the next step the particles were placed in a vessel containing CaCl<sub>2</sub> (5% w/v), and they are held there for 2 hours under continuous stirring (200 rpm) to complete the reaction. Then, the particles were magnetically separated, were repeatedly washed on a porous filter with 100 mL portions of Millipore water (5-6 times), to remove any reagent traces, and finally were dried in vacuum.

### 2.3. Reactive Dyes

The two reactive dyes used in adsorption experiments have the following structures:

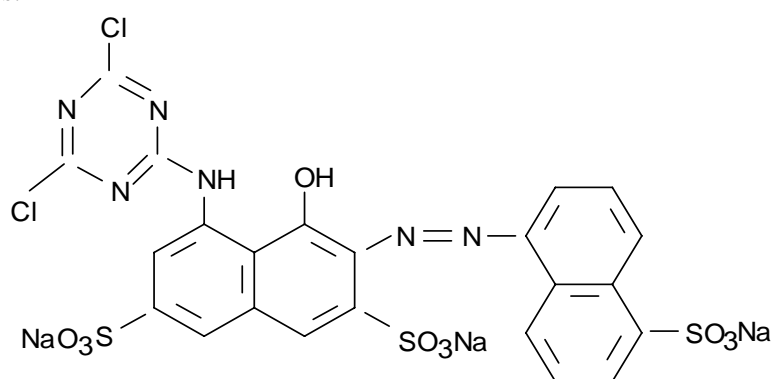


Fig. 1. Structure of RR11 dye.

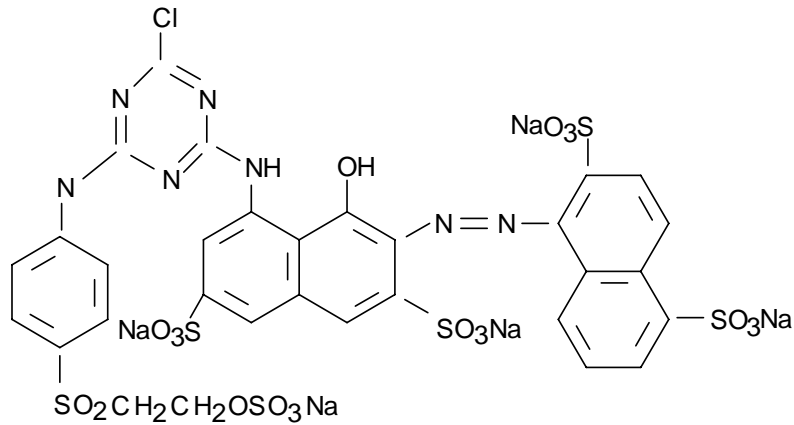


Fig. 2. Structure of RR195 dye.

#### 2.4. Adsorption of Reactive Dyes from Solution

Batch equilibrium adsorption experiments were conducted in 250 mL conical flasks filled with 200 ml aliquots of RR11 and RR195 dyes solutions in the concentration range of

5-800 mg/L. In each flask different amounts of CM dried microparticles were added, at room temperature (25°C).

The amount of dye adsorbed by the microparticles,  $q_e$  (mg/g dried), was calculated by following equation [22]:

$$q_e = \frac{(c_0 - c_e)V}{m} \quad (1)$$

where  $V$  (L) is the volume of the dye solution,  $m$  (g) the weight of the dried microparticles,  $C_0$  (mg/L) the initial dye concentration, and  $C_e$  (mg/L) the dye concentration at equilibrium.

After completion of adsorption, the CM microparticles were separated from aqueous medium by means of a magnet, and then were washed and dried under vacuum.

The dye concentrations were determined at different time intervals by using a UV-Vis spectrophotometer (Varian Cary 100-Bio), and the pH values were measured with an Orion pH-meter model 402A.

#### 2.5. Characterization Techniques

The morphology of the microparticles was determined by using a Scanning Electron Microscope (SEM) Quanta 3D FEG 200/400 (FEI Company) operating at 300 keV.

The particle size distribution and Zeta potential were measured by using a



Zetasizer NanoZS (Malvern) apparatus equipped with a laser emitting at  $\lambda_0 = 633$  nm, and operating at a scattering angle of  $173^\circ$ .

The chitosan-based dry microparticles were characterized by Fourier Transform Infrared (FTIR-ATR) spectroscopy using a Nicolet iN10 FT-IR spectrometer (Thermo Scientific), in the  $550\text{-}4000$   $\text{cm}^{-1}$  wavenumber range, at a spectral resolution of  $4$   $\text{cm}^{-1}$ .

The microparticles specific surface area was determined by BET method based on nitrogen adsorption [24]. The measurements of surface area were determined by adsorption of nitrogen vapors which penetrate into the interior of microparticles mass. The nitrogen adsorption-desorption isotherms were recorded at  $77$  K, in the range of relative pressure from  $0$  to  $1$ , using a Micromeritics-ASAP-2020 volumetric adsorption analyzer. The specific surface areas of the microparticles were calculated using the BET equation.

The magnetic properties of CM microparticles were measured on a High Field Measurement System (Cryogenic Ltd. UK) vibrating sample magnetometer (VSM) having a cryogenic free system working with the sample down to  $1.5$  K and a sensitivity of  $10^{-5}$  emu.

### **3. Results and Discussion**

The coating of magnetite particles was made by a sequential deposition process. At first several layers of chitosan were deposited. Then, they will interact with sodium alginate to form complex polymer layers.

#### ***3.1. Characterization of $\text{Fe}_3\text{O}_4$ Nanoparticles and Formation of Chitosan Layers - Stage I***

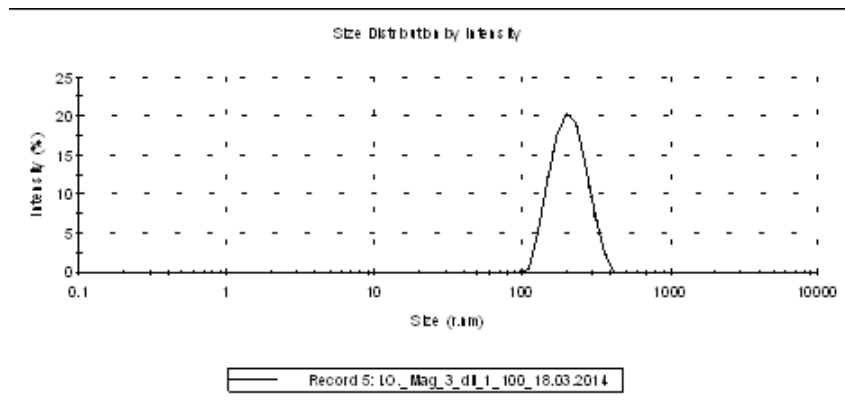
The first layers on the microparticles surface were obtained by coating the  $\text{Fe}_3\text{O}_4$  nanoparticles with chitosan. This coating is favored by the presence of the positive amino groups of chitosan that have a strong affinity for the negatively charged surface of the iron oxide nanoparticles [25].

##### ***3.1.1. DLS measurements and SEM analysis of $\text{Fe}_3\text{O}_4$ nanoparticles***

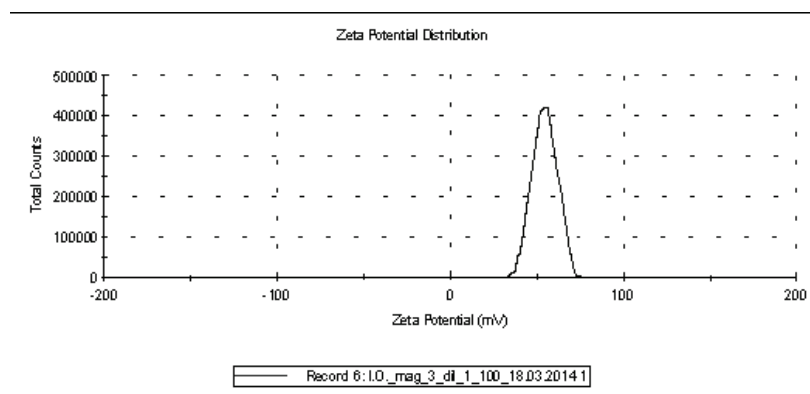
The coating process efficiency was monitored by DLS technique, measuring the size and electrical charge of the chitosan-coated particles.

The results show that the obtained particles have a narrow size distribution, with average diameter of  $420$  nm, and Zeta potential of  $+52.6$  mV (Fig. 3a and b). These data proved that the primary particles have nanometric size and positive charge conferred by the free amino groups of chitosan.

The SEM micrographs confirms that the core particle consists of  $\text{Fe}_3\text{O}_4$  nanocrystallites [25] having cubic shape with homogeneous size of about  $50\text{-}80$  nm (see Fig. 4a).



a)

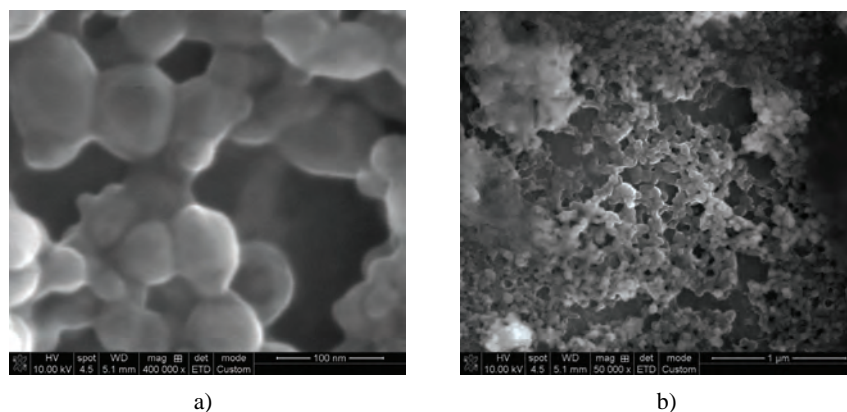


b)

**Fig. 3.** Size particles distribution (a) and Zeta potential (b) of chitosan coated microparticles.

Besides the single  $\text{Fe}_3\text{O}_4$  colloidal particles, there are small aggregates containing magnetite nanoparticles surrounded by chitosan layers. In the Fig. 4b the particles appear surrounded by chitosan layers which have been deposited on their surface.

The particles consist of nano-sized coated spheres which present diameters in-between 100 and 350 nm. They have a nucleus of cubic nanocrystallites surrounded by polymer layers with a relatively homogeneous porosity, and pores of about 15-25 nm.

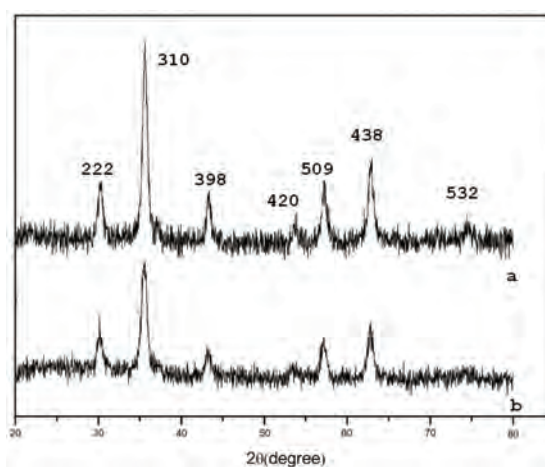


**Fig. 4.** a) Fe<sub>3</sub>O<sub>4</sub> nano-crystallites; b) Chitosan coated Fe<sub>3</sub>O<sub>4</sub> nanoparticles.

The approximate size of nanoparticles determined by SEM microscopy was smaller than that determined by DLS technique in aqueous solution. The difference, probably, arises from the dry state of nanoparticles in the SEM determinations.

### 3.1.2. XRD Diffractograms of the Particles

The particles were structurally characterized by using the XRD method, aiming to prove the presence of crystalline Fe<sub>3</sub>O<sub>4</sub> into magnetite nanoparticles coated with chitosan. The diffraction pattern in Fig. 5a belong to unmodified Fe<sub>3</sub>O<sub>4</sub> particles with six diffraction peaks at 2θ of 222, 310, 398, 420, 509 and 532. These values prove that the obtained nanoparticles are a standard pattern of crystalline magnetite with inverse spinel structure [26].



**Fig. 5.** XRD diffraction patterns of Fe<sub>3</sub>O<sub>4</sub> (a) and Chitosan coated Fe<sub>3</sub>O<sub>4</sub> (CM) microparticles (b).

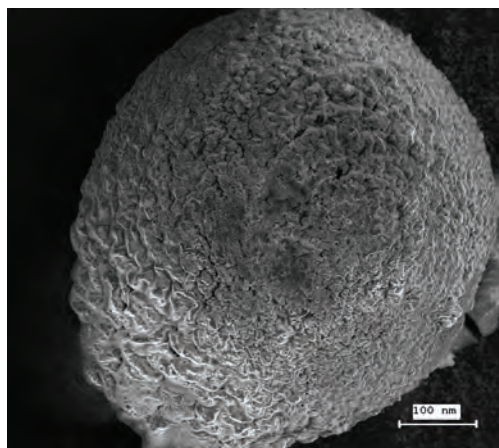
Figure 5b shows the diffractogram of magnetic particles coated with chitosan layers. One may observe that the coating process did not alter the structure of magnetic nanoparticles. These data agree with the previous ones reported in the literature [27]. Therefore our nanoparticles have a core of pure  $\text{Fe}_3\text{O}_4$  with a cubic inverse spinel structure.

### ***3.2. Characterization of Microparticles Coated with Complex Chitosan-Alginate Layers - Stage II***

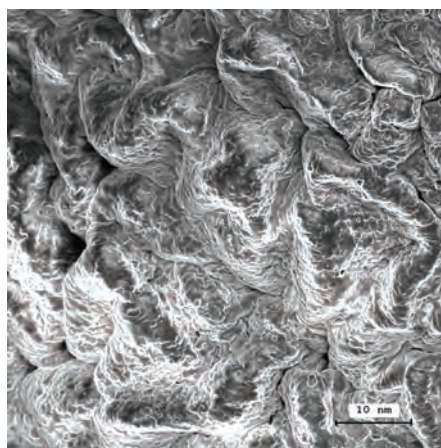
In the second stage of the preparation process, the chitosan coated nanoparticles were treated with sodium alginate solution. As a result of alginate-chitosan interaction, polymer complex multilayers are formed entailing the increase in size of nanoparticles. It is well-known that chitosan nanoparticles can not be used in acidic media and have small surface area and low porosity [28]. These drawbacks can be eliminated by coating of them with chitosan-alginate complex layers as we originally propose in this paper.

#### ***3.2.1. SEM microscopy of CM microparticles***

The SEM images show CM particles having quasi-spherical shape, with diameters between 600-700 nm. They have a rough surface with many pores in the form of scales (Figs. 6 and 7). We presume that porosity of microparticles is the result of the interaction between chitosan and alginate.

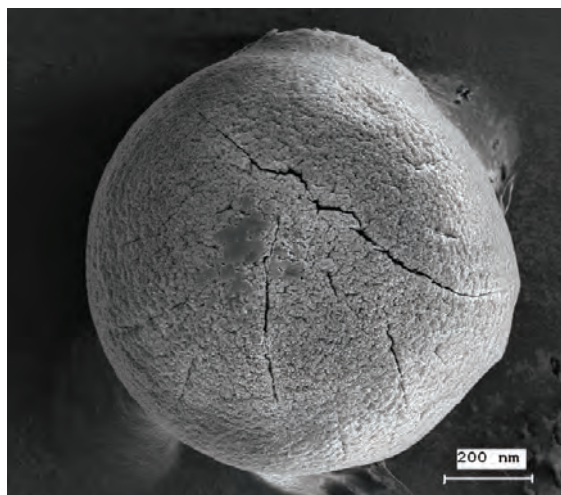


**Fig. 6.** Blank CM particles.



**Fig. 7.** Surface of CM particles.

After adsorption of dyes the size of microparticles increased at about 750-900 nm (Fig. 8). Moreover, the particles changed the appearance presenting a smoother surface with cracks.



**Fig. 8.** CM microparticles after dye adsorption.

### 3.2.2. Microparticles porosity and surface area – BET method

The isotherm of nitrogen adsorption reveals that the nano and micro-particles exhibit significant porosity and high surface area as compared to the bulk material. Taking into account the BET specific surface area values, the differences between particles are due to dissimilar porosities. The smaller pores possess high surface free energy and thus are easily to be filled by the dye molecules [29]. The pore size analysis was made using a simplified Broekhoff and Boer polynomial relationship [30]. The results are presented in the Table 1.

**Table 1.** Particles surface and pore analyzed by nitrogen adsorption method

Particle type	Mean pore radius Broekhoff- de Boer (nm)	Surface area BET method (m <sup>2</sup> /g)
Fe <sub>3</sub> O <sub>4</sub> – Chi (aggregated)	35	4.3
Fe <sub>3</sub> O <sub>4</sub> –Chi (individual)	25	5.5
Fe <sub>3</sub> O <sub>4</sub> –Chi-Alg (CM)	15	9.6

One observes that the magnetic nanoparticles individually coated only with chitosan have a smaller pore size than those which are aggregated, and the surface area for the bulk particles increases compared to those aggregated.

On the other hand, the particles coated with Chi-Alg complex layers show the best characteristics, having many pores with a size of about 15 nm, and high surface area around of 9.6 m<sup>2</sup>/g.

It is noteworthy that individual particles have smaller pores than those of aggregates, but present a larger surface area.

The rough surface with many pores indicates that the polymer coated microparticles are suitable for the adsorption of organic substances, such as dyes.

### 3.2.3. Magnetic properties of chitosan-alginate particles

The magnetic properties of polymer coated particles were characterized by vibrating sample magnetometer method (VSM).

Figure 9 shows a typical magnetization curve of Chi-Alg magnetic microspheres.

The obtained magnetic hysteresis curves reveal superparamagnetic properties (*i.e.* no remanence effect). This proves that the polymer coated microparticles have only a single magnetic domain, a result that matches the previous one [9].

The saturation magnetization of the bulk magnetite microparticles was 71.1 emu/g, while for iron oxide coated microparticles was 37.2 emu/g significantly lower than the original Fe<sub>3</sub>O<sub>4</sub> microparticles [27]. This was due to the existence of the large amount of diamagnetic chitosan-alginate complex in the iron oxide coated microparticles [31].

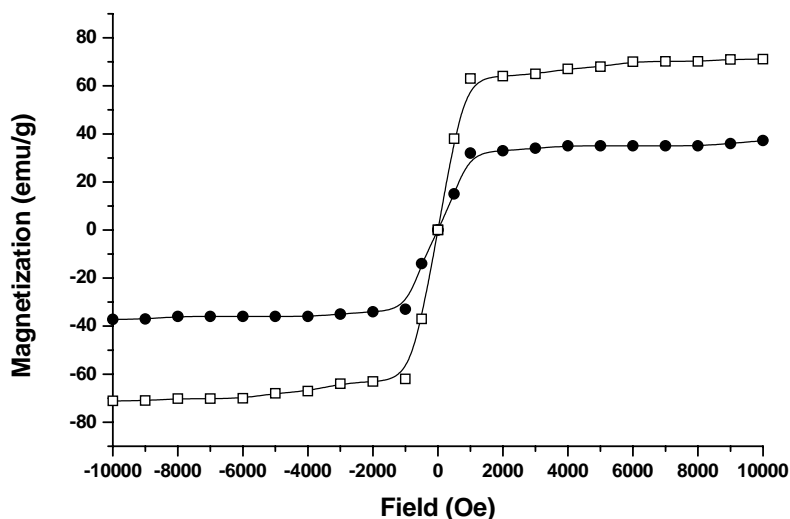


Fig. 9. Magnetic hysteresis curves for Fe<sub>3</sub>O<sub>4</sub> (□) and Chi-Alg particles (●).

One can observe that the saturation magnetization is attenuated in case of CM than for bulk magnetite nanoparticles, which is attributed to the coating with polymer layers [9].

### 3.2.4. Effect of magnetic content on the particle properties

In order to obtain good response to the magnetic field, the effect of magnetic content on the formation of the coated magnetite particles was studied.

When the  $\text{Fe}_3\text{O}_4$  content increased from 0.25 g to 2.0 g, the particle size of coated nanoparticles increased from 255 to 590 nm and the zeta potentials decreased from 72.2 to 29.5 mV (see Fig. 10).

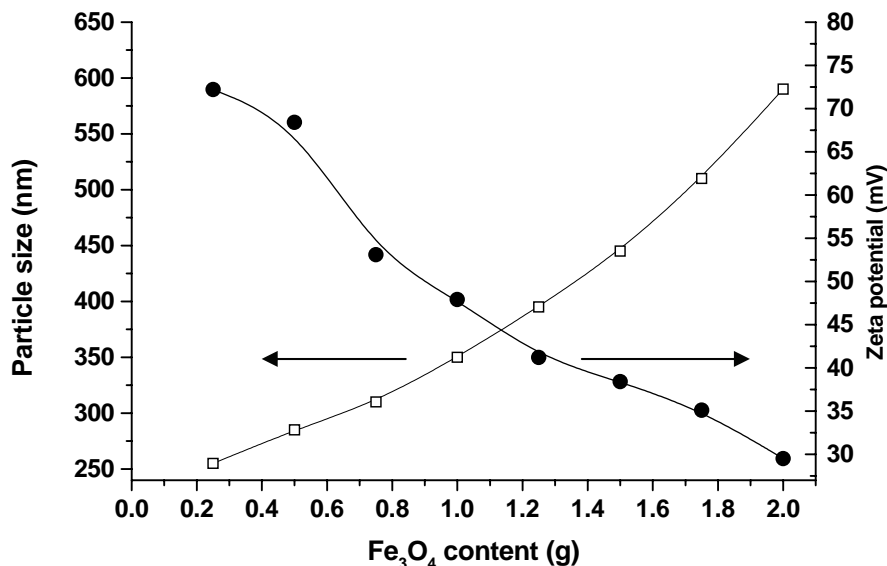


Fig. 10. Particle size ( $\square$ ) and zeta potential ( $\bullet$ ) as function of  $\text{Fe}_3\text{O}_4$  microparticle content.

### 3.2.5. Interaction between chitosan and alginate - the FTIR analysis

To explain the formation of polymer layers, we examined the interaction between specific groups of chitosan and alginate biopolymers on the  $\text{Fe}_3\text{O}_4$  microparticles surface.

The FTIR spectra of sodium alginate, chitosan and chitosan-alginate microparticles are presented in Fig 11. Sodium alginate has characteristic bands of hydroxyl at  $3268\text{ cm}^{-1}$ , carboxyl at  $1593\text{ cm}^{-1}$  and  $1404\text{ cm}^{-1}$ , and of carbonyl at  $1025\text{ cm}^{-1}$ .

It is noteworthy that the characteristic peaks of Chi at  $1642\text{ cm}^{-1}$  for the -NH bending vibration and at  $1585\text{ cm}^{-1}$  for the -NH deformation vibration of the amino groups were affected and shifted to  $1602\text{ cm}^{-1}$  in the spectrum of the Chi-Alg complex.

This proves that the amino group of chitosan have interacted with the alginate carboxyls. Fig. 11 also shows that the chitosan-alginate coated microparticles have a new peak at around  $1416\text{ cm}^{-1}$ . It is attributed to the  $-\text{NH}_3^+$  groups of chitosan interacting with the alginate carboxylate groups. The peak appearing around  $1603\text{ cm}^{-1}$  in the spectrum for chitosan-alginate coated microparticles can be assigned to a symmetric  $-\text{NH}_3\text{C}$  deformation. The absorption

peaks of  $591\text{ cm}^{-1}$  that appear in the spectrum of CM microparticles, are specific for the Fe-O-Fe bands of the magnetite.

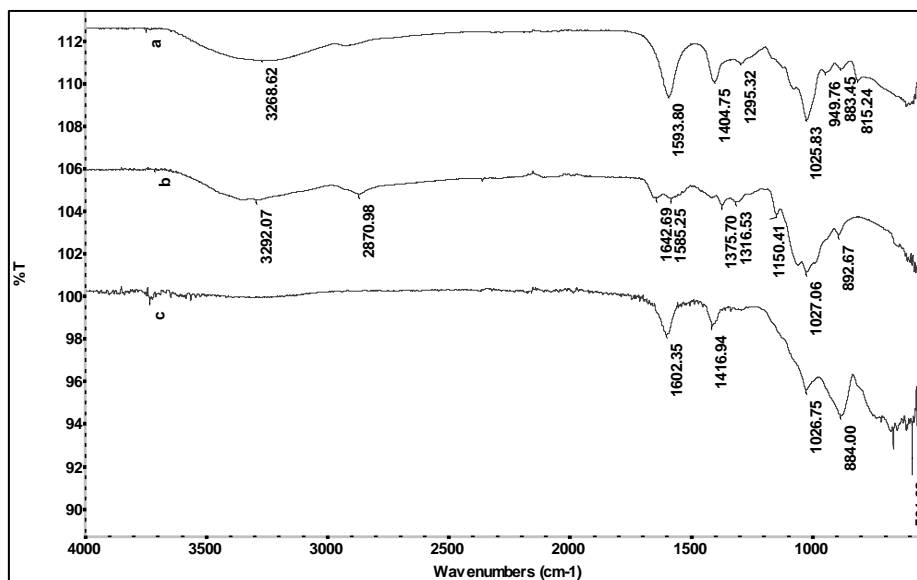


Fig. 11. FTIR spectra: a) Alg powder; b) Chi medium wt; c) CM with Alg-Chi.

The FTIR spectra recorded after the chitosan-alginate interactions demonstrate:

- i) The formation of chitosan-alginate complex layers on the microparticles surface;
- ii) The apparition of new bonds between the positive amino groups of the chitosan-covered microparticles and the negatively charged carboxyl groups of alginate, which led to the displacement of the absorption peaks in the IR spectrum [32].

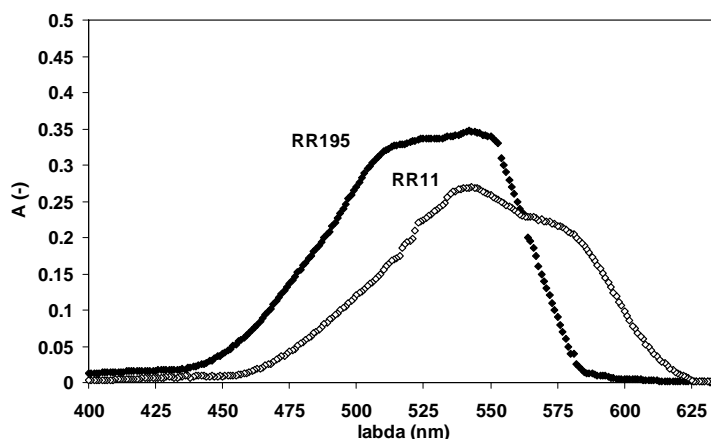
### 3.3. Characterization of Reactive Dyes – the UV-Vis Spectroscopy

The adsorption of two monochlorotriazine reactive dyes by the CM microparticles was spectrophotometrically assessed using a Varian Cary 100 Bio UV-Vis spectrophotometer.

The UV-Vis experiments have been made to detect the absorption maxima of the dyes and use them to draw up calibration graphs for calculation the dye concentration remaining in solution after adsorption by microparticles.

Figure 12 shows the recorded spectra. They point out that RR11 has a maximum absorption wavelength at  $543\text{ nm}$ , while RR195 at  $\lambda_{\text{max}} = 542\text{ nm}$ .





**Fig. 12.** UV-Vis spectrum of RR11 and RR195, at initial concentration of 50 mg/L.

The residual dyes concentration in solution was determined in order to study the pH influence, the effect of microparticles dosage, and the influence of contact time on the adsorption process.

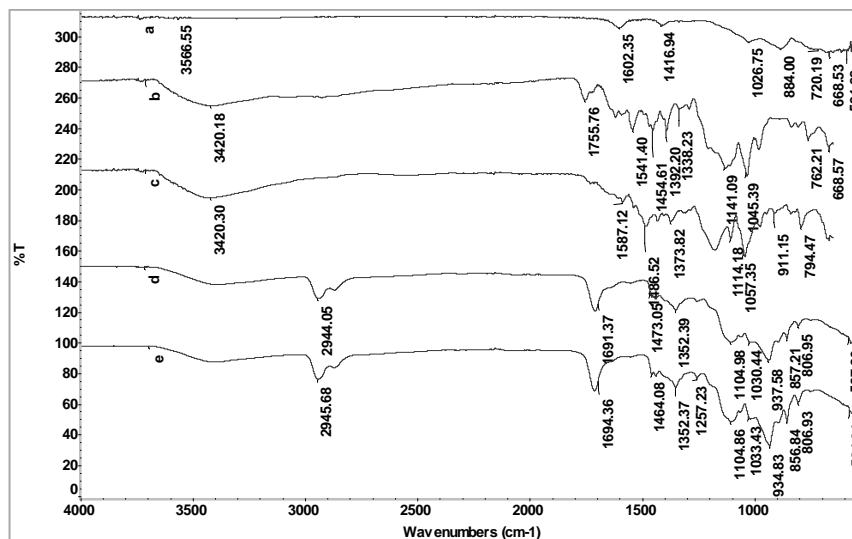
### ***3.4. Adsorption of the Reactive dyes Studied by Interaction of CM Microparticles with the Dyes– the FTIR Spectra***

The FTIR spectra of the CM microparticles after dyes adsorption were compared to those of blank microparticles, in order to determine how their functional groups are involved in the interactions with the two dyes.

#### ***3.4.1. Interaction of CM particles with RR11 and RR195***

As a result of the RR195 dye adsorption, the characteristic absorption peaks of the sulfonic groups stretching vibrations at  $1141\text{ cm}^{-1}$  and  $1045\text{ cm}^{-1}$  are shifted to  $1104\text{ cm}^{-1}$  and  $1030\text{ cm}^{-1}$  respectively. In the case of RR11 dye, we find that the absorption peaks of sulfonic groups stretching vibrations at  $1114\text{ cm}^{-1}$  and  $1057\text{ cm}^{-1}$  are shifted and affected to  $1104\text{ cm}^{-1}$  and  $1033\text{ cm}^{-1}$  respectively (Fig. 13). This proves that the adsorption process affects the sulfonic groups stretching vibrations.

On the other hand in the FTIR spectrum of CM the absorption peaks of amino groups at  $1602\text{ cm}^{-1}$  and  $1416\text{ cm}^{-1}$  do appear. These positively charged polar groups (protonated in acidic medium) are able to form electrostatic bonds with negatively charged groups of the RR195 dye. After the formation of the CM-RR195 complex, the absorption peaks are shifted to  $1691\text{ cm}^{-1}$  and  $1473\text{ cm}^{-1}$  respectively. In the case RR11 dye, the absorption peaks of the CM-RR11 complex are shifted to  $1694\text{ cm}^{-1}$  and  $1464\text{ cm}^{-1}$ , respectively.



**Fig. 13.** FTIR spectra of: a) CM with Alg-Chi; b) RR195 powder; c) RR11 powder; d) CM-RR195 complex; e) CM-RR11 complex.

The FTIR spectrum of CM particles has characteristic Fe-O-Fe bands of magnetite at  $591\text{ cm}^{-1}$ . After the dyes adsorption, the peak of the Fe-O-Fe band is displaced and found for the complexes CM-RR195 and CM-RR11 at  $587\text{ cm}^{-1}$  and  $584\text{ cm}^{-1}$  respectively.

### 3.4.2. The dyes adsorption mechanism - Interaction between CM and reactive dyes

To explain the mechanism of the dyes adsorption on the CM microparticles, we used FTIR spectroscopy determinations. From FTIR spectra we can see that there is a shift of the absorption peaks of both the colorants sulfonate groups, and of the amino groups of the functionalized layers which cover the CM microparticles.

The adsorption mechanism is based on the assumption that electrostatic interactions occur between dyes sulfonate groups and the functionalized surface of the CM microparticles.

Thereby, the adsorption is due to the available positively charged amino groups of CM microparticles which allow formation of electrostatic bonds with negatively charged sulfonate groups of the reactive dyes.

### 3.5. Adsorption of the Reactive Dyes

The obtained functionalized iron oxide microparticles coated with Alg-Chi were used for removal of reactive dyes from aqueous solutions. In this respect we

have studied the effect of pH, the CM dosage, the kinetics of the adsorption process, and the acquired data analyzed using Langmuir and Freundlich models.

### 3.5.1. Effect of pH on dyes adsorption

The influence of pH on dyes adsorption by CM microparticles was studied within the 1.5-9 range, and the obtained results are presented in Fig. 14. Figure 14 shows that removal of dyes increases with pH and has a maximum around pH 5.0-5.5. Then, the removal of dyes decreases with increasing the pH for both dyes.

The increasing part of the curves in Fig. 14, can be explained by the fact that in strong acidic medium (pH=1.5 - 4) more protons are available to protonate the amino groups of chitosan molecules and form  $-\text{NH}_3^+$  groups. This entails the increase of electrostatic attraction between the dyes anionic groups ( $-\text{SO}_3^-$ ) and the protonated amino groups of chitosan-coated particles, causing an enhanced dye adsorption.

The maximum of dye adsorbed is attaining in the range of pH =5.0-5.5. At higher pH values the protonation of amino groups became small and the dye removal considerably lowers.

At the same time at higher pH values of 5.5, a decrease of adsorption is produced. It is presumably due to the abundance of hydroxide ions, and to the saturation of active centers of CM by dyes molecules.

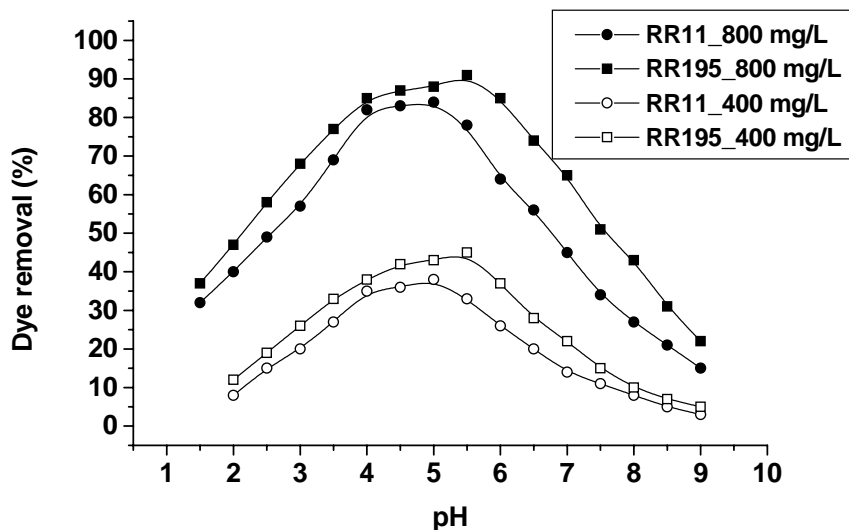


Fig. 14. Effect of pH on removal efficiency of reactive dyes.

It can see that the adsorption maximum is specific for each dye. It depends on pH, and is independent of the dye initial concentration.

For the same quantity of used microparticles we find that RR195 has a better adsorption capacity than RR11. We assume that the phenomenon is due to the structure of RR195 dye that has five sulfonate groups, whereas RR11 has only three.

### 3.5.2. Influence of CM dosage on dye removal efficiency

To determine the optimal dose of microparticles required for a good adsorption, the dyes removal efficiency of dyes was studied according to the quantity of adsorbent, and the initial pollutant concentrations.

The obtained data are presented in Fig. 15. Fig. 15 shows that the removal efficiency of reactive dyes increases with the quantity of microparticles, and the initial concentration of dyes. The data reveal an increasing number of polar groups of CM lead to an increase of the electrostatic interactions with the functional groups of the dyes, and raise the amount of dye adsorbed. The result agrees with the previous one [33].

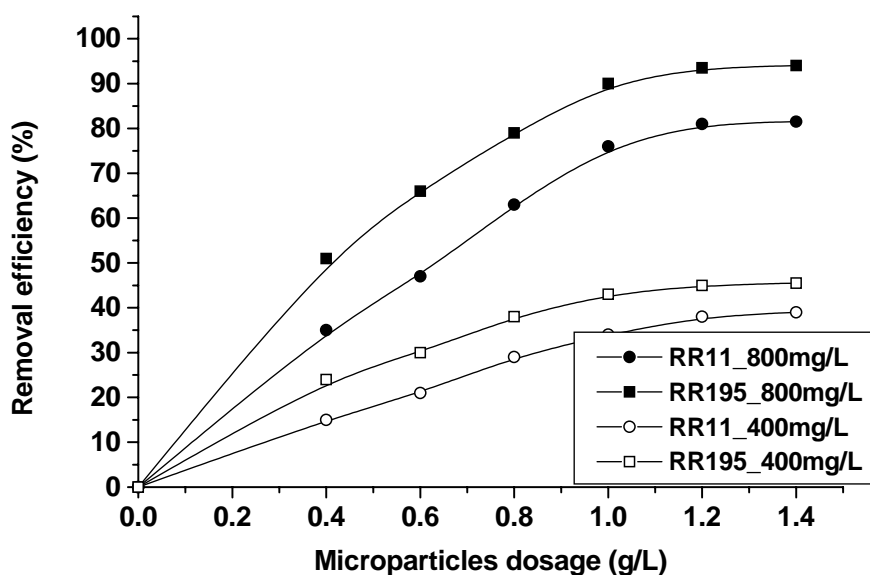


Fig. 15. Dyes removal efficiency versus CM dosage.

By using a dose of 1.4 g/L microparticles, the dye removal is significant, reaching 81.5 % for RR11 and 93.5% in the case of RR195. We have found that for a further increase of the CM dosage, the removal efficiency does not augment significantly.

Due to practical and economical reasons, we worked in the subsequent experiments with a dosage of microparticle of 1.4 g/L.

### 3.5.3. Kinetics of adsorption

The kinetics of dyes adsorption on CM microparticles was spectrophotometrically studied within the concentration range of 5-800 mg/L, at pH = 5.0-5.5 and 25°C.

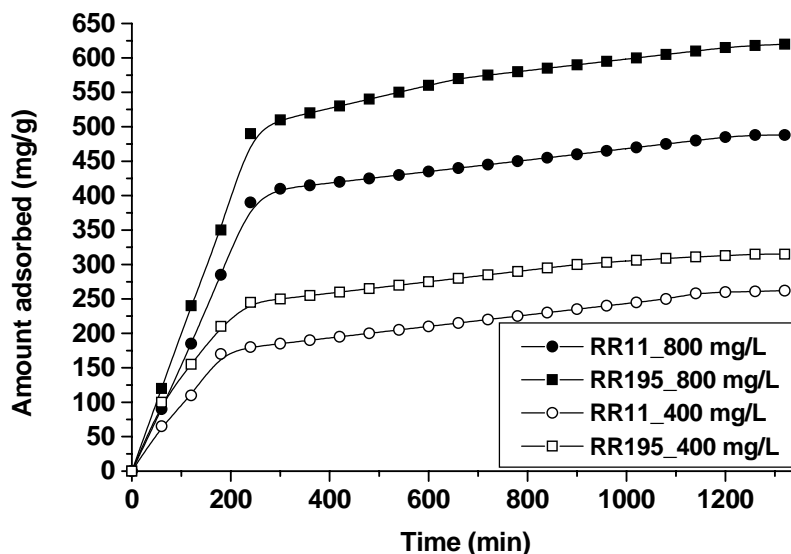


Fig. 16. Effect of contact time and initial dye concentration, on the adsorbed amount of reactive dyes, at 25°C, CM dosage of 1.4 g/L.

The data presented in Fig. 16 show that the quantity of reactive dyes adsorbed by CM microparticles increases with the contact time for all the initial pollutant concentrations.

The process develops in two phases. In the first, the adsorption is rapid and takes about 240 minutes. At this stage, there are several available active centers on the surface of microparticles. In the second stage, the adsorption slows down, and about 1200 minutes are necessarily to reach the equilibrium. At this stage, the number of active sites decreases. The saturation of CM functional groups with dye molecules occur leading to a slowdown in the adsorption process.

The amount of absorbed dye is dependent on the initial concentration of dyes. However, the quantity of adsorbed RR195 is higher than that of RR11 for the studied cases.

### 3.5.4. Adsorption model

The equilibrium adsorption is usually described by an isotherm characterized by specific parameters, which express the surface property and affinity of the

adsorbent. The adsorption of reactive dyes by CM microparticles was investigated, and the experimental data were analyzed using classical Langmuir and Freundlich models.

One of the most used equations for modelling the adsorption process is the Langmuir isotherm [34]. This model assumes monolayer sorption on a surface with a finite number of identical adsorption sites [35].

$$q_e = \frac{K_L q_m C_e}{1 + K_L C_e} \quad (2)$$

where:  $C_e$  is the equilibrium dye concentration,  $K_L$  is the Langmuir isotherm constant and  $q_m$  represent the maximum adsorption capacity. Equation (2) can be written in the following form:

$$\frac{C_e}{q_e} = \frac{1}{K_L q_m} + \frac{C_e}{q_m} \quad (3)$$

The values of Langmuir constants ( $q_m$  and  $K_L$ ) are calculated from the plot of  $C_e/q_e$  versus  $C_e$ .

The adsorption isotherms for RR11 and RR195 were found to be linear over the concentration range from 5 to 800 mg/L (see Figs. 17 and 18).

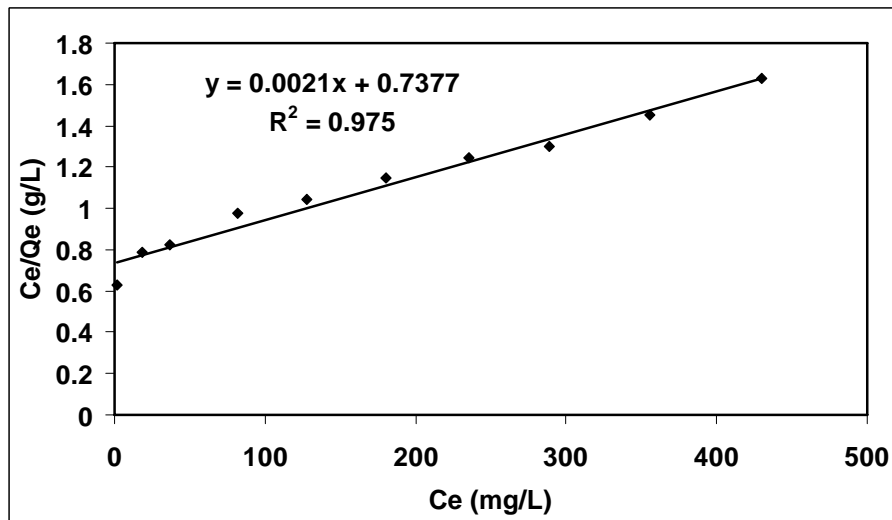


Fig. 17. Langmuir isotherm for RR11; pH=5; 25°C.

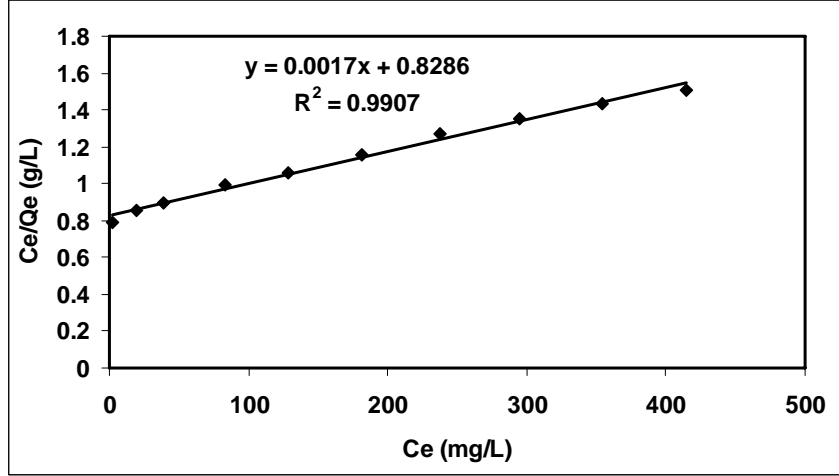


Fig. 18. Langmuir isotherm for RR195; pH=5.5; 25°C.

The adsorbed amount of the dye at equilibrium ( $q_e$ ) increased with the initial dye concentration. The isotherm constants and correlation coefficients obtained by using Langmuir equation, are presented in the Table 2.

Table 2. Isotherm constants and correlation coefficients for reactive dyes adsorbed by CM

	RR11			RR195		
$Q_m$ (mg/g)	$K_L$ (L/mg)	$R^2$	$Q_m$ (mg/g)	$K_L$ (L/mg)	$R^2$	
476.19	0.0029	0.975	588.23	0.002	0.9907	

The data presented in the table above confirms that RR195 were better adsorbed than RR11 on the CM microparticles.

These results are comparable to those obtained for reactive dyes adsorption by crosslinked or non-crosslinked chitosan-based nanostructured systems [36].

The Freundlich model is an empirical isotherm described by the following equation [37]:

$$q_e = K_F C_e^{1/n} \quad (4)$$

where:  $K_F$  is the Freundlich constant related to the adsorbent capacity, and  $n$  is a constant that depends on the adsorption. This equation can be represented as:

$$\log q_e = \log K_F + \frac{1}{n} \log C_e \quad (5)$$

The constant ( $K_F$ ) and the exponent ( $n$ ) are calculated from the intercept and slope of the plot of  $\log q_e$  versus  $\log C_e$ .

When Freundlich equation was applied to the dyes adsorption data, the correlation coefficient ( $R^2$ ) was of 0.8853, which indicates that the adsorption is not consistent with Freundlich model.

#### 4. Conclusions

The results obtained on preparation of  $Fe_3O_4$  magnetic nano and micro-particles coated with polymers allowed us to draw the following conclusions:

1. Microparticles of magnetite coated with polymer complex layers were obtained by the interaction between chitosan and alginate.
2. The coated microparticles have dimensions between 600-700 nm, rough surface with many pores and high adsorption capacity.
3. The magnetic coated microparticles show a pH-dependent behaviour and superparamagnetic properties.
4. The CM microparticles have been successfully used to remove dyes from aqueous solution in the concentration range between 5 and 800 mg/L.
5. The dye removing process takes place by the interaction between the protonated amino groups of coated microparticles and the sulfonate groups of reactive dyes, and was attested by displacements of specific absorption peaks in the FTIR spectra.
6. The dyes removal efficiency increases with increasing the dose of microparticles and the initial pollutant concentration.
7. Kinetic data on reactive dyes removal reveals two stages. The first lasts about 3 hours, the adsorption is rapid, and over 50% of the initial amount of dyes is retained. The second is slower and the adsorption reaches about 93 % at equilibrium.
8. Our experimental data show that the adsorption of reactive dyes on polymer coated microparticles obeys the Langmuir model.

**Acknowledgements.** This research was supported by Romanian Academy, "Ilie Murgulescu" Institute of Physical Chemistry. The support of EU (ERDF) and Romanian Government (POS-CCE O2.2.1 project INFRANANOCHEM, No. 19/2009.03.01) and of (UEFISCDI) (Project PN-II-ID-PCE-2011-3-0916, Contract No. 177/2011) is gratefully acknowledged.

#### References

- [1] H. XU, T. SONG, X. BAO, L. HU, *Site-directed research of magnetic nanoparticles in magnetic drug targeting*, J. Magn. Magn. Mater., **193**, pp. 514–519, 2005.
- [2] Y.F. SHEN, J. TANG, Z.H. NIE, Y.D. WANG, Y. RENC, L. ZU, *Preparation and application of magnetic  $Fe_3O_4$  nanoparticles for wastewater purification*, Sep. Purif. Technol. **68**, pp. 312–319, 2009.
- [3] V. ROCHER, J.-M. SIAUGUE, V. CABUIL, A. BEE, *Removal of organic dyes by magnetic alginate beads*, Water research, **42**, pp. 1290–1298, 2008.



- [4] R. KANT, *Textile dyeing industry an environmental hazard*, Natural Science, **4**(1), pp. 22–26, 2012.
- [5] P.B. NANGARE, D.V. WADKAR, R.S. KARALE, *Impact of Textile Industry on Ground Water Quality*, J. Environ. Res. Develop., **2**(4), pp. 717–725, 2008.
- [6] L. PEREIRA, M. ALVES, *Dyes-Environmental Impact and Remediation, in Environmental Protection Strategies for Sustainable Development*, A. Malik, E. Grohmann (eds.) *Strategies for Sustainability*, Springer Science+Business Media **B.V.**, 2012.
- [7] K. KLEMOLA, J. PEARSON, P. LINDSTROM-SEPPÄ, *Evaluating the toxicity of reactive dyes and dyes fabrics with the HaCaT cytotoxicity test*, AUTEX Research J., **7**(3), pp. 234–255, 2007.
- [8] G. CRINI, P-M. BADOT, *Application of chitosan, a natural aminopolysaccharide, for dye removal from aqueous solutions by adsorption processes using batch studies: A review of recent literature*, Prog. Polym., Sci., **33**, pp. 399–447, 2008.
- [9] Y. WU, J. GUO, W. YANG, C. WANG, S. FU, *Preparation and characterization of chitosan–poly(acrylic acid) polymer magnetic microspheres*, Polymer, **47**, pp. 5287–5294, 2006.
- [10] M.Y. LEE, K.J. HONG, T. KAJIUCHI, J.W. YANG, *Synthesis of chitosan-based polymeric surfactants and their adsorption properties for heavy metals and fatty acids*, Int. J. Biol. Macromol., **36**(3), pp. 152–158, 2005.
- [11] M.-K. JANG, J.-W. NAH, In *Chitin, Chitosan, Oligosaccharides and their Derivatives*; S- K. Kim Ed.; CRC Press, Boca Raton, London, New York, Chapter 24, pp. 325–338, 2011.
- [12] H.Y. ZHU, R. JIANG, L. XIAOB, W. LI, *A novel magnetically separable –  $\gamma$ -Fe<sub>2</sub>O<sub>3</sub> /crosslinked chitosan adsorbent: Preparation, characterization and adsorption application for removal of hazardous azo dye*, J. Hazard. Mater., **179**, pp. 251–257, 2010.
- [13] L. ZHANG, Y. NI, X. WANG, G. ZHAO, *Direct electrocatalytic oxidation of nitric oxide and reduction of hydrogen peroxide based on  $\alpha$ - Fe<sub>2</sub>O<sub>3</sub> nanoparticles-chitosan composite*, Talanta, **82**, pp. 196–201, 2010.
- [14] A. SINHA, J. CHAKRABORTY, S.K. DAS, S. DAS, V. RAO, P. RAMACHANDRARAO, *Oriented arrays of nanocrystalline magnetite in polymer matrix produced by biomimetic synthesis*, Mater. Trans., **42**(8), pp. 1672–1675, 2001.
- [15] S. SI, A. KOTAL, T.K. MANDAL, S. GIRI, H. NAKAMURA, T. KOHARA, *Size-Controlled Synthesis of Magnetite Nanoparticles in the Presence of Polyelectrolytes*, Chem. Mater., **16**, pp. 3489–3496, 2004.
- [16] K.G. PAUL, T.B. FRIGO, J.Y. GROMAN and E.V. GROMAN, *Synthesis of ultrasmall superparamagnetic iron oxides using reduced polysaccharides*, Bioconjugate Chemistry, **15**, pp. 394–401, 2004.
- [17] M. ALLEN, D. WILLITS, J. MOSOLF, M. YOUNG, T. DOUGLAS, *Protein cage constrained synthesis of ferrimagnetic iron oxide nanoparticles*, Adv. Mat., **14**, pp. 1562–1565, 2002.
- [18] B. CHERTOK, B.A. MOFFAT, A.E. DAVID, F. YU, C. BERGEMANN, B.D. ROSS, V.C. YANG, *Iron Oxide Nanoparticles as a Drug Delivery Vehicle for MRI Monitored Magnetic Targeting of Brain Tumors*, Biomaterials, **29**, pp. 487–496, 2008.
- [19] Q.-S. ZHAO, Y.-F. HUANG, Y. LI, J.-M. ZHANG, H.-Y. WANG, *Functionalized Magnetic Microparticles for Fast and Efficient Removal of Textile Dyes from Aqueous Solution*, Water Air Soil Pollut., **225**, pp. 1–12, 2014.
- [20] W.S. WAN NGAH, S. FATINATHAN, *Adsorption of Cu(II) ions in aqueous solution using chitosan beads, chitosan-GLA beads and chitosan–alginate beads*, Chem. Eng. J., **143**, pp. 62–72, 2008.
- [21] T. ANDERSEN, B.L. STRAND, K. FORMO, E. ALSBERG, B.E. CHRISTENSEN. *Alginates as biomaterials in tissue engineering*. In: Rauter AP (ed) *Carbohydrate Chemistry: Chemical and Biological Approaches*, 3<sup>rd</sup> edn. Cambridge, UK, pp. 227–239, 2012.

- [23] K. SARKAR, S. L. BANERJEE, P.P. KUNDU, *Removal of Anionic Dye in Acid Solution by Self Crosslinked Insoluble Dendronized Chitosan*, *Hydrol. Current. Res.*, **3**, pp. 3–15, 2012.
- [24] I.Y. KIMURA, V.T. FÁVERE, A.O. MARTINS, V.A. SPINELLI, A. JOSUÉ, *Adequacy of isotherm adsorption of black 5 reactive dye for crosslinked chitosan microspheres*, *Acta Scientiarum Maringá*, **23** (6), pp. 1313–1317, 2001.
- [25] S. BRUNAUER, P.H. EMMETT, E. TELLER, *Adsorption of gases in multimolecular layers*, *J. Am. Soc.* **60**, pp. 309–319, 1938.
- [26] J. SINGH, M. SRIVASTAVAB, J. DUTTA, P.K. DUTTA, *Preparation and properties of hybrid monodispersed magnetic  $\alpha$ -Fe<sub>2</sub>O<sub>3</sub> based chitosan nanocomposite film for industrial and biomedical applications*, *Int. J. Biological Macromolec.*, **48**, pp. 170–176, 2011.
- [27] Z.Y. MA, Y.P. GUAN, H.Z. LIU, *Synthesis and characterization of micron-sized monodisperse superparamagnetic polymer particles with amino groups*. *J. Polym. Sci. A: Polym. Chem.*, **43**, pp. 3433–3439, 2005.
- [28] J. QU, G. LIU, Y. WANG, R. HONG, *Preparation of Fe<sub>3</sub>O<sub>4</sub>-chitosan nanoparticles used for hyperthermia*, *Adv. Powder Technol.*, **21**, pp. 461–467, 2010.
- [29] J. BERGER, M. REIST, J.M. MAYER, O. FELT, N.A. PEPPAS, R. GURNY, *Structure and interactions in covalently and ionically crosslinked chitosan hydrogels for biomedical applications*, *European J. Pharma. Biopharmaceutics*, **57**, pp. 19–34, 2004.
- [30] C. PENG, Q. ZHAO, C. GAO. *Sustained Delivery of Doxorubicin by Porous CaCO<sub>3</sub> and Chitosan/Alginate Multilayers-Coated CaCO<sub>3</sub> Microparticles*, *Colloid Surf. A*, **353**, pp. 132–139, 2010.
- [31] J.C.P. BROEKHOFF, J.H. DE BOER, *Studies on Pore in Catalysts. X. Calculations of Pore Distributions from the Adsorption Branch of Nitrogen Sorption Isotherms in the Case of Open Cylindrical Pores*. *B Applications, J. Catal.*, **9**, pp. 15–27, 1967.
- [32] A. JORDAN, R. SCHOLZ, P. WUST, H. FÄHLING, R. FELIX, *Magnetic fluid hyperthermia (MFH): cancer treatment with AC magnetic field induced excitation of biocompatible superparamagnetic nanoparticles*, *J. Magn. Magn. Mater.*, **201**, pp. 413–419, 1999.
- [33] Z-T. TSAI, J-F. WANG, H-Y. KUO, C-R. SHEN, J-J. WANG, T-C. YEN, *In situ preparation of high relaxivity iron oxide nanoparticles by coating with chitosan: A potential MRI contrast agent useful for cell tracking*, *J. Magn. Magn. Mater.*, **322**, pp. 208–213, 2010.
- [34] C. SCHATZ, A. DOMARD, C. VITON, *Versatile and efficient formation of colloids of biopolymer-based polyelectrolyte complexes*, *Biomacromolecules*, **5**, pp. 1882–1892, 2004.
- [35] Y. WU, S. ZHANG, X. GUO, H. HUANG, *Adsorption of chromium (III) on lignin*, *Bioresour. Technol.* **99**, pp. 7709–7715, 2008.
- [36] W. HAN, C. LIU, R.A. BAI, *Novel method to prepare high chitosan content blend hollow fiber membranes using a non-acidic dope solvent for highly enhanced adsorptive performance*, *J. Membr. Sci.*, **302**, pp. 150–159, 2007.
- [37] G. ANNADURAI, L.Y. LING, J-F LEE, *Adsorption of reactive dye from an aqueous solution by chitosan: isotherm, kinetic and thermodynamic analysis*, *J. Hazard. Mat.*, **152**, pp. 337–346, 2008.
- [38] F. ROZADA, M. OTERO, A. MORÁN, A.I. GARCÍA, *Adsorption of heavy metals onto sewage sludge-derived materials*, *Bioresour. Technol.*, **99**, pp. 6332–6338, 2008.

# **Key Parameters Controlling The Stability and Reactivity of Micro and Nanostructured Materials: Energetics of Nanomaterials**

Speranta TANASESCU, Florentina MAXIM, Andreea NEACSU,  
Florina TEODORESCU, Alexandru MILEA

Institute of Physical Chemistry "Ilie Murgulescu" of the Romanian Academy,  
Splaiul Independentei 202, P.O. Box12-194, 060021 Bucharest, Romania

Nanotechnology involves the design, production and use of new materials, systems and functional structures having at least one characteristic dimension within the nanometer size regime (1-100nm). Based on the fact that properties of materials change at the nanoscale, nanotechnology takes advantage of this by applying selected property modifications to new applications and beneficial endeavor. At the same time, research to date suggests that some manufactured nanomaterials (MNMs) will present hazards based on their structure - as well as their chemistry - thus challenging many conventional approaches to risk assessment and management.

Due to the unique and unusual physical and chemical properties of the systems and structures at the nanoscale, the understanding of their behavior, especially as concerns their stability and reactivity, presents a host of questions and problems. In the present paper will be argued that the control of the thermodynamic properties and the understanding of their crossover when working at the nano-level are important steps in understanding the nanomaterial stability and the possibilities to interaction with the biologic systems. Some compounds from specific systems were selected for discussion: nanostructured multicomponent transition metal oxides; nanoalloys; bio-nonbio systems.

## **1. The Relationships Between the Morphology and Thermodynamic Properties of Nanocrystalline Perovskites**

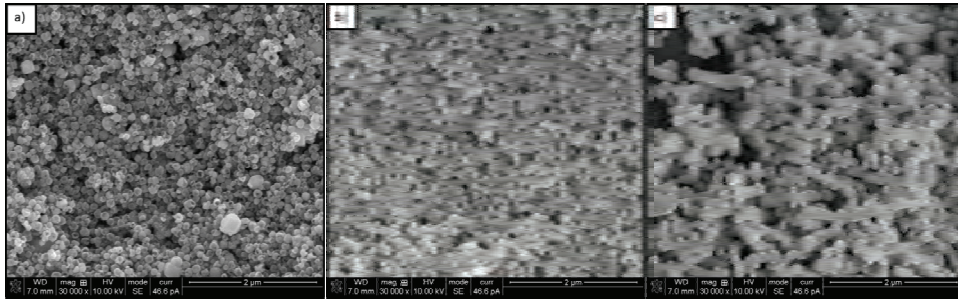
It is usually admitted that the properties of materials, and particularly of iono-covalent oxides, strongly depend on their mode of preparation and on their

biographic story, before and during their use. At the nanometric scale, a large variety of morphologies and related surface properties can exist for the same metal oxide. This means that a great deal of attention must be turned to the energetic parameters which play an important role in the overall properties and behaviour of materials. However thermodynamic aspects related to the changes in the morphology of the nanocrystalline multicomponent oxides have been little studied. In the Chemical Thermodynamics Laboratory from Institute of Physical Chemistry a detailed investigation of the thermodynamic properties of micro and nanostructured multicomponent oxides was initiated in order to evidence new features related to the effect of different compositional variables on the thermodynamic behavior. The focus of the present research was to emphasize modifications of the thermodynamic properties connected with the changes in the morphology in some oxide systems with perovskite structure. As an example one can quote works on the relationships between morphology and thermodynamic properties of nanocrystalline barium titanate ( $\text{BaTiO}_3$ ).

The barium titanate is one of the most studied perovskite-type material because of its dielectric, ferroelectric, and piezoelectric properties having great potential for technological applications in microelectronics, ferroelectrics, and optoelectronics. Of current concern is the extent to which bulk physical properties can be considered for the design of miniaturized thin-layer devices from the micro scale to the nano scale. This is because at nanoscale, a *pseudo* cubic, nonferroelectric structure, and with low dielectric constant value, is stabilized at room temperature [1, 2]. Previous studies showed that among barium titanate nanostructures, the one-dimensional (1D) morphology as nanotubes, nanorods, or nanowires presents a special interest because this kind of nanoparticles can conserve its high dielectric constant and ferroelectric switchability at nanoscale [3]. Our recent research evidenced new features related to the modifications in morphology connected with the synthesis method and demonstrated that the structure, size, and shape-controlled  $\text{BaTiO}_3$  crystalline nanoparticles can be obtained by hydrothermal treatments of precursors at relatively low temperatures (under  $\sim 408$  K) [4, 5]. The focus of the present analysis is to emphasize the relationship between modifications of the thermodynamic properties and the changes in the morphology of the nanocrystalline  $\text{BaTiO}_3$ .

The detailed synthesis procedure of barium titanate nanoparticles with different morphologies was previously reported [4, 5]. In short, the synthesis was performed in a high pressure Berghof BR-100 reactor starting from different precursors: titanium-based nanotubes and barium chloride when BThollow particles have been obtained [4], and from barium – titanium sol in the case of the BTcubes and BT1D nanopowders [5]. The precursors mixture was hydrothermally treated in the presence of sodium hydroxide at up to 408K (135°C) for 24 h. The samples were characterized afterwards by X-ray diffraction, Raman spectroscopy, SEM and TEM.

In Fig. 1 the SEM micrographs of the a) BThollow, b) BTcubes and c) BT1D barium titanate particles are presented. As can be noticed torus-like particles (Figure 1a) and cube-shaped nanoparticles (Fig. 1b) with narrow size distribution and average dimension of 125 nm are obtained by as referred hydrothermal treatment. Figure 1c revealed the formation of faceted elongated particles with average diameter of 147 nm and aspect ratio around 3 suggesting the one-dimensional (1D) feature of this sample.



**Fig. 1.** SEM micrographs of the a) BThollow, b) BTcubes and c) BT1D barium titanate particles.

For a more complex characterization, the morphological and structural analysis has been coupled with the evaluation of the thermodynamic characteristics in relation to significant changes in the overall concentration of defects. Thus, the structural differences between samples could be discussed also in terms of lattice point defects, which are of special importance in functional materials as they control their electronic properties. Because the oxygen vacancies play a key role in aging and fatigue of ferroelectric materials by impeding domain wall motion or by acting as local disturbances of the polarization [6, 7], the information about the concentration and mobility of this type of defects in barium titanate it is of special interest. Tanasescu *et al.* [8, 9] demonstrated that information regarding the concentration and distribution of the oxygen vacancies into the perovskite lattice of complex oxide compounds can be obtained by determining the thermodynamic properties of the oxygen dissolution in the perovskite phase, as well as by the equilibrium partial pressure of oxygen. It is for the first time when the comparison between the thermodynamic properties of hydrothermal prepared BaTiO<sub>3</sub> with different morphologies is discussed.

A solid state electrochemical method [8] was used to obtain the thermodynamic data represented by the relative partial molar free energies, enthalpies and entropies of oxygen dissolution in the perovskite phase ( $\Delta\bar{G}_{O_2}$ ,  $\Delta\bar{H}_{O_2}$ ,  $\Delta\bar{S}_{O_2}$ ), as well as the equilibrium partial pressures of oxygen as a function of temperature. In Figure 2 the  $\Delta\bar{G}_{O_2}$  as a function of temperature, in the

temperature range of 773 – 1273 K, for BThollow, BTcubes and BT1D samples is presented.

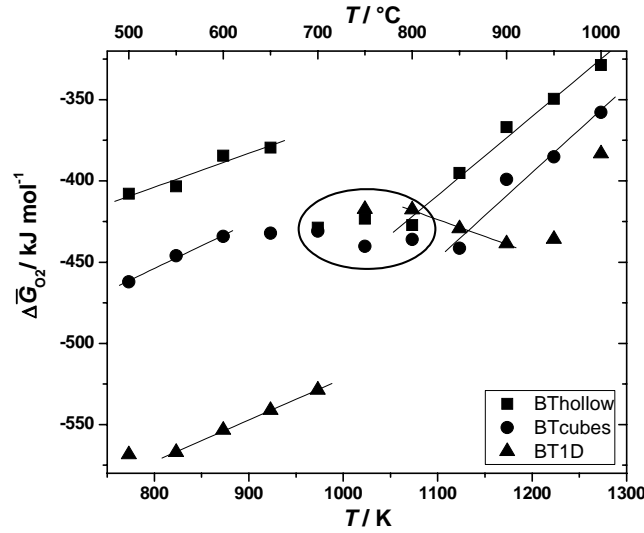
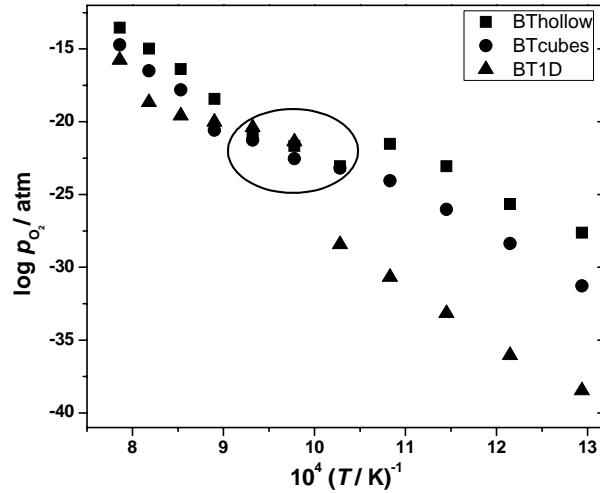


Fig. 2.  $\Delta\bar{G}_{O_2}$  as a function of temperature for BThollow, BTcubes and BT1D samples.

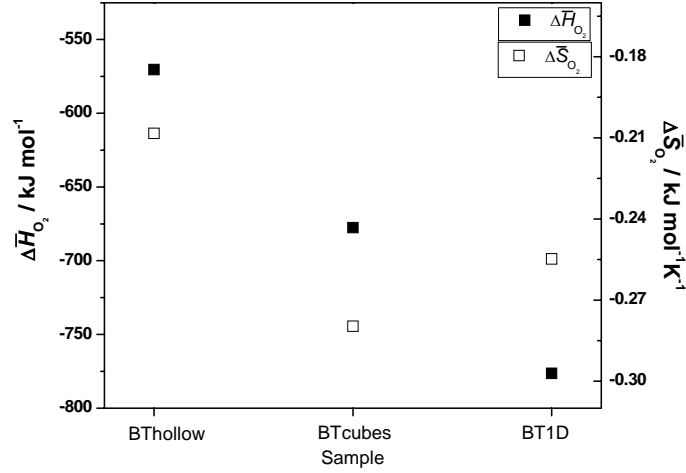
Three temperature regions can be observed for the variation of  $\Delta\bar{G}_{O_2}$ . Until 973 K, the partial molar energy increase with temperature for all samples, however the  $\Delta\bar{G}_{O_2}$  values of BT1D are with almost 100 kJ mol<sup>-1</sup> lower than  $\Delta\bar{G}_{O_2}$  of BTcubes and with more 150 kJ mol<sup>-1</sup> lower than  $\Delta\bar{G}_{O_2}$  of BThollow sample. The lowest the partial molar free energy value, the lowest the oxygen vacancy concentration is [9]. In the 973 – 1173 K temperature range, the  $\Delta\bar{G}_{O_2}$  shows weak temperature dependence for all morphologies with the observation that for 1D morphology the energy shows the constant value of 417 kJ mol<sup>-1</sup> at 1023 K and 1073 K. At temperatures higher than 1073 K, the partial molar energy has an increasing trend for BThollow and BTcubes samples, but for the BT1D only at higher temperature of 1273 K the increase is significant; however one can be noticed that even at this temperature the partial molar energy has lower values comparatively with hollow and cube-shaped nanoparticles.

In Fig. 3 the variation of  $\log p_{O_2}$  as a function of  $1/T$  for all the samples is presented.



**Fig. 3.** Variation of  $\log p_{O_2}$  as a function of  $1/T$  for the samples BThollow, BTcubes and BT1D.

One can be observed that the values of  $p_{O_2}$  obtained for the BT1D sample are almost one order of magnitude lower than the corresponding values of the oxygen partial pressure of the BTcubes and BThollow samples in the temperature range from 773–973 K. Finally, at temperatures higher than 1073 K, the  $p_{O_2}$  values obtained for both nanorods and nanocubes morphologies become comparable, but  $p_{O_2}$  values of BT1D sample are still lower comparatively with the other two morphologies. Based on the above presented results, the variation of  $\overline{\Delta G}_{O_2}$  and  $p_{O_2}$  with temperature suggest the lowest concentration of oxygen vacancies in the perovskite lattice for the barium titanate with 1D morphology in the temperature range below 973 K. Clarifications regarding the binding energy and the order in the oxygen sublattice of  $BaTiO_3$  perovskite structure can be achieved by determining the  $\overline{\Delta H}_{O_2}$  and  $\overline{\Delta S}_{O_2}$  values in temperature ranges in which the partial molar free energies are linear functions of temperature, namely 773–873 K for BTcubes, 823–973 K for BT1D and 773–923 K for BThollow (Fig. 2 and Fig. 4). The decreasing of the enthalpy and the increasing value of the entropy for BT1D suggest the increased binding energy of oxygen and the random distribution of the oxygen vacancies into the perovskite phase for the one-dimension barium titanate nanoparticles.



**Fig. 4.** The variation of  $\Delta\bar{H}_{O_2}$  and  $\Delta\bar{S}_{O_2}$  for the BThollow, BTcubes and BT1D samples.

The variation of the thermodynamic properties  $\Delta\bar{G}_{O_2}$ ,  $\Delta\bar{H}_{O_2}$  and  $\Delta\bar{S}_{O_2}$ , as well as  $p_{O_2}$  with temperature, indicated that 1D BaTiO<sub>3</sub> nanopowders have the lowest concentration of oxygen vacancies randomly distributed into the perovskite lattice and the highest binding energy of oxygen. The obtained results are significant in morphology - properties correlation for the perovskite-type oxide nanomaterials, indicating the enhancement of the thermodynamic properties for 1D shape morphology.

## 2. Thermodynamic Nanostructure Stabilization in the Metastable Alloys Systems

One of the challenging problems related to the understanding and practical exploitation of the enhanced properties of nanocrystalline materials is the thermal stabilization of a nanoscale grain size. The thermal stability of these microstructures is essential for adopting nanocrystalline materials in commercial processes and applications. Because the refinement in grain size is accompanied by a significant increase in volume fraction of grain boundaries, the thermal stability involves not only the stability of the grain structure, *i.e.* microstructure, but also the stability of the structure of the grain boundaries in nanocrystalline materials [12]. The lowering of interfacial energy with grain refinement and lattice strain in nanometer-sized crystallites plays an important role in controlling grain size stability of nanocrystalline materials during the grain growth in nanocrystalline phases [13-17].



By applying different analytical and simulation models, significant stabilization has been predicted for some nanocrystalline alloys synthesized through far from equilibrium processing techniques, such as vapor deposition and mechanical alloying [18-21]. By these methods a metastable equilibrium state at the nanoscale grain size can be produced such that the driving force for grain growth would be eliminated at a critical grain size. However a few systems have been provided experimental evidence that this thermodynamic approach can suppress grain growth and stabilize nanostructured polycrystals [22-24]. Such analyses need the thermodynamic data, because the driving forces for chemical reactions and diffusion can be given properly in terms of thermodynamic properties. Despite of the importance of this issue of research, the experimental information on the thermodynamic functions relevant for the thermodynamic evaluation of the processes associated with the formation of nanoalloy phases it is scarce and need to be investigated.

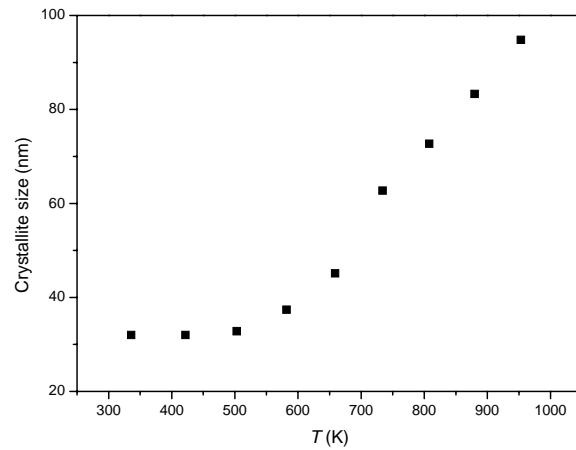
It has been a goal of our recent work [25, 26] to investigate the characteristic parameters that favor stable nanostructured phases in some systems of nanoalloys.

Ag-Cu is one of the nanoalloy systems which have received considerable attention for both applicative and fundamental reasons. Even though Cu and Ag are satisfying the Hume–Rothery criteria to form solid solutions, both elements presenting crystal structure similarity and an atomic size mismatch <15%, however they are mutually immiscible in the solid state under equilibrium conditions, and exhibit positive enthalpy of mixing [27]. Even though these alloys did not easily synthesized by conventional metallurgical methods, however the use of far from equilibrium processing techniques, such as vapor deposition and mechanical alloying, can extend the solid solubility in such systems [18-21]. Of particular interest for us is to evidence the role of the thermodynamic properties in controlling grain size stability of nanocrystalline material with eutectic composition Ag - 28% Cu.

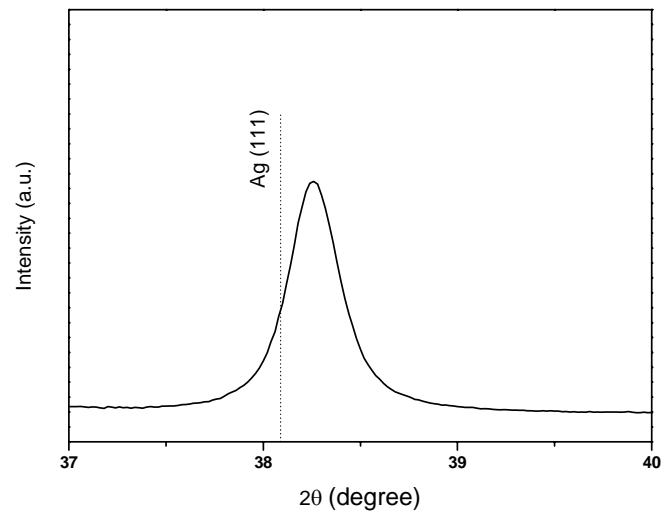
The eutectic composition mixture Ag + 28% wt. Cu has been processed by mechanical alloying (MA) route, starting from powders of Ag (Sigma Aldrich P99.9%) and Cu (Sigma Aldrich 99%) [25, 26]. The powders were mixed in appropriate amounts in a planetary ball mill Pulverisette 6 (Fritsch, Germany) under protective argon atmosphere and at different milling times (from 10 to 80 hours). The detailed technological parameters are described elsewhere [28]. Using Brookhaven 9Plus/BI-MAS technique it was determined that only samples milled for 80 hrs presented nanometric particle size distribution.

The microstructure of the sample after milling, as well as after milling with subsequent controlled annealing, was studied by powder X-ray diffraction (PXRD). The procedure was described in detail in our previous paper [25]. The most intense diffraction line associated with Ag-Cu alloys is shifted compared to the position of the pure Ag line, showing the formation of a solid solution  $\text{AgCu}_{ss}$  (Fig. 5). The medium crystallite size at room temperature and during heating until 973 K was

calculated and represented in Fig. 6 as a function of temperature. The crystallite size variation with temperature is not monotonous. Until about 500–550 K the crystallite size is stable. After this temperature, crystallite size rises with the temperature.



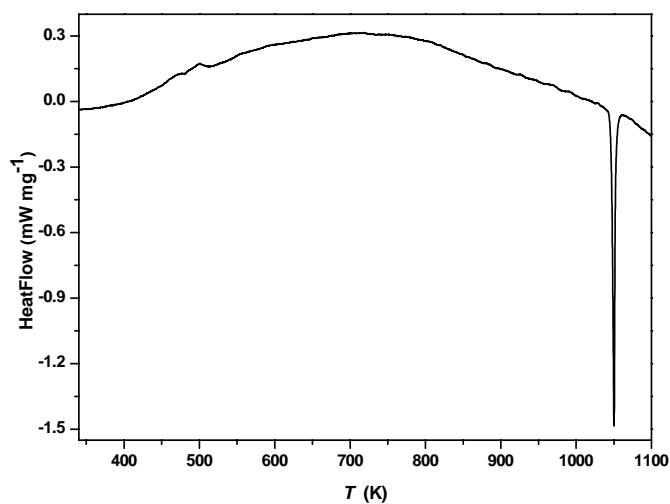
**Fig. 6.** Crystallite size (XRD measurements) of the Ag - 28% Cu mechanical alloyed nanopowders as a function of temperature.



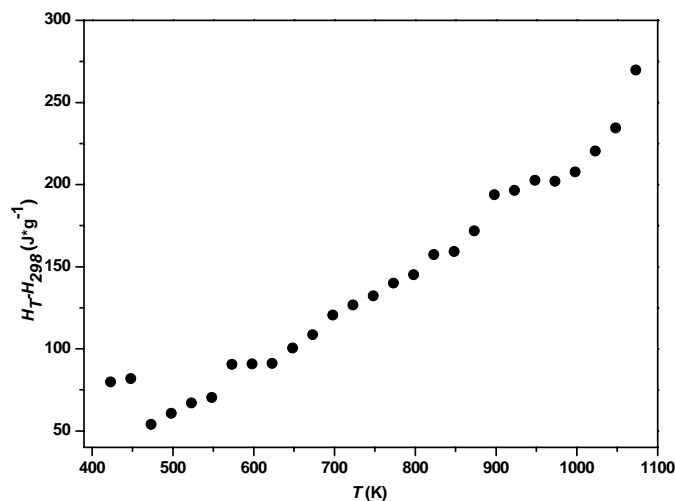
**Fig. 5.** XRD pattern of as-milled sample.

The thermal behavior of the processed samples was investigated under both non-isothermal regimes (by differential scanning calorimetry, using a DSC Setaram SETSYS Evolution 17 equipment) and in isothermal regime (by drop calorimetry

using a multi-detector high temperature calorimeter MHTC-96 of SETARAM in the drop mode (Figs. 7 and 8). A critical comparison of the results obtained by these methods revealed new features related to the occurrence of the micro-relaxation process (at about 448 and 473 450–480 KK), as well as of the correlative effects of decomposition and growth processes (from about 480 K to 973 K). These aspects were in detail discussed in our previous paper [25]



**Fig. 7.** DSC curves of the Ag - 28% Cu powders milled for 80 h.



**Fig. 8.** Temperature dependence of enthalpy increment ( $H_T - H_{298}$ ) of the Ag - 28% Cu powders obtained for 80 h milling times.

In order to further evaluate the previous results, the thermodynamic data represented by the relative entropy and free energy functions for Ag - 28% Cu nanopowders has been derived from the experimental enthalpy data and then represented as a function of temperature in Fig. 9.

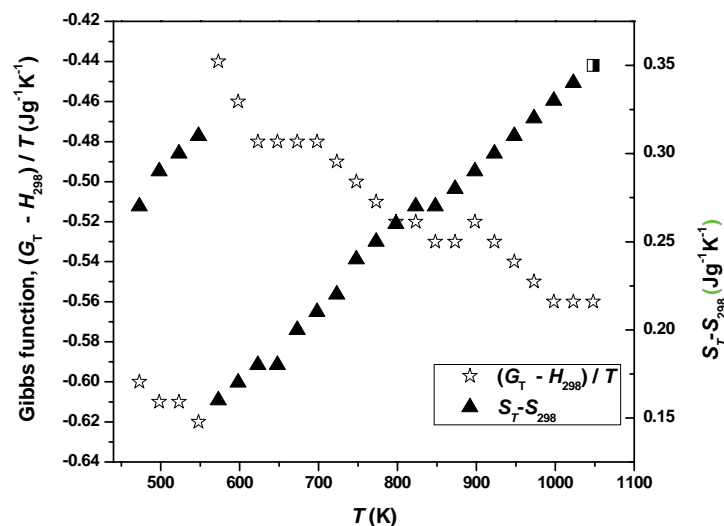


Fig. 9. Gibbs free energy function and relative entropy of the nanozised Ag - 28 % Cu powders as a function of temperature.

Then, the thermodynamic data were correlated with the results obtained from XRD analysis. It was observed an unusual variation of both crystallite size and thermodynamic data during heating (Fig. 6 and Fig. 9). Until temperatures around 500–550 K, the crystallite size does not increase with temperature, the medium crystallite size having about 32 nm. This statement suggests that in this interval the reduction in the grain boundary energy shows weak temperature dependence. Meanwhile, Gibbs function and entropy have particular evolution. The higher values for entropy at low temperatures, around 500 K, are explained by the nanocrystalline structure generated by processing using ball milling technique and are characteristic for the high degree of disorder present at the grain boundaries (Fig. 9). At the same time, the energy dependence has a free energy minimum at these temperatures, which corresponds to the range of stable crystallite size. This means that the free energy of the system reaches a local minimum with respect to the grain growth to some critical value of 32 nm. This result is in agreement with some previous studies [24, 29-33] speaking in the favor of the thermal stabilization of nanocrystalline metals and alloys. The onset temperature for grain growth process and the energy of activation for this process have higher values compared to the conventional materials. In the present case, when the temperature is higher

than 500 K, the crystallite size increases obviously with the increase of heating temperature (Fig. 6), suggesting that the equilibrium grain size decreases, aspect which is also in agreement with the evolution of the energetic parameters (Fig. 9).

The results obtained in the present study give for the first time evidence that the concept of thermodynamic nanostructure stabilization is a real phenomenon for the mechanically alloyed Ag-Cu nanopowders with eutectic composition. At this point further studies are in progress in our laboratory for the investigation of the stability of the Ag-Cu nanoalloys with different Ag/Cu ratio.

### **3. Investigation of the Changes in the Stability of Proteins in the Presence of Nanoparticles**

In the recent years there has been a renewed interest in the nanoparticle – protein interaction. This issue is particular useful for both scientific and applicative reasons. Studying bio-nano interactions is important not only for the understanding the biology functions at the nanoscale which opens new opportunities for more efficient diagnostics, therapeutics and tissue regeneration, so-called nanomedicine, but also to find key findings for nanosafety research which is an emerging field investigated in parallel with development of novel applications [34-36].

The protein adsorption layer that forms on the surface of nanoparticles is set by means of several forces such as hydrogen bonds, solvation forces, Van der Waals interactions, electrical interactions etc. [37, 38]. The nanoparticle surface can induce conformational changes in adsorbed protein molecules and can also introduce thermodynamic instability making it susceptible to chemical denaturation which may affect the overall bio-reactivity of the nanoparticle [39]. Thus, the thermodynamics of protein-nanoparticle interaction is a key issue when searching for both fields: nanomedicine use and assessment of the safety of nanomaterials.

In the Laboratory of Chemical Thermodynamics have been initiated studies having a principal goal the **thermodynamic characterization of the biomolecules–nanoparticle interaction**.

The study involves two important objectives:

- The investigation of the changes in protein stability (protein folding and denaturation) by measuring the thermodynamic properties represented by heat capacity, enthalpy and entropy of the protein thermal denaturation in the presence of nanoparticles.
- The investigation of the thermodynamic parameters characterising the binding biomolecule-nanoparticle interaction, namely:  $K_d$ , dissociation constant;  $n$ , the number of binding sites per biomolecule;  $\Delta H$ , enthalpy changes;  $\Delta G$ , Gibbs energy changes;  $\Delta S$ , entropy changes of binding interaction.

In the present paper will attempt to address the former one, this issue being directly related to the proposed subject of this work.

For the experiments of protein denaturation in the presence of TiO<sub>2</sub> nanoparticle, were chosen human serum albumin (HSA) and TiO<sub>2</sub> rutile nanoparticle (NP) in order to investigate the possibility of a complex formation. HSA is generally used as a model protein in many studies and TiO<sub>2</sub> NP is the widely used in research and industry fields. The aim of this work is to discuss the importance of thermodynamic parameters in predicting the stability of the system HSA-TiO<sub>2</sub> with regard to possible biological consequences.

The human serum albumin (HSA) - purity 99% and TRIS buffered saline (TBS) tablets, pH 7.6 were purchased from Sigma Aldrich Chemical Company. The rutile mineral form of titanium dioxide is a surface area reference material provided by Quantachrome Instruments with a multi-point BET surface area = 13.82 (m<sup>2</sup>/g). The medium crystallite size calculated by powder X-ray diffraction (PXRD) has been of 23.3 nm. The HSA lyophilized solid powder was dissolved in TRIS buffered saline (TBS) solution at pH 7.6. Ultrapure water with conductivity lower than 4.87 μS has been used for the solution preparation. The TiO<sub>2</sub> nanopowders in different concentrations (1, 4, 7 and 10 μg/ml) have been dispersed in the 10 mg/ml HAS-TBS solution using ultrasonic bath (45 kHz) for 3h at 30°C. The resulting suspensions were incubated at 37°C for 1h, under gentle magnetic stirring at 250 rpm. Afterwards, considering that the protein-nanoparticles complexation reaction reached the equilibrium, the mixture was centrifuged using a Hermle centrifuge, model Z 326K at 12000 rpm for 30 min. Two fractions have been obtained: the top fraction containing the protein excess (fraction 1) and the bottom fraction (fraction 2) with the protein-nanoparticles complex. For each TiO<sub>2</sub> suspensions, denoted S<sub>1</sub>, S<sub>2</sub>, S<sub>3</sub>, S<sub>4</sub> corresponding to the initial concentrations of 1, 4, 7 and 10 μg/ml, respectively, fraction 2 has been collected for further analysis. As reference, pure HAS in TBS solution has been considered and the sample was indexed as S<sub>0</sub>.

The thermodynamic behavior of the HSA/TiO<sub>2</sub> systems has been investigated by Calorimetry using a T.A. Instruments differential scanning NanoCalorimeter model 6300, in the temperature range from 293.15 K to 363.15 K at a scanning rate of 2 K/min.

Figure 10 shows the heat capacity versus temperature profiles for the thermal denaturation of HAS in the absence and in the presence of TiO<sub>2</sub> of different concentrations. Changes in the C<sub>p</sub> are believed to originate from the disruption of the forces stabilizing native protein structure [40]. Associated with protein unfolding process, ΔC<sub>p</sub> occurs as a result of changes in hydration of side chains, which are buried in the native conformation but become exposed to the solvent in a denatured state [40-42]. Any change in the conformation would affect the position, sharpness, and shape of transition(s) in DSC scans. One can notice that the DSC profile is sharper in the absence of TiO<sub>2</sub>. The heat capacity corresponding to the transition temperature decrease with the increase in TiO<sub>2</sub> concentration and the transition temperature range enlarged for the sample with higher TiO<sub>2</sub>

concentration. The increase in width of the transition peaks can be due to a larger conformational heterogeneity in the surface-bound proteins and/or a less cooperative heat denaturation process [43].

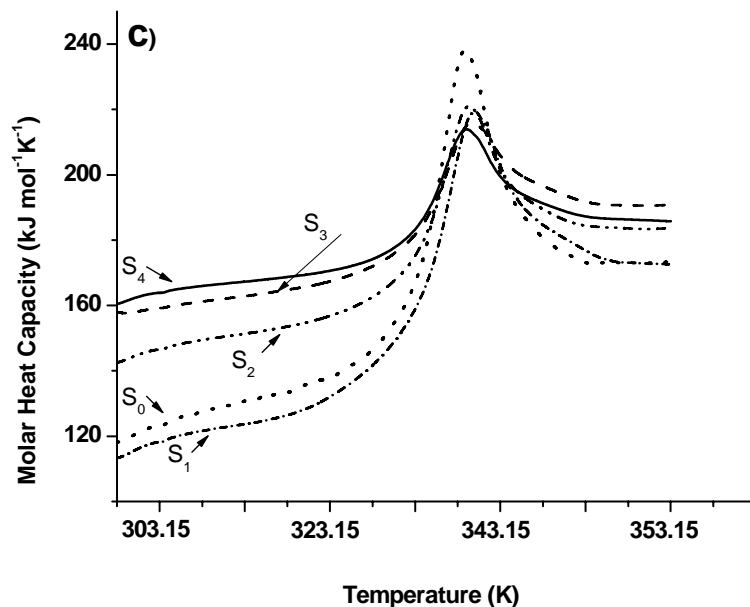


Fig. 10. The variation with temperature of the heat capacity in the presence of TiO<sub>2</sub> of different concentrations.

From DSC experiments, the thermodynamic parameters of unfolding as a result of heat denaturation could be obtained. The enthalpy function can be measured through integration of the Cp:

$$\Delta H = \int_{T_1}^{T_2} \Delta C_p dT \quad (1)$$

$\Delta H$  indicates total heat energy uptake by the sample after suitable baseline correction affecting the transition [43].

Accordingly, the entropy change could be obtained from the equation:

$$\Delta S = \int_{T_1}^{T_2} \frac{\Delta C_p}{T} dT \quad (2)$$

In the Table 1 are presented the thermodynamic functions calorimetrically obtained for fraction 2, together the van't Hoff enthalpy calculated by the van't Hoff equation [44] when the transition is assumed to be of the two-state type, that

is, the native form is converted directly to the denatured form, without passing through an intermediate [40, 45, 46]. In two-stage behavior, the ratio  $\Delta H_{vH} / \Delta H_{cal} = 1$ . However, according to our data, for smaller concentrations of  $TiO_2$ ,  $\Delta H_{vH} / \Delta H_{cal} < 1$ , indicating that the fraction of the macromolecules in the native form decreases, and the result is an enhancement of the equilibrium constant value and the decreasing of  $\Delta H_{vH}$ . Instead, for higher concentrations of  $TiO_2$ ,  $\Delta H_{vH}$  is more than  $\Delta H_{cal}$  and the intermolecular cooperation is shown [40]. So, the results are indicative for complex transitions.

**Table 1.** Calculated thermodynamic data

Sample	$\Delta H_{cal}$ (kJmol <sup>-1</sup> )	$\Delta S$ (kJmol <sup>-1</sup> K <sup>-1</sup> )	$\Delta H_{vH}$ (kJmol <sup>-1</sup> )
S <sub>1</sub>	598.84	1.86	471.61
S <sub>2</sub>	391.47	1.16	378.36
S <sub>3</sub>	301.95	0.93	331.09
S <sub>4</sub>	289.21	0.87	328.27

From the Table 1, one can observe that increasing of the  $TiO_2$  concentration, the enthalpy change is decreasing. The value of the denaturation enthalpy for BSA in the absence of  $TiO_2$  has been also determined and found to be of 737.53 kJmol<sup>-1</sup>. Comparing with this value, it can be concluded that  $\Delta H$  decreases upon adsorption, indicating that BSA has a lower structural stability in the adsorbed state than in solution. Decreases in structural stability due to adsorption have been reported earlier for soft proteins such as BSA [43]. This effect is more pronounced for the higher concentration of  $TiO_2$ .

Further examination of the enthalpy and entropy changes shows that the complexation between NP and BSA involves unfavorable enthalpy change ( $\Delta H > 0$ ) which is compensated by favorable entropy gain ( $\Delta S > 0$ ), resulting in overall negative free energy changes ( $\Delta G$ ) (according to Gibbs law of free energy:  $\Delta G = \Delta H - T\Delta S$ ). This statement is indicative for the enthalpy-entropy compensation process, which is commonly observed for many host-guest complexes [47, 48]. The positive entropy changes obtained for these interactions reflect the extensive desolvation during complexation, being in agreement with some previous results showing that in complexation of smaller proteins like BSA, higher degree of surface interaction results from the release of a large amount of the water of hydration from the binding interface [47].

This result, together the previous analysis resulting by comparing  $\Delta H_{vH}$  and  $\Delta H_{cal}$  speak in the favor of the competition between the stabilizing forces, leading to the unfolding of the protein and the intermolecular cooperation factors [40]. At this point further studies are in progress for the thermodynamic analysis of protein



interactions with nanoparticles by using isothermal titration calorimetry (ITC) which is a powerful tool to resolve the nature of supramolecular interaction which is very crucial for further applications.

#### 4. Conclusions

This article has summarized some of the recent efforts performed in the Laboratory of Chemical Thermodynamics in uncovering the key factors governing the stability and reactivity of some structural nanocrystalline materials. Several conclusions can be drawn from the characterization data obtained so far.

- Exploring the relationships between morphology and thermodynamic properties of nanocrystalline BaTiO<sub>3</sub>, we obtained that particular behavior of the one-dimensional (1D) morphology could be explained not only qualitatively by the structural changes, but also by the fact that the energetic properties are extremely sensitive to the chemical defects in oxygen sites. Comparatively with BThollow and BTcubes, the BT1D nanopowders have the lowest concentration of oxygen vacancies randomly distributed into the perovskite lattice and the highest binding energy of oxygen. The obtained results are significant for the understanding of processing-structure relationships, indicating the role of the thermodynamic properties in obtaining shape-controlled perovskite-type oxide nanomaterials.

- Investigating the metastable phases of nanoalloys synthesized by severe deformation non-equilibrium methods we obtained that the energetic parameters may be used to explain the experimentally observed stability in particular temperature ranges associated with the growth process of nanometer-sized in comparison with that of micrometer-sized samples. We proved for the first time evidence that, the concept of thermodynamic nanostructure stabilization is a real phenomenon for the mechanically alloyed Ag-Cu nanopowders with eutectic composition.

- In relation to bio-reactivity of the nanomaterials, the investigation of the changes in protein stability in the presence of nanoparticle is an important issue of research. As a first step of this study, the temperature-dependence of the heat capacity and the enthalpy measurements generate additional information on the adsorption-induced changes in structural stability of the proteins. The obtained results on the thermal denaturation of BSA in the presence of TiO<sub>2</sub> nanopowder show that the NP surface can introduce thermodynamic instability to the adsorbed protein molecule making it susceptible to chemical denaturation. Further studies by ITC will provide insight into the nature of supramolecular interaction between a biological macromolecule and a nanoparticle.

#### References

- [1] K. UCHINO, E. SADANAGA, T. HIROSE, *Dependence of the Crystal-Structure on Particle-Size in Barium-Titanate*, J Am Ceram Soc, **72**, 8, pp. 1555–1558, 1989.

- [2] M.H. FREY, D.A. PAYNE, *Grain-size effect on structure and phase transformations for barium titanate*, Phys Rev B, **54**, 5, pp. 3158–3168, 1996.
- [3] A.N. MOROZOVSKA, E.A. ELISEEV, M.D. GLIUNCHUK, *Size effects and depolarization field influence on the phase diagrams of cylindrical ferroelectric nanoparticles*, Physica B Condens Matter, **387**(1-2), pp. 358–366, 2007.
- [4] F. MAXIM, D. BERGER, F. TEODORESCU, C. HORNOIU, C. LETE, T. TANASESCU, *Low-Temperature Synthesis and Thermodynamic and Electrical Properties of Barium Titanate Nanorods*, J. Nanomater, **2015**, pp. 1–10, 2015.
- [5] F. MAXIM, I. POENARU, F. TEODORESCU, S. TANASESCU, *Barium Titanate Torus-Like Particles: Low-Temperature Synthesis and Formation Mechanism*, Eur J Inorg Chem, **30**, pp. 5160–5167, 2014.
- [6] U. ROBELS, G. ARLT, *Domain wall clamping in ferroelectric by orientation of defects*, J Appl Phys, **73**(7), pp. 3454–3460, 1993.
- [7] G. ARLT, H. NEUMANN, *Internal bias in ferroelectric ceramics: origin and time dependence*, Ferroelectrics, **87**(1), pp. 109–120, 1988.
- [8] S. TANASESCU, N.D. TOTIR, D.I. MARCHIDAN, *Thermodynamic data of the perovskite-type  $LaMnO_{3\pm\chi}$  and  $La_{0.7}Sr_{0.3}MnO_{3\pm\chi}$  by a solid-state electrochemical technique*, Electrochim Acta **43**, 12-13, pp. 1675–1681, 1998.
- [9] S.TANASESCU, Z. YANG, J. MARTYNCZUK, F. TEODORESCU, A. BOTEAN, N. TOTIR, L.J. GAUCKLER, *Effects of A-site composition and oxygen nonstoichiometry on the thermodynamic stability of compounds in the Ba-Sr-Co-Fe-O system*, J Solid State Chem **200**, pp. 354–362, 2013.
- [10] D.K. LEE, H.I. YOO, *Oxygen nonstoichiometry of undoped  $BaTiO_{3-\delta}$* , Solid State Ionics, **144**(1-2), pp. 87–97, 2001.
- [11] H.S. KWON, H.I. YOO, C.H. KIM, K.H. HUR, *Semiconductor-to-insulator transition of undoped- $BaTiO_3$  in quenched state*, J. Appl Phys, **107**(8), 2010.
- [12] C.C. KOCH, *Processing Structure Property Relationships in Ultrafine Grain and Nanocrystalline Materials*, JPCS **144**, 2009.
- [13] J. WEISSMULLER, *Alloy thermodynamics in nanostructures*, J. Mater. Res., **9**, pp. 4–7, 1997.
- [14] B.S. MURTY, M.K. DATTA, S.K. PABI, *Structure and thermal stability of nanocrystalline materials*, Sadhana **28**, pp. 23–45, 1993.
- [15] K. LU, *Nanocrystalline metals crystallized from amorphous solids: nanocrystallization, structure and properties*, Mater Sci Eng, **16**, pp. 161–221, 1996.
- [16] H. GLEITER, *Nanostructured materials: basic concepts and microstructure*, Acta Mater **48**, pp. 1–29, 2000.
- [17] M.K. DATTA, *Synthesis and characterization of nanocrystalline silicides by mechanical alloying in Fe–Ni–Si system*, PhD thesis, Indian Institute of Technology, Kharagpur, 2001.
- [18] P. DUWEZ, R.H. WILLENS, W. KLEMENT, *Continuous series of metastable solid solutions in silver–copper alloys*, J. Appl Phys **31**, pp. 1136–1137, 1996.
- [19] R.K. LINDE, *Lattice parameters of metastable silver–copper alloys*, J. Appl Phys **37**, pp. 934, 1996.
- [20] K. UENISHI, K.F. KOBAYASHI, K.Y. ISHIHARA, P.H. SHINGU, *Formation of a supersaturated solid solution in the Ag–Cu system by mechanical alloying*, Mater. Sci. Eng. **134**, pp. 1342–1345, 1991.
- [21] J.H. HE, H.W. SHENG, E. MA, *The enthalpy state of amorphous alloys in an immiscible system*, Appl. Phys. Lett. **78**, pp. 1343–1345, 2001.
- [22] A.J. DETOR, C.A. SCHUH, *Grain boundary segregation, chemical ordering and stability of nanocrystalline alloys: Atomistic computer simulations in the Ni–W system*, Acta Mater. **55**, pp. 4221, 2007.

- [23] A.J. DETOR, C.A. SCHUH, *Microstructural evolution during the heat treatment of nanocrystalline alloys*, J. Mater. Res. **22**, pp. 3233, 2007.
- [24] T. CHOOKAJORN, H.A. MURDOCH, C.A. SCHUH, *Design of Stable Nanocrystalline Alloys*, Science **337**, pp. 951–954, 2012.
- [25] A. MILEA, O. GINGU, S. PREDA, G. SIMA, C. NICOLICESCU, S. TANASESCU, *Thermodynamic measurements on Ag-28% Cu nanopowders processed by mechanical alloying route*, J. Alloys Comp. **629**, pp. 214–220, 2015.
- [26] S. TANASESCU, A. MILEA, O. GINGU, F. MAXIM, C. HORNOIU, S. PREDA, G. SIMA, *A correlation between thermodynamic properties, thermal expansion and electrical resistivity of Ag-28% Cu nanopowders processed by the mechanical alloying route*, Phys. Chem. Chem. Phys., 2015, DOI: 10.1039/C5CP01390A.
- [27] J.L. MURRAY, *Calculations and stable of metastable equilibrium diagrams of the Ag–Cu and Cd–Zn systems*, Metall Trans **A 15**, pp. 261–268, 1984.
- [28] O. GINGU, C. NICOLICESCU, G. SIMA, *Research of the milling time influence on Ag–Cu powder particle size processed by mechanical alloying route*, Solid State Phenom **188**, pp. 382–387, 2012.
- [29] H.A. MURDOCH, C.A. SCHUN, *Estimation of grain boundary segregation enthalpy and its role in stable nanocrystalline alloy design*, J. Mater. Res. **28**, pp. 2154–2163, 2013.
- [30] A.J. DETOR, C.A. SCHUH, *Tailoring and patterning the grain size of nanocrystalline alloys*, Acta Mater. **55**, pp. 371–379, 2007.
- [31] M. SABER, C.C. KOCH, R.O. SCATTERGOOD, *Thermodynamic Grain Size Stabilization Models: An Overview*, Mater Res Let. **3**, pp. 65–75, 2015.
- [32] J. WEISSMULLER, P. BUNZEL, G. WILDE, *Two-phase equilibrium in small alloy particles*, Scripta Mater., **51**, pp. 813–818, 2004.
- [33] C.C. KOCH, R.O. SCATTERGOOD, M. SABER, H. KOTAN, *High temperature stabilization of nanocrystalline grain size: Thermodynamic versus kinetic strategies*, J. Mater. Res. **28**, pp. 1785–1791, 2013.
- [34] I. LYNCH, I.L. FEITSHANS, M. KENDALL, *Bio-nano interactions: new tools, insights and impacts: summary of the Royal Society discussion meeting*, Phil Trans R Soc **B 370**, 20140162, 2015.
- [35] *Research progress on environmental, health, and safety aspects of engineered nanomaterials*, National Academy of Sciences, 2013.
- [36] *Nanosafety in Europe 2015-2025: Towards Safe and Sustainable Nanomaterials and Nanotechnology Innovations*, This publication is carried out during the years 2011-2013 by the request of the European Commission.  
<http://www.nanosafetycluster.eu/news/83/66/Nanosafety-in-Europe-2015---2025.html>, Nanosafety cluster, Finnish Institute of Occupational Health, 2013.
- [37] M.S. ZAQOUT, T. SUMIZAWA, H. IGISU, T. HIGASHI, T. MYOJO, *Binding of human serum proteins to titanium dioxide particles in vitro*, J Occup Health **53**(2), pp. 75–83, 2011.
- [38] P. BIHARI, V. MINNAMARI, S. STEPHAN, P. MARC, G.K. ALEXANDER, A.R. CRISTOPH, C. CONRAD, T. TIMO, R. MARKUS, K.FRITZ, *Optimized dispersion of nanoparticles for biological in vitro and in vivo studies*, Part Fibre Toxicol, **5**(14), pp. 1–14, 2008.
- [39] S.R. SAPTARSHI, A. DUSCHL, A.L. LOPATA, *Interaction of nanoparticles with proteins: relation to bio-reactivity of the nanoparticle*, J. Nanobiotechnology **11**(26), 2013.
- [40] P. GILL, T.T. MOGHADAM, B. RANJBAR, *Differential Scanning Calorimetry Techniques: Applications in Biology and Nanoscience*, J Biomol Tech, **21**, pp. 167–193, 2010.
- [41] J. STURTEVANT, *Biochemical applications of differential scanning calorimetry*, Annu Rev Phys Chem, **38**, pp. 463–488, 1987.
- [42] D.T. HAYNIE, E. FREIRE, *Estimation of the folding/unfolding energetics of marginally stable proteins using differential scanning calorimetry*, Anal Biochem **216**, pp. 33–41, 1994.

- [43] H. LARSERICSDOTTER, S. OSCARSSON, J. BUIJS, *Thermodynamic Analysis of Proteins Adsorbed on Silica Particles: Electrostatic Effects*, Journal of Colloid and Interface Science **237**, pp. 98–103, 2001.
- [44] A. COOPER, M.A. NUTLEY, A. WALLOD, *Differential scanning microcalorimetry*. In *Harding SE, Chowdhry BZ (eds): Protein-Ligand Interactions: Hydrodynamics and Calorimetry*, Oxford, UK: Oxford University Press, pp. 287–318, 2000.
- [45] K.J. BRESLAUER, E. FREIER, M. STRAUME, *Calorimetry: a tool for DNA and ligand-DNA studies*, Methods Enzymol **211**, pp. 533–567, 1992.
- [46] L. ISEULT, A.D. KENNETH, J.R. LEAD, E. VALSAMI-JONES, *Macromolecular Coronas and Their Importance in Nanotoxicology and Nanoecotoxicology*, Frontiers of Nanoscience **7**, 2014.
- [47] D.E. MRINMOY, *Engineering the Nanoparticle Surface for Protein Recognition and Applications*, 2009, Dissertation.
- [48] K.N. HOUK, A.G. LEACH, S.P. KIM, X. ZHANG, Angew. Chem. Int. Ed., **42**, pp. 4872–4897, 2003.

# Experiments with Possible Application to the Homogenous Solutions of Solid Nanostructures with Liquid Solvents

Mariana TEODORESCU

Department of Chemical Thermodynamics, "Ilie Murgulescu" Institute of Physical Chemistry, Romanian Academy, Splaiul Independentei 202, 060021 Bucharest, Romania

E-mail: [mateodorescu@icf.ro](mailto:mateodorescu@icf.ro)

**Abstract.** In this paper examples of own data of vapor-liquid equilibrium (VLE), thermodynamic and thermophysical properties of binary ionic liquids (ILs) (1-butyl-3-methylimidazolium chloride, bromide and iodide) with organic solvents (1-butanol or water) mixtures are presented. Two from the ILs are solids in normal conditions. From the data obtained, the vapor-liquid phase diagrams, excess molar Gibbs energy, heats of mixing or excess molar enthalpies, densities and excess molar volumes, refractive indexes, surface tensions, dielectric permittivities and their deviations from ideality, are presented. The data thermodynamic modeling is shown, for their accuracy demonstration. The same type of data can be obtained for systems composed of solid nanostructures with liquid solvents, with practical application in actual top energetic nanotechnologies.

## 1. Introduction

Recently, the ionic liquids (ILs) have become solvents with large applicability because of their very special properties: low melting points and a wide range of temperature in which they exists in liquid state, reasonable viscosity, chemical stability up to very high temperatures, high solubility in nonpolar or polar organic solvents, high conductivity, negligible vapor pressure and therefore non-flammability. These make that ILs be used in so-called green chemistry, for partial or total replacement of volatile organic solvents which are, as it is known, flammable and toxic. They can be very interesting solvents for a variety of industrial applications [1]. Beyond these, they are much discussed as selective solvents (entrainers) for various separation processes [2, 3]. The methods of their synthesis are well developed [4], but for various scopes it should be well known their properties, in many cases for their mixtures with organic solvents. For a better understanding of their thermodynamic behavior, correlated with the development of predictive thermodynamic models, phase equilibria data and thermodynamic and

thermophysical properties are required. As a result, in recent years, various research groups in the world began systematic studies; currently there are more than 12,000 sets of experimental data containing over 58,000 points accumulated in Dortmund Data Bank. They are not far enough, even more many of them are not of satisfactory precision [5] for verifying or development of adequate predictive thermodynamic models involved. Therefore, with our new research project concerning the thermodynamics of ILs with organic solvent mixtures, we aim to enrich the existing data bank and to bring qualitatively original contributions.

It is well known that alcohols form azeotropes with water being difficult to separate and to obtain desired alcohols of high purity without using an appropriate entrainer. It has been shown that new generation green solvent ionic liquids can be good in this role. To describe the VLE for the ternary water-alcohol-IL system, VLE for the constituent binary subsystems are required. The VLE experimental data for 1-butanol + water system are known from old literature [6-8] while for 1-butyl-3-methylimidazolium chloride ([bmim]Cl), bromide ([bmim]Br) or iodide ([bmim]I) + water systems they were already reported [9]. Here, we determined experimental isothermal VLE data for these three ILs with 1-butanol binary systems at the temperature of 363.15 K in a limited composition range due to the reduced quantity of expensive ILs which was at disposal. In addition, refractometric measurements at the temperature of 308.15 K have been performed for whole composition range. From refractive index of mixture and densities of the pure components at the same temperature, the densities, the excess molar volumes, surface tensions and dielectric permittivities and their deviations vs. composition data of the binary mixture have been predicted by Lorenz-Lorentz ( $n_D$ - $\rho$ ) mixing rule [10] or by known equations [11, 12]. As far as we know, no experimental data exist in the literature concerning these binary systems [9]. The phase equilibria, thermodynamic and thermophysical data reported here bring new information required for the design of the separation process of 1-butanol using organic salts as [bmim]Cl, [bmim]Br, and [bmim]I and an insight into specific inter and intra molecular interactions or into structural arrangements existing in the binary IL + 1-butanol system.

Other binary system of industrial interest is that of [bmim]Cl + water. For it, many properties are available [9]. Only excess molar enthalpies are missing [9]. Therefore they were measured in this work. Due to experimental restrictions, these properties have been determined at 303.15 K and high dilution of water, in the range of 0.0009–0.0160 mole fraction of IL.

## **2. Experimental**

### **2.1. Materials**

The chemicals used for the VLE and refractive index measurements were of high purity, imported from commercial sources. The characteristics of the used compounds are summarized in Table 1. After purification, all chemicals were deposited in closed system to dried atmosphere, on calcium chloride, during all

experiments. A good comparison with literature values has been obtained for the density and ultrasonic sound velocity experimental values of the pure compounds. Also a good comparison was found for the refractive index and the vapor pressure of 1-butanol. This is shown in Table 2.

The samples of the ionic liquid 1-butyl-3-methylimidazolium chloride [bmim]Cl for the heat of mixing measurements was vacuum dried at 301.15 K for four days, at 316.15 K for 2 days at 0.1 kPa and stored as described above. Water was double distilled and deionized before use.

**Table 1.** Commercial sources, purities and methods of purification of the used chemical compounds for the VLE and refractive index measurements

Compound	Commercial source	Purity / mass fraction	Purification method
[bmim]Cl	Fluka	> 0.980	Dried in the oven at 70°C and 20 kPa for 48 hours; content of water after drying: 0.0004 mass fraction
[bmim]Br	Fluka	> 0.970	Dried in the oven at 70°C and 0.1 kPa for 10 days; water content after drying: < 0.001 mass fraction
[bmim]I	Aldrich	> 0.990 with $\leq 0.005$ water content	Dried in oven under vacuum of 0.1 kPa at 70°C for 48 hours; water content after purification: 0.0007 mass fraction
1-butanol	Riedel de Hen	> 0.995	Dried and stored on molecular sieves 4Å

**Table 2.** Refractive indices,  $n_D$ , densities,  $\rho$ , and ultrasonic sound velocity,  $s$ , at atmospheric pressure and vapor pressures,  $P$ , of pure compounds

Compound / $T^\circ / \text{K}$	$n_D^a$		$\rho^b / (\text{g cm}^{-3})$		$s^c / (\text{m s}^{-1})$		$P^d / \text{kPa}$	
	This work	Lit.	This work	Lit.	This work	Lit.	This work	Lit.
[bmim]Cl / 308.15	1.4990		1.0754	1.07651 <sup>i</sup> 1.06832 <sup>j</sup>	1839.2	1848 <sup>j</sup>		
[bmim]Br / 308.15	1.5326	1.5420 <sup>f</sup> 1.54 <sup>g</sup>	1.2843	1.290 <sup>f</sup>	1642.1			
[bmim]I / 308.15	1.5781	1.5670 <sup>f</sup>	1.4717	1.480731 <sup>k</sup> 1.450 <sup>f</sup>	1473.3			
1-butanol / 308.15 363.15	1.3931	1.39342 <sup>h</sup>	0.7981	0.79821 <sup>h</sup>	1207.0	1206.26 <sup>b</sup>	33.56	34.19 <sup>l</sup>

Standard uncertainties,  $u$ : <sup>a</sup> $u_{nD} = 0.0001$ , <sup>b</sup> $u_{\rho} = 0.0001 \text{ g cm}^{-3}$ , <sup>c</sup> $u_s = 0.1 \text{ m s}^{-1}$ , <sup>d</sup> $u_P = 0.1\%$  of measured value, and <sup>e</sup> $u_T = 0.01 \text{ K}$  for density, refractive index and speed of sound measurements, <sup>e</sup> $u_T = 0.1 \text{ K}$  for vapor pressure measurements. <sup>f</sup>[13]; <sup>g</sup>[14]; <sup>h</sup>[15]; <sup>i</sup>[16]; <sup>j</sup>[17]; <sup>k</sup>[18]; <sup>l</sup>[19].

## 2.2. Methods

**The vapor pressure measurements** of pure 1-butanol and of the binary mixtures were carried out by an ebulliometric method using a Swietoslawski ebulliometer modified according to Rogalski and Malanowski [20]. The apparatus, is described in details elsewhere along with the experimental procedure [21], usually employed [20, 22, 23].

**The equilibrium temperatures** in the ebulliometer were measured with an accuracy of  $\pm 0.1$  K, by means of mercury thermometers (previously calibrated at National Institute of Metrology, Bucharest).

**The vapor pressure was measured** by means of a mercury manometer. Manometric readings were performed with a cathetometer to an accuracy of  $\pm 0.1$  mm, and pressure reproducibility was estimated to be better than 50 Pa. The accuracy of the pressure measurements is estimated to be 0.1% of measured values. The composition of the liquid phase in equilibrium with the vapor phase was analyzed by the refractometric method making use of a calibration curve obtained by measurements of the refractive index of weighed samples (accuracy better than  $\pm 0.2$  mg by GH-252 A&D Japan balance) at one constant temperature and data correlation with Redlich-Kister polynomials [24] with three parameters in the form:

$$n_D^E = n_D - [xn_{D,1} + (1-x)n_{D,2}] = x(1-x)[a_0 + a_1(1-2x) + a_2(1-2x)^2] \quad (1)$$

The Redlich-Kister parameters  $a_0$ ,  $a_1$ ,  $a_2$  of eq. (1) were obtained by maximum likelihood optimization method using the following objective function:

$$OF = \sum_{i=1}^N \left[ \frac{(x_{i,exp} - x_{i,calc})^2}{\sigma_x^2} + \frac{(n_{D,i,exp}^E - n_{D,i,calc}^E)^2}{\sigma_{n_D^E}^2} \right] \quad (2)$$

**The refractive index** was measured by a digital Abbemat RXA 170 from Anton-Paar (Austria) at the wavelength of the D line of sodium, 589.3 nm, with accuracy better than  $\pm 0.0001$ . The temperature of the Safire prism was controlled by a Peltier element to within  $\pm 0.01$  K and the calibration of the apparatus was carried out with bidistilled and deionized water and by determining refractive indexes at 298.15 K and its deviations for the binary cyclooctane + toluene system at nine compositions. The error resulted from the comparison of our refractive index deviation values,  $n_D^E$ , and those calculated from 2-parameter Redlich-Kister correlation of experimental data from literature [25] was  $2 \cdot 10^{-4}$  in mean absolute average, which it means a good comparison.

The estimated error for  $n_D^E$ , which is defined as

$$n_D^E = n_D - xn_{D,1} - (1-x)n_{D,2} \quad (3)$$



is better than  $2 \cdot 10^{-4}$ . In eqs. (1) and (3),  $n_{D,1}$  and  $n_{D,2}$  represent the refractive indexes of the pure components 1 and 2,  $n_D$  the refractive index for the mixture 1+2, and  $x$  denotes the molar fraction of component 1 (IL) in the binary mixture. Each measurement of refractive index consisted in 4 readings for the same sample. Its averaged value is reported as one experimental point. Special attention was devoted to avoid moisture absorption from the atmosphere in pure chemicals and in their binary mixtures since it is known that water content of the sample has an important effect on refractive index value. By this way, the error in the determination of the liquid phase composition was 0.001 mole fraction.

**The of vapor-liquid equilibrium VLE** apparatus and experimental procedure were successfully verified and used for investigation of different other systems as mentioned previously [26].

**The density and ultrasonic sound** velocity measurements of the pure compounds at 308.15 K were carried out by using a density and sound velocity meter Anton Paar DSA-5000 M with precision of  $\pm 0.000005 \text{ g}\cdot\text{cm}^{-3}$  and  $\pm 0.01 \text{ m s}^{-1}$ . Dried air and distilled deionized ultra pure water at atmospheric pressure were used as calibration fluids for the cell. The probes thermostating was maintained constant at  $\pm 0.01 \text{ K}$ . The experimental measurement uncertainty for density was better than  $0.0001 \text{ g}\cdot\text{cm}^{-3}$  and for the sound velocity better than  $0.1 \text{ m s}^{-1}$ .

**The calorimetric measurements** were carried out in SETARAM C80 3D computer-controlled mixing and reaction calorimeter using reversal mixing cells made from stainless steel. Each reversal mixing vessel is in the form of an 80-mm high vertical cylinder with two compartments. The smaller, lower recipient ( $0.6 \text{ cm}^3$ ) of the measuring cell contained the known amount of [bmim]Cl and was closed by a removable lid. The same amount of water was added to the lower part of the reference cell. The larger, upper container ( $5.0 \text{ cm}^3$ ). of each cell was used to contain the water sample. The measuring and reference cells were placed inside the metallic block of the Calvet-type calorimeter. The temperature was measured by means of a  $100 \text{ } \Omega$  platinum resistance thermometer located between the two vessels, and was held constant to within  $\pm 0.05 \text{ K}$  during each measurement. The working temperature was fixed and, when thermal equilibrium was reached (in cca. 2.5-3 hours), the components in the vessels were mixed by rotation of the calorimeter block using the rocking device. The differential heat-flux was then recorded, and integrated as a function of time to give the heat changes during mixing.

The calorimeter was calibrated electrically using the Joule-effect by means of a special cell with calibrated heaters as recommended by IUPAC [27]. We checked the accuracy of the calorimeter by performing test measurements of the enthalpies of solution at infinite dilution of KCl (crystals) in bidistilled and deionized water. Our value was with 0.6 % or  $0.097 \text{ kJ mol}^{-1}$  lower than literature value [28] at

303.15 K. The reproducibility in determining the mixing enthalpy was  $\pm 0.002 \text{ kJ mol}^{-1}$ .

### 3. Results, Modeling and Discussions

The experimental isothermal ( $P, x$ ) data measured for the binary systems of [bmim]Cl, [bmim]Br and [bmim]I + 1-butanol at 363.15 K are shown in Fig. 1. The vapor pressure of pure 1-butanol has been measured each time for the three investigations presented here. An average value is shown in Table 1, while direct experimental value is shown in Fig. 1. The data for the [bmim]Cl system were correlated with 3<sup>rd</sup> order Redlich-Kister model [24] with ideal assumption of the vapor phase and by using maximum likelihood optimization method. Those for [bmim]Br system were correlated with Wilson model [29] treating vapor phase by virial equation of state and by using Barker optimization method [30]. Finally, the data for the [bmim]I system were correlated with Wilson model treating the vapor phase with virial equation of state and by using maximum likelihood optimization method. The model parameters and standard deviations of the measured properties are shown in Table 3. The regression by means of Barker method and maximum likelihood method was made employing a program described by Hala *et al.* [31]. The objective functions are defined as it follows:

$$S = \sum_{i=1}^N \left( \frac{P_{i,c} - P_{i,e}}{P_{i,e}} \right)^2 \quad (4)$$

for the Barker method, and

$$S = \sum_{i=1}^N \left[ (P_{i,e} - P_{i,c})^2 / \sigma_p^2 + (T_{i,e} - T_{i,c})^2 / \sigma_T^2 + (x_{i,e} - x_{i,c})^2 / \sigma_x^2 \right] \quad (5)$$

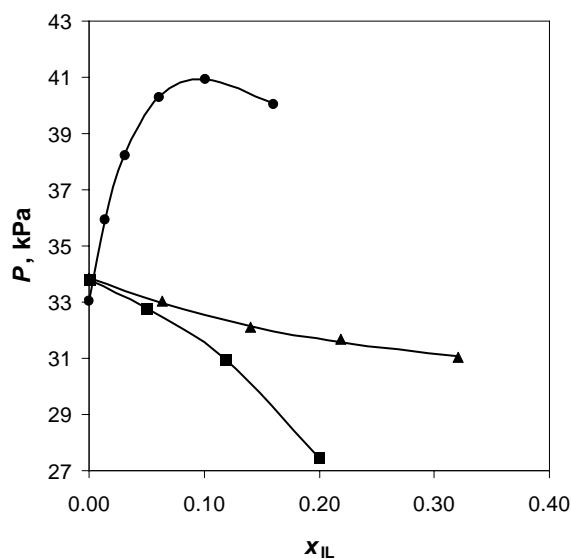
for the maximum likelihood method.  $N$  is the number of experimental points,  $P_{i,e}$ ,  $T_{i,e}$ , and  $x_{i,e}$  are the experimental data and  $P_{i,c}$ ,  $T_{i,c}$  and  $x_{i,c}$  are the corresponding calculated values for pressure, temperature, and liquid composition of component 1 (IL), respectively. In this work, the estimated standard deviations for the measured quantities were set to  $\sigma_p = 0.1\%$  of measured value,  $\sigma_T = 0.1 \text{ K}$ , and  $\sigma_x = 0.001$ , respectively.

All standard deviations of correlations were calculated using the expression:

$\sigma_Z = \left[ \sum (Z_{i,e} - Z_{i,c})^2 / (N - m) \right]^{1/2}$ , where  $Z$  is the value of the property  $P$ ,  $n_D^E$ , and  $x$ ,  $N$  is the number of experimental points and  $m = 2$  in the case of Wilson and 3<sup>rd</sup> order Redlich-Kister models or  $m = 3$  in the case of 4<sup>th</sup> order Redlich-Kister equation (used in correlation of the refractive indexes vs composition variation).

In the case of VLE data, when the real behavior of the vapor phase was considered, it was described by the virial equation of state truncated after second term. The second virial coefficients for both components and for binary mixture

were evaluated by means of the Hayden and O'Connell method [32], while the molar volumes were calculated by using a generalized Watson relation [33]. For the calculations, the experimentally determined vapor pressure of pure 1-butanol, that estimated by Ambrose-Walton method [34] for [bmim]Cl and [bmim]Br, and that estimated from <http://ilthermo.boulder.nist.gov/index.html> for [bmim]I were used. The results of correlations are summarized in Table 3. In the range of the liquid composition measurements, in Fig. 1 and Table 3 it can be seen a good agreement between experimental and calculated bubble curves.



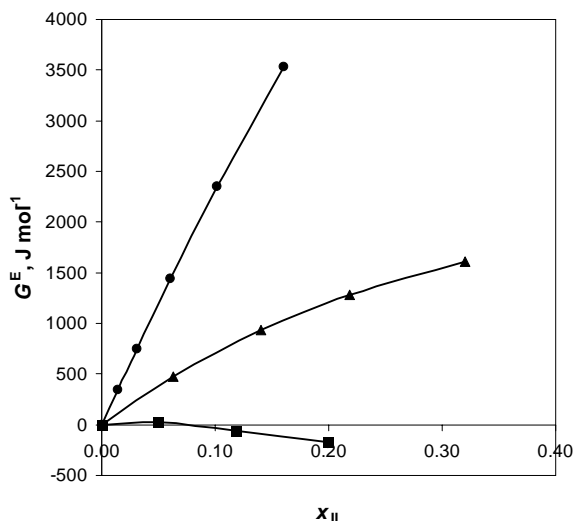
**Fig. 1.** Bubble curves for the [bmim]Cl (●), [bmim]Br (▲), and [bmim]I (■) + 1-butanol binary systems at 363.15 K. Filled symbols are experimental data, lines are correlated data by thermodynamic models from **Table 3**.

**Table 3.** The models, their parameters values and standard deviations of the measured properties for the VLE data of binary [bmim]Cl, [bmim]Br and [bmim]I + 1-butanol systems at 363.15 K.

Mixture	Correlation model	$A_0, A_{12}$	$A_1, A_{21}$	$\sigma(x)$	$\sigma(P)$ , kPa	$\sigma(T)$ , K
[bmim]Cl + 1-butanol	Redlich-Kister	4.7841	-0.4373	0.0002	0.010	0.10
[bmim]Br + 1-butanol	Wilson	3650.40	44733.6	-	0.090	-
[bmim]I + 1-butanol	Wilson	11718.7	-2183.46	0.0004	0.010	0.14

The variation of the excess Gibbs energy,  $G^E$ , with IL liquid composition in the binary system is given in Fig. 2. Analyzing the  $G^E$  values obtained for [bmim]Br or [bmim]Cl or [bmim]I with 1-butanol binary systems [35-37], it results

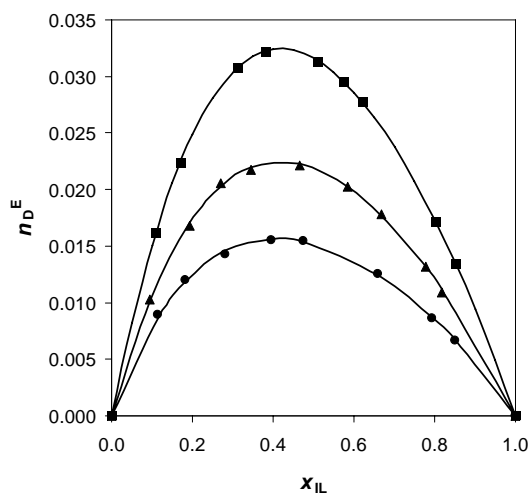
that at constant composition and temperature the  $G^E$  is varying with the nature of the IL in the order: [bmim]Cl > [bmim]Br > [bmim]I. This variation can be explained by higher strength of the interactions between unlike molecules in the case of [bmim]Cl than in the case of the [bmim]Br and in the case of [bmim]I, in the same order of decreasing electronegativity of the halogen ion, thing which is normal.



**Fig. 2.** Calculated excess molar Gibbs energy for the [bmim]Cl (●), [bmim]Br (▲), and [bmim]I (■) + 1-butanol binary systems at 363.15 K. Calculation models can be seen in **Table 3**.

Since the VLE data for the three IL + 1-butanol binary systems were correlated successfully with a thermodynamic model without showing systematic errors, we can say that the VLE data are thermodynamic consistent.

The experimental and calculated isothermal ( $x_I, n_D^E$ ) data for the binary systems have been determined at 308.15 K and they are shown in Fig. 3. The correlation of the primary ( $x_I, n_D$ ) data has been made by 3-parameters Redlich-Kister model by using maximum likelihood method, following the procedure described in the section *Apparatuses and procedures*. The correlation results are presented in Table 4. Due to the small water content of the ionic liquids, expected values for the standard deviations of the liquid compositions have been obtained. It should be mentioned that not complete purification of the organic salt is possible. Similar situation was reported in the literature [18]. From Fig. 3 it can be observed that excess refractive indexes are positive on whole composition interval and increase in the order [bmim]I > [bmim]Br > [bmim]Cl being smaller when the electronegativity of the halogen ion is higher and the molar volume is smaller. This is normal since the steric effects are higher when the size of the molecules is higher.



**Fig. 3.** Excess refractive index variation with composition for the [bmim]Cl (●), [bmim]Br (▲), and [bmim]I (■) + 1-butanol binary systems at 308.15 K. Filled symbols are experimental data, lines are correlated data by Redlich-Kister model with 3 parameters given in **Table 4**.

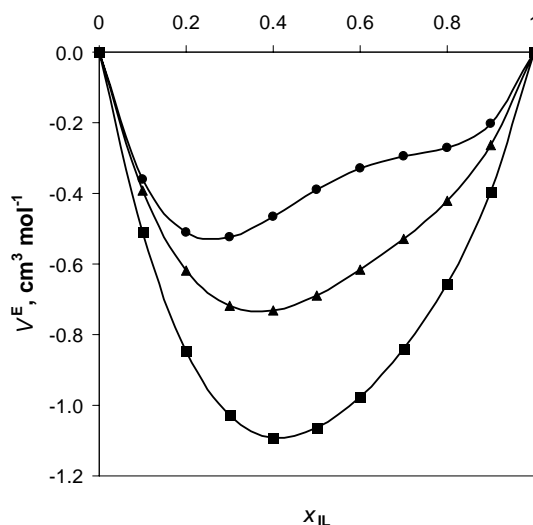
**Table 4.** Redlich-Kister parameters and standard deviations obtained in correlation of the refractive indexes and their excess vs. composition data for the binary [bmim]Cl, [bmim]Br and [bmim]I + 1-butanol systems at 308.15 K.

Mixture	$a_0$	$a_1$	$a_2$	$\sigma(x)$	$\sigma(n_D^E) \times 10^4$
[bmim]Cl + 1-butanol	0.0604	0.0209	0.0148	0.0013	1.9
[bmim]Br + 1-butanol	0.0875	0.0275	0.0123	0.0010	1.9
[bmim]I + 1-butanol	0.1264	0.0394	0.0151	0.0005	0.9

From refractive index vs. composition data and measured densities of the pure compounds at 308.15 K, densities, excess molar volumes, surface tensions and dielectric permittivities at optical frequency and their deviations vs. composition of the binary mixtures were determined by Lorenz-Lorentz mixing rule [10] or by known equations [11, 12]. The selection of the mixing rule was made after analyzing of ten different mixing rules results in giving the refractive indices from experimental densities for twelve binary mixtures of various polarity at 298.15 K [38].

The predicted variation of the excess molar volume with composition for the binary [bmim]Cl, [bmim]Br and [bmim]I + 1-butanol system at 308.15 K is shown in Fig. 4. As can be observed in this figure, the  $V^E$  is negative on whole composition interval; it is more negative when electronegativity of the halogen ion decreases. The ionic liquids can act both as a hydrogen-bond acceptor ( $[Cl]^-$ ,  $[Br]^-$ ,  $[I]^-$ ) and donor ( $[bmim]^+$ ). It is expected to interact with 1-butanol which has both accepting and donating sites. On the other hand, it is well known that 1-butanol is hydrogen-bonded solvent with both high enthalpies of association and association

constant. Hence, it is expected to stabilize the IL with hydrogen-bonded donor sites. For mentioned binary systems at constant temperature the effect of the anion electronegativity on  $V^E$  is not specific to new hydrogen bonds between unlike molecules formation; it is most likely due to the packing between hydrogen acceptor sites of 1-butanol and donor sites of imidazolium ([bmim]<sup>+</sup>) cycle. These packing effects became more dominant when electronegativity of the IL anion is smaller and temperature increase, as it was observed for other systems cited in literature [39].



**Fig. 4.** The predicted excess molar volume variation with composition for the [bmim]Cl (-●-), [bmim]Br (-▲-), and [bmim]I (-■-) + 1-butanol binary systems at 308.15 K by Lorenz-Lorentz mixing rule.

The surface tension of a liquid is a property of great importance in mass transfer processes such as distillation, extraction, or absorption. It is not easily measured, and considerable attention has been paid to the development and analysis of equations allowing its prediction from properties for which data are more readily available as refractive index, for example. The surface tension  $\sigma$  is related to the densities of the liquid  $\rho_L$  and of the vapor  $\rho_V$  phases of the substance by using the Macelod equation [11]:

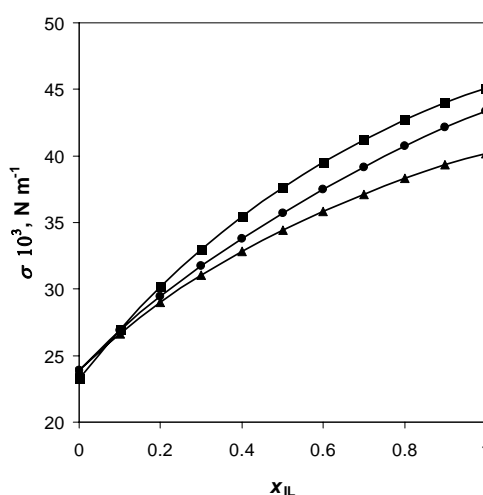
$$\sigma = ct(\rho_L - \rho_V)^4 \quad (6)$$

For a pure liquid compound, multiplying both sides by the molar mass  $M$  and ignoring  $\rho_V$  in comparison with  $\rho_L$  affords the Sugden equation [12]:

$$\sigma^{1/4} M / \rho_L = \sigma^{1/4} V_m = \text{Parachor} \quad (7)$$

from which it results: 
$$\sigma = \left( \frac{\text{Parachor}}{V_m} \right)^4 \quad (8)$$

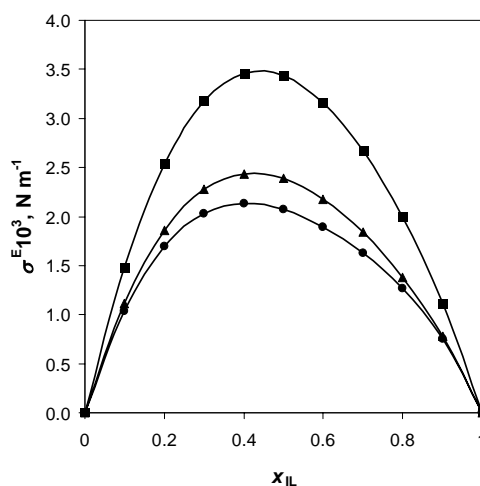
In eqs. (7) and (8), the *Parachor* is assumed as mole-wise additive and molar volume,  $V_m$ , is calculated from experimental densities of pure compounds and those predicted for the mixtures by the Lorenz-Lorentz relation [10] (from Redlich-Kister correlated refractive indices). So, we used eq. (8) to predict the surface tensions of binary liquid mixtures at 308.15 K and after that to calculate the surface tension deviation from ideality by applying a similar equation with eq. (3). Surface tension variation with composition for the three ILs + 1-butanol binary systems at 308.15 K is shown in Fig. 5 and surface tension deviation variation with composition for the same systems and temperature appears in Fig. 6.



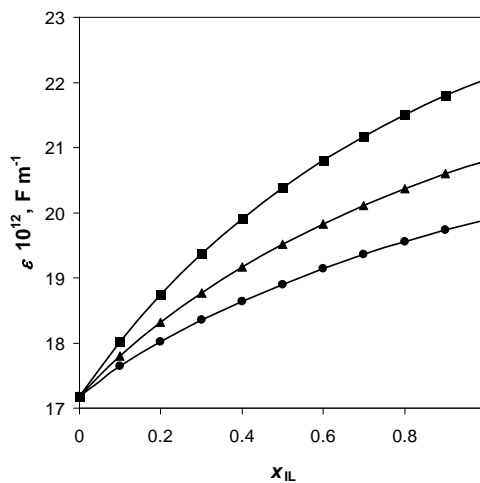
**Fig. 5.** The predicted surface tension variation with composition for the [bmim]Cl (●), [bmim]Br (▲), and [bmim]I (■) + 1-butanol binary systems at 308.15 K.

The parachors of the [bmim]Cl, [bmim]Br and 1-butanol (in the case of chloride and bromide binary systems investigations) pure compounds have been predicted by additive group contribution methods of Tyn and Calus, 1975 [40]. The surface tensions of pure 1-butanol compares well with those determined experimentally in literature [41] with mean absolute relative deviation of 2.7 %. The calculated surface tensions for pure [bmim]Cl are about 20 % lower than those brutish extrapolated from literature experimental data [42]. The parachor of [bmim]I and of 1-butanol (in the case of iodide binary system investigation) has been calculated from the surface tension of the pure component from literature at 308.15 K [43, 41] and molar volume at the same temperatures determined experimentally in this work. Due to the two different modes of estimating parachor

for 1-butanol, it appears a small difference in its surface tension in Fig. 5. As can be seen in Fig. 6, the surface tension deviations predicted here are positive on whole composition range, and increase with decreasing the electronegativity of the IL anion. The positive values are explained by the volume expansion resulted from the new H-bonds and packing between unlike molecules in the binary mixture IL + 1-butanol. It seems that packing of the molecules is dominant since excess surface tension is higher at higher molar volume of the IL.



**Fig. 6.** The predicted excess surface tension variation with composition for the [bmim]Cl (-●-), [bmim]Br (-▲-), and [bmim]I (-■-) + 1-butanol binary systems at 308.15 K.

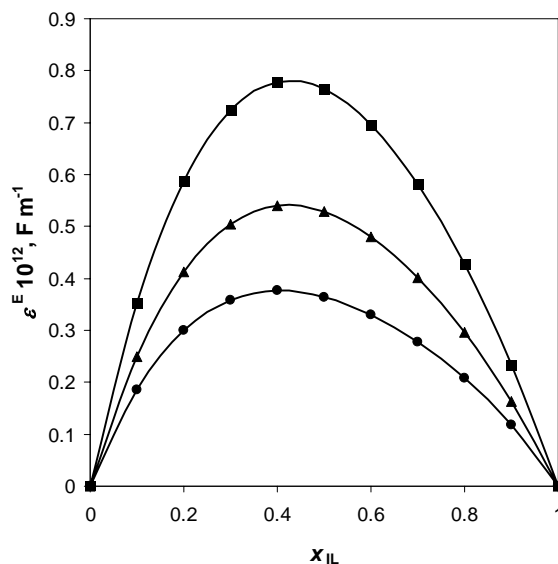


**Fig. 7.** The predicted dielectric permittivity at optical frequency variation with composition for the [bmim]Cl (-●-), [bmim]Br (-▲-), and [bmim]I (-■-) + 1-butanol binary systems at 308.15 K.

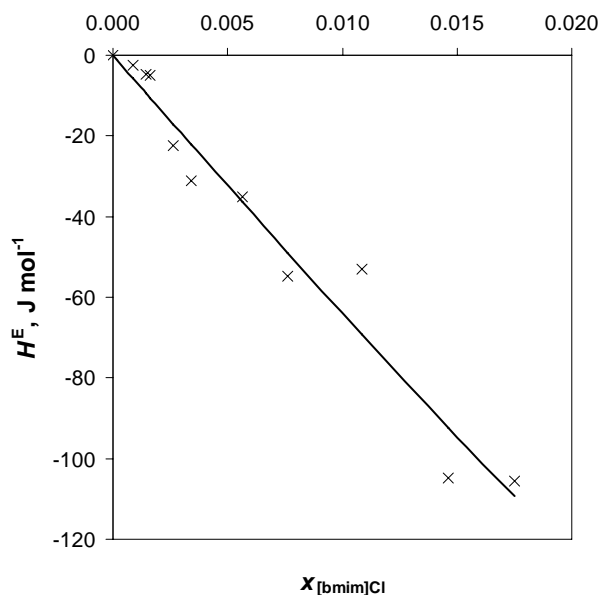


From refractive index data, the relative permittivity at optical frequency can be calculated by squaring the refractive index determined at the wavelength of 589.3 nm. For 1-butanol, the relative permittivity agrees well with that extrapolated at 308.15 K from experimental literature data [44] with mean absolute relative deviation of 0.35%. No data have been found for the ILs for comparison. The dielectric permittivity (Fig. 7) at optical frequency is obtained by multiplying relative permittivity by vacuum permittivity. As it can be observed, this property is higher for [bmim]I. This is the reason why this IL is used in fuel cells. The excess permittivity (Fig. 8) calculated by a similar equation like (3) is found to be positive on whole composition interval and increase with decreasing electronegativity of the IL anion. This indicates again that in each binary IL + 1-butanol system investigated in this work both unlike molecular species interact in such a way that they act as more H-bonded structure than those of pure compounds themselves.

The heat of mixing or excess molar enthalpies for the [bmim]Cl + water system at 303.15 K and in the range of 0.0009–0.0160 mole fraction of IL are presented in Figure 9. The data have been correlated with 4<sup>th</sup> order Redlich-Kister model. As can be seen in this Figure, the data are quite scattered (9.59 J mol<sup>-1</sup> standard deviation) due probably to the fact that the amount of water content of the IL is not negligible. Further measurements will be done with more vacuum dried samples, stored probably under high vacuum during entire experiments. However, for these measurements, the Redlich-Kister parameters obtained from data correlation are:  $a = -2257.65 \text{ J mol}^{-1}$ ,  $b = -2195.16 \text{ J mol}^{-1}$  and  $c = -2134.58 \text{ J mol}^{-1}$ .



**Fig. 8.** The predicted excess dielectric permittivity at optical frequency variation with composition for the [bmim]Cl (●-), [bmim]Br (▲-), and [bmim]I (■-) + 1-butanol binary systems at 308.15 K.



**Fig. 9.** Excess molar enthalpy variation with composition at 303.15 K for the binary [bmim]Cl + water system. Symbols represent experimental data and line the correlation with 4<sup>th</sup> order Redlich-Kister model.

#### 4. Conclusions

The binary 1-butyl-3-methylimidazolium chloride, bromide and iodide + 1-butanol systems have been investigated isothermally at vapor-liquid equilibrium at temperature of 363.15 K. By correlation of the experimental ( $P$ ,  $T$ ,  $x$ ) data with thermodynamics models like 3<sup>rd</sup> order Redlich-Kister or Wilson it was found that the system [bmim]Cl is azeotropic while the other two systems are zeotropic, with positive deviations (the case of [bmim]Cl and [bmim]Br systems) or small positive and negative deviations (the case of [bmim]I system) from ideality. The  $G^E$  values at 363.15 K and constant composition varies in the order: [bmim]Cl > [bmim]Br > [bmim]I due to the decreasing of the specific intermolecular interactions between IL and organic solvent molecules at mixing.

For the same systems, refractive index measurements have been performed at 308.15 K in whole composition interval. Excess refractive index is positive for all systems on whole composition range and increase with decreasing electronegativity of the IL anion and with increasing of the molar volume of the IL. This is attributed to the steric effects which are higher when the size of the molecules is higher.

Using the Lorenz-Lorentz ( $n_D$ - $\rho$ ) mixing rule, the densities, excess molar volumes, surface tensions and surface tension deviations have been predicted. By other known relations, dielectric permittivity and its deviations have been also calculated at the same temperature of 308.15 K. Structural effects for the binary

investigated mixture have been explained again in terms of excess thermophysical properties.

For the [bmim]Cl + water system, the data of excess molar enthalpy have been measured at 303.15 K and at high dilution of water. The heat of mixing is negative indicating strong interaction between this IL and water molecules at mixing. The types of interactions could be of H-bonds and packing between unlike molecules.

Two of the ILs under study ([bmim]Cl and [bmim]Br) were solids in normal conditions of temperature and pressure. Similar research study can be made for solid nanostructures with liquid solvents which form homogenous solutions at mixing. It was proved that even for this type of mixtures is possible to obtain accurate thermodynamic data which are of interest in the actual top energetic nanotechnologies.

**Acknowledgments.** This contribution was carried out within the research programme “Chemical thermodynamics and kinetics. Quantum chemistry” of the “Ilie Murgulescu” Institute of Physical Chemistry, financed by the Romanian Academy. Support of the EU (ERDF) and Romanian Government, which allowed for the acquisition of the research infrastructure under POS-CCE O 2.2.1 Project INFRANANOCHEM - Nr. 19/01.03.2009, is gratefully acknowledged.

## References

- [1] A. MARCINIAK, *Influence of cation and anion structure of the ionic liquid on extraction processes based on activity coefficients at infinite dilution. A review*, *Fluid Phase Equilib.*, **294**, pp. 213–233, 2010.
- [2] J. GMEHLING, *Ionic Liquids in Separation Processes*, Cap. 7 in *Chemical Thermodynamics for Industry* (Ed. Letcher T.M.), The Royal Society of Chemistry, Cambridge, UK, 2004.
- [3] A.B. PEREIRO, J.M.M. ARAUJO, *Ionic liquids in separations of azeotropic systems—A review*, *J. Chem. Thermodyn.*, **46**, pp. 2–28, 2012.
- [4] S. ZHANG, X. LU, Y. ZHANG, Q. ZHOU, J. SUN, L. HAN, G. YUE, X. LIU, W. CHENG, S. LI, *Ionic Liquids and Relative Process Design*, in *Molecular Thermodynamics of Complex Systems*, (Ed. Lu, X., Hu, Y.), In the Series *Structure and Bonding* (Ed. Mingos D.M.P.), Springer **131**, Verlag Berlin Heidelberg, Germany, 2009.
- [5] J.M.S.S. ESPERANC, J.N.C. LOPES, M. TARIQ, L.M.N.B.F. SANTOS, J.W. MAGEE, L.P.N. REBELO, *Volatility of aprotic ionic liquids — A review*, *J. Chem. Eng. Data*, **55**, pp. 3–12, 2010.
- [6] W.N. MACLENNAN, *Part III. The theory of binary solutions, and its application to aqueous – alcoholic solutions*, *J. Chem. Soc. London*, pp. 674–686, 1933.
- [7] C.M. HULL, *Vapor-liquid equilibria and boiling-point compositions relations for system n-butanol – water and isobutanol – water*, *Ind. Eng. Chem. Ind. Ed.*, **23**, pp. 1438–1440, 1931.
- [8] R.F. BONNER, *Vapor-liquid equilibrium still for partially miscible liquids*, *Ind. Eng. Chem.* **41**, pp. 2867–2871, 1949.
- [9] *The Dortmund Data Bank (DDB), DDBST (Software and Separation Technology) GmbH* (Oldenburg), Germany, Version 2015 ([www.ddbst.com](http://www.ddbst.com)).
- [10] H.A. LORENTZ, *Theory of electrons*, B.G. Teubner, Leipzig, 1909.

- [11] R.H. FOWLER, *A tentative statistical theory of Macleod's equation for surface tension, and the parachor*, Proc. Roy. Soc. Lond. **A 159**, pp. 229–246, 1937.
- [12] S. SUGDEN, *A relation between surface tension, density, and chemical composition*, J. Chem. Soc., Trans. **125**, pp. 1177–1189, 1924.
- [13] K.-S. KIM, B.-K. SHIN, H. LEE, *Physical and electrochemical properties of 1-butyl-3-methylimidazolium bromide, 1-butyl-3-methylimidazolium iodide, and 1-butyl-3-methylimidazolium tetrafluoroborate*, Korean J. Chem. Eng. **21**(5), pp. 1010–1014, 2004.
- [14] K.-S. KIM, B.-K. SHIN, H. LEE, F. ZIEGLER, *Refractive index and heat capacity of 1-butyl-3-methylimidazolium bromide and 1-butyl-3-methylimidazolium tetrafluoroborate, and vapor pressure of binary systems for 1-butyl-3-methylimidazolium bromide + trifluoroethanol and 1-butyl-3-methylimidazolium tetrafluoroborate + trifluoroethanol*, Fluid Phase Equilib. **218**, pp. 215–220, 2004.
- [15] S. SINGH, M. AZNAR, N. DEENADAYALU, *Densities, speeds of sound, and refractive indices for binary mixtures of 1-butyl-3-methylimidazolium methyl sulphate ionic liquid with alcohols at T = (298.15, 303.15, 308.15, and 313.15) K*, J. Chem. Thermodyn. **57**, pp. 238–247, 2013.
- [16] B. KUMAR, T. SINGH, K.S. RAO, A. PAL. A. KUMAR, *Thermodynamic and spectroscopic studies on binary mixtures of imidazolium ionic liquids in ethylene glycol*, J. Chem. Thermodyn. **44**, pp. 121–127, 2012.
- [17] V. GOVINDA, P. ATTRI, P. VENKATESU, P. VENKATESWARLU, *Thermophysical properties of dimethylsulfoxide with ionic liquids at various temperatures*, Fluid Phase Equilib. **304**, pp. 35–43, 2011.
- [18] N.V. SASTRY, N.M. VAGHELA, P.M. MACWAN, *Densities, excess molar and partial molar volumes for water + 1-butyl- or, 1-hexyl- or, 1-octyl-3-methylimidazolium halide room temperature ionic liquids at T=(298.15 and 308.15) K*, J. Mol. Liq. **180**, pp. 12–18, 2013.
- [19] T. BOUBLIK, V. FRIED, E. HALA, *The vapour pressures of pure substances*, Elsevier, Amsterdam, 1973.
- [20] M. ROGALSKI, S. MALANOWSKI, *Ebullimeters modified for the accurate determination of vapour—liquid equilibrium*, Fluid Phase Equilib. **5**, pp. 97–112, 1980.
- [21] A. BARHALA, M. TEODORESCU, *Measurement of vapour-liquid equilibria by ebulliometry*, Rev. Roum. Chim. **46**(9), pp. 967–973, 2001.
- [22] S. MALANOWSKI, *Experimental methods for vapour-liquid equilibria. Part I. Circulation methods*, Fluid Phase Equilib. **8**, pp. 197–219, 1982.
- [23] J.D. OLSON, *Measurement of vapor-liquid equilibria by ebulliometry*, Fluid Phase Equilib. **52**, pp. 209–218, 1989.
- [24] O. REDLICH AND A.T. KISTER, *Algebraic representation of thermodynamic properties and the classification of solutions*, Ind. Eng. Chem. **40**, pp. 345–348, 1948.
- [25] B. GONZALES, I. DOMINGUEZ, E.J. GONZALES, A. DOMINGUEZ, *Density, speed of sound, and refractive index of the binary systems cyclohexane (1) or methylcyclohexane (1) or cyclooctane (1) with benzene (2), toluene (2), and ethylbenzene (2) at two temperatures*, J. Chem. Eng. Data **55**, pp. 1003–1011, 2010.
- [26] M. TEODORESCU, D. DRAGOESCU, D. GHEORGHE, *Isothermal (vapour + liquid) equilibria for (nitromethane or nitroethane + 1,4-dichlorobutane) binary systems at temperatures between (343.15 and 363.15) K*, J. Chem. Thermodyn. **56**, pp. 32–37, 2013.
- [27] S.M. SARGE, E. GMELIN, W.H. HOHNE, H.K. CAMMENGA, W. HEMMINGER, W. EYSEL, *The caloric calibration of scanning calorimeters*, Thermochim. Acta **247**, pp. 129–168, 1994.
- [28] A. SANAHUJA, E. CESARI, *Heat of solution of KCl in water at 303.15 K*, Thermochim. Acta **85**, pp. 163–166, 1985.
- [29] G.M. WILSON, *Vapor-liquid equilibrium. XI. A new expression for the excess free energy of mixing*, J. Am. Chem. Soc. **86**, pp. 127–130, 1964.

- [30] J.A. BARKER, *Determination of activity coefficients from total pressure measurements*, Aust. J. Chem. **6**, pp. 207–210, 1953.
- [31] E. HALA, K. AIM, T. BOUBLIK, J. LINEK, I. WICHTERLE, *Vapor-liquid equilibrium at normal and reduced pressures* (in Czech), Academia, Praha, 1982.
- [32] J.G. HAYDEN, J.P. O'CONNELL, *A generalized method for predicting second virial coefficients*, Ind. Eng. Chem., Proc. Des. Develop. **14**, pp. 209–216, 1975.
- [33] O.A. HOUGEN, K.M. WATSON, *Chemical process principles*, Part II, J. Wiley, New York, 1947.
- [34] D. AMBROSE, J. WALTON, *Vapour pressures up to their critical temperatures of normal alkanes and 1-alcohols*, Pure Appl. Chem., **61**(8), pp. 1395–1403, 1989.
- [35] M. TEODORESCU, *Isothermal vapour+liquid equilibrium and thermophysical properties for 1-butyl-3-methylimidazolium chloride + 1-butanol binary system*, Rev. Chim. **66**(4), pp. 529–536, Bucharest, 2015.
- [36] M. TEODORESCU, *Isothermal vapour+liquid equilibrium and thermophysical properties for 1-butyl-3-methylimidazolium bromide + 1-butanol binary system*, Ind. Eng. Chem. Res. **53**, pp. 13522–13528, 2014.
- [37] M. TEODORESCU, *Isothermal (vapour + liquid) equilibrium and thermophysical properties for (1-butyl-3-methylimidazolium iodide + 1-butanol) binary system*, J. Chem. Thermodyn. **87**, pp. 58–64, 2015.
- [38] M. TEODORESCU, C. SECUIANU, *Refractive indexes measurement and correlation for selected binary systems of various polarities at 25 °C*, J. Sol. Chem. **42**(10), pp. 1912–1934, 2013.
- [39] A. VALTZ, M. TEODORESCU, I. WICHTERLE, D. RICHON, *Liquid densities and excess molar volumes for water + diethylene glycolamine, and water, methanol, ethanol, 1-propanol + triethylene glycol binary systems at atmospheric pressure and temperatures in the range of 283.15–363.15 K*, Fluid Phase Equilib. **215**, pp. 129–142, 2004.
- [40] B.E. POLING, J.M. PRAUSNITZ, J.P. O'CONNELL, *The properties of gases and liquids*, 5<sup>th</sup> Ed., McGraw Hill, New York, USA, 2001.
- [41] H. JIANG, Y. ZHAO, J. WANG, F. ZHAO, R. LIU, Y. HU, *Density and surface tension of pure ionic liquid 1-butyl-3-methylimidazolium l-lactate and its binary mixture with alcohol and water*, J. Chem. Thermodyn. **64**, pp.1–13, 2013.
- [42] J.W. RUSSO, M.M. HOFFMANN, *Influence of typical impurities on the surface tension measurements of binary mixtures of water and the ionic liquids 1-butyl-3-methylimidazolium tetrafluoroborate and chloride*, J. Chem. Eng. Data **55**, pp. 5900–5905, 2010.
- [43] K.-S. KIM, D. DEMBERELNYAMBA, B.-K. SHIN, S.-H. YEON, S. CHOI, J.-H. CHA, H. LEE, C.-S. LEE, J.-J. SHIM, *Surface tension and viscosity of 1-butyl-3-methylimidazolium iodide, and 1-butyl-3-methylimidazolium tetrafluoroborate, and solubility of lithium bromide+1-butyl-3-methylimidazolium bromide in water*, Korean J. Chem. Eng. **23**(1), pp. 113–116, 2006.
- [44] V.A. RANA, H.A. CHAUBE, *Static permittivity, density, viscosity and refractive index of binary mixtures of anisole with 1-butanol and 1-heptanol at different temperatures*, J. Molec. Liq. **173**, pp. 71–76, 2012.

# **From Biological Cells to Semiconductor and Metallic Nanoparticles: the Same Recipe With Different Flavors**

Titus SANDU

National Institute for Research and Development in Microtechnologies-IMT Bucharest  
126A, Erou Iancu Nicolae Street, Bucharest, Romania  
Email: `titus.sandu@imt.ro`

**Abstract.** The use of the same boundary integral equation method allows the treatment of different systems with different sizes on different frequency scales of the electromagnetic field. Thus, the radiofrequency behavior of biological cells, the surface optical phonons/polaritons in semiconductor nano- and microparticles, and the collective electronic response in metallic nanoparticles can be described as electrostatic resonances that depend on the shape of the systems and are essentially scale invariant. We will analyze not only the similarities but also the differences between the resonances of these systems. Representative examples and applications will be given for each distinct case.

## **1. Introduction**

One of the fundamental aspects of science and technology is the interaction of electromagnetic fields with matter. Materials respond in a number of ways when an electromagnetic field is applied upon them, depending on their nature, structure and size as well as the intensity and the structure of the impinging field. For example the optical response of a nanoparticle made of a given semiconductor is different from the response of a bulk semiconductor of the same type due to quantum confinement [1]. Another example is the difference between optical linear and non-linear response of materials that is determined by the intensity of light [2]. The microscopic description of materials necessitates the laws of quantum mechanics but there are many situations when classical physics is enough to describe satisfactorily the behavior of nanoscopic materials. Such case is that of metallic nanoparticles whose optical behavior is well

described by Maxwell equations or more simply by Laplace equation in the quasi-static approximation [3]. A comprehensive look at the interaction of radio-frequency fields with dielectric materials down to nanoscale can be found in the review from the US National Institute of Standards and Technology [31].

Although the optical response of metallic nanoparticles is a quantum effect the success of classical description resides in the fact that material properties of metals are calculated with and come from quantum mechanics. In this work we will show that the interaction of electromagnetic fields with three different systems in three different wavelength regions can be treated with the same method. We consider that the electromagnetic radiation has the wavelength much larger than the size of systems under consideration (at most one tenth of the wavelength). While this assumption (also known as the quasi-static approximation) is fulfilled without difficulty in applications involving biological cells interacting with radio-frequency fields and surface optical phonons/polaritons in semiconductor nanoparticles, there is a much greater care when one is dealing with optical properties of metallic nanoparticles [4]. From computational point of view there are a plethora of numerical methods that can treat not only the quasi-static but also the full dynamical regime [4, 41]. Unfortunately these methods are computationally intensive and most of the time they may hide relevant physical information and correlations since they are purely numerical. In the following we will present a boundary integral equation method that works in the quasi-static regime and provides relevant information about shape, number of modes, and dielectric relations in the response of particles to electromagnetic stimuli [5, 6, 7]. By a number of examples we will show the utility of the method in applications.

In the next section we will outline the method and its numerical implementation. Then we will apply it to dielectric spectra of biological cells in radio-frequency, to localized plasmon resonances in metallic nanoparticles, and to surface polar optical phonons/polaritons in semiconductor nanoparticles. The present contribution will end with conclusions and an outlook toward future applications and development.

## **2. Boundary Integral Method**

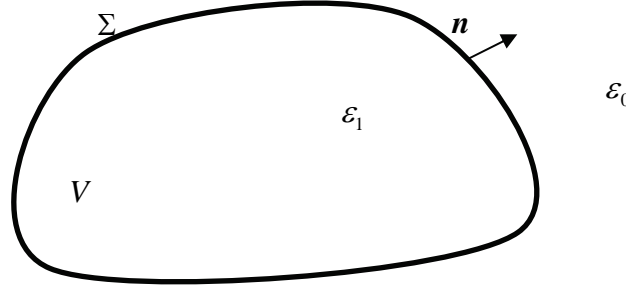
### ***2.1. Basic Equations***

Consider a dielectric homogeneous particle (Fig. 1) of volume  $V$  and complex dielectric permittivity  $\varepsilon_1$ , delimited by surface  $\Sigma$  immersed a host medium of dielectric permittivity  $\varepsilon_0$  and subjected to a spatially homogeneous with an amplitude  $E_0$  and temporally oscillating (harmonic) field with angular frequency  $\omega$ . The Laplace equation in the frequency domain and completed with boundary conditions is:

$$\begin{aligned}
\Delta\Phi(\mathbf{x}) &= 0; \text{ everywhere in 3D space excepting } \Sigma \\
\varepsilon_0 \frac{\partial\Phi}{\partial\mathbf{n}}\Big|_+ &= \varepsilon_1 \frac{\partial\Phi}{\partial\mathbf{n}}\Big|_-; \mathbf{x} \in \Sigma \\
-\nabla\Phi(\mathbf{x}) &\rightarrow E_0, |\mathbf{x}| \rightarrow \infty
\end{aligned} \tag{1}$$

The formal solution of (1) can be cast in terms of single layer distribution:

$$\Phi(\mathbf{x}) = -\mathbf{x} \cdot \mathbf{E}_0 + \frac{1}{4\pi} \int_{y \in \Sigma} \frac{u(\mathbf{y})}{|\mathbf{x} - \mathbf{y}|} d\Sigma_y. \tag{2}$$



**Fig. 1.** Homogeneous particle of permittivity  $\varepsilon_1$  and volume  $V$ , bounded by surface  $\Sigma$  and immersed in a dielectric of permittivity  $\varepsilon_0$ . By  $\mathbf{n}$  we designate the normal to  $\Sigma$ .

In other words, the single layer function  $u(\mathbf{x})$  defines the solution of the problem (1). In the following we use the general formulae for the derivative of the single layer potential. For a potential

$$V = \frac{1}{4\pi} \int_{y \in \Sigma} \frac{u(\mathbf{x})}{|\mathbf{x} - \mathbf{y}|} d\Sigma_y \tag{3}$$

we have the following derivative formulae [8]:

$$\frac{\partial V}{\partial\mathbf{n}}(\mathbf{x})\Big|_+ = -\frac{1}{2}u(\mathbf{x}) - \frac{1}{4\pi} \int_{y \in \Sigma} \frac{u(\mathbf{y})\mathbf{n}(\mathbf{x}) \cdot (\mathbf{x} - \mathbf{y})}{|\mathbf{x} - \mathbf{y}|^3} d\Sigma_y \tag{4}$$

$$\frac{\partial V}{\partial\mathbf{n}}(\mathbf{x})\Big|_- = \frac{1}{2}u(\mathbf{x}) - \frac{1}{4\pi} \int_{y \in \Sigma} \frac{u(\mathbf{y})\mathbf{n}(\mathbf{x}) \cdot (\mathbf{x} - \mathbf{y})}{|\mathbf{x} - \mathbf{y}|^3} d\Sigma_y \tag{5}$$

Rewriting the boundary conditions from (1) for the solution (2) at  $\Sigma$



$$\varepsilon_0 \frac{\partial \Phi}{\partial \mathbf{n}} \Big|_+ = \varepsilon_1 \frac{\partial \Phi}{\partial \mathbf{n}} \Big|_- ; \quad (6)$$

and using (4) and (5) one gets

$$\frac{1}{2\lambda} u(\mathbf{x}) - \frac{1}{4\pi} \int_{y \in \Sigma} \frac{u(\mathbf{y}) \mathbf{n}(\mathbf{x}) \cdot (\mathbf{x} - \mathbf{y})}{|\mathbf{x} - \mathbf{y}|^3} d\Sigma_y = \mathbf{n} \cdot \mathbf{E}_0 \quad (7)$$

or defining the operator  $\hat{M}$  on  $\Sigma$  we have

$$\frac{1}{2\lambda} u(\mathbf{x}) - \hat{M}[u] = \mathbf{n} \cdot \mathbf{E}_0 , \quad (8)$$

with  $\lambda = (\varepsilon_1 - \varepsilon_0) / (\varepsilon_1 + \varepsilon_0)$  , a dielectric factor. The operator  $\hat{M}$  is not symmetric, but it has the same eigenvalues as its adjunct operator  $\hat{M}^\dagger$  , which has the following expression

$$\hat{M}^\dagger[v] = \frac{1}{4\pi} \int_{y \in \Sigma} \frac{v(\mathbf{y}) \mathbf{n}(\mathbf{y}) \cdot (\mathbf{x} - \mathbf{y})}{|\mathbf{x} - \mathbf{y}|^3} d\Sigma_y . \quad (9)$$

Moreover the relation between  $u_k$  , the eigenfunctions of  $\hat{M}$  , and  $v_k$  , the eigenfunctions of  $\hat{M}^\dagger$  , is given by  $v_k = \hat{S}u_k$  where

$$\hat{S}[u] = \frac{1}{4\pi} \int_{y \in \Sigma} \frac{u(\mathbf{y})}{|\mathbf{x} - \mathbf{y}|} d\Sigma_y \quad (10)$$

is a symmetric operator derived from the single-layer potential [7]. The eigenfunctions  $u_k$  and  $v_k$  are completely defined by the bi-orthonormality relation  $\langle v_i | u_j \rangle = \delta_{ij}$  . The operator  $\hat{M}$  has the spectral decomposition

$$\hat{M}(u) = \sum_k \chi_k \hat{P}_k [u] = \sum_k \chi_k |u_k\rangle \langle v_k | u \rangle . \quad (11)$$

Here  $\hat{P}_k$  and  $\chi_k$  are the spectral projector of the operator  $\hat{M}$  and its corresponding eigenvalue, respectively. Now applying Eq. (11) to Eq. (8) we will have

$$\sum_k \left( \frac{1}{2\lambda} - \chi_k \right) \hat{P}_k [u] = \sum_k \hat{P}_k [\mathbf{n} \cdot \mathbf{E}_0] . \quad (12)$$

The spectral projectors  $\hat{P}_n$  are linearly independent; therefore Eq. (12) provides the solution of (8) as

$$u = \sum_k \frac{1}{\frac{1}{2\lambda} - \chi_k} \hat{P}_k [\mathbf{n} \cdot \mathbf{E}_0] = \sum_k \frac{n_k E_0}{\frac{1}{2\lambda} - \chi_k} u_k. \quad (13)$$

In Eq. (13)  $\mathbf{E}_0 = E_0 \mathbf{N}$  with  $\mathbf{N}$  the normalized vector and  $n_k = \langle v_k | \mathbf{n} \cdot \mathbf{N} \rangle$  with  $\langle | \rangle$  the scalar product defined on  $\Sigma$  [7]. We make several remarks. The induced charge  $u$  contains explicitly information about dielectric properties of the particles along with information about the shape. The response defined by  $u$  also is decomposed in eigenmodes that may have physical relevance with respect to different multipoles of the response. We will see those by analyzing concrete examples. Additionally, the main response provided by  $u$  is a dipolar response that is evaluated by calculating the dipole moments of  $u$ .

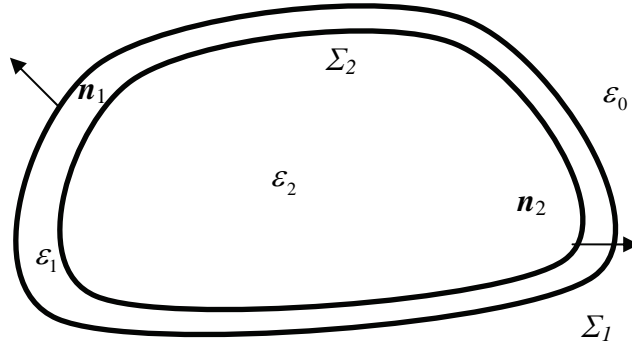


Fig. 2. A model for shelled particle.

## 2.2. Shelled Particles and Their Homogenization

Another case that will be discussed below is that of shelled particles with dielectric permittivities  $\varepsilon_0$ ,  $\varepsilon_1$ , and  $\varepsilon_2$  for outside, for the shell (usually thin), and for inside the shell, respectively. Boundary conditions are needed to be set on both interfaces  $\Sigma_1$  and  $\Sigma_2$  (Fig. 2). Thus, the single-layer solution looks like

$$\Phi(\mathbf{x}) = -\mathbf{x} \cdot \mathbf{E}_0 + \frac{1}{4\pi} \int_{y \in \Sigma_1} \frac{\mu_1(\mathbf{y})}{|\mathbf{x} - \mathbf{y}|} d\Sigma_y + \frac{1}{4\pi} \int_{y \in \Sigma_2} \frac{\mu_2(\mathbf{y})}{|\mathbf{x} - \mathbf{y}|} d\Sigma_y, \quad (14)$$

where  $\mu_1$  and  $\mu_2$  are the induced charge densities on surfaces  $\Sigma_1$  and  $\Sigma_2$  of the shell, respectively. Similar operators may be defined

$$\hat{M}_{ij}[\mu_j] = \frac{1}{4\pi} \int_{\substack{y \in \Sigma_j \\ x \in \Sigma_j}} \frac{\mu_j(y) \mathbf{n}_i(\mathbf{x}) \cdot (\mathbf{x} - \mathbf{y})}{|\mathbf{x} - \mathbf{y}|^3} d\Sigma_y \quad (15)$$

and the solution comprised of  $\mu_1$  and  $\mu_2$  will obey the following equations

$$\begin{aligned} \frac{1}{2\lambda_1} \mu_1(x) - \hat{M}_{11}[\mu_1] - \hat{M}_{12}[\mu_2] &= \mathbf{n}_1 \cdot \mathbf{E}_0 \\ \frac{1}{2\lambda_2} \mu_2(x) - \hat{M}_{21}[\mu_1] - \hat{M}_{22}[\mu_2] &= \mathbf{n}_2 \cdot \mathbf{E}_0 \end{aligned} \quad (16)$$

with  $\lambda_i = (\varepsilon_i - \varepsilon_{i-1}) / (\varepsilon_i + \varepsilon_{i-1})$ .

Now, let us consider that the outer surface of the shell is obtained by expanding the inner surface by a factor  $\eta > 1$ . We want to define a homogenization process to replace the shelled particle with a particle that is homogeneous and generates the same field outside. Thus the equivalence of a shelled particle with a homogeneous one that satisfies the analogous of Eq. (8) with an equivalent charge density  $\mu_e$  is obtained in a following manner. First, one can notice that the operators  $\hat{M}_{11}$  and  $\hat{M}_{22}$  have the same eigenvalues/eigenvectors. The potentials generated outside by the homogeneous particle with charge density  $\mu_e$  and the shelled particle must be the same. This condition is fulfilled if one imposes same Neumann boundary condition on the outer surface [5, 9]

$$\left. \frac{\partial \Phi_e^+}{\partial \mathbf{n}} \right|_{\Sigma_1} = \left. \frac{\partial \Phi^+}{\partial \mathbf{n}} \right|_{\Sigma_1}. \quad (17)$$

Equation (17) can be written as

$$\frac{1}{2} \mu_e(x) + \hat{M}[\mu_e] = \frac{1}{2} \mu_1(x) + \hat{M}_{11}[\mu_1] + \hat{M}_{12}[\mu_2] \quad (18)$$

Then using the first equation of (16) we obtain

$$\frac{1}{2} \left( 1 + \frac{1}{\lambda_1} \right) \mu_1(x) - \frac{1}{2} \mu_e(x) - \hat{M}[\mu_e] = \mathbf{n}_1 \cdot \mathbf{E}_0 \quad (19)$$

The solution of (19) is found by the decomposition of  $\mu_i$  and  $\mu_e$  in the basis generated by the eigenvectors of  $\hat{M} \equiv \hat{M}_{11}$  and work within each subspace generated by the spectral projectors:

$$\mu_{e,k} = \frac{1}{\frac{1}{2} + \chi_k} \left[ \frac{1}{2} \left( 1 + \frac{1}{\lambda_1} \right) \mu_{1,k} - \hat{P}_k [\mathbf{n} \cdot \mathbf{E}_0] \right]. \quad (20)$$

Here  $\mu_{1,k}$  and  $\mu_{e,k}$  are the expansion coefficients of  $\mu_1$  and  $\mu_e$ . If we write (20) in analogy with (12) then in each individual subspace generated by the spectral projectors we have

$$\left( 1 + \frac{1}{\lambda_1} \right) \mu_{1,k} = \left( 1 + \frac{1}{\lambda_{k\_effective}} \right) \mu_{e,k}. \quad (21)$$

Combining (20) and (21) one finds  $\lambda_{k\_effective}$  as a function of  $\mu_{1n}$

$$\left( 1 + \frac{1}{\lambda_{k\_effective}} \right) = \frac{\left( 1 + \frac{1}{\lambda_1} \right) \mu_{1k} \left( \frac{1}{2} + \chi_k \right)}{\frac{1}{2} \left( 1 + \frac{1}{\lambda_1} \right) \mu_{1k} - \hat{P}_k [\mathbf{n} \cdot \mathbf{E}_0]}. \quad (22)$$

A meaningful relation, as we will see shortly, is obtained if we parameterize  $\lambda_{k\_effective}$  as

$$\lambda_{k\_effective} = \frac{\varepsilon_{k\_eff} - \varepsilon_0}{\varepsilon_{k\_eff} + \varepsilon_0}. \quad (23)$$

### 2.3. Solution in the Dipole Approximation

The next step is to solve Eqs. (16) in order to find  $\lambda_{k\_effective}$  and  $\varepsilon_{k\_eff}$  from Eq. (22). To solve (16) we make approximations consistent with the dipole approximation, namely: (a) the normal component of the electric field falls off as  $r^{-3}$  outside the surface and (b) it is constant inside the surface. Thus the dipole approximation reads [5, 9]

$$\begin{aligned} \hat{M}_{12} [\mu_2] &\approx \frac{1}{\eta^3} \left( \frac{1}{2} \mu_2 + \hat{M}_{22} [\mu_2] \right) \\ \hat{M}_{21} [\mu_1] &\approx -\frac{1}{2} \mu_1 + \hat{M}_{11} [\mu_1]. \end{aligned} \quad (24)$$

Equations (16) together with the dipole approximation (24) can be reformulated in terms of a direct product of Hilbert spaces for operators  $\hat{M}$  defined on surfaces  $\Sigma_1$  and  $\Sigma_2$ , respectively. In matrix form the solution is

$$\boldsymbol{\mu} = \begin{pmatrix} \mu_1 \\ \mu_2 \end{pmatrix}. \quad (25)$$

Equations (16) and (24) can be combined and then written in the following matrix form:

$$\begin{pmatrix} \frac{1}{2\lambda_1} - M & -\frac{1}{\eta^3} \left( \frac{1}{2} + M \right) \\ -\left( \frac{1}{2} + M \right) & \frac{1}{2\lambda_2} - M \end{pmatrix} \begin{pmatrix} \mu_1 \\ \mu_2 \end{pmatrix} = \begin{pmatrix} \mathbf{n} \cdot \mathbf{E}_0 \\ \mathbf{n} \cdot \mathbf{E}_0 \end{pmatrix}, \quad (26)$$

where  $M$  is the matrix form of  $\hat{M}$ . Equation (26) is solved by matrix inversion. Cumbersome but straightforward algebra manipulations lead to the following expression of  $\varepsilon_{k\_eff}$

$$\varepsilon_{k\_eff} = \varepsilon_1 \left( 1 + \frac{\varepsilon_2 - \varepsilon_1}{\varepsilon_1 + \delta(1/2 - \chi_k)\varepsilon_2 + \delta(1/2 + \chi_k)\varepsilon_1} \right), \quad (27)$$

with parameter  $\delta = \eta^3 - 1 = 1$ . To summarize, the solution for the effective charge of a homogeneous particle that is equivalent with a shelled particle is

$$\mu_{ek} = \sum_k \frac{1}{\frac{1}{2\lambda_{k\_effective}} - \chi_k} \hat{P}_k[\mathbf{n} \cdot \mathbf{E}_0], \quad (28)$$

with  $\lambda_{k\_effective}$  and  $\varepsilon_{k\_eff}$  given by Eqs. (23) and (27). Therefore, by the process of homogenization Eq. (28) is similar to Eq. (13) but with a dielectric factor  $\lambda$  that is geometry-dependent and has different values for different eigenmodes.

#### 2.4. Effective Permittivity of a Random Assembly of Particles

In the quasi-static regime the incident field  $\mathbf{E}_0$  is constant such that only the dipolar part of the induced charge contributes to response of the system [5]. In a concise manner the dipolar response is given by the volume weighted or specific polarizability that is induced by the incident field. The specific polarizability is the volume weighted dipole moment of the induced charge along the applied field, *i. e.*,

$$\alpha = \frac{1}{V} \sum_k \frac{1}{\frac{1}{2\lambda} - \chi_k} \langle \mathbf{x} \cdot \mathbf{N} | \hat{p}_k | \mathbf{n} \cdot \mathbf{N} \rangle = \frac{1}{V} \sum_k \frac{p_k}{\frac{1}{2\lambda} - \chi_k}, \quad (29)$$

where  $V$  is the volume of the particle and  $\mathbf{x}$  is the position vector pointing to the surface  $\Sigma$ . There are two sum rules needed to be fulfilled, one of them being of the form  $\sum_k p_k = 1$  [5, 10].

The effective response of a collection of randomly arranged particles to a macroscopic field is obtained by summing the specific polarizabilities of the constituent particles. There are several effective theories that describe with certain success the effective permittivity of random assemblies of particles. The oldest one is the Maxwell-Garnett formula which considers a dilute collection of spheres situated in a uniform field (applied plus induced) [11]. A more refined mixture formula is the Bruggeman's [12], which, supposedly, works for larger volume fractions of spherical particles in an assembly. A recent review on mixture formulas can be found in [13]. We proceed in a different manner. If we apply a mean field approximation [14], which is also valid in the limit of low-volume fractions, the effective permittivity of the suspension is

$$\varepsilon_{sus} = \varepsilon_0 + f \frac{\langle \alpha \rangle \varepsilon_0}{1 - f \frac{\langle \alpha \rangle}{3}}. \quad (30)$$

In Eq. (30)  $\langle \alpha \rangle$  is orientation averaged specific polarizability. It can be shown that  $\langle \alpha \rangle$  may be calculated as an average over three orthogonal orientations. In the dilute limit, *i.e.*,  $p \ll 1$ ,  $\varepsilon_{sus}$  is linear in  $p$ , such that the linear approximation of Eq. (30) combined with Eqs. (28) and (29) will lead to :

$$\varepsilon_{sus} = \varepsilon_0 \left( 1 + f \sum_k p_k \frac{\varepsilon_{k\_eff} - \varepsilon_0}{(1/2 + \chi_k) \varepsilon_0 + (1/2 - \chi_k) \varepsilon_{k\_eff}} \right). \quad (31)$$

The influence of geometry on the dielectric response of the system is given by  $p_k$  and  $\chi_k$ , hence Eqs. (30) and (31) show a clear distinction between electric and geometric parameters. In applications the effective permittivity given by Eqs. (30) and (31) is a complex-valued quantity, which considers not only the dielectric polarization but also the losses into the system. These equations can be valid for mixtures like suspensions of biological cells in radio-frequency as well as of semiconductor micro- and nanocrystals for surface optical phonons/polaritons and of metallic nanoparticles

for localized plasmons [13]. Equations (30) and (31) are generalizations of Maxwell-Garnett formula to particles of arbitrary shapes.

### 2.5. Numerical Approach

In the general case, only numeric solutions can be obtained for Eqs. (13) and Eq. (28). We adopt a spectral method that, contrary to any type of finite element or other discrete versions, uses basis defined on the whole domain, which is in our case the surface  $\Sigma$  [4, 5]. Thus if we choose a basis of functions

$$\{ |a_n(x)\rangle \}_{n=0, \infty}. \quad (29)$$

that are defined on the surface  $\Sigma$ , Eq. (13) will be written in matrix form as

$$\sum_{n=0}^N \left[ \frac{1}{2\lambda} \delta_{mn} - M_{mn} \right] A_n = B_m, \quad (30)$$

$m = \overline{0, N}$ .  $N$  is the (finite) number of basis functions considered for simulation. The matrix has the form

$$M_{mn} = \frac{1}{4\pi} \int_{\Sigma_y} \int_{\Sigma_x} a_m^*(\mathbf{x}) a_n(\mathbf{y}) \frac{(\mathbf{x} - \mathbf{y}) \cdot \mathbf{n}(\mathbf{x})}{|\mathbf{x} - \mathbf{y}|^3} d\Sigma_y d\Sigma_x \quad (31)$$

and the column vectors are expressed by

$$\begin{aligned} A_n &= \int_{\Sigma_x} u(\mathbf{x}) a_n(\mathbf{x}) d\Sigma_x \\ B_n &= \int_{\Sigma_x} (\mathbf{n}(\mathbf{x}) \cdot \mathbf{N}) a_n(\mathbf{x}) d\Sigma_x. \end{aligned} \quad (32)$$

The choice of basis  $\{ |a_n(\mathbf{x})\rangle \}$  determines not only the way the matrix defined by Eqs. (7) and (8) can be calculated but also the modality of solving the system of linear equations (29). A convergence criterion in these methods is the accuracy by which the sum rules are fulfilled. Another issue is how to define a basis for a given particle shape. We consider here surfaces  $\Sigma$  that are diffeomorphic with a sphere [5,6]. Therefore, the correspondence between  $\Sigma$  and the sphere is given by differentiable functions  $\theta(\mathbf{x})$  and  $\varphi(\mathbf{x})$ , where  $\theta$  and  $\varphi$  are the angles that define the sphere and  $\mathbf{x}$  is the vector that defines  $\Sigma$ . A basis for smooth surfaces is

$$\tilde{Y}_{lm}(\mathbf{x}) = \frac{1}{\sqrt{s(\mathbf{x})}} Y_{lm}(\theta(\mathbf{x}), \varphi(\mathbf{x})), \quad (33)$$

where  $s(x)$  is a (smooth) function which defines a measure on surface  $\Sigma$ , *i. e.*,  $d\Sigma = s(\mathbf{x})d\Omega_x$ ,  $Y_{lm}(\theta, \varphi)$  are the spherical harmonics defined on sphere, and  $d\Omega_x$  is the solid angle element also related to the sphere equivalent to  $\Sigma$ . The choice given by Eq. (33) is not as general as it might seem. This is one of the drawbacks of this methods [4, 14]. But as we already noticed [15,16] when the spectral method may be applied it has an exponential convergence [14].

### 3. Applications

#### 3.1. Dielectric Spectra of Living Cell in Radio-Frequency

The use of radio-frequency fields in biological applications is advantageous due to its non-invasive nature. The radio-frequency fields are used either for manipulation [17, 18] or for cell imaging and bio-impedance measurements and analysis [19, 20]. The progress made by micro- and nano-fabrication enables dielectric measurements at a single cell within the concept of Lab-on-a-chip [32]. In radio-frequency and further in the microwave region there are encountered three interaction mechanisms of biological cells with electromagnetic fields called  $\alpha$ -,  $\beta$ -, and  $\gamma$ -relaxations[33]. The interaction of electromagnetic fields with ions and counter-ions around the cell membrane is responsible for  $\alpha$ -relaxation. It occurs at very low frequency about few kHz and usually is very tricky to identify it because its complex capacitance competes with the capacitance resulted from polarization of measurements electrodes. The second relaxation, the  $\beta$ -relaxation, is due to the Maxwell-Wagner relaxation mechanism. In this mechanism the main physical property that plays a defining role is the cell polarization which, in principles, can be found from dielectric spectroscopy measurements. The Maxwell-Wagner relaxation is a structural property depending on both the shape and the dielectric parameters of cells. It takes place in the MHz region of frequencies and is the most used in applications. The third relaxation mechanism present in the microwave (GHz) region of the electromagnetic spectrum is  $\gamma$ -relaxation arising from the permanent dipole relaxation of bound water present in cells. Below we will treat and discuss the  $\beta$ -relaxation which is the most known and used in applications regarding the interaction of electromagnetic fields of radio-frequency with living cells.

In order to calculate the behavior of dielectric objects interacting with electromagnetic fields one needs to know the dielectric response of bulk materials from



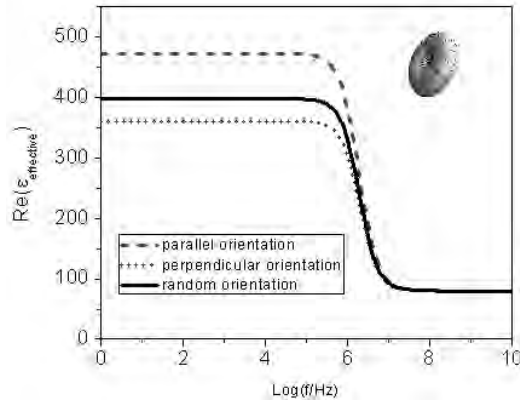
which the dielectrics are made. We start out with the Drude dielectric function [1], which is the model of free electrons and describes metals. The Drude dielectric function is

$$\varepsilon^* = \varepsilon_r - \frac{\omega_p^2}{\omega(\omega + i\gamma)}, \quad (34)$$

where the \* means complex quantities and  $\varepsilon_r$  is the real part of permittivity including  $\varepsilon_\infty$ ,  $\omega_p$  is plasmon frequency and  $\gamma$  is the ohmic-type loss. As we will see below it will be used for metals at optical frequencies and also for dielectrics with losses. In the limit of low frequency  $\omega \rightarrow 0$  we have  $\varepsilon^* = \varepsilon_r + i\omega_p^2/(\gamma\omega)$ . Usually in dielectric spectroscopy the following form of the complex dielectric constant is used

$$\varepsilon^* = \varepsilon_r - i\varepsilon_{im} = \varepsilon_r - i\sigma/\omega, \quad (35)$$

with  $\sigma$  the ionic and/or electronic conductivity. Equation (35) considers a compact form for the continuity of normal components of the electric induction and for the continuity relation of electrical current at the interface. The sign issue between Eq. (35) and the low frequency limit of (34) comes from the definition of the imaginary part of complex permittivity. Equation (35) is the usual expression of complex dielectric functions used in materials including biological systems in radio-frequency [31].



**Fig. 3.** Real part of the effective dielectric constant of a red blood cells in suspension. The dashed/dotted lines represent the effective dielectric constant of a suspension of aligned but otherwise randomly positioned cells in suspension for parallel/perpendicular field orientation. The solid line represents the real part of the effective dielectric constant for random positions and orientations of the cells. The volume fraction of the cells in solution is 5%.

The minimal model of biological cells is a particle covered by a thin shell (membrane) with a very low conductivity. We consider here such a case for biological cells. Models of multi-shelled cells can be easily studied by using the homogenization procedure described in the previous section. If the dielectric constants of the form given by Eq. (35), it is easy to show that the equivalent permittivity  $\varepsilon_{k\_eff}$  in Eq. (27) can be expressed as a term with one Debye relaxation term for each eigenmode whose weight  $p_k \neq 0$ , *i. e.*,

$$\varepsilon_{k\_eff} = \varepsilon + \Delta\varepsilon_k / (1 + i\omega T_k). \quad (36)$$

More generally, a suspension of particles with  $m$  shells has  $m+1$  Debye relaxation terms [21] for each eigenmode. The relaxation time  $T_k$  is the inverse of the relaxation frequency where the impedance of the system changes significantly and the real part of the dielectric function has a visible drop. For a single shell the relaxation time is given by [5]

$$T_{k1} \approx \frac{(1 + \delta/2 + \delta\chi_k)\varepsilon_1 + \delta(1/2 - \chi_k)\varepsilon_2}{(1 + \delta/2 + \delta\chi_k)\sigma_1 + \delta(1/2 - \chi_k)\sigma_2}, \quad (37)$$

which provides the value of the relaxation time induced by the shell in the experimentally accessible  $\varepsilon_{sus}$ . Assuming that the shell has similar dielectric properties with the cytoplasm, which will be the case for post-relaxation frequencies, then  $T_{k1} \approx \varepsilon_1/\sigma_1$ . However, if we consider a non-conductive shell ( $\sigma_1 = 0$ ), the relaxation time is

$$T_{k1} \approx \frac{\varepsilon_1}{\delta\sigma_2(1/2 - \chi_k)}, \quad (38)$$

displaying the leading role of the thickness of the shell, and of the shape of the cell. On the other hand the dielectric decrement  $\Delta\varepsilon_k$  of the relaxation is also inverse proportional to  $\delta$ ,

$$\Delta\varepsilon_k \approx \frac{f p_k \varepsilon_1}{\delta(1/2 - \chi_k)}. \quad (39)$$

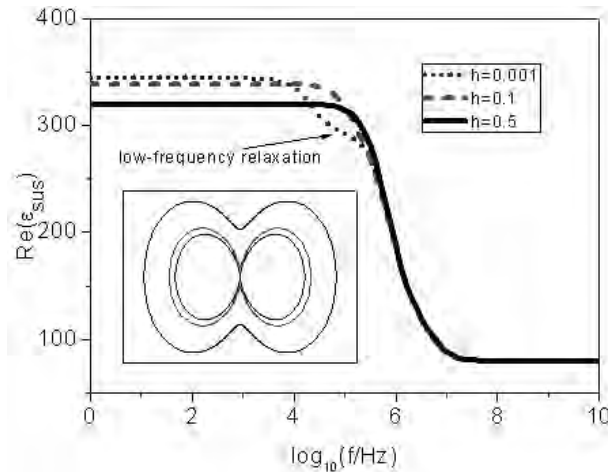
Both parameters of the relaxation, namely the relaxation time and the dielectric decrement, depend inverse proportionally with the generalized depolarization factor  $(1/2 - \chi_k)$  [5].

In Fig. 3 we plot the dielectric spectra of a 5% volume fraction suspension of red blood cells. The shape of the cells are Cassini ovals given by the following equation in  $(x,y)$ -plane and polar coordinates

$$r^4 - 2a^2 r^2 \cos(2\theta) = b^4 - a^4 \quad (40)$$

The shape is obtained by rotation about y-axis. We considered that the minimum thickness of the cell is  $u = 2\sqrt{b^2 - a^2} = 0.81 \mu\text{m}$  and the diameter of the cell is  $v = 2\sqrt{b^2 + a^2} = 7.82 \mu\text{m}$ . The membrane is 1/100 of the total size and the electrical parameters are: the relative permittivity of the cytoplasm is 51 and its conductivity is 0.73 S/m; the relative permittivity of the membrane is 9 and its conductivity is 0.0001 S/m; and the relative permittivity of outer medium is that of water, i. e., 81, and its conductivity is 0.1 S/m. We see in Fig. 3 that there is basically one relaxation that is given by membrane and is practically the dipole part of the dielectric response. Although there are several eigenmodes contributing to the relaxation shown in Fig. 3, it appears as a single relaxation due to two factors: their relative close position and the broad character of the dielectric relaxation itself.

However, situation changes when one of the eigenvalues is very close to the largest eigenvalue which is 1/2. This can be the case of clusters of slightly connected cells or alternatively in very elongated cells. Thus, in these cases a distinct relaxation emerges at very low frequency. In Fig. 4 we present a case of two connected cells with the shape depicted in the inset of the figure. The electric parameters of the cells are those from Fig. 3 and the volume fraction of the cells is also 5%. The gap between cells is varied such that below a threshold gap a distinct relaxation appears at lower frequencies. Other cases are presented also in [6]. Similar situation will be found below when we discuss localized plasmon resonances in metallic nanoparticles.



**Fig. 4.** Real part of the effective dielectric constant of a suspension of connected cells for three gap sizes  $h$ : 0.5, 0.1, and 0.001 of the cell size. The inset shows a cross-section of the connected cells in these three cases.

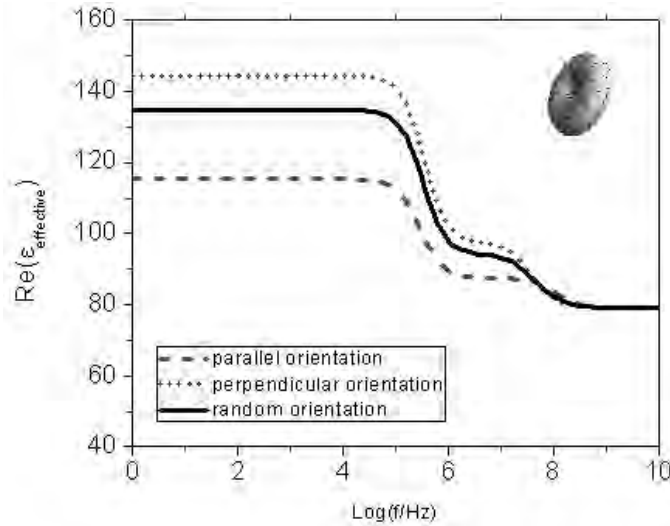
According to the general theory outlined above for each eigenmode there are two relaxations of shelled particles. Thus, at frequencies larger than membrane relaxation frequency, the cell permittivity and conductivity are determined by the dielectric properties of cytoplasm and/or of outer medium. The second relaxation is visible whenever the conductivity ratio of outer medium and cytoplasm is either  $\ll 1$  or  $\gg 1$ . The relaxation time is either

$$T_{k2} \approx \frac{\varepsilon_1}{\sigma_1} \quad (41)$$

or, correspondingly,

$$T_{k2} \approx \frac{\varepsilon_0}{\sigma_0}. \quad (42)$$

In Fig. 5 we depict the case where the conductivity of the suspension medium is lowered from 0.1 S/m to 0.001 S/m.



**Fig. 5.** Same as Fig. 3, but the conductivity of the outer medium is 0.001 S/m.

The examples shown above demonstrate the usefulness of the BIE method as a tool in studying and describing  $\beta$ -relaxation. It reveals that, depending on the shape and on the electric parameters of the cells, there are three distinct regions of relaxations whose parameters are defined by Eqs. (36)-(39) and (40)-(41). These equation and additional ones given in [6] can be a starting point in a process of fitting and thus monitoring electric and shape parameters from dielectric measurements.

### 3.2. Localized Plasmon Resonances in Metallic Nanoparticles

Metallic nanoparticles made of noble metals interact strongly with light through localized surface plasmon resonances (LSPRs) which are collective excitations of conduction electrons [22]. Classically, the LSPRs appear at a dielectric interface where the real part of the dielectric constant on one side of the interface is negative. For metals and, more notably, for noble metals the dielectric constant is negative in the frequency range  $[\gamma, \omega_p]$ , which is at optical frequencies, hence the LSPRs are mostly located in visible (VIS) and near-infrared (NIR). The LSPRs confine the electric field nearby the surface of nanoparticles enabling their use as sensors like refractive-index sensors [23] or sensors based on surface enhanced Raman scattering (SERS) [24] and surface enhanced infrared scattering (SEIRS) [25]. Metallic nanoparticles can be also used to enhance the near-field microscopy [26], photoluminescence [27], second or higher harmonic generation [28, 29], etc.

The specific polarizability  $\alpha$  also defines the optical spectrum of LSPRs. In fact, the far-field expressed by the extinction spectrum is characterized by the cross-section extinction and is proportional to the imaginary part of  $\alpha$  [6]

$$C_{ext} = \frac{2\pi}{\lambda} \text{Im}(\alpha V) \quad (43)$$

The eigenmode decomposition of  $\alpha$  allows also an eigenmode decomposition of the extinction spectrum. The Drude model, moreover, allows explicit modal expressions of  $\alpha$  like in the following equation [6]

$$\alpha(\omega) = \sum_k \frac{p_k (\varepsilon_m - \varepsilon_d)}{\varepsilon_k} \frac{p_k \varepsilon_d}{1/2 - \chi_k} \frac{\tilde{\omega}_{pk}^2}{\omega(\omega + i\gamma) - \tilde{\omega}_{pk}^2} \quad (44)$$

which provides the square of the localized plasmon resonance frequency by  $\tilde{\omega}_{pk}^2 = ((1/2 - \chi_k) \omega_p^2) / \varepsilon_k$  and  $\varepsilon_k = (1/2 + \chi_k) \varepsilon_0 + (1/2 - \chi_k) \varepsilon_r$  is an effective permittivity. Similar to the expressions for membrane relaxation in living cells the term  $(1/2 - \chi_k)$  is the depolarization factor of the eigenmode.

The near-field properties can be calculated with similar expressions like those used for far-field because the near-field is generated by the same induced charge density  $u$ . In [7] we have shown that the near-field enhancement at the surface  $\Sigma$  can be calculated from the eigenfunctions of  $\hat{M}$  and  $\hat{M}^\dagger$ . Thus if an incident field of strength  $\mathbf{E}_0$  acts on nanoparticle, the normal and tangent components with respect to  $\Sigma$  of the enhancements are given by

$$E_n/E_0 = \sum_k \frac{n_k (\chi_k + 1/2)}{\frac{1}{2\lambda} - \chi_k} u_k \quad (45)$$

and

$$E_t/E_0 = -\sum_k \frac{n_k}{\frac{1}{2\lambda} - \chi_k} \nabla_t v_k. \quad (46)$$

where  $\nabla_t$  is the gradient in the tangent plane to  $\Sigma$ . The total field enhancement at the surface  $\Sigma$  is of the following form

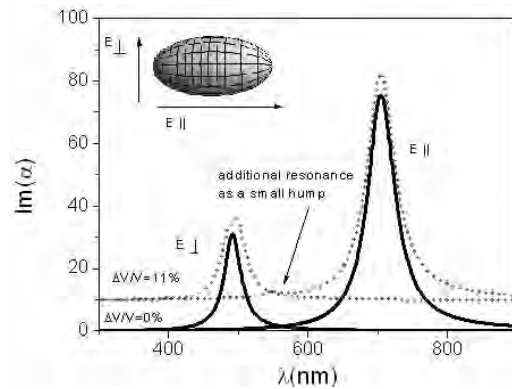
$$E_{total}/E_0 = \sqrt{(E_n/E_0)^2 + (E_t/E_0)^2 + 1}. \quad (47)$$

As in the case of the extinction spectrum equations (45)-(47) provide also the near-field decomposition over the eigenmodes of  $u$  and an intuitive and a direct relationship between the LSPRs and the near-field enhancement. Actually the total electric field is complex-valued, hence its modulus represents the strength of the enhancement and its phase is just the phase shift between the applied and the total field. Equations (44) - (47) show elegantly the shift between near-field and far-field peak intensities in LSPRs [30].

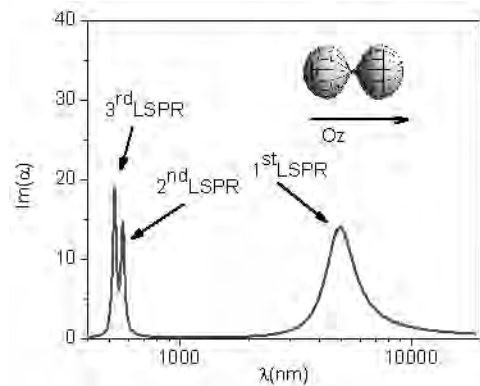
Equation (8) indicates that an LSPR is determined by the eigenmode weight  $p_k$  as well as its eigenvalue  $\chi_k$ . In the following we consider gold nanoparticles with the Drude parameters also used in [7]. In Fig. 6 we show the influence of shape modification on LSPR of prolate spheroid with an aspect ratio of 2:1 [15]. The shape changes illustrated by volume variation of 11% may induce change in the LSPR spectrum of metallic nanoparticles. The change appears for light polarization across smallest dimension of the nanoparticle which is the transverse direction in our case. Moreover, it was shown in [15] that the variation in the LSPR spectrum is made by the variation of both the eigenmode weight  $p_k$  and the eigenvalue  $\chi_k$ . For shape changes with volume variations greater than 12% additional eigenmodes may appear in the spectrum of LSPR. This kind of study is important in the design of plasmonic devices when a supplementary care must be considered for smaller dimensions of devices. In a recent paper we also shown that near-field properties are much greater influenced by shape variation because the near-field is more sensitive to local changes of the shape in contrast to the far-field which rather depends on the overall changes of shape [34].

Dimers of metallic nanoparticles are very attractive for plasmonic applications since they exhibit very large field enhancement [35, 36, 37]. Significant progress has been made toward fabrication of dimers made of slightly connected nanoparticles due to their advantage over non-connected dimers by the emergence of new strong resonances in infrared [38]. In Fig. 7 we depict the far-field spectrum of a dimer made

of two almost spherical nanoparticles shown in the inset of the figure. The polarization of the incident field is parallel with the symmetry axis of the dimer. The first LSPR is a new resonance specific to the dimer; it is in infrared and is called charge-transfer resonance [7, 9]. The second resonance is also specific to dimers, it is a “molecular mode” because the charge is localized in the dimer gap like the hybrid molecular orbitals in molecular physics [7]. Only the third one is specific to the sphere and is also a hybrid mode of the two constituent spheres.

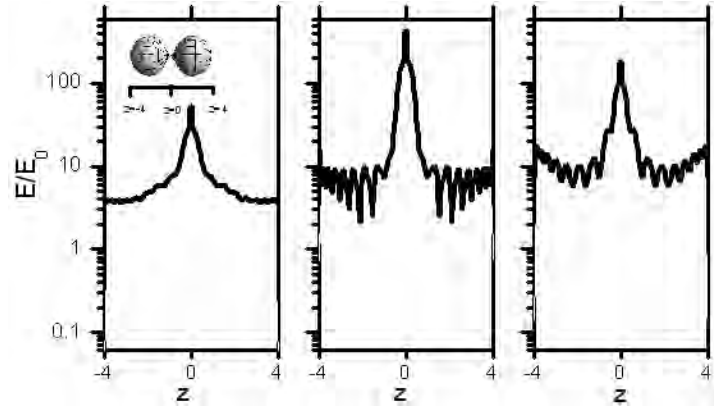


**Fig. 6.** Shape variation of LSPR spectrum by volume change of 11%. Solid/dotted line represents the LSPR spectrum of the pristine/deformed spheroid for parallel (resonance at longer wavelength) and perpendicular light polarization. The LSPR spectrum of deformed spheroid was shifted upward for a better visualization.



**Fig. 7.** Imaginary part of specific polarization,  $\alpha$ , which is proportional to extinction spectrum of a closely touching dimer. There are three mainly LSPRs. The inset shows the dimer and the direction of polarization.

The location of the third LSPR is almost the same as that of a single sphere [7]. In Fig. 8 we plotted the near-field enhancement at the surface on the nanoparticle. We can easily see that the largest field enhancement is found in the gap between the particles, the second mode having the strongest field enhancement of about 500. The third mode has a field enhancement of 200, while the enhancement of the first mode is about 70. We notice here that the near-field enhancement of a single sphere is about 20, which is an order of magnitude smaller than the similar eigenmode (the third) of the dimer.



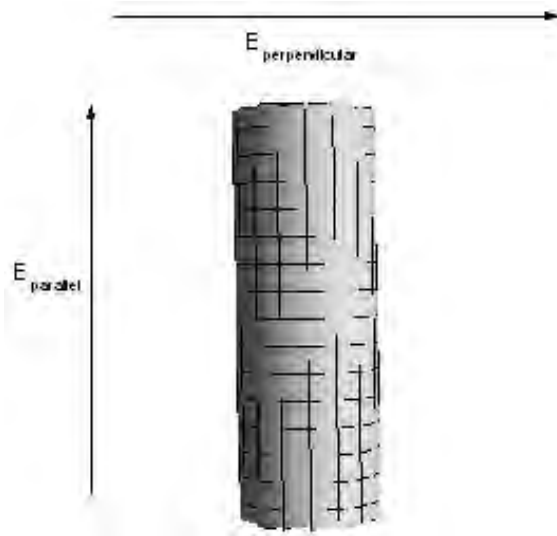
**Fig. 8.** The near-field enhancement of the LSPRs shown in Fig. 7. The first is plotted on the left-hand side, while the third on right-hand side. The field enhancement is plotted against the  $z$ -coordinate and has an axial symmetry around the same axis. The inset shows the  $z$ -defined dependence of the dimer surface.

Other plasmonic systems of interest are nano-rods. Metallic nano-rods are attractive because they are relatively easy to fabricate. Thus, by controlling their aspect ratio one can tune the plasmon resonance from visible to infrared [37, 40]. An example is presented in Fig. 9 with its ends being almost flat. Usually hemispherical capping is considered. For hemispherically capped rods there is a scaling law which also is valid in the quasi-static limit [40]. The aspect ratio of the nano-rod is 3:1. In Table 1 we present the relevant eigenmodes, their weights and the field polarization for which they are “bright”. By relevant it is meant all modes whose weight is larger than 2%. A “bright” mode is the mode with  $p_k \neq 0$ , otherwise the mode is “dark”.

From Table 1 and from Fig. 10 we notice that only eigenmodes with  $p_k > 0.2$  can be effectively seen in the spectrum. In the case of parallel (longitudinal) polarization there is one major mode, *i. e.*, dipolar, with  $p_k \approx 0.9$ . There is a second mode, much weaker and not actually seen in the spectrum. The second mode is basically formed as



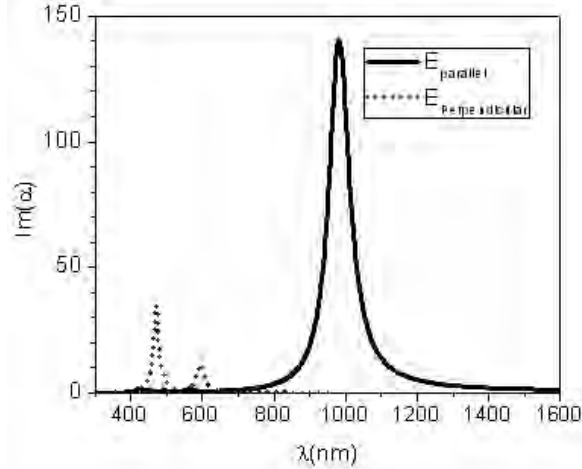
two aligned dipoles as we have seen it from its eigenfunction (not shown here). When the polarization is perpendicular there are several modes with relevant weights but only two can be easily detected in the spectrum. The heights of these resonances are much smaller than the height of the longitudinal resonance. So this example shows that nano-rods can be used as successful plasmonic devices only for field polarization parallel with nano-rod axis.



**Fig. 9.** A metallic nano-rod with flat ends. It is also shown the two directions of light polarization considered in the main text.

**Table 1.** The most representative eigenmodes of the metallic rod depicted in Fig. 9. Both polarizations are considered, *i.e.*, parallel and perpendicular

	$P_k$	$\chi_k$		$P_k$	$\chi_k$
<b>parallel</b>	0.8939	0.4160	perpendicular	0.147221	0.24298
	0.0427	-0.116		0.0246591	-0.0990
	0.0218	-0.027		0.0419887	0.0968179
			0.0484039	0.0438715	
			0.407311	0.0382197	
			0.249318	0.0358536	
			0.0438867	-0.012240	



**Fig. 10.** Extinction spectrum of the nano-rod described in the main text. The solid line corresponds to longitudinal polarization while the dotted line corresponds to transverse direction of the electric field.

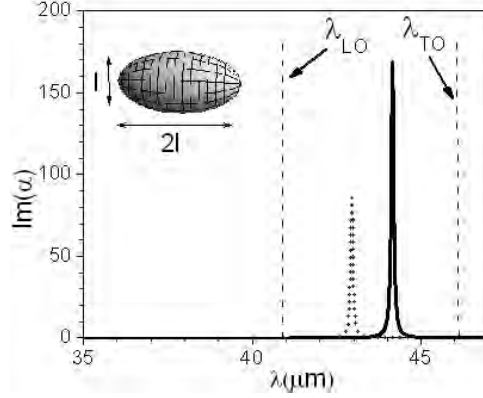
### 3.3. Surface Optical Phonons

In nanostructures beside electrons and holes also phonons are confined [42]. For phonons continuum models are very successful in describing their properties in structures at nanoscale. Thus, in continuum models the boundary conditions at the interface delimitating the nanostructures are very important. For acoustic modes the displacement and normal component of stress tensor must be continuous while optical modes require the continuity of the electric potential and the normal component electric induction. In layered nanostructures [42] as well as in nanocrystals [43] there are both interface and confined optical phonons. Phonons in nanostructures were first studied in layered structures mostly due to their relations with the electron-phonon coupling [44-49]. In nanocrystals or quantum dots there are several studies concerning polar optical phonons more notably [50, 51] that suggest similar behavior of surface optical phonons with plasmon resonances of metallic nanoparticles. They are called localized phonon polaritons. Along with their role in affecting the electron-phonon coupling and the lifetime of charge carriers in nanostructures the localized polaritons have been used recently also in characterizing aerosols [52] and as alternate plasmonic materials in IR and THz due to their low energy loss [53].

In the IR light couples with optical phonons leading to strong absorption in the band called reststrahlen [1], between  $\omega_T$  and  $\omega_L$ , the frequencies of transverse optical phonons and longitudinal optical phonon branches at the Brillouin zone center,

respectively [1, 53, 54]. This band appears only in polar crystals and the dielectric constant in this band is [1, 53, 54]

$$\varepsilon = \varepsilon(\infty) \left( 1 + \frac{\omega_L^2 - \omega_T^2}{\omega_T^2 - \omega^2 + i\Gamma\omega} \right). \quad (48)$$



**Fig. 11.** Extinction spectrum of the InAs spheroidal nanodot. The solid line corresponds to longitudinal polarization while the dotted line corresponds to transversal direction of the electric field. The inset shows the spheroid and its dimensions in a ale invariant theory. The dashed vertical lines are the lines defining the wavelengths associated with longitudinal optical and transverse optical branches at the Brillouin zone center [1, 53].

From Eq. (48) one can check that  $\varepsilon$  is negative if  $\omega$  is between  $\omega_T$  and  $\omega_L$ . Thus, nanocrystals exhibit localized polaritons in the reststrahlen band. In fact one can show similar relations like those described by Eqs. (44)-(47) for localized surface plasmons. Moreover, these localized polaritons have a much smaller frequency range than localized plasmons since they are located between  $\omega_T$  and  $\omega_L$ . In Fig. 11 we show the localized polaritonic spectrum of an InAs nanoparticle of spheroidal shape with an aspect ratio of 2:1. The horizontal coordinate is the wavelength of the IR radiation expressed in  $\mu\text{m}$ . The parameters of the dielectric constant given by Eq. (48) are taken from [1] and [54]. Similar to LSPRs, localized polaritons display stronger absorption when the field is polarized in the direction of longer dimensions because it is also proportional to  $1/(1/2 - \chi_k)$ . Moreover, the above formalism can also describe crystal microparticles with sizes of few  $\mu\text{m}$  given that the resonances are at wavelengths above  $40 \mu\text{m}$  (we remind that, in order to obey the quasi-static approximation, the size of the particle should be much smaller than the radiation

wavelength, usually by a factor of 10).

#### 4. Concluding Remarks

In this work we have presented a spectral approach to the boundary integral equation method that can be used in a variety of frequency ranges of the electromagnetic field and for different classes of micro- and nano-structures. We have shown that the method obtains a modal decomposition of the response to electromagnetic excitations and each mode has a definite dependence on electrical and geometric parameters of the system. Maxwell-Wagner relaxation in biological cells, localized plasmon resonance in metallic nanoparticles and localized surface polaritons in quantum dots can be successfully analyzed by this approach. Insights into physical properties and direct dependences on electric and geometric factors are provided.

The approach can be further developed and improved in several directions. For biological cells the method permit the development of some procedures by which one can extract electrical and geometrical parameters of the cell from dielectric measurements. For localized plasmon and polariton resonances the theory can be extended beyond the quasi-static limit to consider retardation [55]. Non-local effects, which are purely quantum, can be considered in many other ways [56, 57]. Fully quantum calculations are quite expensive from computational point of view [58], consequently other quantum effects like tunneling can be successfully described by quantum corrected models [59]. As a result, the calculation method presented in this work is by itself a valuable tool for studying nanostructures and also is a good starting point for more refined procedures that that may describe in an intelligible manner the physics at the nanometer level.

#### References

- [1] P.Y. YU and M. CARDONA, *Fundamentals of Semiconductors*, 4th ed., Springer, Heidelberg, New York, 2010.
- [2] R.W. BOYD, *Nonlinear Optics*, 3<sup>rd</sup> ed. Academic Press, 2008
- [3] C. DUPAS, P. HOUDY, M. LEHMANNI (eds.), *Nanoscience-Nanotechnology and Nanophysics*, Springer-Verlag, Berlin Heidelberg 2007.
- [4] I. TSUKERMAN, *Computational Methods for Nanoscale Applications*, Spinger, New York, 2008.
- [5] T. SANDU, D. VRINCEANU, E. GHEORGHIU, *Linear dielectric response of clustered living cells*, *Phys. Rev. E* **81**, pp. 021913, 2010.
- [6] T. SANDU, D. VRINCEANU, E. GHEORGHIU, *Surface plasmon resonances of clustered nanoparticles*, *Plasmonics* **6**, pp. 407–412, 2011.
- [7] T. SANDU, *Eigenmode decomposition of the near-field enhancement in localized surface plasmon resonances of metallic nanoparticles*, *Plasmonics* **8**, pp. 391–402, 2013.

- [8] D. KHAVISON, M. PUTINAR, H.S. SHAPIRO, *Poincaré's variational problem in potential theory*, Arch. Rational.Mech. Anal. **185**, pp. 143, 2007.
- [9] C. PRODAN and E. PRODAN, *The dielectric behaviour of living cell suspensions*, J. Phys. D, **32**, pp. 335, 1999.
- [10] D.J. BERGMAN, D. STROUD, *Solid State Physics, Advances in Research and Applications*, H. EHRENREICH and D. TURNBULL (eds.), Academic **46**, p. 147. San Diego, CA, 1992.
- [11] J.C. MAXWELL-GARNETT, *Colours in metal glasses and metal films*, Philos. Trans. R. Soc. London, Sect. A **203**, pp. 385–420, 1904.
- [12] D.A.G. BRUGGEMAN, *Berechnung verschiedener physikalischer Konstanten von heterogenen Substanzen*, Ann. Phys. (Leipzig) **24**, pp. 636–679, 1935.
- [13] E. TRUNCER, *Dielectric mixtures-importance and theoretical approaches*, IEEE Electrical Insulation Magazine **29**, pp. 49–58, 2013.
- [14] J.P. BOYD, *Chebyshev and Fourier Spectral Methods*, Dover, New York, 2001.
- [15] T. SANDU, *Shape effects on localized surface plasmon resonances in metallic nanoparticles*, J. Nanopart. Res. **14**, pp. 905, 2012.
- [16] T. SANDU, G. BOLDEIU, V. MOAGAR-POLADIAN, *Applications of electrostatic capacitance and charging*, J. Appl. Phys. **114**, pp. 224904, 2013.
- [17] R. PETHIG, *Review Article-Dielectrophoresis: Status of the theory, technology, and applications*, Biomicrofluidics **4**, pp. 022811, 2010.
- [18] T.B. JONES, *Basic theory of dielectrophoresis and electrorotation*, IEEE Engineering in Medicine and Biology Magazine **22**, pp. 33–42, 2003.
- [19] K. HEILEMAN, J. DAOUD, M. TABRIZIAN, *Dielectric spectroscopy as a viable biosensing tool for cell and tissue characterization and analysis*, Biosensors and Bioelectronics **49**, pp. 348–359, 2013.
- [20] K. ASAMI, *Characterization of heterogeneous systems by dielectric spectroscopy*, Prog. Polym. Sci. **27**, pp. 1617–1659, 2002.
- [21] T. HANAI, H. Z. ZHANG, K. SEKINE, K. ASAKA, K. ASAMI, *The number of interfaces and the associated dielectric relaxations in heterogeneous systems*, Ferroelectrics **86**, pp. 191, 1988.
- [22] E. OZBAY, *Plasmonics: Merging Photonics and Electronics at Nanoscale Dimensions*, Science **311**, pp. 189, 2006.
- [23] S. LAL, S. LINK, N.J. HALAS, *Nano-optics from sensing to waveguiding*, Nat. Photonics, **1**, pp. 641, 2007.
- [24] S. NIE, S.R. EMORY, *Probing Single Molecules and Single Nanoparticles by Surface-Enhanced Raman Scattering*, Science **275**, pp. 1102, 1997.
- [25] F. NUEBRECH, A. PUCCI, T.W. CORNELIUS, S. KARIM, A. GARCIA-ETXARRI, J. AIZPURUA, *Resonant Plasmonic and Vibrational Coupling in a Tailored Nanoantenna for Infrared Detection*, Phys. Rev. Lett. **101**, pp. 157403, 2008.
- [26] J.J. MOCK, M. BARBIC, D.R. SMITH, D.A. SCHULTZ, S. SCHULTZ, *Shape effects in plasmon resonance of individual colloidal silver nanoparticles*, J. Chem. Phys. **116**, pp. 6755, 2002.
- [27] F. TAM, G.P. GOODRICH, B.R. JOHNSON, N.J. HALAS, *Plasmonic Enhancement of Molecular Fluorescence*, Nano Lett. **7**, pp. 496, 2007.
- [28] M. DANCKWERTS, L. NOVOTNY, *Optical Frequency Mixing at Coupled Gold Nanoparticles*, Phys. Rev. Letters **98**, pp. 026104, 2007.
- [29] S. KIM, J. JIN, Y. KIM, I. PARK, Y. KIM, S. KIM, *High-harmonic generation by resonant plasmon field enhancement*, Nature **453**, pp. 757, 2008.

- [30] J. ZULOAGA, P. NORDLANDER, *On the energy shift between near-field and far-field peak intensities in localized plasmon systems*, Nano Lett. **11**, pp. 1280, 2011.
- [31] J. BAKER-JARVIS, S. KIM, *The Interaction of Radio-Frequency Fields With Dielectric Materials at Macroscopic to Mesoscopic Scales*, Journal of Research of the National Institute of Standards and Technology **117**, pp. 1–60, 2012.
- [32] H. MORGAN, T. SUN, D. HOLMES, S. GAWAD, N.G. GREEN, *Single cell dielectric spectroscopy*, J. Phys. D: Appl. Phys. **40**, pp. 61–70, 2007.
- [33] H. P. SCHWAN, *The Practical Success of Impedance Techniques from an Historical Perspective*, Annals of the New York Academy of Sciences **873**, pp. 1–12, 1999.
- [34] T. SANDU, G. BOLDEIU, *How shape affects plasmonic properties of metallic nanospheres*, Digest Journal of Nanomaterials and Biostructures **9**, pp. 1255–1262, 2014.
- [35] W. RECHBERGER, A. HOHENAU, A. LEITNER, J.R. KRENN, B. LAMPRECHT, F.R. AUSSENEGG, *Optical properties of two interacting gold nanoparticles*, Optics Communications **220**, pp. 137–141, 2003.
- [36] J.T. ATAY, J.H. SONG, A.V. NURMIKKO, *Strongly Interacting Plasmon Nanoparticle Pairs: From Dipole–Dipole Interaction to Conductively Coupled Regime*, Nano Lett. **4**, pp. 1627–1631, 2004.
- [37] J. AIZPURUA, G.W. BRYANT, L.J. RICHTER, and F.J. GARCIA DE ABAJO, *Optical properties of coupled metallic nanorods for field enhanced spectroscopy*, Phys. Rev. **B 71**, pp. 235420, 2005.
- [38] F. WEN, Y. ZHANG, S. GOTTHEIM, N.S. KING, Y. ZHANG, P. NORDLANDER, N.J. HALAS, *Charge Transfer Plasmons: Optical Frequency Conductances and Tunable Infrared Resonances*, ACS Nano **9**, pp. 6428–6435, 2015.
- [39] L. LIU, Y. WANG, Z. FANG, and K. ZHAO, *Plasmon Hybridization Model Generalized to Conductively Bridged Nanoparticle Dimers*, J. Chem. Phys. **139**, pp. 064310, 2013.
- [40] T. SANDU, *Near-Field and Extinction Spectra of Rod-Shaped Nanoantenna Dimers*, Proceedings of the Romanian Academy, Series **A 15**, pp. 338–345, 2014.
- [41] C. BROSEAU, A. BEROUAL, *Computational electromagnetics and the rational design of new dielectric heterostructures*, Progress in Materials Science **48**, pp. 373–456, 2003.
- [42] B.K. RIDLEY, *Electrons and Phonons in Semiconductor Multilayers*, Cambridge Studies in Semiconductor Physics and Microelectronic Engineering, 1996.
- [43] R. ENGLMAN, R. RUPPIN, *Optical Phonons in Finite Crystals*, Phys. Rev. Lett. **16**, pp. 898–891, 1966.
- [44] R. FUCHS, K.L. KLIEWER, *Optical Modes of Vibration in an Ionic Slab*, Physical Review, **140**, pp. A2076–A2088, 1965.
- [45] C. TRALLERO-GINER, F. GARCIA-MOLINER, V.R. VELASCO, M. CARDONA, *Analysis of the Phenomenological Models for Long-Wavelength Polar Optical Modes in Selection of Major Theoretical Papers: Optical Modes Semiconductor Layered Systems*, Physical Review **B 45**(11), pp. 944–948, 1992.
- [46] F. COMAS, C. TRALLERO-GINER, M. CARDONA, *Continuum Treatment of Phonon Polaritons in Semiconductor Heterostructures*, Physical Review **B 56**, pp. 4115–4127, 1997.
- [47] J.J. LICARI, R. EVRARD, *Electron-Phonon Interaction in a Dielectric Slab: Effect of Electronic Polarizability*, Physical Review **B 15**, pp. 2254–2264, 1977.
- [48] L. WENDLER, *Electron-Phonon Interaction in Dielectric Bilayer System: Effects of Electronic Polarizability*, Physics Status Solidi **B 129**, pp. 513–530, 1985.
- [49] K.J. NASH, *Electron-Phonon Interactions and Lattice Dynamics of Optic Phonons in Semiconductor Heterostructures*, Physical Review **B 46**, pp. 7723–7744, 1992.

- [50] P.A. KNIPP, T.L. REINECKE, *Classical interface modes of quantum dots*, Phys. Rev. B **46**, pp. 10310, 1992.
- [51] E. ROCA, C. TRALLERO-GINER, M. CARDONA, *Polar optical vibrational modes in quantum dots*, Phys. Rev. B **49**, pp. 13704, 1994.
- [52] T.C. PRESTON, R. SIGNORELL, *Vibron and phonon hybridization in dielectric nanostructures*, PNAS **108**, pp. 5532–5536, 2011.
- [53] J.D. CALDWELL, L. LINDSAY, V. GIANNINI, I. VURGAFTMAN, T.L. REINECKE, S.A. MAIER, O.J. GLEMBOCKI, *Low-loss, infrared and terahertz nanophotonics using surface phonon polaritons*, Nanophotonics **4**, pp. 44–68, 2015.
- [54] C. KITTEL, *Introduction to Solid State Physics*, 7th ed., John Wiley & Sons, Inc., New York, 1996.
- [55] I.D. MAYERGOYZ, D.R. FREDKIN, Z. ZHANG, *Electrostatic (plasmon) resonances in nanoparticles*, Phys. Rev. B **72**, pp. 155412, 2005.
- [56] F.J. GARCIA D.E. ABAJO, *Nonlocal Effects in the Plasmons of Strongly Interacting Nanoparticles, Dimers, and Waveguides*, J. Phys. Chem. **112**, pp. 17983–17987, 2008.
- [57] N.A. MORTENSEN, S. RAZA, M. WUBS, T. SONDERGAARD, S.I. BOZHEVOLNYI, *A generalized non-local optical response theory for plasmonic nanostructures*, Nature Communications **5**, pp. 3809, 2014.
- [58] J. ZULOAGA, E. PRODAN, P. NORDLANDER, *Quantum Description of Plasmon Resonances of a Nanoparticle Dimer*, Nano Lett. **9**, pp. 887–891, 2009.
- [59] R. ESTEBAN, A.G. BORISOV, P. NORDLANDER, J. AIZPURUA, *Bridging quantum and classical plasmonics with a quantum-corrected model*, Nature Communications **3**, pp. 825, 2012.

# Numerical Study of Metallic Nanoparticles Handling in Electric Field With Application in Cell Electroporation

Oana Tatiana NEDELUCU<sup>1</sup>, George BOLDEIU<sup>1</sup>, Ramona CORMAN<sup>1</sup>,  
Otilia Ludmila CINTEZA<sup>2</sup>, Dana STAN<sup>3</sup>

<sup>1</sup>Institutul National de Cercetare-Dezvoltare pentru Microtehnologie IMT Bucuresti  
E-mail: oana.nedelcu@imt.ro; george.boldeiu@imt.ro;  
ramona.corman@imt.ro

<sup>2</sup>Facultatea de Chimie, Universitatea Bucuresti  
E-mail: ocinteza@yahoo.com

<sup>3</sup>SC DDS Diagnostic SRL  
E-mail: dana\_stan2005@yahoo.com

**Abstract.** This paper presents results on metallic nanoparticles behaviour in a micro-electro-fluidic system for cell separation and electroporation. The microsystem has a fluidic layer with channel, reservoirs and electrodes in contact to liquid media in the channel. The functionalities of the microsystems include cell separation by dielectrophoresis and cell electroporation by membrane permeabilization. Metallic nanoparticles are used to be attached to specific cells for detection and also contribute to increasing the field local intensity inside the channel. Simulation results were obtained for electric field distribution and nanoparticles migration by electrophoresis and dielectrophoresis.

**Keywords:** metallic nanoparticles, microfluidics, cell electroporation.

## 1. Introduction

Nanotechnology remains today the research area with the broadest field of applications, from material chemistry to electronics, optics and medicine. Magnetic nanoparticles are one of the most studied nanomaterial, due to its very interesting properties, especially SPIONs (superparamagnetic iron oxide nanoparticles). Magnetic nanoparticles, with various size and compositions are an attractive research material in a variety of topics, including biomedicine [1-3].

Cell labelling using magnetic nanoparticles is an increasingly used approach for various applications, from cell recognition in diagnosis devices to tracking therapeutic cells following infusion or transplantation in vivo, due to their



outstanding biocompatibility and superparamagnetic properties. Magnetic forces are used to separate cells in vitro [4], but also to attract cells by an external stimulus with applicability for tissue engineering [5] or for cell therapy [6].

Magnetic labelling of living cells creates opportunities for numerous biomedical applications, from individual cell manipulation to MRI tracking of subsequence differentiation of these therapeutic cells, T-cell or stem cells, allowing a better understanding of cancer development and intervention mechanisms [7, 8]. In this type of applications the main requirement is to make sure that cells possess sufficient magnetization to allow a suitable reaction to the external magnetic field, without major changes in cell viability and functionalities.

The control of the size and monodispersity is very important because the properties of the magnetic nanoparticles strongly depend upon the dimension. For the biomedical application, size, size distribution, and chemical and physical properties of magnetic nanoparticles are essential to be known and quantified.

Since the MNPs are intensively studied for the last four decades, there are many methods developed to prepare iron oxide nanoparticles, usually magnetite  $\text{Fe}_3\text{O}_4$  or maghemite  $\text{Fe}_2\text{O}_3$  nanoparticles, such as co-precipitation from the solution of ferrous/ferric-salt mixture in alkaline medium [9], oxidation of  $\text{Fe}(\text{OH})_2$  by  $\text{H}_2\text{O}_2$  [10], chemical vapour deposition [11], the sol-gel method [12], thermal decomposition [13] etc.

The surface functionalization and encapsulation in various carriers allow the interaction of magnetic nanoparticles with cells. Superparamagnetic iron oxide (SPIO) nanoparticles could be directly attached onto cell surfaces [14]. They can be also internalized via a receptor-mediation (they induce specific recognition with receptors at the surface of targeted cell) or transfection agent-mediated endocytosis pathway, with a non-specific mechanism of interaction with plasma membrane [15].

There are various types of labelled cells, aside from common cells, using the functionalization of magnetic nanoparticles with biological ligands that ensure specific recognition from the receptors on the cell membrane. The size, zeta potential, stability in culture medium of the formed complexes and interactions with cells are finely tuned by the nature of the ligand and the functionalization procedure. [16,17]. Recent studies pointed out that ligand- SPIO nanoparticles complexes may precipitate and be absorbed on the plasma membrane of cells rather than internalization [18], leading to a control of their properties hardly achievable.

Up to now, a series of potential markers were adopted as imaging targets for pancreatic islets, but none of these targets or tracer probes has allowed for islet imaging successfully in humans as yet, mainly due to the unfavorable signal-to-background ratio. Superparamagnetic iron oxide nanoparticle (SPIO) has made important contributions for developing negative contrast agent for in vivo imaging of transplanted pancreatic islets, and possibly for future beta cell imaging [19]. Much endeavor has been aimed at developing suitable procedures for efficient intracellular labeling, given the fact that precise localization of stem cells after

transplantation is critical for understanding cell-fate and therapeutic efficacy [20].

One of the most important applications of SPIONs in medicine is as superior contrast agent in MRI [21]. Magnetic nanoparticles with polymeric coating for increased biocompatibility are used, but still have not reached their full potential in terms of internalizing efficiency, MRI sensitivity, and especially lack of toxicity. Numerous studies already demonstrated the *in vivo* tracking of SPION-labeled MSC by MRI in various tissues, such as brain, liver, kidney, spinal cord, myocardial heart and traumatic muscle tissue [22-24].

Several studies describe the use of complexes made up of transfection agents and SPIO nanoparticles which were used to enhance the labelling efficiency of the magnetic nanoparticles. Also in this case the surface functionalization of the magnetic nanoparticles play an important role in the interaction with the cells [25]. The anionic surface charges are reported to be unfavorable for internalization due to the electrostatic repulsion between the anionic charged particles and the anionic charged cell membrane [26]. Moreover, it is clear that cationically charged nanoparticles could internalize into the cells more easily [27]. The transfection agents, cationic compounds, are helpful in transporting SPIO nanoparticles to the target cells, some of them allowing adhesion to the culture dish surface via *in vitro* cell cultivation [28, 29]. Transfection agents (TAs) include cationic peptides, lipids, polyamines, and dendrimers. Cationic thiolated surface stabilized superparamagnetic iron oxide nanoparticles (TSS-SPIONs) were established by chelation between thiolated chitosan–thioglycolic acid (chitosan–TGA) hydrogel and iron ions ( $\text{Fe}_2^+/\text{Fe}_3^+$ ) [20].

Another simpler magnetic nanoparticles were also used for cell tracking, nonpolymer-coated SPIONs stabilized with monomers or chelating agents with anionic charges, such as citrate or dimercaptosuccinic acid [30]. There were performed type- and dose-dependent cell labeling studies evaluating the intracellular iron uptake and the MRI signal loss, including determination of the impact of magnetic labeling on mesenchymal stem cell function.

However, for the biomedical applications such as to track the transplanted cells *in vivo*, to monitor cellular biodistribution, or assessing the efficiency and safety of cell-based therapies the issues related to the increased biocompatibility, stability and size control of the MNPs are still needed. Therefore, many researches are devoted to formulate new surface modified SPIONs with improved biocompatibility, appropriate MRI sensitivity and efficient internalization into therapeutic cells.

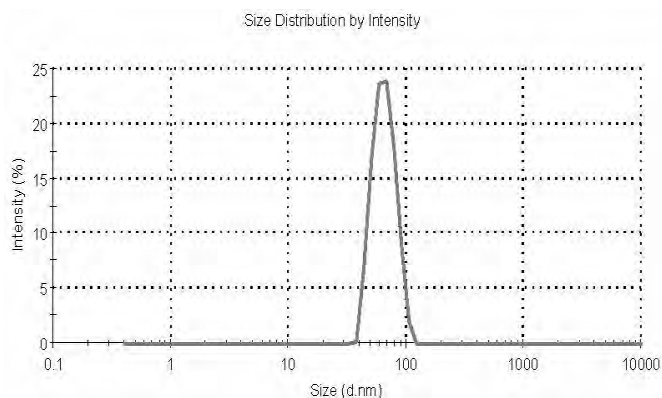
The purpose of this study is to investigate the movement of MNPs under effect of electric field in a microsystem dedicated to cell separation by dielectrophoresis and cell irreversible electroporation to release intracellular content for further biomedical analysis. The ferromagnetic particles are functionalized with specific cellular antibodies to form bioconjugates and they are used for cells capture and detection.

## 2. Synthesis and Characterization of Magnetic Nanoparticles (MNPs)

Reactants  $\text{FeCl}_2 \cdot 4\text{H}_2\text{O}$ ,  $\text{FeCl}_3 \cdot 6\text{H}_2\text{O}$ , ammonia (25% solution) were Aldrich reagents. Citric acid and hydrochloric acid were Fluka reagents. All chemicals were of analytical grade and were used without any further purification. For the synthesis and washing distilled water was used.

The nanoparticles used in this study were prepared in aqueous media, since the post-synthesis modification to obtain water dispersible MNPs is quite difficult procedure and the persistance of the organic reactants is very common. The  $\text{Fe}_3\text{O}_4$  magnetic nanoparticles were prepared according the Massart co-precipitation method with minor changes [31]. Briefly, an aqueous mixture containing 9.36 g  $\text{FeCl}_3$  and 3.44 g  $\text{FeCl}_2$  dissolved in 100 ml of bidistilled water was slowly dropped into an alkaline solution obtained from 50 ml of ammonia (25%) diluted in 50 ml of water, under moderate stirring, at  $75^\circ\text{C}$ . The resulting mixture was left to react for 60 minutes under  $\text{N}_2$  atmosphere. The obtained black precipitate was magnetically separated, washed with bidistilled water and stabilized by adding hydrochloric acid. To obtain  $-\text{COOH}$  functionalized magnetic nanoparticles, a further complexation was performed by adding citric acid under constant stirring at  $50^\circ\text{C}$  for 2 hours. Finally, MNPs were magnetically separated, washed three times with distilled water. The hydrodynamic particle diameter of the MNPs was measured by dynamic light scattering and the zeta potential was determined by laser Doppler velocimetry module, using a ZetaSizer Nano ZS instrument. The particle size measurements were performed in distilled water, and zeta potential was measured in 1 mM NaCl.

The preparation of  $\text{Fe}_3\text{O}_4$  nanoparticles using co-precipitation method leads to the formation of rather monodisperse samples, with nanoparticle size around 72 nm, as it is shown in figure 1. The zeta potential is - 25.7 mV, a value that suggests a stable dispersion of magnetic nanoparticles.



**Fig.1.** Hidrodynamic radius of the MNPs.

### 3. Electrokinetic Theory for Metallic Nanoparticles

The electrokinetic motion of the particles occurs when suspensions in a liquid solution migrates under effect of an electric field [32]. Electrokinetic phenomena include electrophoresis, electroosmosis and dielectrophoresis. Electrophoresis refers to the migration of electrically charged particles in the presence of an applied electric field. The electrophoretic velocity of the particle related to suspending medium is proportional to the applied electric field strength:

$$\vec{v}_{ep} = \mu_{ep} \vec{E} \quad (1)$$

where  $\mu_{ep}$  is the electrophoretic mobility given by [33]:

$$\mu_{ep} = \frac{2\zeta\epsilon_p}{3\eta} \quad (2)$$

Here,  $\zeta$  denotes the zeta potential of electrical double layer at solid/liquid interface,  $\epsilon_p$  is dielectric constant of particle and  $\eta$  is the liquid medium viscosity. The electrical double layer (EDL) is a thin layer around particles that contains ions of opposite charge to the nanoparticles surface charge. Zeta potential is the electric potential at the interface of EDL. For nanoparticles as ferromagnetic, gold or covered with gold, zeta potential is in range of [-45..-30] mV [33, 34].

Another electrokinetic phenomena is dielectrophoresis (DEP) that represents the movement of polarisable particles in non-uniform electric field. When placed in a non-uniform electrical field, the particles are electrical polarized and experience a translational force. This force depends on electrical properties of the particles and fluid, as well on the intensity and frequency of the applied electrical field [35]. The DEP force is given by relation:

$$\vec{F}_{DEP} = \frac{1}{2} V_p \text{Re}(\alpha^*) \nabla |\vec{E}|^2 \quad (3)$$

where  $V_p$  is particle volume and  $\alpha^*$  is the particle polarizability, which depends on complex permittivity of medium ( $\epsilon_m^*$ ) and particles ( $\epsilon_p^*$ ), and angular frequency of electric field  $\omega$ :

$$\alpha^* = 3\epsilon_m \left( \frac{\epsilon_p^* - \epsilon_m^*}{\epsilon_p^* + 2\epsilon_m^*} \right) = 3\epsilon_m K \quad (4)$$

The term  $K$  is called Clausius–Mossotti factor. DEP velocity and mobility can be further written:

$$\vec{v}_{DEP} = \mu_{DEP} \nabla |\vec{E}|^2 \quad (5)$$

$$\mu_{\text{DEP}} = \frac{V_p \alpha}{2f} \quad (6)$$

where  $\alpha = \text{Re}(\alpha^*)$ ,  $R$  is the radius of particle and  $f = 6\pi\eta R$  is the Stokes factor. For spherical metallic particles it is assumed that resistivity  $\rho \rightarrow 0$ , and  $\epsilon_p \rightarrow \infty$  [36] and the force and mobility become:

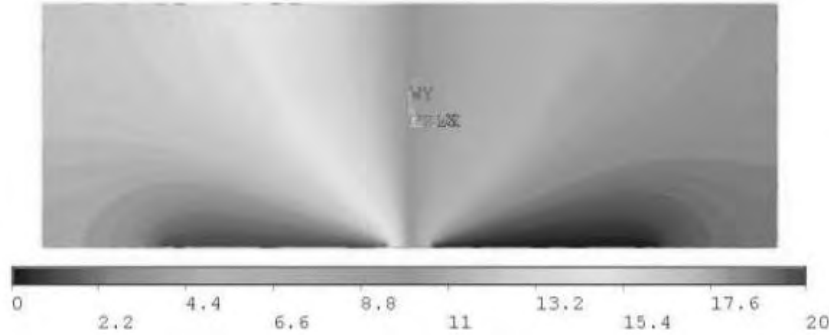
$$\vec{F} = 2\pi r_p^3 \epsilon_m \nabla \left( |\vec{E}|^2 \right); \quad \mu_{\text{DEP}} = \frac{2\pi r_p^3 \epsilon_m}{f} \quad (7)$$

DEP force on metallic particles is therefore in direction of largest field.

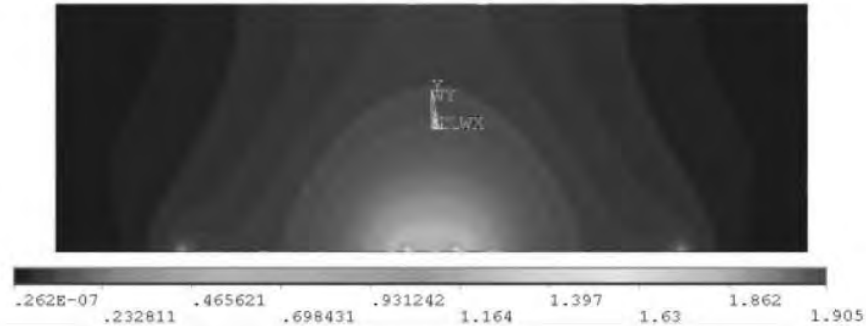
## 4. Simulation Results

### *Electrostatic*

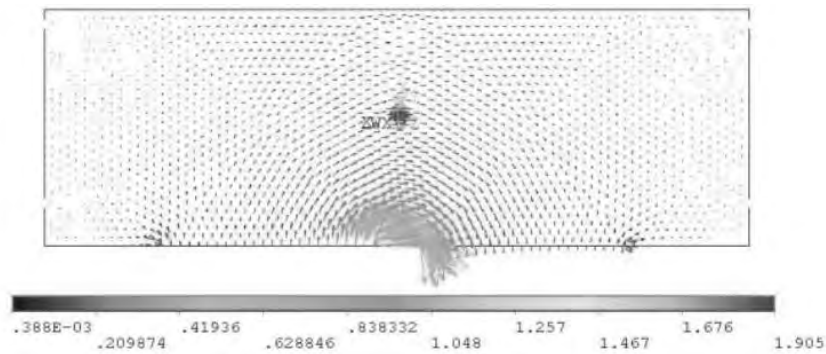
For numerical study of metallic nanoparticles behaviour under electric field, a microchannel of 1 mm length, 300  $\mu\text{m}$  width and 100  $\mu\text{m}$  was designed. On the top surface the electrodes area were defined for boundary condition in applied voltage. A first study was performed using ANSYS Multiphysics. A cross section was considered for 2D simulation. The fluid media was deionized water (relative permittivity 80 and conductivity  $6.6 \times 10^{-5}$  S/m at 20°C).  $\text{Fe}_3\text{O}_4$  nanoparticles (14.2 relative permittivity) of 100 nm diameter were considered in volume. Figure 2 illustrate the distribution of voltage for 20 V applied between electrodes and for 30  $\mu\text{m}$  interelectrode gap. Electrodes are placed on the bottom side. In absence of particles, the electric field reach a maximum value of 1.9 V/ $\mu\text{m}$  (fig. 3). When nanoparticles are taken into account, the local field around it are increasing (fig 4).



**Fig. 2.** Voltage distribution (V).

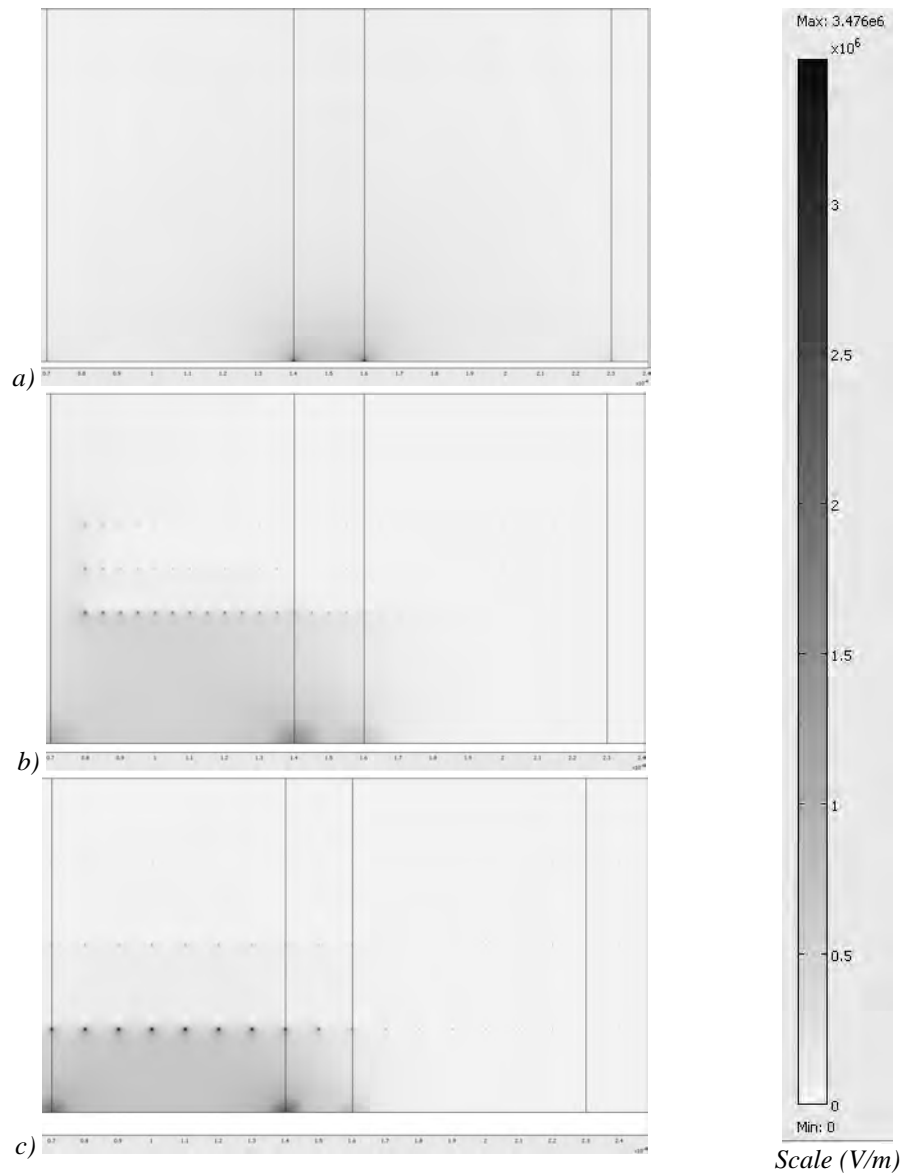


**Fig. 3.** Electric field distribution ( $V/\mu m$ ) in absence of particles.



**Fig. 4.** Electric field distribution: vector orientation in the presence of particles.

Another set of simulations were performed in Comsol Multiphysics by considering nanoparticles of 100 nm and 50 nm diameter distributed as 90 spheres in a matrix of 10 lines and 30 columns. Their positions are symmetric related to channel centre. The distance between two adjacent spheres is  $5\ \mu m$  on X axis and  $12.5\ \mu m$  on Y axis. The analysis were done for  $20\ \mu m$  interelectrode gap and 20 V applied. In figure 5 electric field distribution is represented three versions: in absence of nanoparticles, with particles of 100 nm diameter and with particles of 50 nm diameter. For comparison, the value of  $3.476\ V/\mu m$  (or  $3.476 \times 10^6\ V/m$ ), which is the maximum field value in absence of particles, was kept as reference on the scale for comparison, while the area marked by dark colour show the region where field is higher than this value. The local field in the vicinity of nanoparticles become higher and the increase is greater for smaller particles. The increase of electric field for a given voltage in the presence of nanoparticles show that phenomena as dielectrophoresis and cell membrane permeabilization can be obtained with lower voltage and the Joule effect is minimized.



**Fig. 5.** Electric field distribution (V/m): a) in absence of particles; b) with 100 nm diameter particles; c) with 50 nm diameter particles.

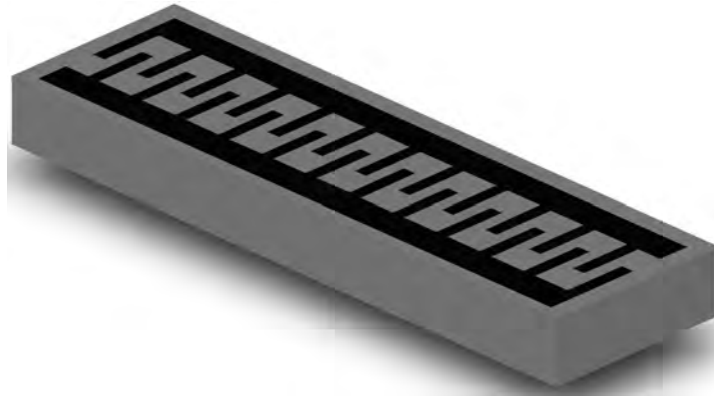
### ***Electrophoresis***

Electrokinetic simulation were performed using Coventorware 2012 software package for evaluation of metallic nanoparticle migration under effect of electric field. The particles moves by electrophoresis and dielectrophoresis. The 3D

geometry is illustrated in figure 6; the area corresponding to electrodes in contact with liquid are placed on top surface. The finger of the electrodes have 100  $\mu\text{m}$  length and 20  $\mu\text{m}$  width and they are partially interdigitated along 50  $\mu\text{m}$ . The interelectrode gap is 20  $\mu\text{m}$ . The mobilities and diffusion coefficients are listed in table 1. Due to size variation, DEP velocity, that depends on particle volume, is lower for smaller particles while diffusion coefficient is higher.

**Table 1.** Nanoparticles properties used in simulations

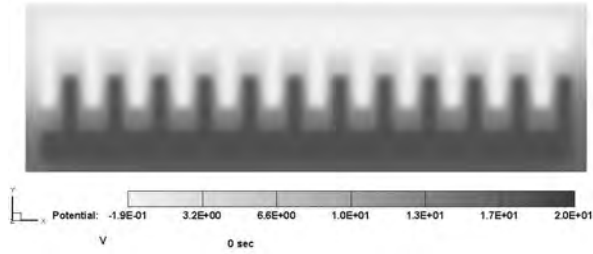
Nanoparticles	100 nm diameter	50 nm diameter
Concentration	1 $\mu\text{Moles/liter}$	1 $\mu\text{Moles/liter}$
Electrophoretic mobility	$2.328324 \times 10^3 \mu\text{m}^2/(\text{V s})$	$-2.328324 \times 10^3 \mu\text{m}^2/(\text{V s})$
Dielectrophoretic mobility at 100 Hz	$5.479212 \times 10^2 \mu\text{m}^4/(\text{V}^2 \text{ s})$	$1.369803 \times 10^2 \mu\text{m}^4/(\text{V}^2 \text{ s})$
Diffusion coefficient	$3.974261 \mu\text{m}^2/\text{s}$	$7.948523 \mu\text{m}^2/\text{s}$



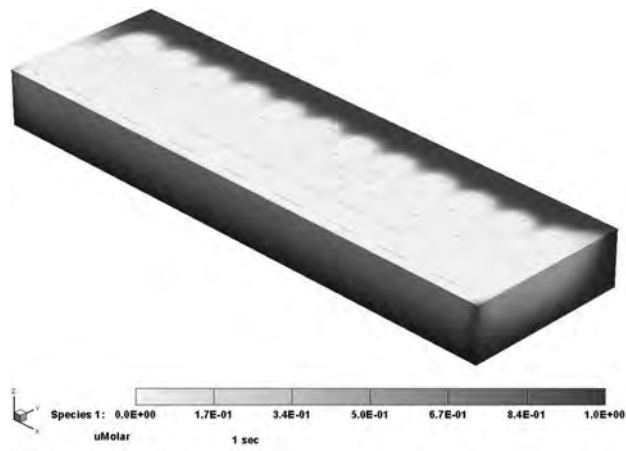
**Fig. 6.** Channel geometry with electrodes on top surface.

Electrophoretic analysis were made for various time interval considering that at  $t=0$  s, the voltage is applied (fig.7). The simulation results show that particles migrate to electrode of negative charge (top surface, right side). For 20 V applied, nanoparticles with 50 nm diameter require 10 s to be extracted from volume. The volume and surface particle concentration at  $t=1$ s are shown in figure 8 in 3D representation. Species 1 denotes particles in volume and Species 2 refers to particles on surface. Variation of concentration in time is represented in figures 9-10 in longitudinal sections - (X-Z) plane and (X-Y) plane. The volume concentration decreases while the surface concentration is increasing. The concentration in volume decreases first in the opposite channel region related to electrode where particles migrate.

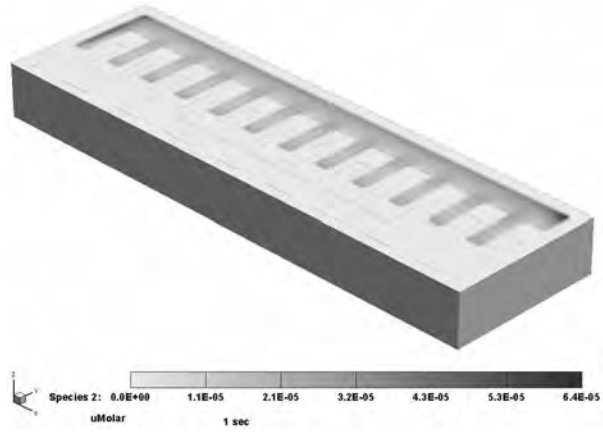




**Fig. 7.** Voltage distribution (V) for 20 V applied between electrodes, top view.

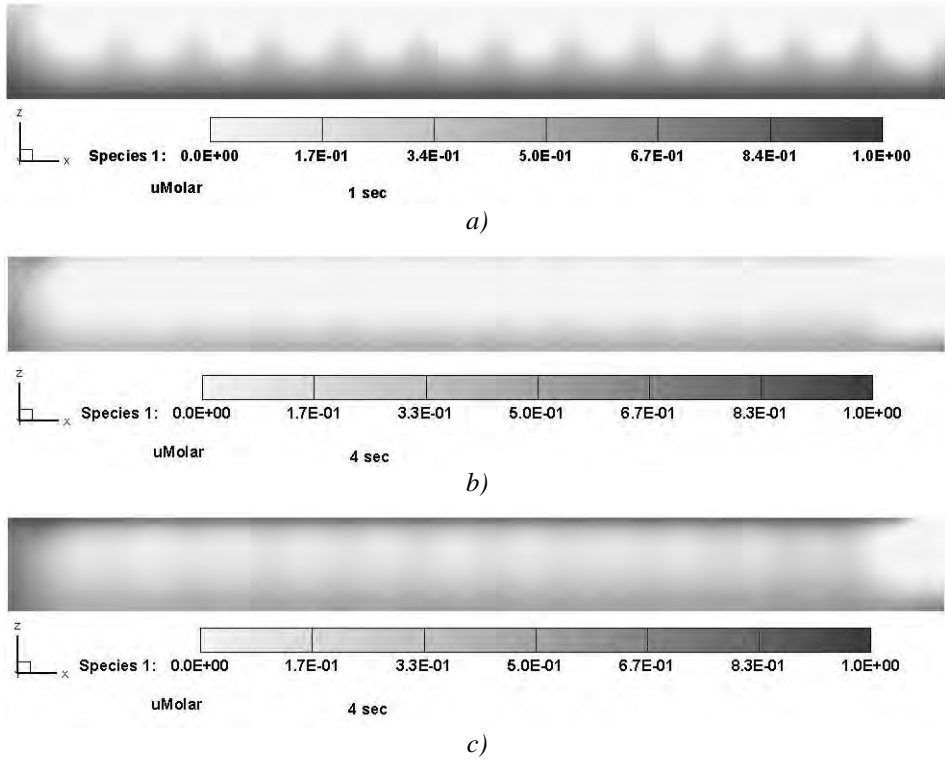


a)

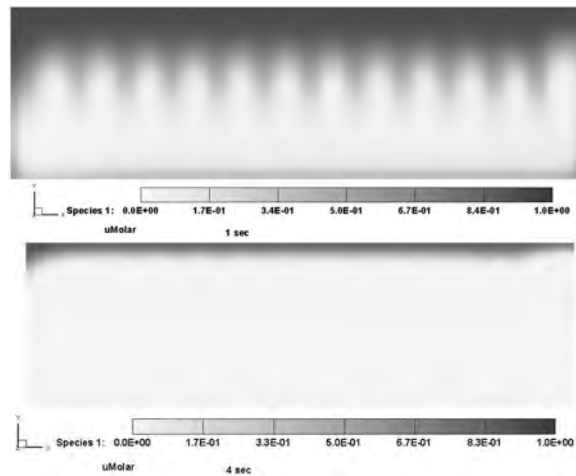


b)

**Fig. 8.** Concentration distribution in channel volume: a) Volume concentration ( $\mu\text{Moles/liter}$ );  
b) Surface concentration ( $\mu\text{Moles/cm}^2$ ).

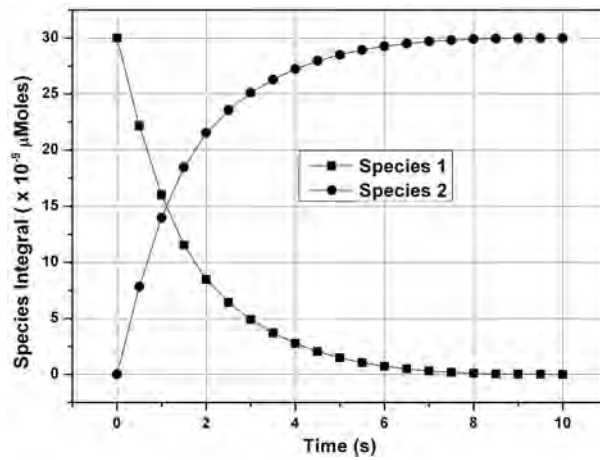


**Fig. 9.** Distribution of volume concentration ( $\mu\text{Moles/liter}$ ) in (X-Z) plane;  
a) middle, t=1 s b) middle, t=4s; c) near edge, t=4 s.

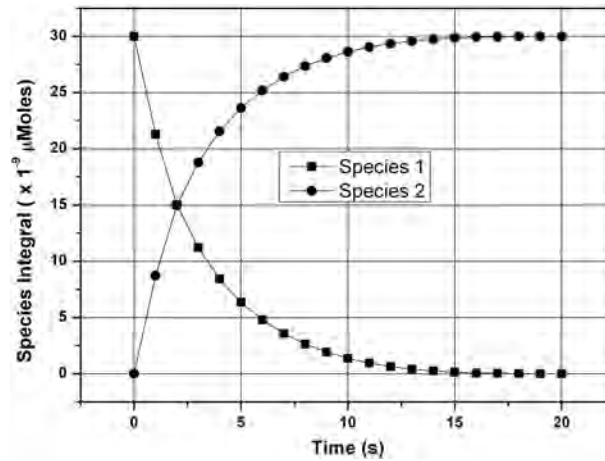


**Fig. 10.** Distribution of volume concentration ( $\mu\text{Moles/liter}$ )  
in (X-Y) plane at  $Z=50 \mu\text{m}$ ; a) t=1 s; b), t=4s.

In figure 11, the variation of total quantities of particles in volume and on surface are obtained. These values are obtained by volume and surface intergration respectively. Before applying voltage, the quantity of particles in volume is  $3 \times 10^{-8}$   $\mu\text{Moles}$  corresponding to initial concentration of 1  $\mu\text{Moles/liter}$ . After voltage is applied, the particles migrate to the electrode; the quantity in volume decreases. Since no flow is considered, there is no outlet flux; the sum of volume and surface quantities is constant over time. In case of 20 V applied medium velocity 33  $\mu\text{m/s}$ ), approximately 89% from all particles reach the electrode surface in 6 seconds. For 10 V the particles are separated on electrode in 20 s.



a)

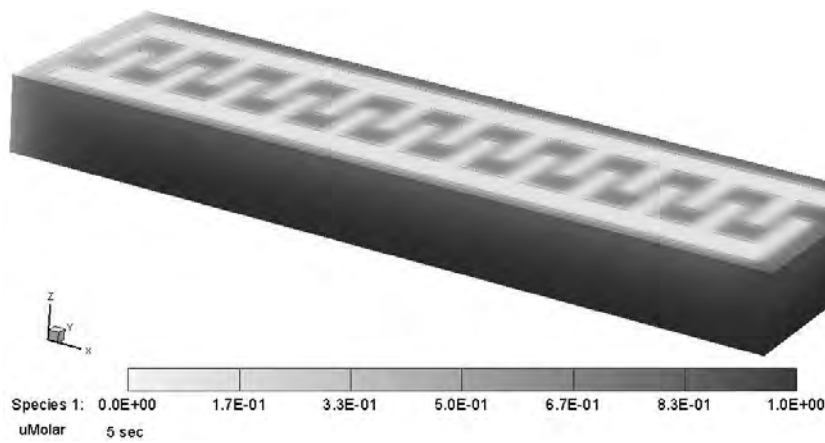


b)

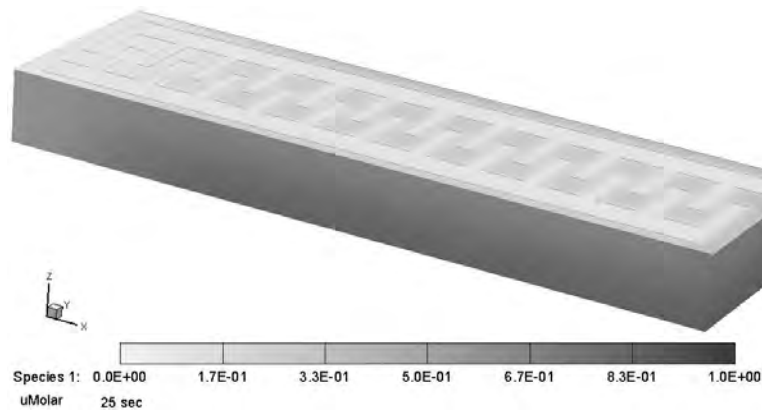
**Fig. 11.** Variation of particle quantities ( $\mu\text{Moles}$ ): a) 20 V; b) 10 V.

### *Dielectrophoresis*

In a first stage, dielectrophoretic analysis was performed for the same time interval as electrophoresis (10 s) without flow. The results showed that only particles in the vicinity of the electrodes (in a region up to 10  $\mu\text{m}$  in depth). For better results it is necessary to investigate the separation by DEP in a longer period of time. The necessary time for particles to migrate in region of high electric field is 120 s. In figures 12-13 the concentration in the channel in 3D and sections is represented at 5 s and 25 s to illustrate the variation in time. By DEP separation of nanoparticles in the region of highest field, the volume concentration decreases starting with region near electrodes. Figure 5 illustrates the concentration at 5 s and 25 s in case of flow.

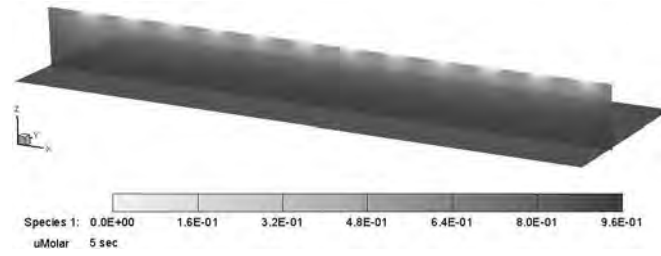


a)

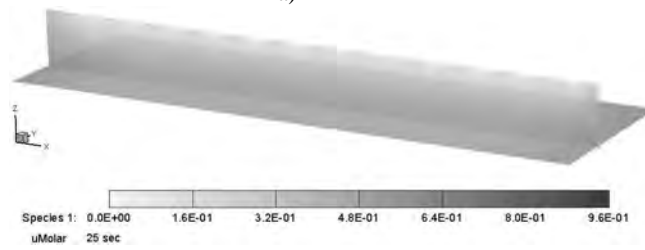


b)

**Fig. 12.** Distribution of concentration in channel volume: a) at 5 s; b) at 25 s

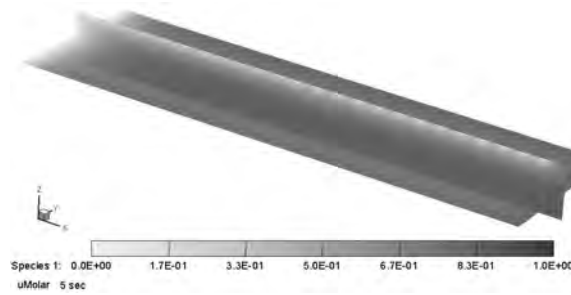


a)

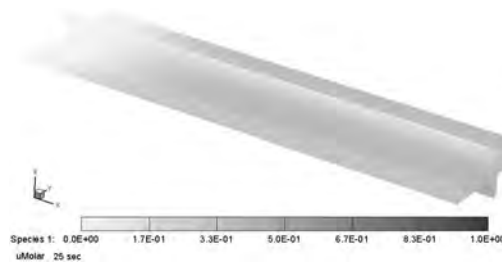


b)

**Fig. 13.** Distribution of concentration in longitudinal sections: a) at 5 s; b) at 25 s.



a)



b)

**Fig. 14.** Distribution of concentration in longitudinal sections in case of flow : a) at 5 s; b) at 25 s.

Figure 15 illustrate the quantity on nanoparticles that decrease to a value under  $5 \times 10^{-9}$   $\mu\text{Moles}$  (representing 0,16% of initial value) in 100 seconds. The DEP velocity depends on particle volume and it is higher for particles of 100 nm diameter; as consequence, these particles will be extracted from volume faster than in case of 50 nm diameter and, at a given time step, the remaining quantity in volume is lower.

In case of fluid flow, there is a convective flux of particles trough outlet even at low flow rates. In figure 16, a comparative variation of particles quantities are represented. For 0.01 Pa applied between inlet and outlet, the medium flow velocity (computed by flow rate divided by cross area) is  $19.6 \mu\text{m}$ , 15% of particles are carried trough outlet.

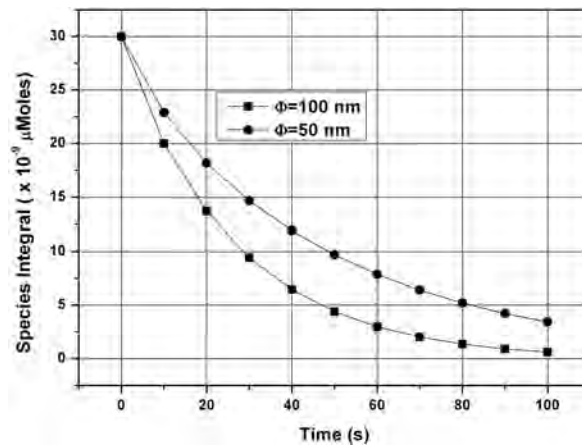


Fig. 15. Variation of particle quantities in case of no flow ( $\mu\text{Moles}$ ).

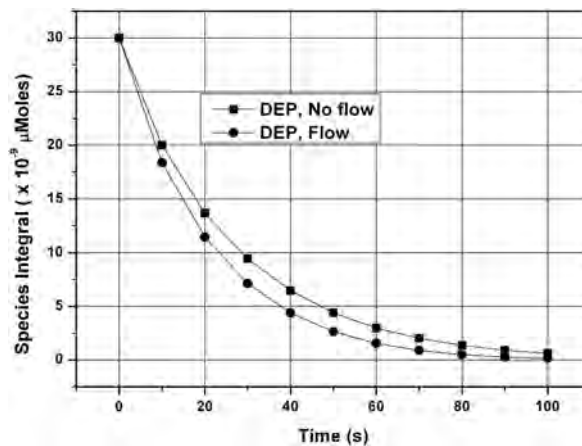


Fig. 16. Variation of particle quantities in case of flow ( $\mu\text{Moles}$ ).

## 5. Conclusions

A numerical study on metallic nanoparticles behaviour in the presence of electric field inside a microfluidic channel is reported. Fe<sub>3</sub>O<sub>4</sub> nanoparticles were obtained using co-precipitation method; the measured zeta potential is - 25.7 mV, that signifies a stable dispersion of nanoparticles. The presence on nanoparticles in carrier fluid lead to local increasing of electric field; this effect can be used to obtain required field for dielectrophoresis and electroporation with lower applied voltage. The particles migrate to electrode by electrophoresis and in region of high field by dielectrophoresis. The electrophoretic velocity is much higher than DEP velocity; the migration by electrophoresis dominates and the particles are separated on electrode area. If carrier fluid flow trough the channel, part of nanoparticles leave the channel trough outlet by convective flux and the quantity on the electrode is reduced. In order to avoid the particle loss, after initial pulse flow for filling the channel, the particles manipulation by electric field shall be performed in non flow regime.

**Acknowledgements.** This work was supported by PN-II-PT-PCCA National Programme, Contract no. 30/2014.

## References

- [1] W. PENG, X. HU, D. ZHANG, *Bioinspired fabrication of magneto-optic hierarchical architecture by hydrothermal process from butterfly wing*, J. Magn. Mater. **323**(15), pp. 2064–2069, Aug., 2011.
- [2] V.H.B. HO, M.J. SMITH, N.K.H. SLATER, *Effect of magnetite nanoparticle agglomerates on the destruction of tumor spheroids using high intensity focused ultrasound*, Ultrasound Med. Biol. **37**(1), pp. 169–175, Jan., 2011.
- [3] Y. ZHANG, J. ZHANG, *Surface modification of monodisperse magnetite nanoparticles for improved intracellular uptake to breast cancer cell*, J. Colloid Interface Sci. **283**(2), pp. 352–357, March 2005.
- [4] N. PAMME, C. WILHELM, *Continuous sorting of magnetic cells via on-chip free flow magnetophoresis*, Lab Chip **6**(8), pp. 974–80, Aug., 2006.
- [5] A. ITO, Y. TAKIZAWA, H. HONDA, K. HATA, H. KAGAMI, M. UEDA, *et al.*, *Tissue engineering using magnetite nanoparticles and magnetic force: heterotypic layers of co-cultured hepatocytes and endothelial cells*, Tissue Eng **10**(5–6), pp. 833–40, May-Jun., 2004.
- [6] A.S. ARBAB, E.K. JORDAN, L.B. WILSON, G.T. YOCUM, B.K. LEWIS, J.A. FRANK, *In vivo trafficking and targeted delivery of magnetically labeled stem cells*, Hum Gene Ther **15**(4), pp. 351–60, April, 2004.
- [7] S.V. PISLARU, A. HARBUZARIU, R. GULATI, T. WITT, N.P. SANDHU, R.D. SIMARI, *et al.*, *Magnetically targeted endothelial cell localization in stented vessels*, J Am Coll Cardiol **48**(9), pp. 1839e45, Nov., 2006.
- [8] F. SONVICO, S. MORNET, S. VASSEUR, C. DUBERNET, D. JAILLARD, J. DEGROUARD, *et al.*, *Folate-conjugated iron oxide nanoparticles for solid tumor targeting as potential specific magnetic hyperthermia mediators: synthesis, physicochemical characterization, and in vitro experiments*, Bioconjug Chem **16**(5), pp. 1181–8, Sept.-Oct., 2005.

- [9] M. DARROUDI, M. HAKIMI, E. GOODARZI, R.K. OSKUEE, *Superparamagnetic iron oxide nanoparticles (SPIONs): Green preparation, characterization and their cytotoxicity effects*, *Ceramics International* **40**(9), pp. 14641–14645, Nov., 2014.
- [10] H.Y. LUO, Z.X. YUE, J. ZHOU, *Synthesis and high-frequency magnetic properties of sol-gel derived Ni-Zn ferrite-for sterite composites*, *J. Magn. Magn. Mater.* **210**(1), pp. 104–108, Feb., 2000.
- [11] L.T. CHAO, M. WEI, J.L. MACMANUS-DRISCOLL, *Synthesis and characterization of nanocrystalline iron oxides via ultrasonic spray assisted chemical vapour deposition*, *J. Phys.* **26**, pp. 304–307, 2006.
- [12] M. TADIĆA, V. KUSIGERSKI, D. MARKOVIĆ, M. PANJAN, I. MILOŠEVIĆ, V. SPASOJEVIĆ, *Highly crystalline superparamagnetic iron oxide nanoparticles (SPION) in a silica matrix*, *J. Alloys Compd.* **525**, pp. 28–33, 2012.
- [13] Y. ZHU, F.Y. JIANG, K. CHENA, F. KANG, Z.K. TANG, *Size-controlled synthesis of monodisperse superparamagnetic iron oxide nanoparticles*, *J. Alloys Compd.* **509**(34), pp., 8549–8553, Aug., 2011.
- [14] T. Chou, M. Sano, M. Ogura, Y. Morishima, H. Itagaki, Y. Tokuda, *Isolation and transplantation of highly purified autologous peripheral CD34+ progenitor cells: purging efficacy, hematopoietic reconstitution following high dose chemotherapy in patients with breast cancer: results of a feasibility study in Japan*, *Breast Cancer* **12**(3), pp. 178-88, 2005.
- [15] Z.M. QIAN, H. LI, H. SUN, K. HO, *Targeted drug delivery via transferrin receptor mediated endocytosis pathway*, *Pharmacol Rev* **54**(4), pp. 561–87, Dec., 2002.
- [16] H. KALISH, A.S. ARBAB, B.R. MILLER, B.K. LEWIS, H.A. ZYWICKE, J.W. BULTE, *et al.*, *Combination of transfection agents and magnetic resonance contrast agents for cellular imaging: relationship between relaxivities, electrostatic forces, and chemical composition*, *Magn Reson Med* **50**(2), pp., 275–82, Aug., 2003.
- [17] K. MONTET-ABOU, X. MONTET, R. WEISSLEDER, L. JOSEPHSON, *Cell internalization of magnetic nanoparticles using transfection agents*, *Mol Imag* **6**(1), pp. 1–9, Jan.-Feb., 2007.
- [18] R. SCHAFFER, R. KEHLBACH, J. WISKIRCHEN, R. BANTLEON, J. PINTASKE, B.R. BREHM, *et al.*, *Transferrin receptor upregulation: in vitro labeling of rat mesenchymal stem cells with superparamagnetic iron oxide*, *Radiology* **244**(2), pp. 514–23, Aug., 2007.
- [19] B. ZHANG, B. YANG, C. ZHAI, B. JIANG, Y. WU, *The role of exendin-4-conjugated superparamagnetic iron oxide nanoparticles in beta-cell-targeted MRI*, *Biomaterials* **34**(23), pp. 5843-5852, Jul., 2013.
- [20] G. SHAHNAZ, C. KREMSER, A. REINISCH, A. VETTER, F. LAFFLEUR, D. RAHMAT, J. IQBAL, S. DÜNNHAUPT, W. SALVENMOSER, R.TESSADRI, U. GRIESSER, A. BERNKOP-SCHNÜRCH, *Efficient MRI labeling of endothelial progenitor cells: Design of thiolated surface stabilized superparamagnetic iron oxide nanoparticles*, *European Journal of Pharmaceutics and Biopharmaceutics* **85**(3 Pt A), pp. 346–355, Nov., 2013.
- [21] T. SHEN, R. WEISSLEDER, M. PAPISOV, A. BOGDANOV JR., T.J. BRADY, *Monocrystalline iron oxide nanocompounds (MION): physicochemical properties*, *Magn. Reson. Med.* **29**(5), pp. 599–604, May 1993.
- [22] C. BOS, Y. DELMAS, A. DESMOULIERE, A. SOLANILLA, O. HAUGER, C. GROSSET, *et al.*, *In vivo MR imaging of intravascularly injected magnetically labeled mesenchymal stem cells in rat kidney and liver*, *Radiology* **233**(3), pp. 781–9, Dec., 2004.
- [23] T. WINKLER, P. VON ROTH, M.R. SCHUMAN, K. SIELAND, G. STOLTENBURG-DIDINGER, M. TAUPITZ, *et al.*, *In vivo visualization of locally transplanted mesenchymal stem cells in the severely injured muscle in rats*, *Tissue Eng Part A* **14**(7), pp. 1149–60, Jul., 2008.
- [24] P. JENDELOVA, V. HERYNEK, L. URDZIKOVA, K. GLOGAROVA, J. KROUPOVA, B. ANDERSSON, *et al.*, *Magnetic resonance tracking of transplanted bone marrow and embryonic stem cells labeled by iron oxide nanoparticles in rat brain and spinal cord*, *J Neurosci Res* **76**(2), pp. 232–43, Apr., 2004.



- [25] C. WILHELM, F. GAZEAU, *Universal cell labeling with anionic magnetic nanoparticles*, *Biomaterials* **29**(22), pp. 3161–3174, Aug., 2008.
- [26] L. WANG, K.G. NEOHB, E.T. KANG, B. SHUTER, S.C. WANG, *Biodegradable magnetic fluorescent magnetite/poly(dl-lactic acid-co-a, b-malic acid) composite nanoparticles for stem cell labeling*, *Biomaterials* **31**(13), pp. 3502–3511, May, 2010.
- [27] L.M.A. JASMIN, H.M.P. TORRES, NUNES, J.A. PASSIPIERI, L.A. JELICKS, E.L. GASPARETTO, *et al.*, *Optimized labeling of bone marrow mesenchymal cells with superparamagnetic iron oxide nanoparticles and in vivo visualization by magnetic resonance imaging*, *J. Nanobiotechnol.* **9**(4), pp. 1–13, Feb., 2011.
- [28] J.A. FRANK, B.R. MILLER, A.S. ARBAB, H.A. ZYWICKE, E.K. JORDAN, B.K. LEWIS, *et al.*, *Clinically applicable labeling of mammalian and stem cells by combining superparamagnetic iron oxides and transfection agents*, *Radiology* **228**(2), pp. 480–7, Aug., 2003.
- [29] X. WANG, F. WEI, A. LIU, L. WANG, J. WANG, L. REN, W. LIU, Q. TU, L. LI, J. WANG, *Cancer stem cell labelling using poly(L-lysine)-modified iron oxide nanoparticles*, *Biomaterials* **33**(14), pp. 3719–3732, May, 2012.
- [30] K. ANDREAS, R. GEORGIEVA, M. LADWIG, S. MUELLER, M. NOTTER, M. SITTINGER, J. RINGE, *Highly efficient magnetic stem cell labeling with citrate-coated superparamagnetic iron oxide nanoparticles for MRI tracking*, *Biomaterials* **33**(18), pp. 4515–4525, June, 2012.
- [31] A. BEE, R. MASSART, S. NEVEU, *Synthesis of very fine maghemite particles*, *J. Magn. Magn. Mater.*, **149**(1-2), pp. 6–9, Aug., 1995.
- [32] Y. KANG, D. LI, *Electrokinetic motion of particles and cells in microchannels*, *Microfluid Nanofluid*, **6**(4), pp. 431–460, 2009.
- [33] R. TANTRA, P. SCHULZE, P. QUINCEY, *Effect of nanoparticle concentration on zeta-potential measurement results and reproducibility*, *Particuology* **8**(3), pp. 279–285, 2010.
- [34] N. GOLDSTEIN, L. F. GREENLEE, *Influence of synthesis parameters on iron nanoparticle size and zeta potential*, *J Nanopart Res* **14**(760), March, 2012.
- [35] D. Li, Editor, *Encyclopedia of microfluidics and nanofluidics*, Springer, New York, 2008.
- [36] K.K. SIRKAR, *Separation of Molecules, Macromolecules and Particles: Principles, Phenomena and Processes*, Cambridge University Press, 2014.

# Nanoelectronic Devices Based on Atomically Thin Materials

Mircea DRAGOMAN<sup>1</sup>, Adrian DINESCU<sup>1</sup>, Daniela DRAGOMAN<sup>2</sup>,  
Alina CISMARU<sup>1</sup>, Martino ALDRIGO<sup>1</sup>, Antonio RADOI<sup>1</sup>

<sup>1</sup>National Research and Development Institute in Microtechnology, Str. Erou Iancu Nicolae  
126A, 077190 Bucharest, Romania

<sup>2</sup>Univ. Bucharest, Physics Faculty, P.O. Box MG-11, 077125 Bucharest, Romania

## 1. Introduction

The first atomically thin material was a single atom-sheet matter consisting of carbon atoms known as graphene. After ten years from its discovery now graphene is a hot topic in research [1] and is produced by many companies [2] due to its many applications in various branches of industry. Meanwhile starting four years ago hundreds of new atomically thin materials were discovered and researched [3]. Graphene is now a main topic in nanoelectronics [4] and photonics [5]. The THz devices or graphene are at the border between electronics and photonics [6]. Graphene was first obtained by using a scotch tape and was detached as flakes from graphite with a subsequent transfer it on a doped Si/ SiO<sub>2</sub> substrate [7]. The method is still applied today for graphene other 2D materials originating from bulk layered materials. Nowadays, the graphene grown by CVD methods is the key technology for batch production of graphene monolayer at 4 -inch and 6-inch wafer scale and even 12 -inch and followed by the transfer method on various substrate either solid or flexible[8]. The physical properties of these atomically thin materials are have new physical new properties with many applications in electronics, harvesting, biosensing and photonics [9], [10].

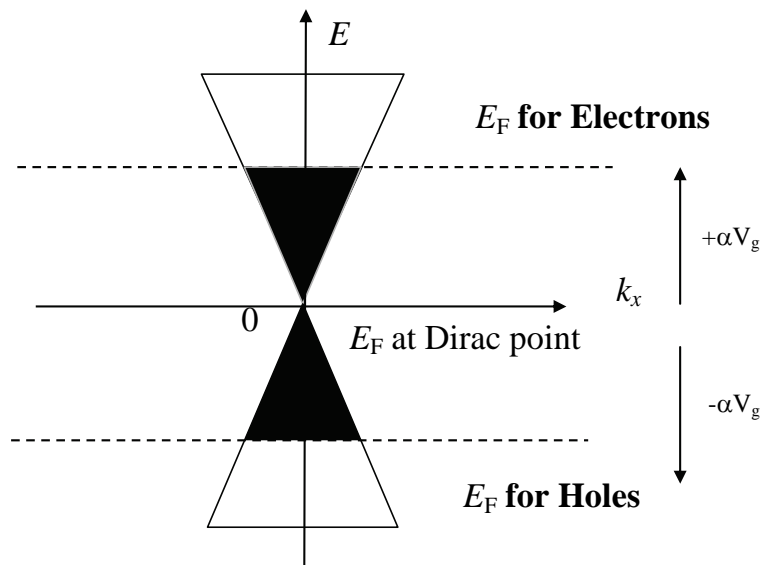
The main physical properties of graphene are summarized in Table 1.

The mean-free path and the ballistic transport in graphene monolayers are probably the main advantage of graphene over any other materials, which could eventually achieve comparable mean-free path values only at very low temperatures. The room-temperature ballistic transport regime in high-quality graphene monolayers is preserved for mean-free paths of up to 400 nm if graphene is deposited on SiO<sub>2</sub>, or up to 1  $\mu$ m in graphene deposited over boron nitride [11].

Very recently, it was demonstrated that these already impressive mean-free paths at room temperatures could attain even larger values, of more than 10  $\mu\text{m}$  [12], for 20-100 nm wide graphene nanoribbons epitaxially grown on SiC. The remarkable ballistic transport in graphene is the result of the dispersion relation which is unique compared to any other known material displayed in Fig. 1. What is graphene? According to the dispersion relation is a semiconductor with no energy gap- a gapless semiconductor or a semimetal, because the valence and conduction bands are overlapping only at one single point – the Dirac point where  $E_F$  is zero.

**Table 1.** Graphene physical properties.

<b>Parameter</b>	<b>At room temperature</b>
<b>Mean-free-path</b>	400 nm, even 1 $\mu\text{m}$ for graphene deposited on hexagonal BN
<b>Mobility</b>	40000 $\text{cm}^2/\text{Vs}$ (intrinsic), 100000 $\text{cm}^2/\text{Vs}$ in suspended graphene or in graphene deposited on hexagonal BN
<b>Effective mass of carriers</b>	0 near the Dirac point
<b>Thermal conductivity</b>	5000 W/mK, better than in many metals



**Fig. 1.** Graphene dispersion relation.

The unusual linearity of the dispersion relation of graphene around Dirac point, means simply that that the effective mass of charge carriers is zero,

indicating a ballistic transport *i.e.* the lack of collisions during the transport of carriers travelling the graphene device over distances smaller than the mean-free-path. However, the ballistic carriers are travelling with the Fermi velocity  $v_F \cong c/300$ , where  $c$  is the speed of light. Thus, the dispersion relation is:

$$E = \pm \hbar |\mathbf{k}| v_F \quad (1)$$

In striking contrast with a semiconductor, the holes and electrons have identical physical properties, and the same role in transport of carriers, their selection is done by a gate voltage shifting above and below the Fermi level from Dirac point. Moreover, via the gate voltage it is selected also the carrier density via the relation :

$$n = \varepsilon_0 \varepsilon_d V_g / t e \cong \alpha V_g \quad (2)$$

where  $\varepsilon_0$  and  $\varepsilon_d$  are the dielectric permittivities of air and SiO<sub>2</sub>, respectively and  $t$  is the isolation dielectric thickness. The above relation is the most important for graphene and tells us that we can have a doping in graphene only due to an applied DC voltage. This electrostatic doping is the ultimate doping mechanism having as precursor the chemical doping without which no progress in semiconductor science and technology was possible. The relation (2) is the physical reason for any tunable device working at any frequency based on graphene.

Since ballistic transport is very fast and allows very high frequency cutoff frequencies of graphene devices attaining tens of THz. Therefore, the electromagnetic properties of graphene will be subject of the next paragraph.

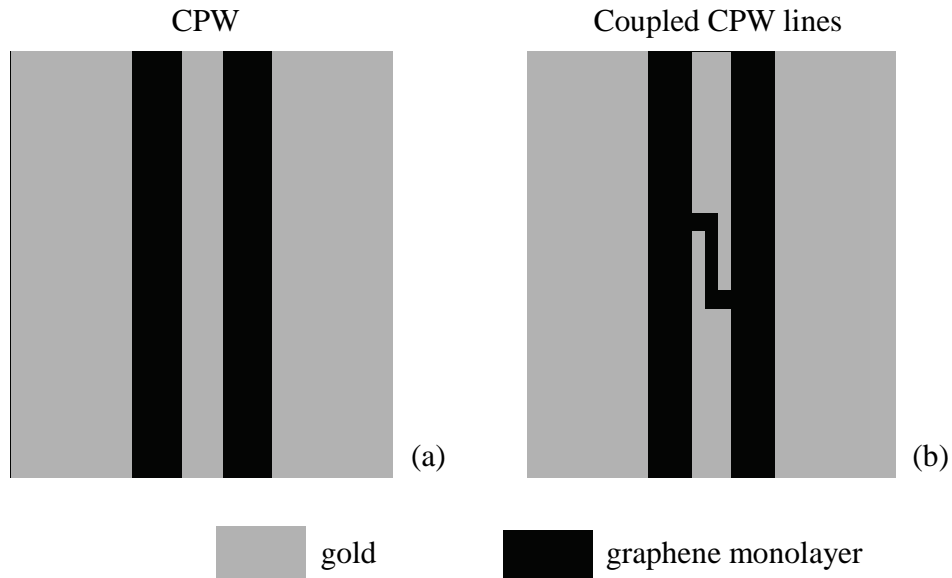
## 2. Electromagnetic Field Properties of Graphene

In the optical range graphene has an index of refraction of 2.6 in an ultrawide band of wavelengths ranging from UV up to NIR and a constant absorption of 2.3 % large for an atomically-thin material [13], but rather weak compared with other 2D materials, for example in MoS<sub>2</sub> monolayers the absorption is larger than 10 %. However, the index of refraction in graphene is tunable as it was recently demonstrated at 1550 nm where the index of refraction was varied between 0.1-3 for back-gate voltage ranging from -80 V up to +80V [14].

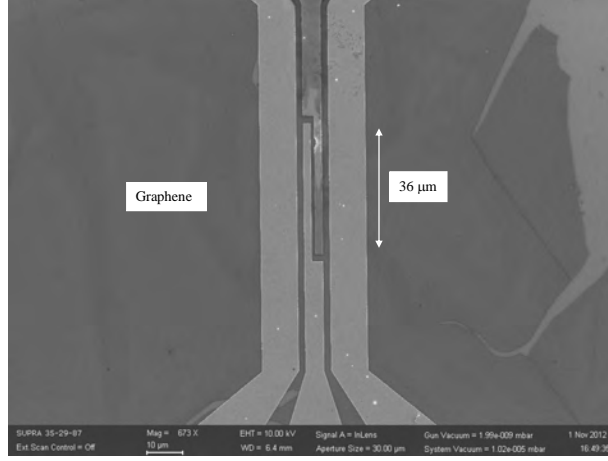
To study the microwave properties of graphene, we have fabricated first a metallic coupled coplanar line (CPW) placed over a graphene monolayer, as shown in Figs. 2a) and 2b). The CPW consists of three metallic electrodes, the central one being a signal electrode, while the outer electrodes are ground electrodes. The graphene monolayer is deposited on a high-resistivity Si substrate, having the resistivity of 8 kΩ, on top of which 300 nm of SiO<sub>2</sub> were thermally grown. The graphene was fabricated by Graphene Industries and its quality was tested by Raman spectroscopy. We have found that the graphene is of high quality (the

absence of D band), and that it is indeed a monolayer (the ratio of 2D and G peaks is greater than 2).

The coupling distance between the central lines is  $1\ \mu\text{m}$  in Fig. 2b), and the coupling length is  $36\ \mu\text{m}$ . It is known that the information needed to extract the electrical permittivity is the dependence on frequency  $f$ , of the phase difference  $\Delta\varphi(f)$  between the transmission of the CPW, denoted further  $S_{12}(f)$ , deposited over graphene and the transmission of an identical CPW in a reference structure, without graphene under the CPW electrodes. Therefore, we have fabricated first a graphene CPW and its corresponding reference structure and measured the phases of both structures with a VNA. Because we have observed that  $\Delta\varphi$  is very small, not exceeding  $2\text{-}3^\circ$ , and thus no significant phase difference is observed in such structures, we decided to choose the configuration in Fig. 2b). In this structure, the discontinuity of the central electrode exposes a region where the graphene is uncovered by metals and the electric field lines are coupling through it to get a larger phase difference between the coupled CPW reference structure (no graphene) and the coupled CPW with graphene. The SEM image of the device corresponding to that in Fig. 2b) is represented in Fig. 3 [15].



**Fig. 2.** (a) Standard CPW configuration and (b) coupled CPW lines.

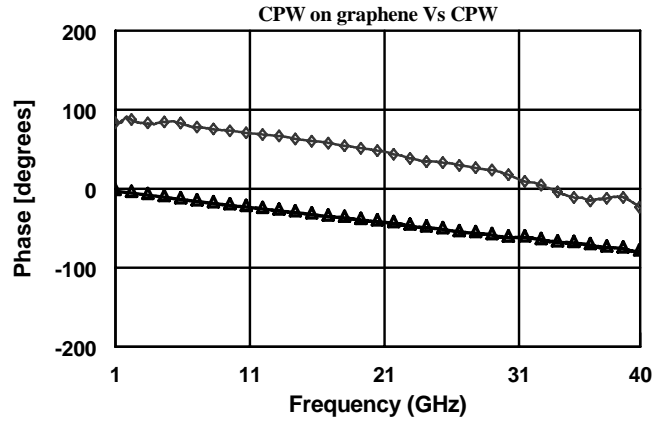


**Fig. 3.** The SEM image of the graphene device (from [15]).

The phase of the graphene coupled CPW and the reference coupled CPW structure is depicted in Fig. 4. Such relative large phases originate only from the coupled line region of the CPW, where the attenuation is very small: 0.018 dB/μm for 1 μm coupling distance. In these conditions, the effective permittivity formula as extracted from is :

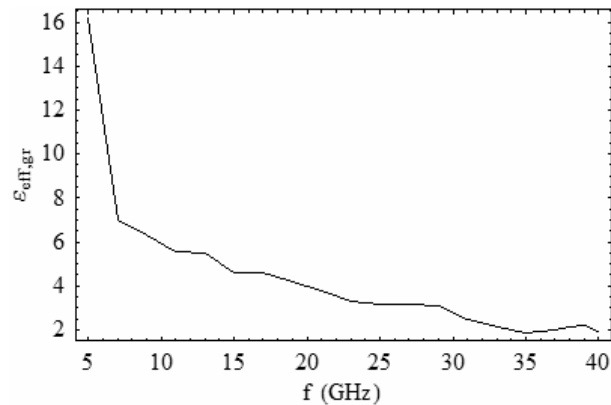
$$\varepsilon_{eff,gr} = (\varphi_{gr,CPW}^2 / \varphi_{CPW}^2) \varepsilon_{CPW} \quad (3)$$

where  $\varphi_{gr,CPW}$  is the phase shift of the coupled CPW on graphene,  $\varphi_{CPW}$  is the phase of the coupled reference structure, while  $\varepsilon_{CPW}$  is the electrical permittivity of the Si/SiO<sub>2</sub> substrate.



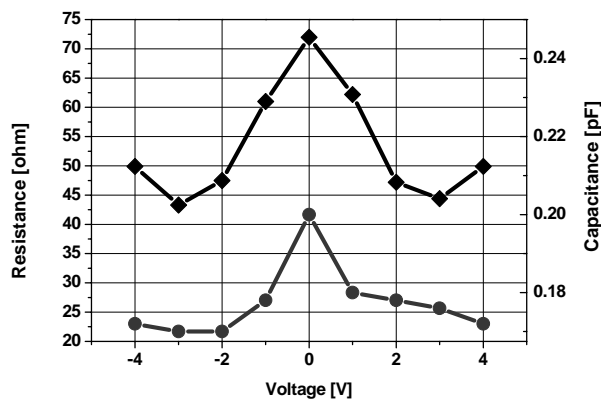
**Fig. 4.** The phase of coupled CPW on graphene (triangles) and of the coupled CPW reference structure (rhombs) (from [15]).

The electrical permittivity is displayed in Fig. 5. We can see that at the low frequency part of the spectrum we have a relative abrupt decrease of the effective permittivity, while between 10 and 40 GHz the effective permittivity has a slow decrease with frequency, with an average value of 3. Thus, the graphene monolayer behaves as a low-permittivity dielectric, almost constant over three decades of frequency within the microwave and millimeter spectrum.



**Fig. 5.** The dependence of effective electrical permittivity of graphene on frequency (from [15]).

On the other hand the S21 in amplitude is dependent on the applied voltage. In [16] it was shown that the graphene is behaving up to 110 GHz as a tunable resistor in parallel with capacitor (see Fig. 6). The resistance has a maximum near Dirac point and then decreases since the density of carriers are modulated by the applied voltages ranging from -2V up to +2V. The decrease of C with the bias originates in the screening effect, which becomes important as the carrier concentration increases.



**Fig. 6.** The voltage dependence of the parameters of the equivalent circuit of the CPW on graphene:  $R$  (full rhombs) and  $C$  (full circles) (from [16]).

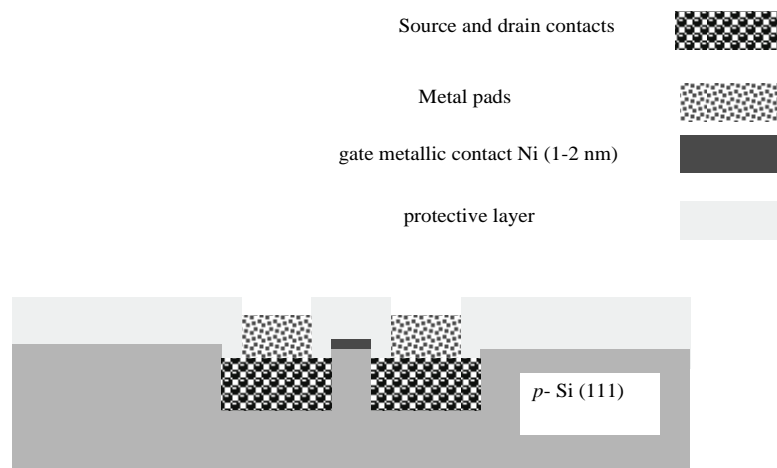
Although this results is origination from an equivalent circuit consisting from a variable resistance and capacitance in parallel in the range 0.04-110 GHz, the results are similar for the DC measurements in which the graphene has the same behavior *i.e.* the resistance has a maximum at 0V and decreases as soon as a voltage is applied on it.

### 3. Electronic Devices Based on Graphene

There are many devices based on graphene diodes, transistors, sensors and even integrated circuits, but by far the most studied is the graphene transistor [17], [18]. In fact, the discovery of the graphene was the result of searching a metallic transistor [7].

The electric-field-effect (EFE) in metals is not possible due the vary large number of carrier to be controlled by an electric field, so other experiments were performed with semimetals such as bismuth, antimony and graphite simple because the carrier density is much smaller compared to a metal [19]. However, the breakthrough is originating from graphite via graphene. An in-depth review of EFE in many materials is found in [20]. The quest for a metallic transistor was successful in 2012 [21] using a Ni ultrathin film having a thickness of 1-2 nm, the transistor having a graphene transistor -like behavior. Further, metallic switches and logic gates were developed based on thin films of 2H-TaS<sub>2</sub> which is semimetal without bandgap [22]. The EFE is now investigated in other 2D materials such as atomically thin MoS<sub>2</sub>, black phosphorus.

The first metallic transistor has a channel which is an induced two-dimensional electron gas located at the interface between an ultrathin metallic film of Ni and a *p*-type Si(111) substrate. The metallic transistor structure [21] is depicted in Fig. 7.



**Fig. 7.** The graphene-like metallic and dielectricless transistor (from [21]).



The transconductance of the graphene-like FET for a drain voltage of 3 V, 6 V and 9 V is 0.8 mS, 0.6 mS and respectively 0.2 mS at a gate voltage of 1V. The mobility of carriers is 12000 cm<sup>2</sup>/Vs.

The physics behind this metallic transistor is found in a recent experiment [23] which shows that very small carrier effective masses as in graphene are obtained at a metal/*n*-Si(111) interface, where the metal is one (or few) monolayer(s) thick. In such the ultrathin metal film/*n*-Si(111) nanostructures, the surface states induce a quantum well in the Si inversion layer and thus the effective mass of charge carriers in Si is dramatically decreasing due to repulsive forces. So, such nanostructures show an almost linear dispersion relation and a similar carrier effective mass as in graphene, of only  $m_{eff} = 0.0075 m_0$ , where  $m_0$  is the electron rest mass; this value is 20 times smaller than in bulk Si. The surface states located near the induced quantum well are localized states and are confining all the carriers at the surface so playing an analogous role to the gate dielectric in a normal FET. So, this is a metallic channel transistor without any isolation gate material. We note that the selection of Si(111) as a substrate is done because it displays a honeycomb lattice, similar to graphene, and calculations and the dispersion relation is linear close to the K point, with the (massless) Dirac fermions moving with a velocity of 10<sup>4</sup> m/s.

Despite, the ballistic FET transistor is working at room temperature is the most desired device in graphene, only recently was fabricated [24]. The main problem of graphene transistors is the lack of the bandgap and thus the relation between drain current  $I_D$  and the drain voltage  $V_D$  is linear and no saturation currents are occurring.

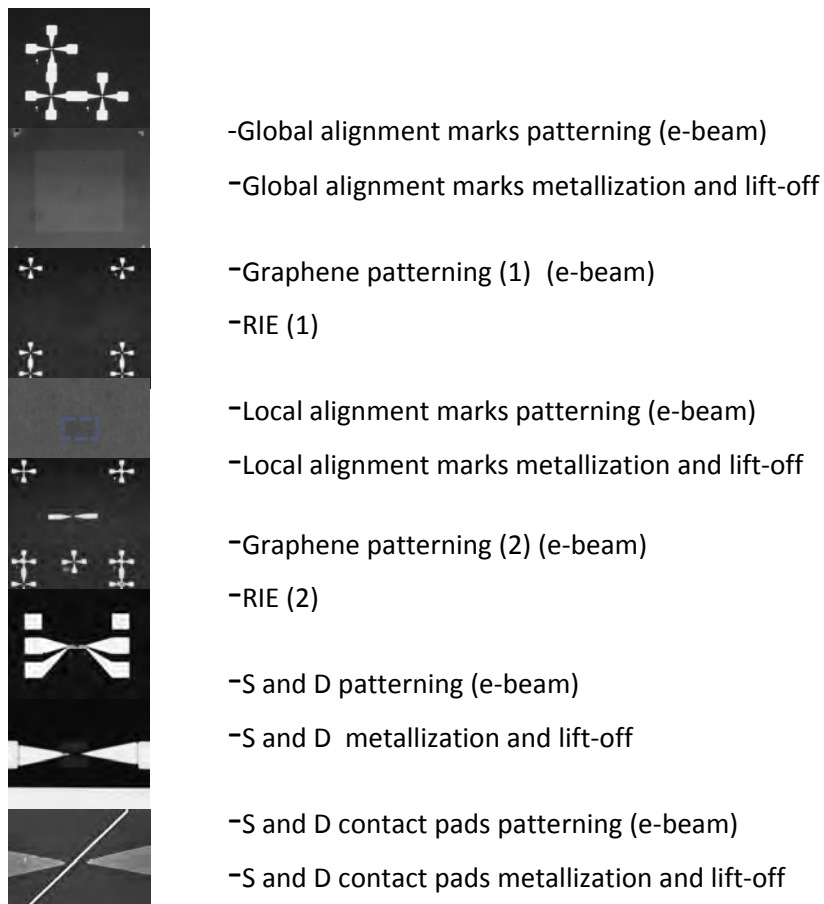
The creation of a bandgap in graphene monolayers is based on rather difficult technological procedures all of them destroying the physical properties of the graphene monolayer. However, only in the ballistic graphene devices an oblique gate modulates the transmission between the two electrodes: drain and source. In the ballistic transport regime, the lack of an energy bandgap makes the transmission to be constant and equal to 1 when the gate is normal to the direction of electron propagation, irrespective of gate biases. However, an oblique gate at an angle of 45°, for instance, is producing a transmission bandgap of about 0.3 eV. No degradation of graphene is made in this case [24]-[27]. Moreover, an oblique gate having the role of a barrier [10], induces a negative differential resistance [26], [27]. The NDR in ballistic graphene devices with oblique gates is due to an abrupt drop to zero of the transmission of charge carriers over a certain range of  $V_D$ , due to the lack of charge carrier propagation through the gated region. Such a drastic drop in the transmission is corresponding to a minimum in  $I_D$  versus  $V_D$  characteristic. A bias applied on the oblique gate of the ballistic graphene FET can shift the NDR region of the  $I_D$ - $V_D$  dependence and can affect the peak-valley ratio of the (PVR of the ballistic device. The technological process is explained in detail in [24].

We have fabricated FETs with oblique gates on a chip of CVD graphene transferred on a doped 4 inch silicon wafer (back gate) having 285 nm thin film of silicon dioxide on top of it.

The HSQ was selected as dielectric for the transistor having an electrical permittivity around 3, because it was used many times as gate dielectric in graphene FETs since it does not destroy the graphene monolayer. The thickness of the HSQ is about 50 nm. On the top of the gate insulating layer, there is a tilted electrode for the top gate consisting of a Cr/Au electrode with a thickness of 45 nm fabricated by e-beam lithography and lift-off. The gate length is 40 nm, at the state-of-art of graphene FETs

The graphene ballistic transistors was fabricated in 12 distinct steps (see Fig. 8).

The transistor is depicted in Fig. 9.



**Fig. 9.** The technological process for graphene ballistic transistor.

The NDR of the above transistor with a tunable PVR is dependent on the top-gate voltage and is displayed in Fig. 10, where the  $I_D$ - $V_D$  curves were measured at top gates of  $V_{TG} = 0$  V (dashed line), 0.5 V (dotted line) and 1 V (solid line). The PVR ratio is enhanced by the gate voltage because the Fermi level in graphene is shifted by the top gate voltage and changes the behaviour of the NDR. The maximum drain current is  $105 \mu\text{A}$  at a drain voltage of 1.5 V and a gate voltage of 1 V, and drops dramatically to  $12 \mu\text{A}$  at  $V_D = 2$  V and we have a very large PVR of 8.75. When there is no gate voltage the maximum and minimum  $I_D$  values are about  $95 \mu\text{A}$  and  $12 \mu\text{A}$ , and PVR is becoming 7.9. This NDR behavior was retrieved in many graphene FETs with oblique gates having PVRs (see Fig. 10). This graphene ballistic transistor has the cutoff frequency of 2.5 THz.

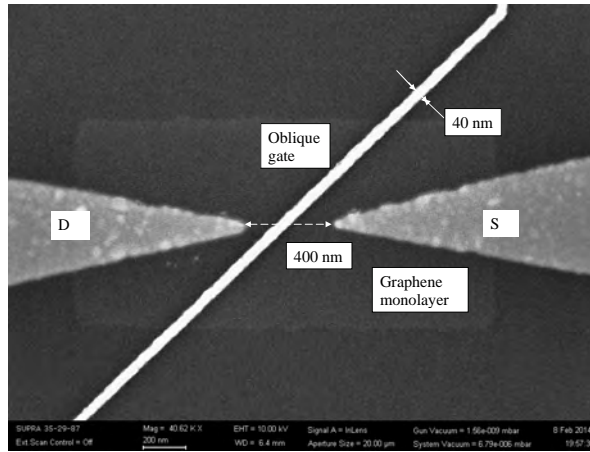


Fig. 9. The ballistic graphene transistor after [24].

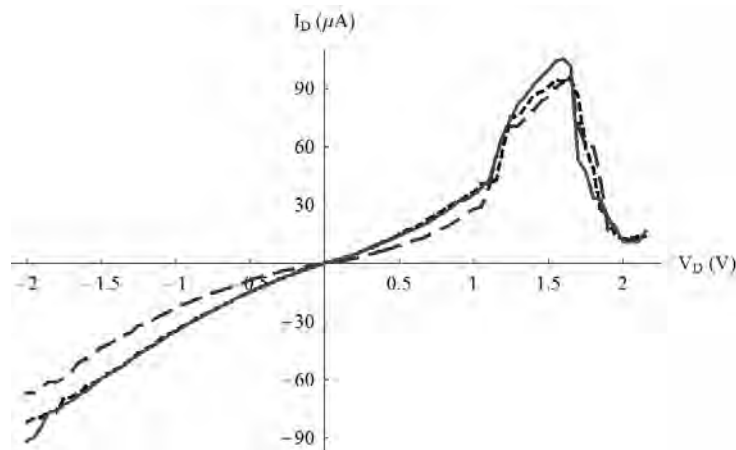


Fig. 10. The NDR behavior of the graphene ballistic FET (after [24]).

#### 4. The new world of 2D materials

After a couple of years after graphene discovery the world of 2D materials was enriched with hundreds of new 2D materials , so an atlas of 2D materials was necessary[28].

By far the two-dimensional (2D) transition metal dichalcogenides (TMD) most studied 2D materials after graphene [29]. MoS<sub>2</sub> monolayers and multilayers are fabricated using the exfoliation procedures as for graphene in the case of graphene. In this way, transistors [30], photodectors [31], and sensors were fabricated with very good performances [32]. However, little is know about microwave performances of MoS<sub>2</sub> and we have recently started to study the device sbased on MoS<sub>2</sub> for RF applications[33]. Very recently, we have measured the effective permittivity and loss tangent of MoS<sub>2</sub> in a very large bandwidth using an electromagnetic –bandgap resonator. Details about resonator fabrication, dimension, MoS<sub>2</sub> deposition are found in [33]. Below we show the SEM images of MoS<sub>2</sub> monolayers deposited over the resonator. It is evident from this image the layered structure of MoS<sub>2</sub> thin films formed from millions of MoS<sub>2</sub> monolayers.

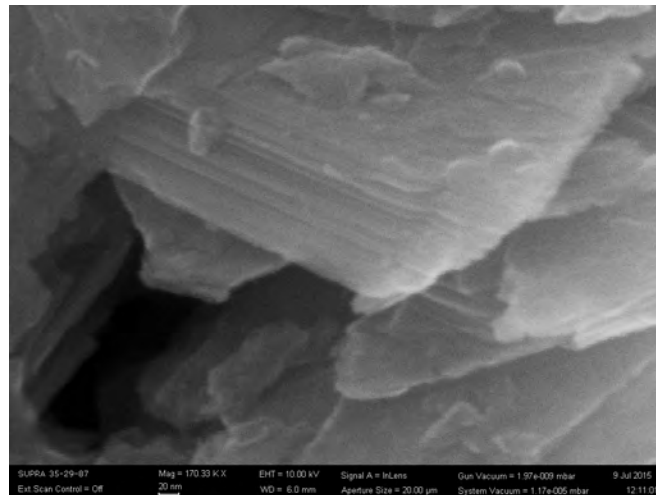
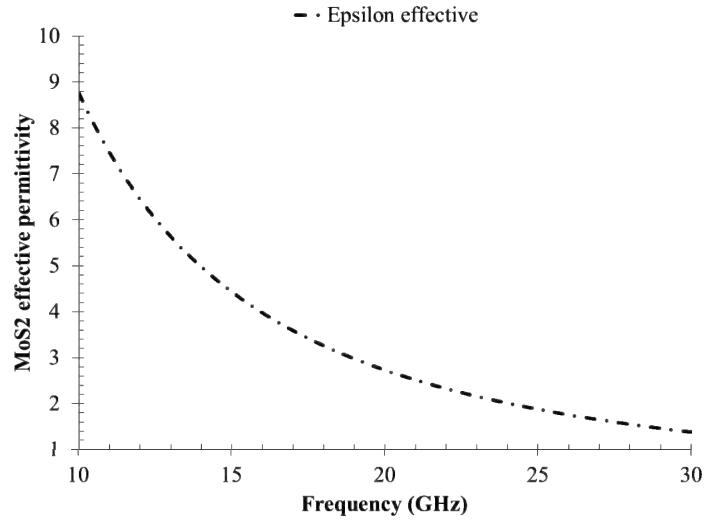
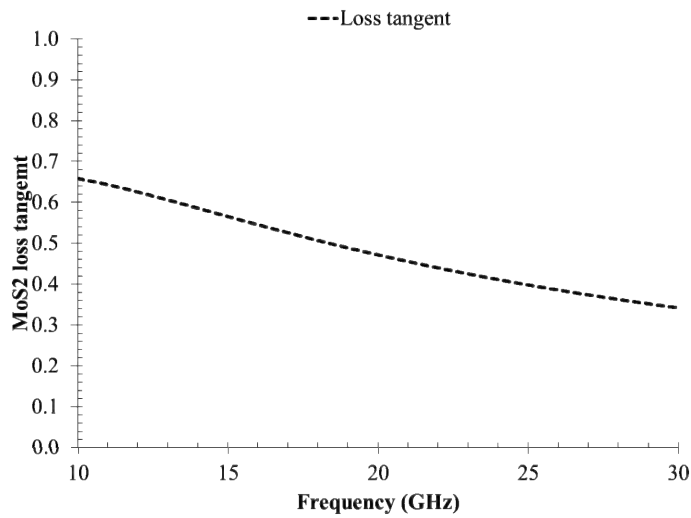


Fig. 11. The SEM image of MoS<sub>2</sub> monolayers.

The effective permittivity and the tangent loss were extracted from S-parameters measurement of MoS<sub>2</sub> deposited on resonator and are represented in Fig. 12 and 13. We see that effective permittivity is rather low while the loss tangent is indicating moderate losses.



**Fig. 12.** Effective permittivity of MoS<sub>2</sub> thin film made of millions of monolayers.



**Fig. 13.** The loss tangent of MoS<sub>2</sub> of millions of monolayers.

## 5. Conclusions

The paper has presented a short review of the graphene and other 2D materials applications in the area of RF. We see that although the technologies of

fabrication are tedious and challenging enhanced nanodevices working at very high frequencies are emerging.

**Acknowledgments.** We acknowledge the financial support of the Romanian National Authority for Scientific Research, CNCS-UEFISCDI, project number PN-II-ID-PCE-2011-3-0071, and of the European Commission for the financial support via the FP 7 NANO RF (grant agreement 318352) and Nucleu program, project PN 09290112.

## References

- [1] A.K GEIM, *Graphene: Status and Prospects*, Science **324**, pp. 1530–1534, 2009.
- [2] W. REN, H.-M. CHENG, *The global growth of graphene*, Nature Nanotechnology **9**, pp. 726–730, 2014.
- [3] H. ZHANG, *Ultrathin two-dimensional nanomaterials*, ACS Nano **9**, pp. 9451–9469, 2015.
- [4] D. DRAGOMAN, M. DRAGOMAN, *Transport properties in carbon nanotube and graphene*, in *Carbon nanotubes and graphene*, eds. K. Tanaka and S. Iijima, Elsevier pp. 151–165, 2014.
- [5] F. XIA, H. WANG, D. XIAO, M. DUBEY, A. RAMASUBRAMANIAM, *Two-dimensional material nanophotonics*, Nature Photonics **8**, pp. 899–907, 2014.
- [6] R.R. HARTMANN, J KONO, M.E. PORTNOI, *Terahertz science and technology of carbon nanomaterials*, Nanotechnology **25**, pp. 320201, 2014.
- [7] K.S. NOVOSELOV, A.K. GEIM, S.V. MOROZOV, D. JIANG, Y. ZHANG, S.V. DUBONOS, I.V. GRIGORIEVA, A.A. FIRSOV, *Electric field effect in atomically thin carbon films*, Science **306**, pp. 666–669, 2004.
- [8] A. ZURUTUZA, C. MARINELLI, *Challenges and opportunities in graphene commercialization*, Nature Nanotechnology **9**, pp. 730–734, 2014.
- [9] M. DRAGOMAN, D. DRAGOMAN, *Nanoelectronics: Principles and Devices*, Artech House, Boston, 2011.
- [10] D. DRAGOMAN, M. DRAGOMAN, *Bionanoelectronics*, Springer, 2012.
- [11] S. MAYOROV, R.V. GORBACHEV, S.V. MOROZOV, L. BRITNELL, R. JAIL, L.A. PONOMARENKO, K.S. NOVOSELOV, K. WATANABE, T. TANIGUCHI, A.K. GEIM, *Micrometer-scale ballistic transport in encapsulated graphene at room temperature*, Nano Lett. **11**, pp. 2396, 2011.
- [12] J. BARINGHAUS, J.M. RUAN, F. EDLER, A. TEJEDA, M. SICOT, A. TALEB-IBRAHIMI, A.-P. LI, Z. JIANG, E.H. CONRAD, C. BERGER, C. TEGENKAMP, W.A. DE HEER, *Exceptional ballistic transport in epitaxial graphene nanoribbons*, Nature **506**, pp. 349–354, 2014.
- [13] Q. BAO, K.P. LOH, *Graphene photonics, plasmonics, and broadband optoelectronic devices*, ACS Nano **6**, pp. 3677, 2012.
- [14] F. XU, S. DAS, Y. GONG, Q. LIU, H.-C. CHIEN, H.-Y. CHIU, J. WU, R. HUI, *Complex refractive index tunability of graphene at 1550nm wavelength*, Appl. Phys. Lett. **106**, pp. 031109, 2015.
- [15] M. DRAGOMAN, A. CISMARU, A. STEFANESCU, A. DINESCU, M. DRAGOMAN, *The electromagnetic properties of graphene in the microwave and millimeterwave spectrum*, European Microwave Conference (EuMC), Nurnberg, Germania, Octombrie 2013.
- [16] M. DRAGOMAN, D. NECULOIU, A. CISMARU, A.A. MULLER, G. DELIGEORGIS, G. KONSTANTINIDIS, D. DRAGOMAN, R. PLANA, *Coplanar waveguide pn graphene in the range 40 MHz-110 GHz*, Appl. Phys. Lett. **99**, pp. 2011.

- [17] F. SCHWIERZ, *Graphene transistors: status, prospects, and problems*, Proc. IEEE **101**, pp. 1567–1584, 2013.
- [18] G. FIORI, F. BONACCORSO, G. IANNACCONEI, T. PALACIOS, D. NEUMAIER, A. SEABAUGH, S.K. BANERJEE, L. COLOMBO, *Electronics based on two-dimensional materials*, Nature Nanotechnology **9**, pp. 768–779, 2014.
- [19] A.K. GEIM, *Nobel Lecture: Random walk to graphene*, Rev.Mod. Phys. **83**, pp. 851–862, 2011.
- [20] C.H. AHN, A. BHATTACHARYA, M.DI VENTRA, J.N. ECKSTEIN, C. DANIEL FRISBIE, M.E. GERSHENSON, A.M. GOLDMAN, I.H. INOUE, J. MANNHART, A.J. MILLIS, A.F. MORPURGO, D. NATELSON, J.-M. TRISCONI, *Electrostatic modification of novel materials*, Rev. Mod. Phys. **78**, pp. 1185–1212, 2006.
- [21] M. DRAGOMAN, G. KONSTANTINIDIS, K. TSAGARAKI, T. KOSTOPOULOS, D. DRAGOMAN, D. NECULOIU, *Graphene-like metal-on-silicon field-effect transistor*, Nanotechnology **23**, pp. 305201, 2012.
- [22] J.R. RENTERIA, C. SAMNAKAY, T.R. JIANG, P. POPE, Z. GOLI, YAN, D. WICKRAMARATNE, T.T. SALGUERO, A.G. KHITUN, R.K. LAKE, A.A. BALANDIN, *All-metallic electrically gated 2H-TaSe<sub>2</sub> thin-film switches and logic circuits*, **115**, pp. 034305, 2014.
- [23] K.S. KIM, S.C. JUNG, M.H. KANG, H.W. YEOM, *Nearly massless electrons in the silicon interface with metal film*, Phys. Rev. Lett. **104**, pp. 246803, 2010.
- [24] M. DRAGOMAN, A. DINESCU, D. DRAGOMAN, *Negative differential resistance in graphene based ballistic field-effect transistor with oblique top gate*, Nanotechnology **25**, pp. 415201, 2014.
- [25] M.I. KATSNELSON, K.S. NOVOSELOV, A.K. GEIM, *Chiral tunnelling and the Klein paradox in graphene*, Nature Physics **2**, pp. 620, 2006.
- [26] D. DRAGOMAN, M. DRAGOMAN, *Negative differential resistance of electrons in graphene barrier*, Appl. Phys. Lett. **90**, pp. 143111, 2007.
- [27] D. DRAGOMAN, M. DRAGOMAN, R. PLANA, *Graphene-based ultrafast diode*, J. Appl. Phys. **108**, pp. 084316, 2010.
- [28] P. MIRO, M. AUDIFFRED, T. HEINE, *An atlas of two-dimensional materials*, Chem. Soc. Rev. **43**, pp. 6537–6554, 2014.
- [29] Q.H. WANG, K. KALANTAR-ZADEH, A. KIS, J.C. COLEMAN, M. STRANO, *Electronic and optical properties of two-dimensional transition metal dichalcogenides*, Nature Nanotechnology **7**, pp. 699–712, 2012.
- [30] F. SCHWIERZ, J. PEZOLDT, R. GRANZNER, *Two-dimensional materials and their prospects in transistor electronics*, Nanoscale **7**, pp. 8261–8283, 2015.
- [31] F. XIA, HAN WANG, D. XIAO, M. DUBEY, A. RAMASUBRAMANIAM, *Two-dimensional material nanophotonics*, Nature Photonics **8**, pp. 899–907, 2014.
- [32] Y. HUANG, J. GUO, Y. KANG, Y. AI\*A, C. M. LI, *Two dimensional atomically thin MoS<sub>2</sub> nanosheets and their sensing applications*, Nanoscale **7**, pp. 19358–19376, 2015.
- [33] M. DRAGOMAN, A. CISMARU, M. ALDRIGO, A. RADOI, D. DRAGOMAN, *Switching microwaves via semiconductor-isolator reversible transition in a thin-film of MoS<sub>2</sub>*, J. Appl. Phys. **118**, pp. 045710, 2015.

# Effect of Different Solvents in the Exfoliated Graphite Nanoplatelets Systems at (313.15 and 318.15) K Temperatures

Florinela SIRBU<sup>a</sup>, Alina Catrinel ION<sup>b</sup>, and Ion ION<sup>b</sup>

<sup>a</sup>“Ilie Murgulescu” Institute of Physical Chemistry of Romanian Academy,  
202 Splaiul Independentei str., 060021, Bucharest, Romania  
E-mail: sflorinela@yahoo.com

<sup>b</sup>“Politehnica” University of Bucharest, Faculty of Applied Chemistry and Material  
Science, 1-7 Polizu str., 011061, Bucharest, Romania  
E-mail: ac\_ion@yahoo.com, i\_ion@chim.upb.ro

**Abstract.** The study of physicochemical behavior in the exfoliated graphite nanoplatelets mixtures with different solvents is important for further separations of environmental contaminants and industrial applications.

The density, speed of sound, and refractive index of diluted binary mixtures of exfoliated graphite nanoplatelets and active carbon dispersed in tetrahydrofuran, water, and *N,N*-dimethylformamide, respectively, at various compositions of solvate and at various temperatures have been measured. The acoustic and optical parameters from the experimental data obtained were calculated.

The results of xGnP + THF binary mixture have been used to identify molecular interactions in the mixtures, including structural changes of exfoliated graphite nanoplatelets in different solvents.

**Key words:** physicochemical study; exfoliated graphite nanoplatelets (xGnP); active carbon (AC); solvents; tetrahydrofuran (THF); binary mixtures; optical and acoustical properties.

## 1. Introduction

The investigation of some physicochemical properties contributes to better understand of the physicochemical behavior of binary and multi-component liquid blends. The experimental values of thermodynamic and thermophysical properties in combination with other analytical data of liquid mixtures are of high fundamental practical importance, with applicability in industry and chemical analysis. Moreover, these properties significantly influence the dispersion of the nanomaterials in the studied solvents, offering new information on the structure and interactions of mixed solvents [1]. In this way, the properties of these dispersed



nanostructured materials in different solvents can be easily controlled by adjusting a variety of factors such as: pH, surface chemistry, and ionic strength [2, 3].

The nanoplatelets from graphite (10-100 graphene layers, 3-30 nm thick) are usually named exfoliated graphite nanoplatelets (xGnP), independent of the number of layers show similar electrochemical behavior [4]. Although the number of studies on xGnP is increasing [5], there is still a lack of data on their thermodynamic properties [6], the thermophysical description and molecular modeling properties [7].

In order to characterize the type and magnitude of the molecular interactions between the tetrahydrofuran (THF) and the xGnP, the density, speed of sound, and refractive index of the pure solvent and of the blends are provided in this study, no effort being done till the moment to study these molecular interactions. xGnP dispersed in THF provide potential environmental applications [8] being used in composite nanomaterials for sensors [9], in field sensing systems to monitor the environmental stress and for sorbents [10], or removing contaminants from water [11] and soils.

The state of science and prototyping for both sensors and sorbents using nanostructured materials is the most advanced in the field of nanotechnology, but the basic level of knowledge concerning interactions at molecular level is not at the same level of study.

As a continuation of our research on solutions blends behavior [12, 13, 14], this work presents the physicochemical properties in binary systems of exfoliated graphite nanoplatelets (xGnP)/ active carbon (AC) in tetrahydrofuran (THF), for which no such experimental data are available. The variation of the studied acoustic and optical parameters versus composition was useful in understanding the nature and the extent of interaction between unlike molecules.

## **2. Experimental Section**

### ***2.1. Materials and Methods***

Exfoliated graphite nanoplatelets (xGnP) containing a mass fraction more than 0.95 carbon was provided from XG Sciences, Lansing, MI, USA (thickness approximately 15 nm, diameter 25  $\mu\text{m}$ , surface area 50-80  $\text{m}^2\cdot\text{g}^{-1}$ ) and was characterised in our laboratory. Activated carbon with a mass fraction more than 0.99% carbon have been purchased from Sigma-Aldrich. Tetrahydrofuran solvent has been supplied by Merck. xGnP and AC were used without any pre-treatment because of their mass fraction purity higher than 0.95. The details of the used chemicals for samples preparation are presented in the Table 1.

**Table 1.** Specification of Exfoliated Graphite Nanoplatelets, Active Carbon and THF Compounds Used in Samples

Chemical Name	Source	Initial Mass Fraction Purity	Purification Method	Final Mass Fraction Purity	Analysis Method
xGnP <sup>a</sup>	XG Sciences, Lansing, MI, USA	> 0.95 Carbon	none	> 0.95 Carbon	-
AC <sup>b</sup>	Sigma Aldrich	> 0.99 Carbon	none	> 0.99 Carbon	-
THF <sup>c</sup>	E. Merck	p.a.	none	p.a.	-

<sup>a</sup>xGnP = Exfoliated Graphite Nanoplatelets

<sup>b</sup>AC = Active Carbon

<sup>c</sup>THF = Tetrahydrofuran

Doubly distilled, de-ionized, and degassed water with a specific conductance of  $5 \cdot 10^{-5} \text{ S} \cdot \text{m}^{-1}$  at 298.15 K has been used for calibration and measurements, according to the recommendations of the manufacturer. The all working samples of different compositions xGnP/AC + THF were prepared at temperature of 298.15 K.

## 2.2. Apparatus and Measurements Procedure.

The data concerning density and speed of sound of the stock binary solutions were measured with an Anton Paar DSA 5000 digital (Austria) instrument, with an accuracy of  $\pm 10^{-6} \text{ g} \cdot \text{cm}^{-3}$ . The sample temperature during the density measurements has been controlled with a precision of  $\pm 10^{-3} \text{ K}$ , several Peltier units being used. The density and speed of sound values obtained for air and twice distilled water by calibration have been reproducible within  $\pm 5 \cdot 10^{-6} \text{ g} \cdot \text{cm}^{-3}$  and  $\pm 5 \cdot 10^{-2} \text{ m} \cdot \text{s}^{-1}$ , respectively. The refract meter was calibrated by measuring the refractive index of doubly distilled water.

**Table 2.** Comparison of experimental densities ( $\rho$ ), ultrasonic velocities ( $c$ ), and refractive indices ( $n_D$ ) of pure tetrahydrofuran with literature values at temperatures of (313.15 and 318.15) K

$\frac{T}{K}$	$\rho / \text{g} \cdot \text{cm}^{-3}$			$c / \text{m} \cdot \text{s}^{-1}$			$n_D$		
	Expt.	Lit.		Expt.	Lit.		Expt.	Lit.	
<b>THF</b>									
313.15	0.86561	0.86719	[15]	1207.30	1150.00	[16]	1.39663	1.3000	[16]
		0.87262	[17]		1202.00	[18]			
318.15	0.85996	0.86223	[15]	1183.50	1176.18	[16]	1.39392	1.3000	[16]
		0.86872	[17]						

## 3.2. Theory and Calculation

The following thermodynamic acoustical and optical properties were estimated using the standard relations employed in previous studies [12, 14]. The acoustic impedance ( $Z$ ) was calculated using the following relation [19]:

$$Z = \rho c \quad (1)$$

where  $\rho$  is the density ( $\text{kg}\cdot\text{m}^{-3}$ ), and  $c$  is the speed of sound ( $\text{m}\cdot\text{s}^{-1}$ ) in the mixture. The isentropic compressibility coefficient  $k_s$  for the pure solvent and liquid mixtures have been estimated from the density  $\rho$  and the speed of sound  $c$  using the Laplace equation [20].

$$k_s = \frac{1}{K} = \frac{1}{\rho c^2} \quad (2)$$

where  $K$  is the bulk modulus of the solution.

According to the method of Gerecze [21] and Lorentz-Lorenz [22], the space-filling factor ( $S$ ) has been computed from refractive index (sodium D line) data using the following relation [23]:

$$S = \frac{B}{V} = \frac{n_D^2 - 1}{n_D^2 + 2} \quad (3)$$

where,  $B$  is the effective volume occupied by molecules per mole,  $V$  is the molecular volume and  $n_D$  is the refractive index of the aqueous solution.

The specific refraction ( $r_D$ ) has been estimated from the density ( $\rho$ ) and space-filling factor ( $S$ ) using the Lorentz and Lorenz equation, which is based on the electromagnetic theory of light, where as the other equations are of empirical origin [24]:

$$r_D = \frac{n_D^2 - 1}{n_D^2 + 2} \frac{1}{\rho} \quad (4)$$

The relaxation strength ( $r$ ) has been calculated using the following equation [25]:

$$r = 1 - \frac{c^2}{c_{ct}^2} \quad (5)$$

where  $c$  is the speed of sound in the experimental solution, and  $c_{ct}$  is a constant with a value of  $1600 \text{ m}\cdot\text{s}^{-1}$  [24].

The specific concentration dependence on density and on ultrasound speed obtained in the two systems was correlated by a polynomial type equation:

$$F(Y) = \sum_{i=1}^n A_i C^{i-1} \quad (6)$$

where  $Y$  represents the properties measured in general ( $\rho$ ,  $c$ ) and  $C$  represents the specific concentration.

Correlations of  $\rho$ ,  $c$ ,  $k_s$  and  $r$  as a function of concentration (Eq. 7) along with the absolute average percentage deviation (AAD) were analyzed. The absolute average percentage deviation (AAD %) was determined using the following relationship:

$$AAD(Y) = \frac{100}{N} \sum_i^n \left| \frac{Y_{Expt.} - Y_{Calc.}}{Y_{Expt.}} \right| \quad (7)$$

where  $N$  is the number of experimental data points. The subscripts “Expt.” and “Calc.” represent the values of the experimental and calculated property, respectively.

### 3. Results and Discussion

Based on the values of the measured properties of xGnP + THF mixtures, the derived thermophysical parameters as a function of the specific concentration fraction at two different temperatures of (313.15 and 318.15) K were calculated and presented in Table 3.

**Table 3.** Experimental Values of the Density  $\rho$ , Ultrasound Speed  $c$  and Refractive Index at Various Temperatures  $T$  and Specific Concentration  $C$  of (xGnP), for the System xGnP + THF<sup>a</sup>

$T/K$	$\rho/\text{kg}\cdot\text{m}^{-3}$	$c/\text{m}\cdot\text{s}^{-1}$	$n_D$	$\rho/\text{kg}\cdot\text{m}^{-3}$	$c/\text{m}\cdot\text{s}^{-1}$	$n_D$
	$C/\text{kg}\cdot\text{m}^{-3} = 0$			$C/\text{kg}\cdot\text{m}^{-3} = 20$		
313.15	865.61	1207.3	1.39663	865.76	1207.35	1.39604
318.15	859.96	1183.5	1.39392	860.16	1183.55	1.39384
	$C/\text{kg}\cdot\text{m}^{-3} = 40$			$C/\text{kg}\cdot\text{m}^{-3} = 60$		
313.15	865.87	1207.38	1.39567	866.05	1207.4	1.39595
318.15	860.32	1183.62	1.39378	860.48	1183.69	1.39401
	$C/\text{kg}\cdot\text{m}^{-3} = 80$			$C/\text{kg}\cdot\text{m}^{-3} = 100$		
313.15	866.18	1207.39	1.39623	866.33	1207.38	1.39703
318.15	860.67	1183.73	1.39427	860.73	1183.76	1.39531

<sup>a</sup> $C/\text{kg}\cdot\text{m}^{-3}$  is the specific concentration of xGnP in the THF solvent. Standard uncertainties  $u$  are  $u(T) = 0.001$  K for  $\rho$  and  $c$ ;  $u(T) = 0.01$  K for  $n_D$  and the combined expanded uncertainties  $U_c$  are  $U_c(\rho) = 0.01$   $\text{kg}\cdot\text{m}^{-3}$ ,  $U_c(c) = 0.1$   $\text{m}\cdot\text{s}^{-1}$ ; (level of confidence = 0.95,  $k = 2$ ) and  $U_c(n_D) = 0.00001$ .

The experimental data for AC + THF mixture as a function of the specific concentration of AC at the same temperatures are presented also, in Table 4.

**Table 4.** Experimental Values of the Density  $\rho$ , Ultrasound Speed  $c$  and Refractive Index at Various Temperatures  $T$  and Specific Concentrations  $C$  of AC, for the AC + THF<sup>a</sup> System

$T/K$	$\rho/\text{kg}\cdot\text{m}^{-3}$	$c/\text{m}\cdot\text{s}^{-1}$	$n_D$	$\rho/\text{kg}\cdot\text{m}^{-3}$	$c/\text{m}\cdot\text{s}^{-1}$	$n_D$
	$C/\text{kg}\cdot\text{m}^{-3} = 0$			$C/\text{kg}\cdot\text{m}^{-3} = 20$		
313.15	865.61	1207.3	1.39663	865.63	1207.32	1.39664
318.15	859.96	1183.5	1.39392	860.02	1183.53	1.39392
	$C/\text{kg}\cdot\text{m}^{-3} = 40$			$C/\text{kg}\cdot\text{m}^{-3} = 60$		
313.15	865.65	1207.38	1.39665	865.7	1207.46	1.39667
318.15	860.04	1183.61	1.39393	860.1	1183.76	1.39396
	$C/\text{kg}\cdot\text{m}^{-3} = 80$			$C/\text{kg}\cdot\text{m}^{-3} = 100$		
313.15	865.75	1207.58	1.39668	865.82	1207.58	1.39668
318.15	887.80	1303.72	1.40733	887.87	1303.72	1.40733

<sup>a</sup> $C/\text{kg}\cdot\text{m}^{-3}$  is the specific concentration of AC in the THF solvent. Standard uncertainties  $u$  are  $u(T) = 0.001$  K for  $\rho$  and  $c$ ;  $u(T) = 0.01$  K for  $n_D$  and the combined expanded uncertainties  $U_c$  are  $U_c(\rho) = 0.01$   $\text{kg}\cdot\text{m}^{-3}$ ,  $U_c(c) = 0.05$   $\text{m}\cdot\text{s}^{-1}$ ; (level of confidence = 0.95,  $k = 2$ ) and  $U_c(n_D) = 0.00001$ .

The density, ultrasound speed and refractive index values as a function of specific concentration of exfoliated graphite nanoplatelets (xGnP) are shown in Figs. 1, 2 and 3, respectively, comparing the three binary xGnP + THF, xGnP + H<sub>2</sub>O [12], xGnP + DMF [14] systems, along of polynomial correlated values ( $\rho$ ,  $c$ ).

The measured densities of the xGnP dispersion in THF increase by increasing xGnP composition.

As shown in Figure 1, the density of the xGnP + DMF system increases with an increasing the xGnP concentration up to 60  $\text{kg}\cdot\text{m}^{-3}$ , then decreases up to  $C = 100$   $\text{kg}\cdot\text{m}^{-3}$ .

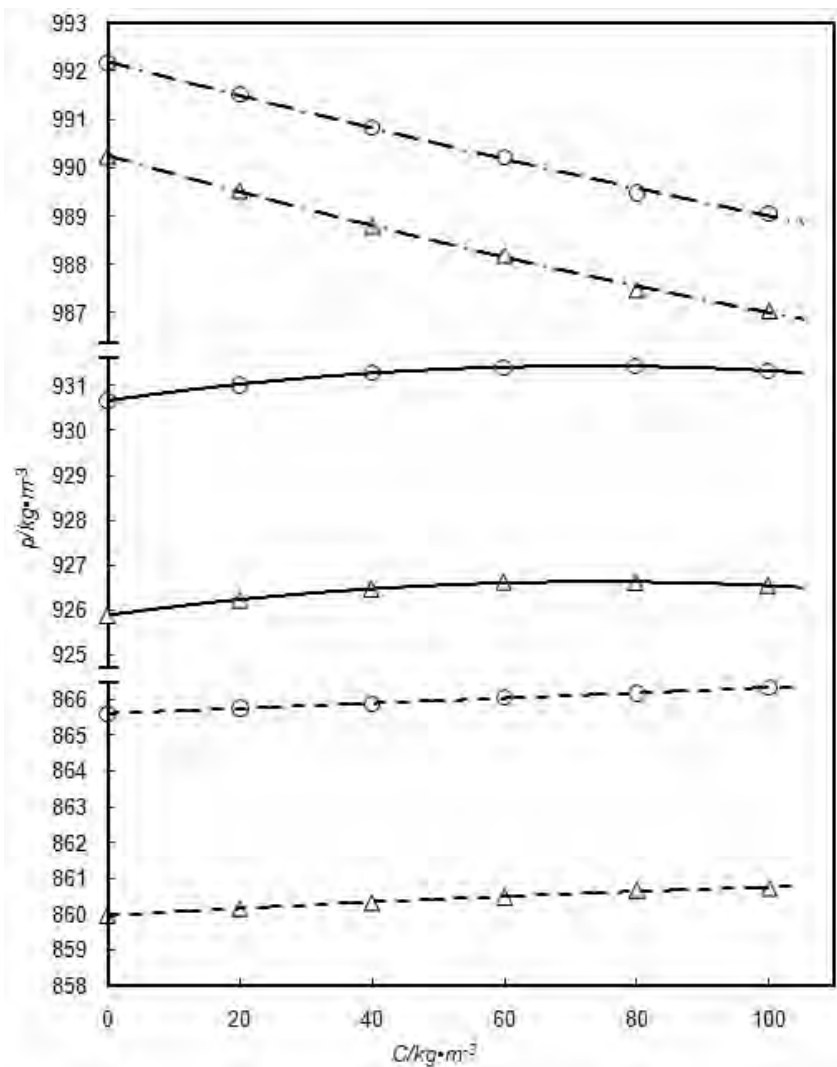
The values of the densities of xGnP in water mixtures decrease by increasing xGnP composition and vary according to the relation: xGnP + DMF < xGnP + THF < xGnP + H<sub>2</sub>O in binary mixtures.

The measured density values of xGnP in all studied solvents are decreasing by increasing temperature from (313.15 up to 318.15) K.

A similar behavior for the variation of the refractive index in all studied xGnP dispersions in THF/DMF/H<sub>2</sub>O is reported in this work, presented in Table 3 and Figs. 1 and 3.

Good dispersion of the nanostructured material is influenced by the surface tensions and solubility parameters of the solvents, being found that an efficient solvent has a surface tension equivalent to that of graphene. Good solvents for graphene provide stable colloidal dispersions for nanosized graphene material [25].

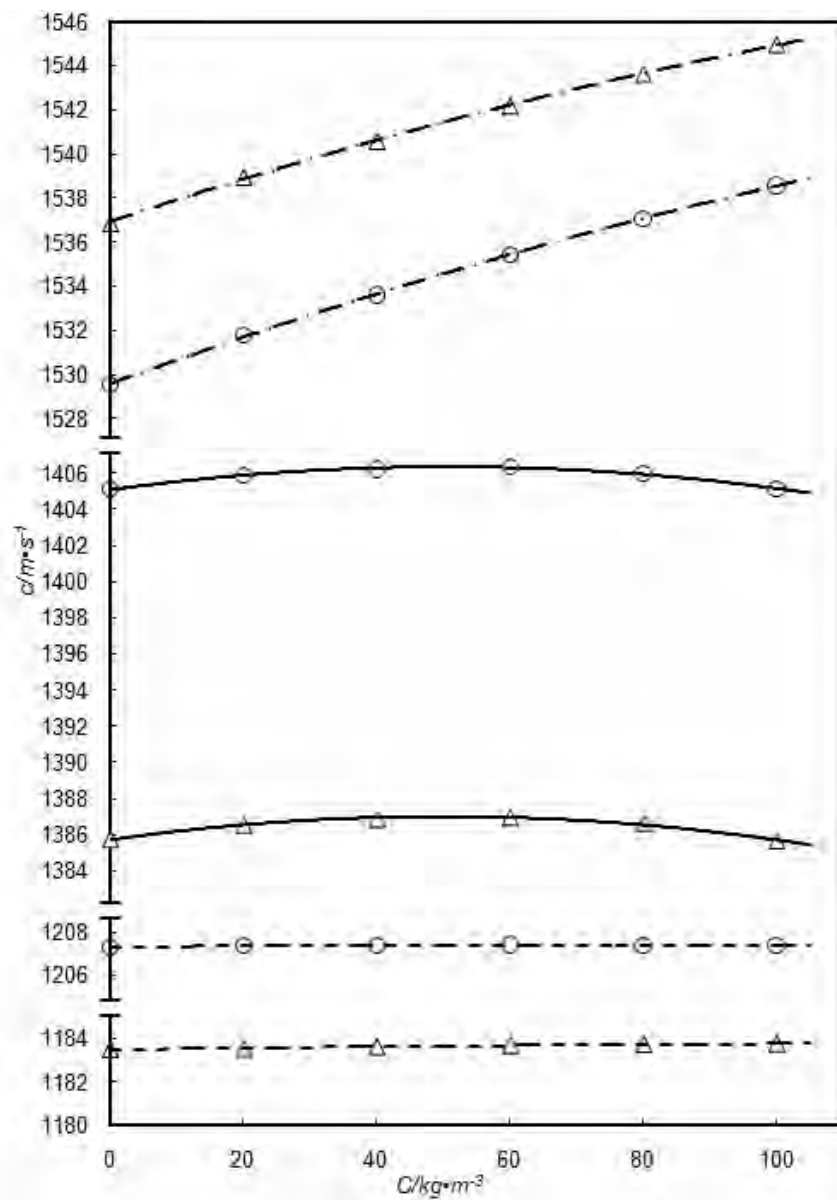
The solvent molecules can insert between the graphite layers providing a colloidal stability by ultrasonic treatment.



**Fig. 1.** Comparative representation of the density of binary xGnP + THF, xGnP + H<sub>2</sub>O [12], and xGnP + DMF [14] systems versus concentration of solute at various temperatures, T/K: ○, 313.15; △, 318.15; ---, for THF; —, for DMF; ···, H<sub>2</sub>O-polynomial correlated values.

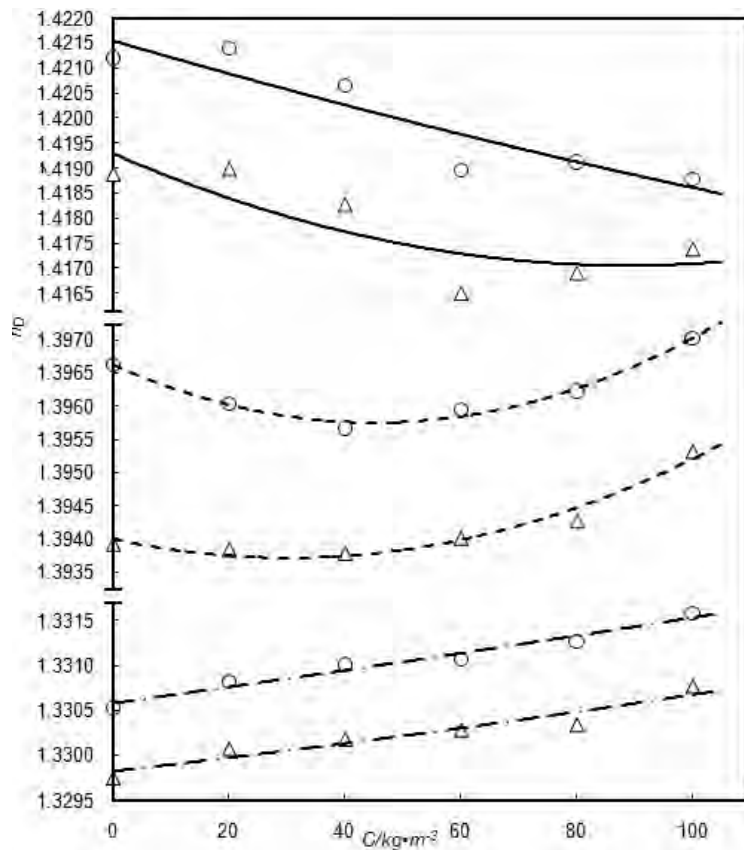
The speed of sound (Fig. 2) of xGnP dispersed in all solvents is increasing by increasing xGnP composition.

The values for measured speed of sound in the xGnP + THF/DMF systems are decreasing, but in the dispersion xGnP + H<sub>2</sub>O they increase by increasing temperature.



**Fig. 2.** Comparative representation of the ultrasound speed of binary xGnP + THF, xGnP + H<sub>2</sub>O [12], and xGnP + DMF [14] systems versus concentration of solute at various temperatures, T/K:  $\circ$ , 313.15;  $\Delta$ , 318.15; - · -, for THF; —, for DMF;  $\circ$ , H<sub>2</sub>O - polynomial correlated values.

The dependence of the refractive indices on the concentration of xGnP dispersed in THF, DMF, and H<sub>2</sub>O is presented in Fig. 3.



**Fig. 3.** Comparative representation of the refractive index of binary xGnP + THF, xGnP + H<sub>2</sub>O [12], and xGnP + DMF [14] systems versus concentration of solute at various temperatures, T/K: ○, 313.15; △, 318.15; ---, for THF; —, for DMF; ···, H<sub>2</sub>O - polynomial correlated values.

The measured refractive index of xGnP dispersion in DMF decrease by increasing xGnP composition.

From Figure 3, the refractive index of the xGnP + THF mixture decreases by increasing xGnP concentration up to 60 kg·m<sup>3</sup>, then increases up to C = 100 kg·m<sup>3</sup>.

The values of the refractive index of xGnP in water mixture increase by increasing xGnP composition and vary according to the relation: xGnP + H<sub>2</sub>O < xGnP + THF < xGnP + DMF in binary mixtures.

The measured refractive index values of xGnP in all studied solvents are decreasing, by increasing temperature from (313.15 up to 318.15) K. The behavior is similar with that of the density, as seen from Table 3 and Figs. 1 and 3.

From the experimental results of the measured properties, the derived thermophysical parameters as a function of the specific concentration fraction at temperatures of (313.15 and 318.15) K were calculated and presented in Table 5.



**Table 5.** Calculated Values of the Acoustic Impedance  $Z$ , Isentropic Compressibility  $k_s$ , Space Filling Factor  $S$ , Specific Refraction  $r_D$ , and Relaxation Strength  $r$  at Various Temperatures  $T$ , Specific Concentration  $C$  of (xGnP), for the Systems xGnP and AC + THF

$T/K$	$\frac{Z}{10^5 \cdot \text{kg} \cdot \text{m}^{-2} \cdot \text{s}^{-1}}$	$\frac{k_s}{10^{-9} \cdot \text{m}^2 \cdot \text{N}^{-1}}$	$S$	$\frac{r_D}{10^{-3} \cdot \text{m}^3 \cdot \text{kg}^{-1}}$	$r$
<i>xGnP+ THF</i>					
<i>C/kg·m<sup>-3</sup> = 0</i>					
313.15	10.45051	7.92588	0.24062	0.27797	0.43064
318.15	10.17763	8.30205	0.23916	0.27811	0.45286
<i>C/kg·m<sup>-3</sup> = 20</i>					
313.15	10.45275	7.92385	0.24030	0.27756	0.43059
318.15	10.18042	8.29942	0.23912	0.27799	0.45282
<i>C/kg·m<sup>-3</sup> = 40</i>					
313.15	10.45434	7.92245	0.24010	0.27729	0.43056
318.15	10.18292	8.29689	0.23909	0.27790	0.45275
<i>C/kg·m<sup>-3</sup> = 60</i>					
313.15	10.45669	7.92054	0.24025	0.27741	0.43054
318.15	10.18542	8.29437	0.23921	0.27799	0.45269
<i>C/kg·m<sup>-3</sup> = 80</i>					
313.15	10.45817	7.91948	0.24040	0.27754	0.43055
318.15	10.18801	8.29198	0.23935	0.27810	0.45265
<i>C/kg·m<sup>-3</sup> = 100</i>					
313.15	10.45990	7.91824	0.24083	0.27799	0.43056
318.15	10.18898	8.29098	0.23991	0.27873	0.45262
<i>AC + THF</i>					
<i>C/kg·m<sup>-3</sup> = 0</i>					
313.15	10.45051	7.92588	0.24062	0.27797	0.43064
318.15	10.17763	8.30205	0.23916	0.27811	0.45286
<i>C/kg·m<sup>-3</sup> = 20</i>					
313.15	10.45092	7.92543	0.24062	0.27797	0.43062
318.15	10.17859	8.30105	0.23916	0.27809	0.45283
<i>C/kg·m<sup>-3</sup> = 40</i>					
313.15	10.45168	7.92446	0.24063	0.27797	0.43056
318.15	10.17952	8.29973	0.23917	0.27809	0.45276
<i>C/kg·m<sup>-3</sup> = 60</i>					
313.15	10.45298	7.92295	0.24064	0.27797	0.43048
318.15	10.18152	8.29705	0.23918	0.27809	0.45262
<i>C/kg·m<sup>-3</sup> = 80</i>					
313.15	10.45462	7.92092	0.24064	0.27796	0.43037
318.15	10.18332	8.29461	0.23919	0.27808	0.45249
<i>C/kg·m<sup>-3</sup> = 100</i>					
313.15	10.45651	7.91871	0.24066	0.27796	0.43026
318.15	10.18523	8.29207	0.23922	0.27809	0.45236

Fitting parameters  $A_i$  and absolute average percentage deviation results are reported in Table 6 for binary AC in THF mixtures at all temperatures studied.

**Table 6.** Fitting Parameters  $A_i$ , Correlation Coefficient ( $R^2$ ) Obtained for Density  $\rho$ , Ultrasonic Speed  $c$ , Isentropic Compressibility  $k_s$  and Relaxation Strength  $r$  Along with the Absolute Average Percentage Deviation (AAD %) for Binary (xGnP) and (AC) in THF Mixtures.<sup>a</sup>

$T/K$	$C/kg\cdot m^{-3}$	$A_1/kg\cdot m^{-3}$	$A_2/kg^0\cdot m^0$	$A_3/kg^{-1}\cdot m^3$	$R^2$	AAD %
<i>xGnP + THF</i>						
$\rho/kg\cdot m^{-3}$						
313.15	0-100	865.61	0.0068429	0.0000036	0.99786	0.002
318.15	0-100	859.96	0.0105036	-0.0000259	0.99488	0.002
$T/K$	$C/kg\cdot m^{-3}$	$A_1/kg^0\cdot m^{-1}\cdot s$	$A_2/kg\cdot m^{-4}\cdot s$	$A_3/kg^2\cdot m^{-7}\cdot s$	$R^2$	AAD %
$c/m\cdot s^{-1}$						
313.15	0-100	1207.30	0.002825	-0.000021	0.99279	0.000
318.15	0-100	1183.49	0.003711	-0.000010	0.99263	0.001
$T/K$	$C/kg\cdot m^{-3}$	$A_1$	$A_2$	$A_3$	$R^2$	AAD %
$n_D$						
313.15	0-100	1.39662	-0.000038562	0.000000426	0.98242	0.117
318.15	0-100	1.39399	-0.000018614	0.000000307	0.95877	0.088
$T/K$	$C/kg\cdot m^{-3}$	$A_1/10^{10}\cdot kg^0\cdot m^2\cdot N^{-1}$	$A_2/10^{-9}\cdot kg^{-1}\cdot m^5\cdot N$	$A_3/10^{-9}\cdot kg^{-2}\cdot m^8\cdot N^{-1}$	$R^2$	AAD %
$k_s/10^{-10}\cdot m^2\cdot N^{-1}$						
313.15	0-100	7.92586	-0.000997	0.000020	0.997669	0.002
318.15	0-100	8.30219	-0.001534	0.000004	0.996496	0.002
$T/K$	$C/kg\cdot m^{-3}$	$A_1/kg^0\cdot m^0$	$A_2/kg^{-1}\cdot m^3$	$A_3/kg^2\cdot m^{-6}$	$R^2$	AAD %
$r$						
313.15	0-100	0.43064	-0.000002825	0.000000021	0.99279	0.001
318.15	0-100	0.45287	-0.000003287	0.000000008	0.99157	0.001
<i>AC + THF</i>						

$T/K$	$C/kg\cdot m^{-3}$	$A_1/kg\cdot m^{-3}$	$A_2/kg^0\cdot m^0$	$A_3/kg^{-1}\cdot m^3$	$R^2$	AAD %
$\rho/kg\cdot m^{-3}$						
313.15	0-100	865.61	0.0004339	0.0000165	0.99838	0.009
318.15	0-100	859.97	0.0018929	0.0000054	0.99180	0.011
$T/K$	$C/kg\cdot m^{-3}$	$A_1/kg^0\cdot m^{1\cdot s}$	$A_2/kg\cdot m^{-4}\cdot s$	$A_3/kg^2\cdot m^{-7}\cdot s$	$R^2$	AAD %
$c/m\cdot s^{-1}$						
313.15	0-100	1207.30	0.000782	0.000033	0.99868	0.010
318.15	0-100	1183.49	0.002130	0.000035	0.99364	0.017
$T/K$	$C/kg\cdot m^{-3}$	$A_1$	$A_2$	$A_3$	$R^2$	AAD %
$n_D$						
313.15	0-100	1.39663	0.000000325	0.000000004	0.98879	0.0002
318.15	0-100	1.39392	-0.000000209	0.000000013	0.99135	0.0002
$T/K$	$C/kg\cdot m^{-3}$	$A_1/10^9\cdot kg^0\cdot m^2\cdot N^{-1}$	$A_2/10^{-9}\cdot kg^{-1}\cdot m^5\cdot N^{-1}$	$A_3/10^{-9}\cdot kg^{-2}\cdot m^8\cdot N^{-1}$	$R^2$	AAD %
$k_s/10^{10}\cdot m^2\cdot N^{-1}$						
313.15	0-100	7.92592	-0.000014486	-0.000000582	0.99943	0.001
318.15	0-100	8.30217	-0.000048339	-0.000000544	0.99613	0.002
$T/K$	$C/kg\cdot m^{-3}$	$A_1/kg^0\cdot m^0$	$A_2/kg^{-1}\cdot m^3$	$A_3/kg^{-2}\cdot m^{-6}$	$R^2$	AAD %
$r$						
313.15	0-100	0.43064	-0.000000998	-0.000000029	0.99836	0.001
318.15	0-100	0.45287	-0.000001925	-0.000000033	0.99373	0.003

$$^a A_i \text{ and } R^2 \text{ were obtained from Eq. 7; AAD \% : } AAD(Y) = \frac{100}{N} \sum_i^n \left| \frac{Y_{Expt.} - Y_{Calc.}}{Y_{Expt.}} \right|,$$

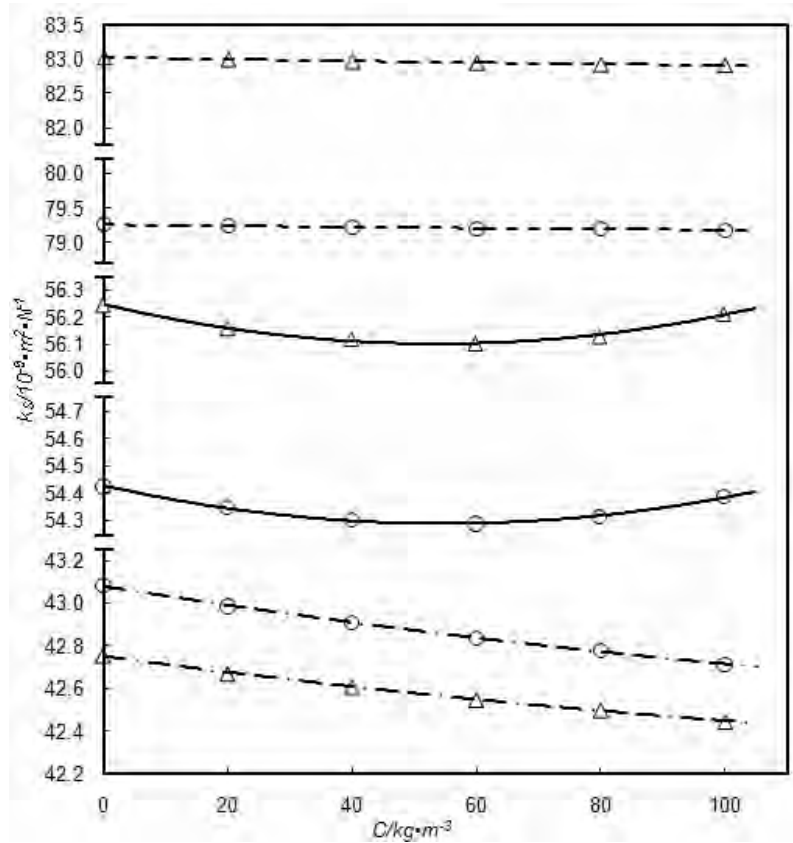
where N = 6 number of experimental data at each temperature.

The behaviour of the isentropic compressibility on the concentration of the xGnP solute is illustrated in Figure 4.

The computed values of the isentropic compressibility of xGnP dispersion in THF decrease by increasing xGnP composition.

As shown in Figure 4, the isentropic compressibility of the xGnP + DMF mixture decreases by increasing the solute concentration up to 60 kg·m<sup>3</sup>, then increases up to 100 kg·m<sup>3</sup> xGnP composition.

The values of the refractive index of xGnP in water mixture decrease by increasing xGnP composition and vary according to the relation: xGnP + H<sub>2</sub>O < xGnP + DMF < xGnP + THF in binary mixtures.



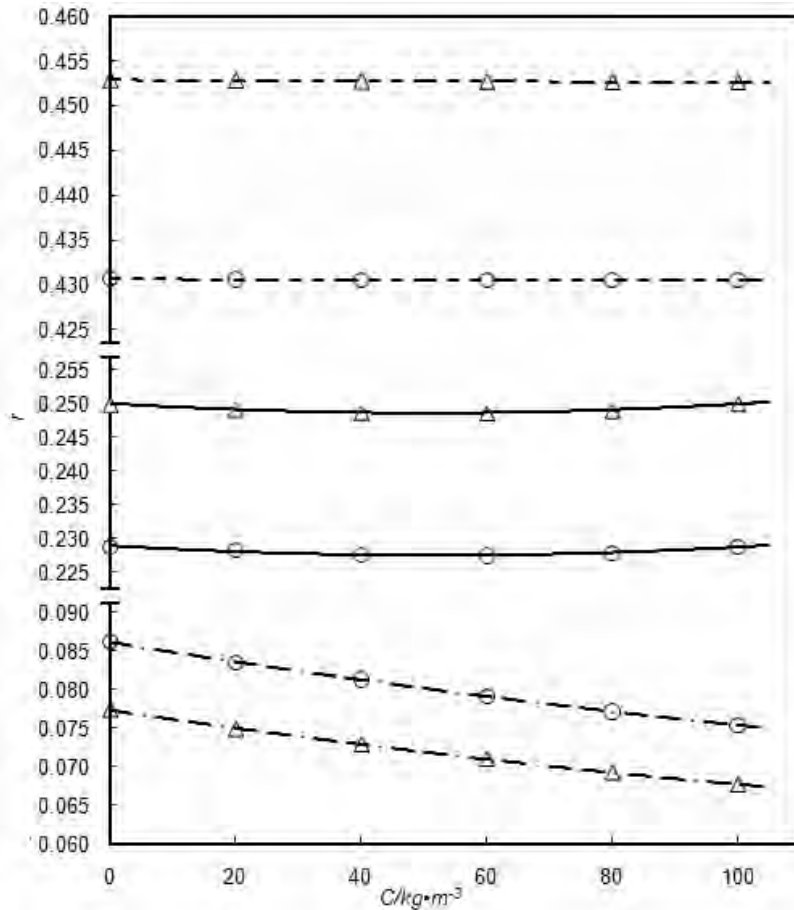
**Fig. 4.** Comparative representation of the isentropic compressibility of binary xGnP + THF, xGnP + H<sub>2</sub>O [12] and xGnP + DMF [14] systems versus concentration of solute at various temperatures, T/K: ○, 313.15; △, 318.15; - - -, for THF; —, for DMF; , H<sub>2</sub>O - polynomial correlated values.

The relaxation strength behaviour on the temperature of the three systems shows differences, as evidenced in Fig. 5.

The relaxation strength results in the xGnP + THF mixture decrease by increasing the xGnP concentration up to 60 kg·m<sup>3</sup>, then increase up to C = 100 kg·m<sup>3</sup> for the temperature of 313.15 K; for a temperature of 318.15 K the values of the relaxation strength decrease by increasing xGnP composition, as seen from Fig. 5.

The calculated relaxation strength values of xGnP dispersion in DMF decrease by increasing xGnP composition up to C = 60 kg·m<sup>3</sup>, then increase up to 100 kg·m<sup>3</sup> xGnP concentration.

The values of the relaxation strength of xGnP in water mixture decrease by increasing xGnP composition.



**Fig. 5.** Comparative representation of the relaxation strength of binary xGnP + THF, xGnP + H<sub>2</sub>O [12] and xGnP + DMF [14] systems versus concentration of solute at various temperatures, T/K: ○, 313.15; △, 318.15; ---, for THF; —, for DMF; ○, △, H<sub>2</sub>O-polynomial correlated values.

In the xGnP + THF binary mixture, the relaxation strength decreased as in the xGnP + H<sub>2</sub>O system. The relaxation strength variation in xGnP + DMF decreased up to a solute composition of 60 kg·m<sup>3</sup> and increased after by increasing the solute concentration, suggesting the predominance of molecular interactions [26].

In the xGnP + THF and xGnP + H<sub>2</sub>O binary mixtures, the relaxation strength increased by increasing the temperature and decreased by increasing the concentration. As the composition of THF, DMF, and water gradually increased, various interactions such as H-bonding, dipole-dipole and dipole induced dipole

interactions occurred between molecules.

The effect of the studied THF, DMF, and H<sub>2</sub>O solvents used for dispersing increasing concentrations of exfoliated graphite nanoplatelets vary in the following order: THF < DMF < H<sub>2</sub>O for the density and speed of sound, H<sub>2</sub>O < THF < DMF for the refractive index, and H<sub>2</sub>O < DMF < THF for the isentropic compressibility and relaxation strength.

The rise of temperature has a significant effect on increasing the isentropic compressibility and relaxation strength of binary xGnP + DMF and xGnP + THF dispersions. Water solvent decreased the isentropic compressibility and relaxation strength in the xGnP + H<sub>2</sub>O blend by increasing temperature.

The presence of oxygenated functional groups reduces the micro pore volume accessible to THF and H<sub>2</sub>O molecules and does not affect the micro pore volume accessible to DMF molecules.

#### 4. Conclusions

In the present work there were measured the densities, speeds of sound, and refractive index of the exfoliated graphite nanoplatelets and active carbon dispersions in tetrahydrofuran, over the whole composition range at temperatures of (313.15 and 318.15) K.

The characterization of the graphene-based nanomaterials dispersed in three different solvents, based on the experimental results of some thermodynamic parameters was investigated by comparison.

The effect of different solvents over increasing concentrations of dispersed exfoliated graphite nanoplatelets vary as follows: THF < DMF < H<sub>2</sub>O for the density and speed of sound, H<sub>2</sub>O < THF < DMF for the refractive index, and H<sub>2</sub>O < DMF < THF for the isentropic compressibility and relaxation strength.

The obtained results show that the studied physicochemical parameters depend on mixture compositions, which could be an indicative type and strength of molecular interactions in the studied solutions.

**Acknowledgments.** The present study was carried out within the research programme Chemical Thermodynamics of “Ilie Murgulescu” Institute of Physical Chemistry, which was financed by the Romanian Academy of Sciences. Support from the EU (ERDF) and Romanian Government, which allowed for the acquisition of the research infrastructure under POS-CCE O 2.2.1 project INFRANANOCHEM - Nr. 19/01.03.2009 is gratefully acknowledged.

#### References

- [1] A.B. BOURLINOS, V. GEORGAKILAS, R.ZBORIL, T.A. STERIOTIS, A.K. STUBOS, *Liquid-Phase Exfoliation of Graphite Towards Solubilized Graphenes*, Small **5**, pp. 841 – 1845, Aug., 2009.

- [2] M. TAGAWA, M. IKEMURA, Y. NAKAYAMA, Y. OHMAE, *Effect of Water Adsorption on Microtribological Properties of Hydrogenated Diamond-Like Carbon Films*, Tribol. Lett. **17**, pp. 575- 580, Oct., 2004.
- [3] C.M. WHITE, D.H.SMITH, K.L. JONES, A.L. GOODMAN, S.A. JIKICH, R.B. LAKOUNT, S.B. DU BOSE, E. OZDEMIR, B.I. MORSI, K. T. SCHROEDER, *Sequestration of Carbon Dioxide in Coal with Enhanced Coalbed Methane Recovery – A Review*, Energy Fuels **19**, pp. 659 -724, Mar., 2005.
- [4] J.N. COLEMAN, *Liquid-Phase Exfoliation of Nanotubes and Graphene*, Adv. Funct. Mater. **19**, pp. 3680-3695, Nov., 2009.
- [5] C.J. SHIH, S. C. LIN, M. S. STRANO, D. BLANKSCHTEIN, *Understanding the stabilization of liquid-phase-exfoliated graphene in polar solvents: molecular dynamics simulations and kinetic theory of colloid aggregation*, J. Am. Chem. Soc. **132** (41), pp. 14638-14648, 2010.
- [6] M.S. STRANO, V.C. MOORE, M.K. MILLER, M.J. ALLEN, E.H. HAROZ, C. KITTRELL, *The role of surfactant adsorption during ultrasonication in the dispersion of single-walled carbon nanotubes*, NanoSci. Nanotechnol. **39** (3), pp. 81-86, 2003.
- [7] C.E. HAMILTON, J.R. LOMEDA, Z.Z. SUN, J.M. TOUR, A.R. BARRON, *High-Yield Organic Dispersions of Graphene*, Nano Lett. **9**, pp. 3460-3462, 2009.
- [8] L.D. BELYAKOVA, A.V. KISELEV, N.V. KOVALEVA, *Gas-chromatographic determination of isotherms and heats of adsorption of water benzene and methanol vapours on graphitised carbon black*, Russ. J. Phys. Chem., Ussr. **42**(9), pp. 1204-1208, 1968.
- [9] Y. HERNANDEZ, M. LOTYA, D. RICKARD, S.D. BERGIN, J.N. COLEMAN, *Measurement of multicomponent solubility parameters for graphene facilitates solvent discovery*, Langmuir **26**, pp. 3208-3213, Mar., 2010.
- [10] A. STRIOLO, A.A. CHAILVO, P.T. CUMMINGS, K.E. GUBBINS, *Water adsorption in carbon-slit nanopores*, Langmuir, **19**, pp. 8583-8591, 2003.
- [11] J.C. LIU, P. A. MONSON, *Does water condense in carbon pores?*, Langmuir, **21**, pp. 10219-10225, 2005.
- [12] I. ION, F. SIRBU, A.C. ION, *Thermophysical Investigations of Exfoliated Graphite Nanoplatelets and Active Carbon in Binary Aqueous Environments at Different Temperatures*. J. Mater. Sci., **50** (2), pp. 587-598, 2015.
- [13] E. RADU, A.C. ION, F. SIRBU, *Adsorption of endocrine disruptors on exfoliated graphene nanoplatelets*. Environ. Eng. Manag. J., **14** (3), pp. 551-558, 2015.
- [14] I. ION, F. SIRBU, A.C. ION, *Density, refractive index, and ultrasound speed in mixtures of active carbon and exfoliated graphite nanoplatelets dispersed in N,N-dimethylformamide at temperatures from (293.15 to 318.15) K*. J. Chem. Eng. Data. **58**, pp. 1212–1222, 2013.
- [15] A.K. NAIN, *Densities and Volumetric Properties of Binary Mixtures of Tetrahydrofuran with Some Aromatic Hydrocarbons at Temperatures from 278.15 to 318.15 K*, J. Solution Chem., **35**, pp. 1417–1439, 2006.
- [16] R.R. MISHRA, *Measurements of the Ultrasonic Velocity for the Organic Liquids at Various Temperatures and Concentrations*, VSRD-TNTJ, **2** (9) pp., 405-412, 2011.
- [17] V. BELANDRIA, A.H. MOHAMMADI, D.RICHON, *Volumetric properties of the (tetrahydrofuran + water) and (tetra-n-butyl ammonium bromide + water) systems: Experimental measurements and correlations*, J. Chem. Thermodyn. **41**, pp. 1382–1386, 2009.
- [18] S. SINGH, I. VIBHU, M. GUPTA, J.P. SHUKLA, *Excess Acoustical and Volumetric Properties and the Theoretical Estimation of the Excess Thermodynamic Functions of Binary Liquid Mixtures*, Chinese J. Phys., **45** (4), pp. 412-424, 2007.
- [19] C. GONZALEZ, J.M. RESA, J. LANZ, M. IGLESIAS, *Intermolecular interactions in soybean oil + different organic solvents by ultrasonic velocity measurements*, J. Food Eng. **77**, pp. 152-161, 2006.

- [20] J.S. ROWLINSON, F.L. SWINTON, *Liquid and Liquid Mixtures*, Butterworths, London, 3rd. ed., 1982.
- [21] N.G. GERECZE, *Ultrasonic studies in solution of poly(ethylene glycol)*, *Acoustica*. **38**, pp. 51- 57, 1977.
- [22] G.A.C.M. SPIERINGS, G.P. MELIS, *Refractive index and density of alkali lime borogermanosilicate glasses*, *J. Mater. Sci.* **16**, pp. 1059-1062, 1981.
- [23] V.N. REDDY, K.S.W.K. RAO, M.C.S. SUBHA, K.C. RAO, Miscibility behaviour of dextrin/PVA blends in water at 35 C, International Conference on Advances in Polymer Technology, India, Feb. 26–27, pp. 356–368, 2010.
- [24] R.D. ALLEN, A new equation relating index of refraction and specific gravity, *Am. Mineralogist* **41**, pp. 245-257, 1956.
- [25] Y. LIANG, D. WU, X. FENG, K. MULLER, *Dispersion of Graphene Sheets in Organic Solvent Supported by Ionic Interactions*, *Adv. Mater.* **21**, pp. 1679-1683, 2009.
- [26] D.R. DREYER, S. PARK, C.W. BIELAWSKI, R.S. RUOFF , *The chemistry of graphene oxide*, *Chem. Soc. Rev.* **39**, pp. 228-240, 2010.



# Development of an Aptasensor for Lysozyme Based on Graphene Oxide Through the Layer-by-Layer Method

Alina VASILESCU, Alis VEZEANU, Sorin DAVID, Szilveszter GASPAR

International Centre of Biodynamics, 1 B Intrarea Portocalelor,  
sector 6, 060101, Bucharest, Romania  
E-mail: avasilescu@biodyn.ro

**Abstract.** This work investigates the use of graphene oxide for developing biosensors, appropriate for optical (by Surface Plasmon Resonance-SPR) and electrochemical detection. A polycationic polymer, poly(diallyldimethylammonium-PDDA) and graphene oxide (GO) were deposited on gold interfaces by a layer-by-layer (LBL) approach to obtain PDDA/GO coated sensors. Functionalisation with a lysozyme aptamer by 2 different methods (through avidin-biotin affinity binding and covalent immobilisation by carbodiimide chemistry) was demonstrated to produce biosensors, that can sensitively detect lysozyme. The short time required and the easiness of coating by the described LBL method, recommend GO as a good alternative to self-assembled monolayers, previously investigated with lysozyme aptasensors.

## 1. Introduction

Graphene oxide, the oxidised form of graphene, is a single layer of carbon arranged in a honeycomb-like lattice, that presents oxygen-containing functional groups such as hydroxyl, epoxide, carbonyl and carboxylic groups. It is obtained from graphite by exfoliation with strong oxidizing agents. (*e.g* potassium permanganate and sulfuric acid as per Hummer's method [1]). Due to its high content of oxygen-containing species, graphene oxide is hydrophilic and therefore easily dispersed in water. By chemical or electrochemical reduction, graphene oxide may be transformed into reduced graphene oxide which displays very different electrical and optical properties. Due to its hydrophilic character, the high surface-to-volume ratio and oxygen functional groups contained that can facilitate immobilisation of biomolecules, graphene oxide was a preferred material in recent years for developing biosensors with both optical and electrochemical detection [2-5].

Biosensors, combinations between a biorecognition element able to specifically bind or convert the target analyte and a physical transducer, hold great

promise as better (*i.e* faster, easier, cheaper, more sensitive) alternatives to classic detection methods for many analytes. One example of analyte for which various biosensors have been developed so far is lysozyme, a small protein of 14 kDa with complex biochemical and functional properties, relevant for both human health and food safety. Increased levels of human lysozyme in serum and urine are associated with kidney diseases, while lysozyme extracted from hen-egg white is allowed to use in food industry in wines, cheese, sausages etc. as an antimicrobial or fining agent. Hen-egg lysozyme being an allergen, its presence in small quantities in food matrices needs to be sensitively detected.

In this work we investigated the utility of graphene oxide in the development of a biosensor for lysozyme that could be interrogated by Surface Plasmon Resonance or electrochemical methods. More specifically, gold interfaces were coated with a graphene oxide layer that served further for immobilisation of the biorecognition element, the lysozyme aptamer. Aptamers are nucleic acid selected *in vitro* to bind specifically a selected ligand. They are increasingly used in biosensors due to their stability, ease of production and further modification with functional groups, fluorescent and redox labels etc. [6]. Our group has previously developed aptasensors with SPR detection for lysozyme, based on Au interfaces covered with self-assembled monolayers (SAMs) of thiols [7-9]. While convenient, SAMs present some disadvantages related to long –term stability, therefore we investigate whether replacing SAMs with GO could yield better modified surfaces for use in biosensors or not. To deposit GO on gold, we use a layer-by-layer approach, which consists in alternating layers of oppositely charged components that exhibit attractive forces between them [10.] This versatile approach allows to obtain multilayer coatings with controlled composition, thickness and functionality, being very useful for the development of biosensors [11]. Here we report modification of Au interfaces by successive immersion in a polycationic polymer, poly(diallyldimethylammonium) (PDDA) and graphene oxide for controlled time. PDDA is a polyelectrolyte that displays strong electron withdrawing capacity due to positively charged nitrogen ( $N^+$ ) in its chemical structure. It adsorbs strongly and transfers electrons from C atoms in graphene. After obtaining interfaces modified with PDDA/GO using the LBL method, we studied their applicability in electrochemical and SPR biosensors and investigated two strategies for immobilising an aptamer as biorecognition element. The performances of aptamer-PDDA/GO-Au sensors were compared to those of similar sensors developed by our group, based on SAM- coated Au interfaces.

## **2. Material and Methods**

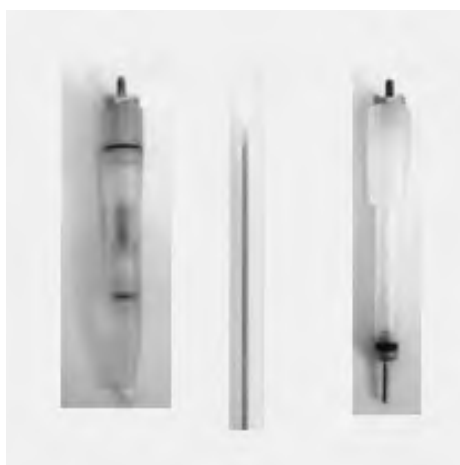
### **2.1. Reagents**

Graphene oxide was kindly provided by Professor Sabine Szunerits from Interdisciplinary Research Institute, Lille, France. It was synthesized from graphite

by a modified Hummer's method [12]. The lysozyme aptamer with the sequence 5'-/5-Biosg\_TTT TTT TTT TTT TTT TTT GCA GCT AAG CAG GCG GCT CAC AAA ACC ATT CGC ATG CGG C-3' was purchased from Integrated DNA Technologies, Belgium. Neutravidin was purchased from Pierce, hydrogen peroxide was purchased from Carl Roth and potassium hexacyanoferrate (III) from Merck. Hen-egg lysozyme, PDDA and all other reagents were from Sigma-Aldrich, Germany. Glassy carbon electrodes were from BAS.

## 2.2. Electrochemical Studies

Electrochemical measurements were performed using a potentiostat/galvanostat VSP (Bio-Logic S.A, France), equipped with the EC-Lab software EC-Lab and a conventional 3-electrode setup that includes a gold wire with a surface of 0.378 cm<sup>2</sup> as working electrode, a Ag/AgCl (3M) reference electrode and a Pt counter electrode (Fig. 1).



**Fig. 1.** The 3-electrode system used for electrochemical testing includes a gold wire as working electrode, a Ag/AgCl (3M) reference electrode and a Pt counter electrode.

Au electrodes were immersed for 10 minutes in a 1:1 mixture of 0.5 M KOH: H<sub>2</sub>O<sub>2</sub>, followed by rinsing with water. An electrochemical cleaning was next carried out by cyclic voltammetry in 0.5 M H<sub>2</sub>SO<sub>4</sub> (from -0.4 to +1.6 V with a scan rate of 100 mV/s, for at least 15 cycles) until the typical voltammogram of clean gold was observed.

## 2.3. Surface Plasmon Resonance Studies

The Surface Plasmon Resonance (SPR) studies were performed using a SPREETA system (Nomadics Inc. USA) connected to a syringe pump and a

computer for data acquisition and processing [13]. A 2-channel PDMS (polydimethylsiloxane Sylgard 184, Dow Corning, USA) flow cell was fitted to the SPR system. The system is controlled by a Labview-based software developed at the International Centre of Biodynamics, Bucharest. Measurements were performed in 20 mM MES buffer pH 6 with 50 mM NaCl, 1 mM MgCl<sub>2</sub> and 0.05% Tween-20. The Au interfaces used for SPR testing were fabricated at the International Centre of Biodynamics, Bucharest by Physical Vapour Deposition and consist in a 50 nm Au layer deposited on glass with a 3 nm titanium adhesion layer. Prior to modification with PDDA and GO the interfaces were cleaned by overnight immersion in a 1:10 hypochlorite aqueous solution, followed by 10 minutes in a 1:1 0.5 M KOH: 30% H<sub>2</sub>O<sub>2</sub> mixture, and final cleaning for 10 min in a 0.5 M NaBH<sub>4</sub> solution (prepared in a 1:1 mixture of water and ethanol). Between these steps and at the end of cleaning, the gold chips were washed with Millipore water and then dried under a gentle stream of nitrogen.

#### ***2.4. Atomic Force Microscopy Studies***

Atomic Force Microscopy (AFM) images were obtained using a Nanowizard II instrument (from JPK Instruments AG), silicon PPP-NCSTPt cantilevers (resonance frequency 76-263 kHz, force constant 1.2 – 29 N/m, from Nanosensors) and intermittent contact mode in air (setpoint ~ 690 mV, line rate 0.8 Hz). The lines of the AFM images were corrected by matching height median using Gwyddion software (version 2.26).

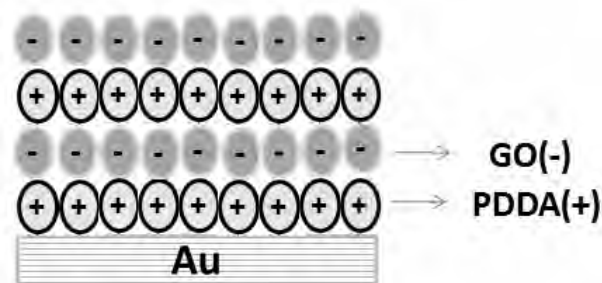
#### ***2.5. Production of LBL Modified Interfaces with GO for Electrochemical and SPR Testing***

The Au interfaces (SPR chips and electrodes) were immersed alternatively in 5 % PDDA solutions in 0.1M NaCl and in 0.2 mg/mL solutions of GO in water (30 minutes in each solution each time). Between switching to the next solution the interfaces were rinsed with water and dried under a nitrogen stream.

### **3. Results and Discussion**

#### ***3.1. Deposition of GO on Au Through the Layer-by-Layer Method and Characterisation by SPR and Electrochemical Methods***

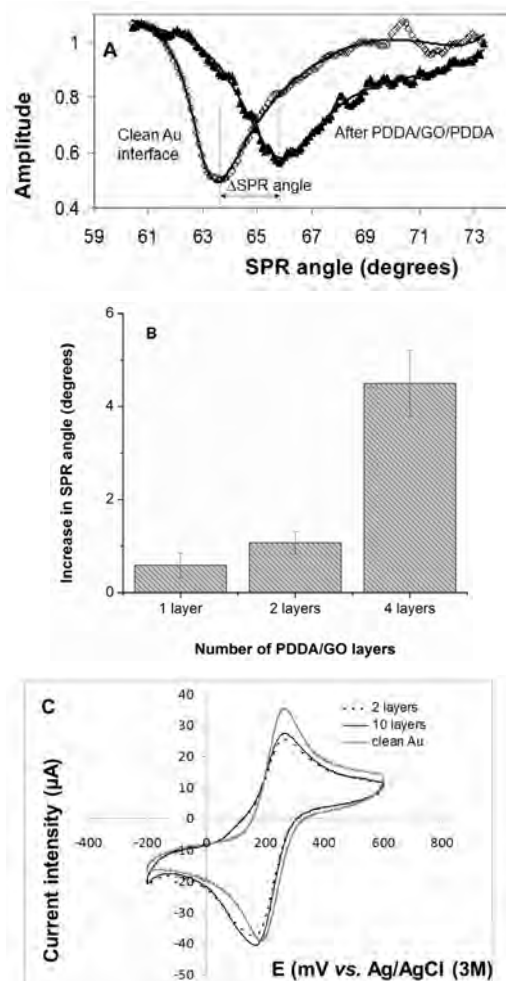
The gold interface coated with GO by the LBL approach is presented schematically in Fig. 2.



**Fig. 2.** Schematic representation of a surface coated with GO through LBL method, using alternating layers of PDDA and GO.

Deposition of consecutive layers of PDDA and GO was observed through the change in the reflectivity curve in SPR, the curve becoming broader and the minimum of the curve (the “dip”) moving to higher SPR angles (Fig. 3 A): These effects were more pronounced as the number of layers increased (Fig. 3 B).

With graphene-modified SPR interfaces, a compromise must be reached between the increase in adsorption and immobilisation capacity for biomolecules, brought by an increased GO content and the decrease in sensitivity associated with thicker deposits, due to the SPR curve broadening as emphasized in Fig. 3A. Initial studies concerning the influence of the number of PDDA/GO layers on the sensitivity for lysozyme testing did not reveal a substantial improvement when modifying the Au interfaces with more than 2 layers of PDDA/GO. Additionally, Au electrodes coated with 2, 4, 6, 8 and respectively 10 layers of PDDA/GO were analysed by electrochemistry to probe their differences with respect to charge transfer, using ferricyanide as electrochemical redox probe. Compared to clean gold electrodes, for those modified with 2-10 layers of PDDA/GO the intensity of the anodic peaks of ferricyanide diminishes and the separation between the anodic and cathodic peaks increases from  $93 \pm 1.6$  mV for a clean electrode to 107-109 mV for PDDA/GO-Au electrodes (Fig. 3C). This proves a slower electron transfer at the interface of PDDA/GO coated electrodes compared to clean gold. However, current intensity remains still high enough and appropriate for developing electrochemical biosensors. Increasing the number of deposited layers does not bring a dramatic modification in electron-transfer abilities proved with the ferricyanide probe. Consequently, considering both the results from SPR and electrochemical testing, all interfaces used in further experiments were modified with 2 layers of PDDA/GO.

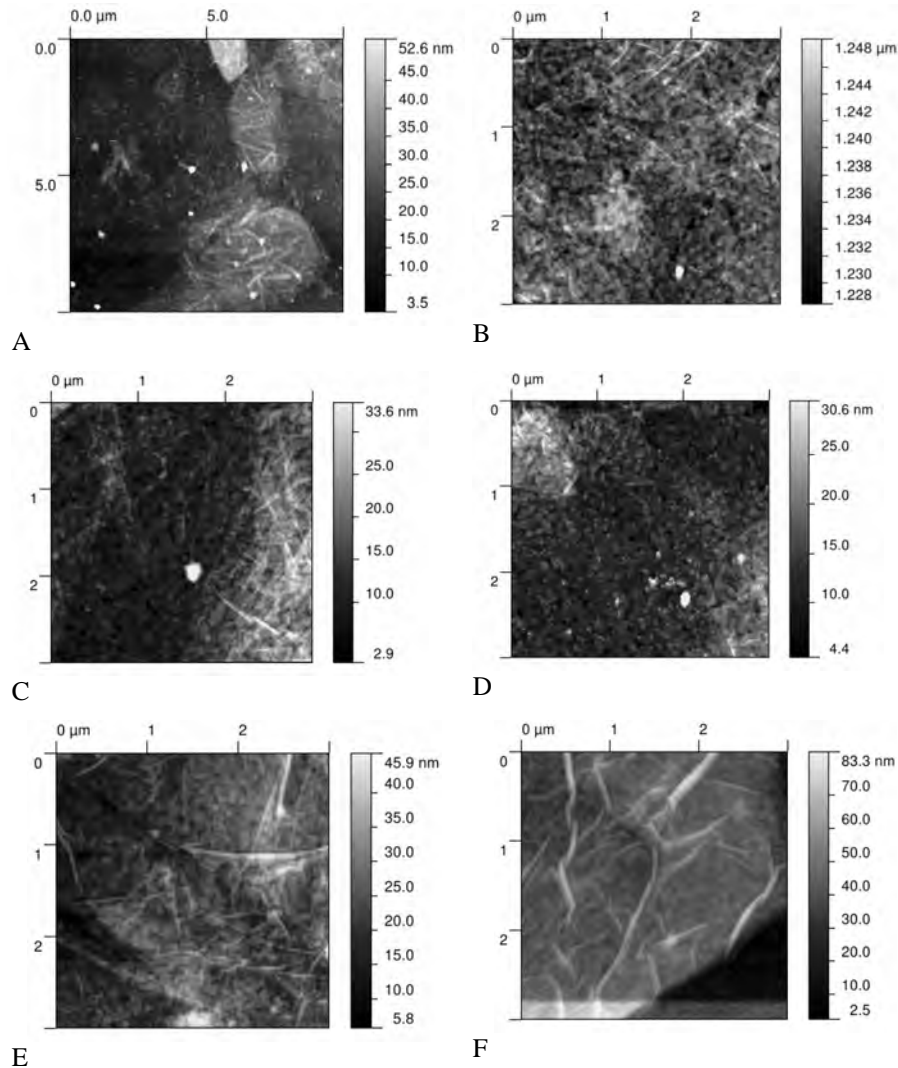


**Fig. 3.** A: Changes in the SPR reflectivity curve of clean Au after modification with PDDA/GO. B: Net variation of the angle corresponding to SPR minimum, after depositing various numbers of PDDA/GO layers on clean Au interfaces. C: Cyclic voltammograms obtained with 1 mM  $K_3[Fe(CN)_6]$  in 0.1 M KCl for clean Au electrodes and electrodes modified with 2, respectively 10 layers of PDDA/GO.

### 3.2. AFM Study of Au Interfaces Coated with PDDA/GO

Gold interfaces modified with PDDA/GO by the LBL method were investigated by Atomic Force Spectroscopy. By scanning large areas, *e.g.*  $10\ \mu\text{m} \times 10\ \mu\text{m}$  it is observed that most of the surface of the sensor is covered with GO flakes of different lateral dimension and thickness (Fig. 4A). The different thickness of the GO flakes was confirmed by scanning smaller areas, of  $3\ \mu\text{m} \times 3\ \mu\text{m}$ . While thin GO flakes (see Figs. 4B to 4D) do not “cover” the topography of

the PDDA-modified gold, thick GO flakes (see Figs. 4E and 4F) “cover” well the topography of the substrate and display more pronounced “wrinkles”.

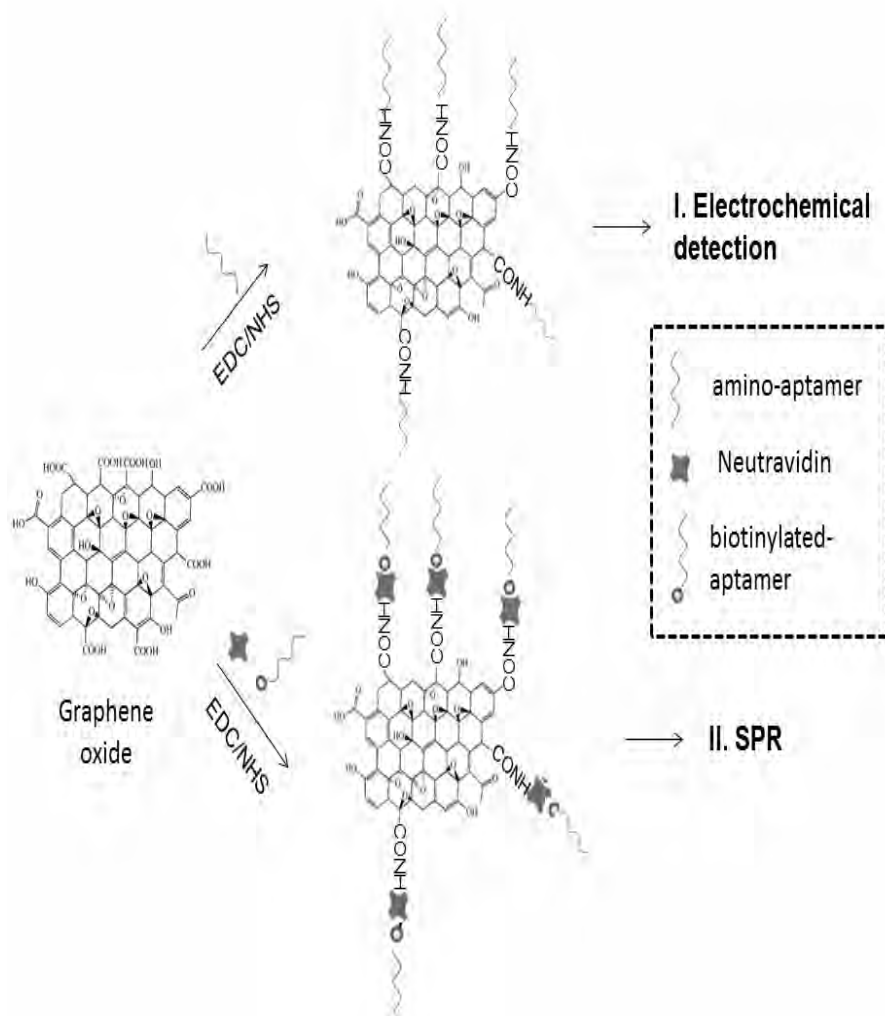


**Fig. 4.** AFM images of the PDDA and GO modified surfaces. A:  $10\ \mu\text{m} \times 10\ \mu\text{m}$  scans showing that most of the surface of the sensor is covered with GO flakes of different lateral dimension and thickness. B-F:  $3\ \mu\text{m} \times 3\ \mu\text{m}$  scans emphasizing the different thickness of the GO flakes from thin GO flakes (B to D) to thick GO flakes (E and F).

Thus, AFM tests confirm the successful and relatively homogeneous modification of Au interfaces with GO by the LBL approach.

### 3.3. Design of Aptasensors Based on PDDA/GO-Au for Electrochemical and SPR Detection of Lysozyme

To investigate the usefulness of PDDA-GO coated Au interfaces for the development of biosensors, we studied two immobilisation strategies for lysozyme aptamer and two detection methods. One aptasensor was obtained by immobilising the aptamer covalently on the PDDA/GO-Au and was used in electrochemical detection of lysozyme. In the second sensor, lysozyme aptamer was immobilised by avidin-biotin affinity and the obtained aptasensor was used for SPR measurements, as illustrated schematically in Fig. 5.



**Fig. 5.** Design of lysozyme aptasensors based on PDDA/GO-Au featuring two aptamer immobilisation strategies and two detection methods.



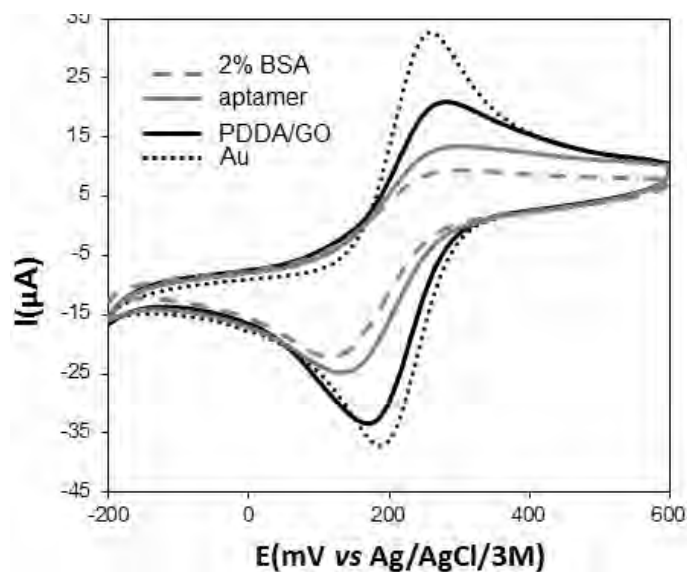
Furthermore, the two aptasensors obtained were evaluated with respect to their response to lysozyme.

### 3.4. Electrochemical Studies

To build an aptasensor starting from the PDDA/GO-Au electrodes, there are various functionalisation possibilities, including adsorption of aptamer (through  $\pi$ - $\pi$  interaction with GO), covalent or affinity immobilisation. A simple approach for efficient covalent immobilisation of aptamer is to use an amine-ended aptamer and immobilise it using classic carbodiimide chemistry, by taking advantage of the carboxyl groups in GO. This strategy was followed here.

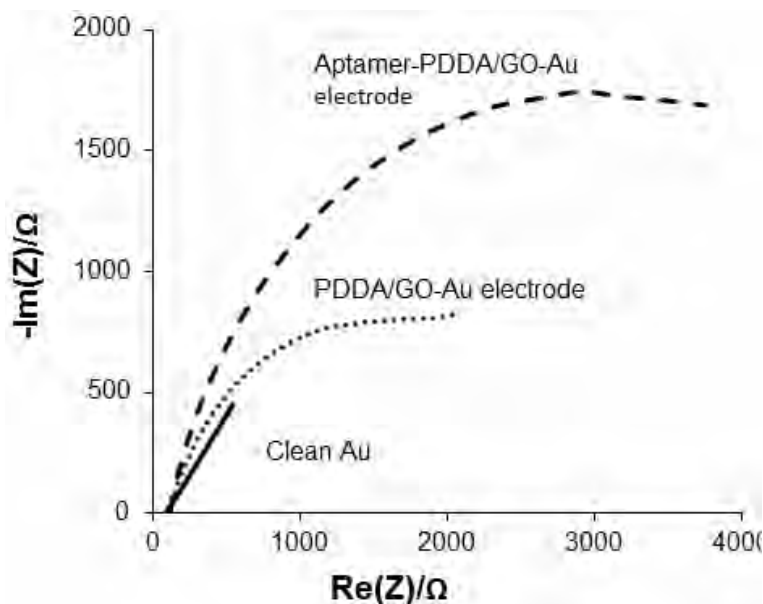
#### 3.4.1. Functionalization of the sensor with lysozyme aptamer

Lysozyme aptamer having an amine group at the 5' end was immobilised on the surface of PDDA/GO-Au by classic carbodiimide chemistry, by taking advantage of the carboxyl groups in GO. After grafting the aptamer, the sensor was immersed for 1 hour in 2% BSA to block non-specific adsorption. Cyclic voltammetry and electrochemical impedance spectroscopy experiments were performed in order to check the effectiveness of aptamer immobilisation (Figs. 6 and 7).



**Fig. 6.** Cyclic voltammograms recorded in 1mM  $\text{K}_3[\text{Fe}(\text{CN})_6]$  in 0.1 M KCl, illustrating the various steps in the development of lysozyme aptasensor: from clean gold electrode, coating with PDDA/GO through LBL method, functionalization with lysozyme aptamer and blocking with 2% BSA. The voltammograms were recorded in the range from -200 to 600 mV vs Ag/AgCl (3M), at a scan rate of 100mV/s .

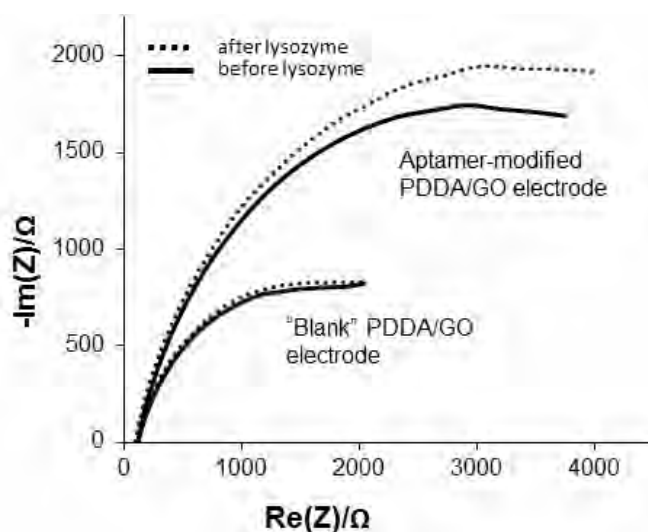
As illustrated in Fig. 6, the intensities of the anodic and cathodic peaks of the redox probe ferricyanide decrease with every step in the construction of aptasensor: clean gold > PDDA/GO-Au > aptamer-PDDA/GO-Au > BSA-aptamer-PDDA/GO-Au. In the same time, the separation between the anodic and cathodic peaks increases in the same order, thus proving a slower electron transfer with any additional modification of the Au electrode. The drastic change in electrical properties of electrode solution interface (*i.e.* the increased resistance to charge transfer) was also observed in EIS experiments (as shown in the Nyquist plots in Fig. 7).



**Fig. 7.** Nyquist plots showing the increase of the resistance to charge transfer after modifying a clean Au electrode with PDDA/GO through the LBL method, followed by further functionalisation with lysozyme aptamer by amine coupling. Measurements were performed in 10 mM  $K_3[Fe(CN)_6]$  /  $K_4[Fe(CN)_6]$  solution in 0.1 M KCl at the formal potential of  $Fe(CN)_6^{3-/4-}$  couple (0.23 V vs Ag/AgCl), in the frequency range 9.5 KHz - 1 Hz with an amplitude of 10 mV.

### 3.3.2. Testing the aptamer-modified sensor with lysozyme

To test whether the aptamer-modified PDDA/GO electrodes could potentially function as a biosensor for lysozyme, the sensors were incubated with a 10  $\mu$ g/mL lysozyme solution in 20 mM TRIS pH 7.4 with 50 mM NaCl, 1 mM  $MgCl_2$  and 0.05 % Tween 20 for 30 minutes. Figure 8 shows an example of the change in the EIS spectra for a blank and an aptamer-modified electrode respectively, after incubation with lysozyme.



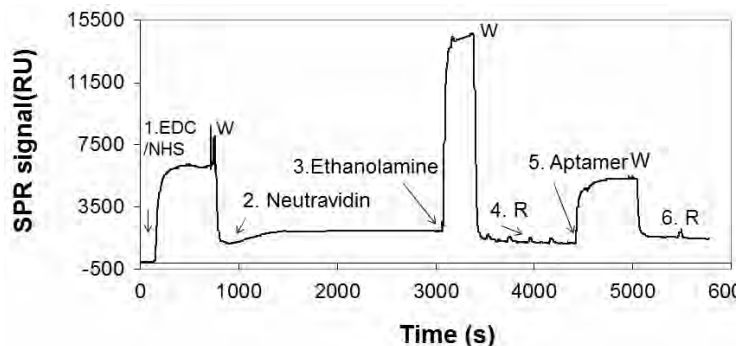
**Fig. 8.** Nyquist plots for EIS experiments with a “blank” and an aptamer-modified PDDA/GO-Au electrode respectively, before and after incubation for 30 minutes with 10  $\mu\text{g/mL}$  lysozyme in 20 mM TRIS pH 7.4 with 50 mM NaCl, 1 mM  $\text{MgCl}_2$  and 0.05 % Tween 20. Measurements were performed in 10 mM  $\text{K}_3[\text{Fe}(\text{CN})_6]$  /  $\text{K}_4[\text{Fe}(\text{CN})_6]$  solution in 0.1 M KCl at the formal potential of  $\text{Fe}(\text{CN})_6^{3-}/\text{Fe}(\text{CN})_6^{4-}$  couple (0.23 V vs Ag/AgCl), in the frequency range 9.5 KHz – 1 Hz with an amplitude of 10 mV.

The resistance to charge transfer of the aptasensor increases after incubation with lysozyme, while no significant change was observed for the blank electrode. This proves both the effectiveness of the blocking step with BSA in preventing non-specific interactions and the possibility to develop an electrochemical aptasensor for sensitive detection of lysozyme. Moreover, these results confirm the potential of PDDA/GO-Au electrodes to be used as supports for aptamer immobilisation. The aptasensor will be developed further and optimised in the future to achieve the high sensitivity that is required in applications related to the determination of lysozyme in food matrices or biological samples.

### 3.4. Surface Plasmon Resonance studies

#### 3.4.1. Functionalization of the sensor with lysozyme aptamer

Neutravidin was covalently immobilised on PDDA/GO-Au by classic amine coupling. Unreacted carboxyl groups were inactivated with ethanolamine. Next, the biotinylated aptamer was immobilised by avidin-biotin affinity binding. All steps in the sensor functionalisation process with neutravidin and aptamer were monitored by SPR (Fig. 9).

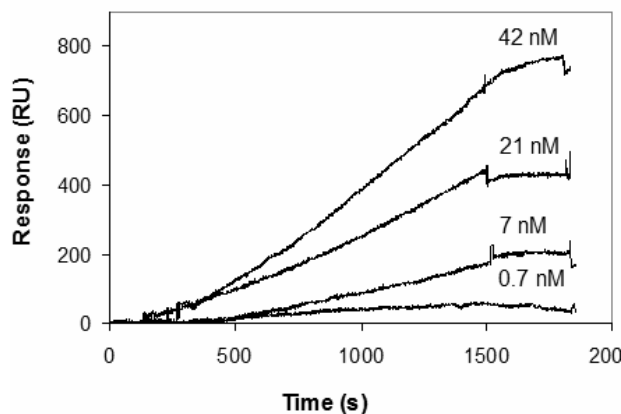


**Fig. 9.** Steps in sensor functionalisation with aptamer: activation of carboxyl groups from GO with EDC/NHS (1); immobilisation of Neutravidin (2); blocking with ethanolamine (3); regeneration (4); immobilization of biotinylated aptamer (5); regeneration (6). W=washing with water, R=regeneration with 50 mM NaOH and 0.1 M glycine pH 2.

The stability of the obtained aptasensor was tested in two common buffers, previously used with lysozyme testing [7-9]: 20 mM pH 7.4 with 100 mM NaCl, 5 mM MgCl<sub>2</sub> and 0.05% Tween and 20 mM MES pH 6 with 50 mM NaCl, 1 mM MgCl<sub>2</sub> and 0.05% Tween-20. The sensor was found to be stable for 3 days of operation in both buffers.

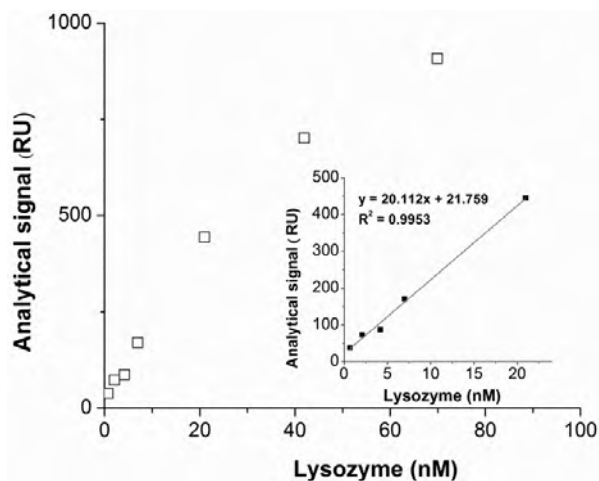
### 3.4.2. Calibration with lysozyme solutions

Calibration experiments of the aptasensor were next performed using lysozyme solutions of various concentrations in the range 0.7-70 nM (Fig. 10).



**Fig. 10.** Example of sensorgrams recorded with the PDDA/GO based aptasensor for several concentrations of lysozyme : 0.7; 2.1; 7; 21 and 42 nM. Protein solutions were circulated through the flow cell for 10 minutes at 100  $\mu$ L/min, followed by rinsing with buffer solution for 5 minutes.

The signal recorded at  $t=900$  s from the sample injection (corresponding to a 10 minutes flowing of sample solution followed by 5 minutes washing with buffer) was taken as the analytical signal and plotted against lysozyme concentration (Fig. 11).



**Fig. 11.** Calibration plot for the detection of lysozyme in buffer solutions using the PDDA/GO-based aptasensor and SPR.

The calibration plot for lysozyme emphasized a linear range from 2 to 21 nM and a detection limit of 0.7 nM. This detection limit is similar to that obtained with a graphene-coated SPR interface coated with electrophoretically-deposited graphene and with aptamer adsorbed on the surface [14].

### 3.4.3. Comparison with previously developed aptasensors

We have compared these preliminary results obtained with the aptasensor with those obtained with a previous aptasensor developed by our group, with similar design but based on Au interface coated with a SAM of thiol [9].

**Table 1.** Comparison of PDDA/GO-Au – based aptasensor with a SAM-based aptasensor [9]. The results correspond to the average of 3 replicate experiments.

Parameter	SAM-based aptasensor	PDDA/GO-Au based aptasensor
Stability in 20 mM MES pH 6 with 50 mM NaCl, 1 mM MgCl <sub>2</sub> and 0.05% Tween-20	> 3 days	> 3 days
Stability in 20 mM TRIS pH 7.4 with 100 mM NaCl, 5 mM MgCl <sub>2</sub> and 0.05% Tween-20	> 3 days	> 3 days
Immobilised neutravidin (RU)	2329 ±110	1342 ±236
Immobilised aptamer (RU)	487 ±52	351 ±101
Linear range (nM)	3.4-70 nM	2-21
Detection limit (nM)	2.4 nM	0.7

As observed from Table 1, the amount of neutravidin immobilised in the PDDA/GO aptasensor was significantly lower than that in SAM aptasensor, hence, the smaller quantity of biotinylated aptamer immobilised by (neutr)avidin-biotin affinity binding. Furthermore, the lower amount of aptamer immobilised on the sensor lead to a narrower linear range. The quantitation limit (taken as the lower limit of the calibration range) was similar for both sensors, proving the potential of PDDA/GO sensor to be applied for the sensitive quantitative detection of lysozyme. It should be emphasized here that while the SAM-based aptasensor was optimised, the results obtained with the PDDA/GO aptasensor represent preliminary data. Better characteristics might be observed by improving the aptamer immobilisation procedure and changing the operational conditions.

We have also compared the preliminary data hereby reported for the aptamer-PDDA/GO SPR sensor with other biosensors for lysozyme reported in literature (Table 2).

**Table 2.** Comparison of PDDA/GO sensor with other biosensors for lysozyme reported in literature

method	interface	LOD	Linear range	Ref
Fluorescence/	GO, aptamer + signal probe, amplification using exonuclease III	0.08 µg/mL (5.6 nM)	0.125 µg/ml to 1 µg/ml (8.7 -70nM)	15
QCM	MIP	1.2 ng/mL (0.084 nM)	0.2–1500µg/mL (0.014-105 µM)	16
EIS	Chitosan/graphene oxide	28.5	Up to 1 µg/mL (70 nM)	17
DPV	SPCE,aptamer-antibody sandwich	4.3 fM	5 fM–5 nM	19
SPR	rGO-gold, aptamer	0.5 nM	0.5-200 nM	14
EIS	GR–GCE-aptamer	6 fM	0.01–0.5 pM	19
SWV	Au NP	0.3 pg/mL (0.02 nM)	1-50 pg/mL (0.07-3.5 nM)	20
SPR	PDDA/GO-gold,aptamer	0.7 nM	2-21 nM	This work

MIP: molecularly imprinted polymer; SPCE: screen-printed carbon electrode; GCE: glassy carbon electrode; GR: electrochemically reduced graphene oxide; rGO: reduced graphene oxide.

As emphasized in Table 2, very diverse methods have been reported so far for quantitative detection of lysozyme. Some of them display exquisite sensitivity achieved by some sort of signal amplification (*e.g* with aptamer-antibody sandwiches or Au nanoparticles). Compared to literature, the aptasensor based on PDDA/GO displays good analytical characteristics that might be further improved.

#### 4. Conclusions

This work describes a LBL method for coating Au interfaces with GO, by consecutive immersions in PDDA and GO solutions. The procedure was applied to both Au wire electrodes used for electrochemistry experiments and to SPR chips,

leading in both cases to stable coatings and allowing further functionalization. The utility of PDDA/GO-Au interfaces in biosensors was demonstrated by applying two different procedures for immobilising a lysozyme aptamer and by investigations with both electrochemical and SPR detection. An aptasensor was obtained by immobilising a biotinylated aptamer to a neutravidin-modified PDDA/GO –Au interface. Even without optimisation, the aptasensor allowed reaching a detection limit of 0.7 nM lysozyme in buffer solutions using the SPR assay, similar to other lysozyme aptasensors developed by our group and others. Importantly, the LBL approach proves to be a simple and economically-efficient way of coating Au interfaces with GO, for further use in biosensors and a viable alternative to the intensively used approach of coating Au interfaces with SAMs of thiols. By optimising the sensor and operational conditions for either SPR or electrochemical detection, the analytical performances of the aptasensor based on PDDA/GO-coated gold can be further improved. We are currently pursuing more extensive characterisation of PDDA/GO coated interfaces, as well as further development and optimisation of the electrochemical and SPR aptasensors for lysozyme. The methods described here for the lysozyme aptasensor could be easily adapted for other compounds of interest.

**Acknowledgments.** AV acknowledges the financial support from Marie Curie International Reintegration Grant FP7 PEOPLE-2010-RG-277126. SD acknowledges the Romanian Executive Unit for Higher Education, Research Development and Innovation Funding for funding through Grant PN-II-RU-PD-2012-3-0467. We would like to express our gratitude to Professor Sabine Szunerits from the Interdisciplinary Research Institute, Lille, France for providing the GO used in this work.

## References

- [1] Pumera, “Graphene in biosensing”, *Materials Today*, **14**, pp. 308-315, 2011.
- [2] N-F. Chiu, T-Y Huang, H-C Lai, K-C. Liu, “Graphene oxide-based SPR biosensor chip for immunoassay applications”, *Nanoscale Research Letters*, **9**, pp. 445, 2014.
- [3] I. Kaminska, M.R. Das, Y. Coffinier, J. Niedziolka-Jonsson, J. Sobczak, P. Woisel, J. Lyskawa, M. Opallo, R. Boukherroub, S. Szunerits, “Reduction and Functionalization of Graphene Oxide Sheets Using Biomimetic Dopamine Derivatives in One Step”, *ACS Appl. Mater. Interfaces*, **4**(2), pp 1016–1020, 2012.
- [4] W.S. Hummers, R.E. Offeman, “Preparation of Graphitic Oxide”, *J. Am. Chem. Soc.* **80**, pp. 1339, 1958.
- [5] S. Szunerits, N. Maalouli, E. Wijaya, J-P. Vilcot, R. Boukherroub, Recent advances in the development of graphene-based surface plasmon resonance (SPR) interfaces, *Anal Bioanal Chem*, **405**, pp. 1435–1443, 2012.
- [6] C.K. O’Sullivan, “Aptasensors – the future of biosensing?”, *Anal. Bioanal. Chem*, **372**, pp. 44–48, 2002.

- [7] A. Vasilescu, S. Gaspar, I. Mihai, A. Tache, S.C. Litescu, "Development of a label-free aptasensor for monitoring the self-association of lysozyme", *Analyst*, **138**, pp. 3530-3537, 2013.
- [8] I. Mihai, A. Vezeanu, C. Polonschii, S. David, S. Gaspar, B. Bucur, C. Blaszykowski, S. Sheikh, M. Thompson, A. Vasilescu, "Low-fouling SPR detection of lysozyme and its aggregates", *Anal. Meth.*, **6**, pp. 7646-7654, 2014.
- [9] I. Mihai, A. Vezeanu, C. Polonschii, C. Albu, G-L. Radu, A. Vasilescu, "Label-free detection of lysozyme in wines using an aptamer based biosensor and SPR detection", *Sens. Act.s B Chem.*, **206**, pp. 198-204, 2015.
- [10] G. Decher, "Fuzzy nanoassemblies: toward layered polymeric multicomposites", *Science*, **277**, pp. 1232-1237, 1997.
- [11] J. Ma, P. Cai, W. Qi, D. Kong, H. Wang, "The layer-by-layer assembly of polyelectrolyte functionalized graphene sheets: A potential tool for biosensing", *Coll.Surf. A: Physicochem. Eng. Aspects*, **426**, pp. 6-11, 2013.
- [12] M. R. Das, R. K. Sarma, R. Saikia, V. S. Kale, M. V. Shelke and P. Sengupta, *Colloid Surf. B: Biointerfaces*, **83**, pp. 16, 2011.
- [13] C. Polonschii, S. David, S. Tombelli, M. Mascini, M. Gheorghiu, "A novel low-cost and easy to develop functionalization platform. Case study: aptamer-based detection of thrombin by surface plasmon resonance", *Talanta*, **80**, pp. 2157-2164, 2010.
- [14] P. Subramanian, A. Lesniewski, I. Kaminska, A. Vlandas, A. Vasilescu, J. Niedziolka-Jonsson, E. Pichonat, H. Happy, R. Boukherroub, S. Szunerits, "Lysozyme detection on aptamer functionalized graphene-coated SPR interfaces", *Biosens.Bioelectron.*, **50**, pp. 239-243, 2013.
- [15] C. Chen, J. Zhao, J. Jiang, R. Yu, "A novel exonuclease III-aided amplification assay for lysozyme based on graphene oxide platform", *Talanta*, **101**, pp. 357-61, 2012.
- [16] G. Sener, E. Ozgur, E. Yılmaz, L. Uzun, R. Sayc, A. Denizli, "Quartz crystal microbalance based nanosensor for lysozyme detection with lysozyme imprinted nanoparticles", *Biosens. Bioelectron.*, **26**, pp. 815-821, 2010.
- [17] E.E. A. Erdem, Chitosan graphene oxide based aptasensor for the impedimetric detection of lysozyme, *Colloids Surf. B: Biointerfaces*, **115C**, pp. 205-211, 2013.
- [18] C. Ocana, A. Hayat, R. Mishra, A. Vasilescu, M. del Valle, J.L. Marty. "A novel electrochemical aptamer-antibody sandwich assay for lysozyme detection", *Analyst*, **140**, pp. 4148-4153, 2015.
- [19] Y. Xiao, Y. Wang, M. Wu, X. Ma, X. Yang, "Graphene-based lysozyme binding aptamer nanocomposite for label-free and sensitive lysozyme sensing", *J. Electroanal. Chem.*, **702**, pp 49-55, 2013.
- [20] D. Xie, C. Li, L. Shangguan, H. Qi, D. Xue, Q. Gao, et al., "Click chemistry assisted self assembly of DNA aptamer on gold nanoparticles modified screen printed carbon electrodes for label free electrochemical aptasensor", *Sens. Actuators B:Chem.*, **192**, pp. 558-564, 2014.



# TiO<sub>2</sub> Anatase and ZnO Nanopowders Electrochemically Synthesized Involving Choline Chloride Based Ionic Liquids

Liana ANICAI, Stefania COSTOVICI, Marius ENACHESCU

Center for Surface Science and Nanotechnology, University Politehnica of Bucharest,  
Splaiul Independentei nr. 313, Bucharest, Romania

E-mail: lanicai@itcnet.ro; stefania\_costovici@yahoo.com;  
marius.enachescu@upb.ro

**Abstract.** This work presents some experimental results regarding the electrochemical synthesis of TiO<sub>2</sub> anatase and ZnO nanopowders through anodic dissolution of Ti, respectively of Zn metal in choline chloride based eutectic mixtures, also known as “deep eutectic solvents (DES)”. A detailed characterization of the obtained oxides has been performed, using various techniques, including XRD, Raman spectroscopy, XPS, SEM associated with EDX analysis and UV–vis diffuse reflectance spectra. These novel ionic media proved to be an environmentally friendly alternative with a large range of applications in materials chemistry and electrochemistry in a green synthetic strategy.

## 1. Introduction

Semiconducting oxide materials have been the subject of a great interest due to their numerous practical applications, usually related to their electronic properties, mainly depending on the nature of cation-oxygen bonding. For example, a closed-shell compound as Al<sub>2</sub>O<sub>3</sub>, is an insulator exhibiting large band-gaps. These insulators may serve as effective host materials for efficient luminescence when doped with rare earth or transition metals cations. On the other hand, for closed-shell oxides based on cations with relatively high electronegativity, such as in ZnO and SnO<sub>2</sub>, the more covalent nature of bonding yields semiconductors with relatively high carrier mobility. In addition, many oxides show interesting metal-insulator transitions dependent on the temperature (*e.g.* V<sub>2</sub>O<sub>3</sub>), pressure (*e.g.* NiO) or magnetic fields (*e.g.*, LaMnO<sub>3</sub>, SrMnO<sub>3</sub>) [1, 2].

Among these oxides, a particular interest is devoted to the fundamental

aspects and applications of semiconducting wide band-gap oxide materials, such as nanosized TiO<sub>2</sub> and ZnO, which show a wide range of electrical and optical properties. Usually, they are applied in different areas such as catalysts, sensors, photoelectron devices [3-6].

TiO<sub>2</sub> is a non-toxic, environmentally friendly semiconductor photocatalyst, frequently used in paints, white pigments and sun-blockers. Because of its large band gap (anatase: 3.2 eV; rutile: 3.0 eV), only a small UV fraction of solar light may be used for photocatalytic reactions. Extensive efforts have been made to develop titanium oxide photocatalysts that can efficiently utilize solar or indoor light, including various doping procedures with transition-metal ions or their corresponding oxides and/or non-metals [7-15]. Nanosized titania in its anatase phase possess higher photocatalytic performance as compared to other phases and its bulk counterpart [15-17]. There are reported various synthesis methods, including precipitation, microemulsion, sol-gel, as well as physical or chemical vapor deposition [2, 18, 19].

Zinc oxide (ZnO) is a wide band gap semiconductor with an energy gap of 3.37 eV. It has been used considerably for its catalytic, electrical, optoelectronic, and photochemical properties [20-23]. ZnO nanostructures have a great advantage to apply to a catalytic reaction process due to their large surface area and high catalytic activity [24]. Since zinc oxide shows different physical and chemical properties depending upon the morphology of nanostructures, not only various synthesis methods but also the physical and chemical properties of synthesized zinc oxide are to be investigated in terms of its morphology. Many methods have been described in the literature for the production of ZnO nanostructures including laser ablation [25], hydrothermal methods [26], electrochemical depositions [27], sol-gel method [28], chemical vapor deposition [29], thermal decomposition [30], by ultrasound [31], anodization [32], co-precipitation [33] and electrophoretic deposition [34]. Rodrigues-Paez *et al.* [35] synthesized zinc oxide nanoparticles with different morphologies by controlling different parameters of the precipitation process such as solution concentration, pH, and washing medium. Kumar *et al.* [3] reported the synthesis of ZnO nanostructures using a simple precipitation method, based on zinc sulfate heptahydrate and sodium hydroxide as precursors.

All above mentioned routes usually involve many steps, expensive alcoxide-precursors and equipment.

A quite novel approach adequate to prepare nanostructured metal oxide materials involving electrochemical procedures takes into account the use of ionic liquids [36-38], which are gaining wide recognition as potential environmentally benign solvents and widespread application in materials chemistry and electrochemistry in a green synthetic strategy [39-42]. Room temperature ionic liquids (RTILs or ILs) are organic salts, composed entirely of ions, with low melting points of below 100°C.

Formation of ionic liquids from eutectic mixtures of quaternary ammonium

salt, mostly used choline chloride (2-hydroxy-ethyl-trimethyl ammonium chloride), with hydrogen bond donor species such as amides, glycols or carboxylic acids [41, 43, 44] has recently been shown. These media, also known as “deep eutectic solvents (DES)” exhibit good air and water stability, they are potentially recyclable, biodegradable and bring no harm to human health. These kinds of ionic liquids represent a low cost alternative to classical ILs.

Thanks to these properties the ionic liquids have attracted considerable interest in the preparation of porous crystalline materials. Porous nano-titanium dioxide particles with anatase framework and crystallite sizes of approximately 15 nm were prepared by using *N,N*-bis [2-methylbutyl] imidazolium hexafluorophosphate ([PPim][PF6]) [45]. Farag *et al.* [46] reported the synthesis of titania in the ionic liquid 1-butyl-1-methylpyrrolidinium bis(trifluoromethylsulphonyl)amide (Py14TFSA) via sol-gel method, the nanopowder being characterized by a high thermal stability and BET surface area of 97 m<sup>2</sup>g<sup>-1</sup>. Oumahi *et al.* [47] reported the synthesis of Au/TiO<sub>2</sub> heterogeneous catalysts involving two imidazolium-based ILs (1-butyl-3-methylimidazolium hexafluorophosphate (BMIMPF6) and trifluoromethanesulfonate (BMIMOTf)) or a DES (eutectic of choline chloride and urea).

Azaceta *et al.* [48, 49] selected 1-butyl-1-methylpyrrolidinium bis(trifluoromethanesulfonyl) imide ionic liquid as reaction media at 100-150<sup>o</sup>C for the electrodeposition of ZnO based hybrid films; zinc bis(trifluoromethanesulfonyl) imide and either bubbled oxygen or *N*-butyl-*N*-methyl pyrrolidinium nitrate were used as precursors.

Harati *et al.* [50] has reported the electrochemical preparation of ZnO thin films in a deep eutectic ionic liquid based on choline chloride – urea (1:2) mixture containing zinc perchlorate as one of the precursors and Mo/glass substrate as substrate. Differential pulse voltammetry (DPV) were carried out in the above electrolyte at 90<sup>o</sup>C, in the absence and presence of oxygen. Transparent and uniform ZnO film was cathodically deposited on Mo at -1.500 V (vs. ferrocene reference) and this process was explained by reaction of zinc cations with the generated superoxide ions from reduction of dissolved oxygen; zinc oxide film can be formed through a peroxide route. The influence of the electrodeposition duration up to 120 min on the film morphology properties was investigated. UV-vis absorption spectra, EDX, XPS, Raman, and XRD results confirmed the possible of these ZnO films for applications in thin film solar cells.

Our group recently reported the successful electrochemical synthesis of TiO<sub>2</sub> anatase and ZnO nanopowders involving anodic dissolution of Ti, respectively of Zn metal in DES based electrolytes [51, 52].

Despite of the growing interest in the field of “tailor-made” inorganic materials production, very few published works were devoted to the effect of DES electrolyte on the anodic behavior of valve metals and on the morphology of the obtained oxide nanostructures. Additional information in this field may

significantly contribute to the extension of the practical applications of these systems. With this in view, this work presents some more experimental results regarding the formation of TiO<sub>2</sub> and ZnO nanopowders using anodic dissolution of Ti, respectively of Zn metal in some choline chloride based ionic liquids.

## 2. Experimental

### 2.1. Chemicals and Materials

To perform experiments, choline chloride-based ionic liquids were synthesized as shown in Table 1.

**Table 1.** Ionic liquids systems involved in TiO<sub>2</sub> and ZnO electrochemical synthesis

System type	Electrolyte composition
<i>TiO<sub>2</sub> electrochemical synthesis</i>	
ILEG - EtOH	2:1 (volume ratio) ILEG : EtOH +1-5 mM TBAB
IL - EtOH	1:1 (volume ratio) IL: EtOH + 1-5 mM TBAB
<i>ZnO electrochemical synthesis</i>	
ILEG-H <sub>2</sub> O <sub>2</sub> -ZnAc	ILEG (ChCl:EG 1:2 molar ratio) + 0.01M Zn(CH <sub>3</sub> COO) <sub>2</sub> ·2H <sub>2</sub> O + 1.5 mL/L H <sub>2</sub> O <sub>2</sub>
ILEG -TBAB	ILEG (ChCl:EG 1:2 molar ratio) + 0.01M Zn(CH <sub>3</sub> COO) <sub>2</sub> ·2H <sub>2</sub> O + 1.5 mL/L H <sub>2</sub> O <sub>2</sub> + 5 mM of TBAB
ILEG-PVP	ILEG (ChCl:EG 1:2 molar ratio) + 0.01M Zn(CH <sub>3</sub> COO) <sub>2</sub> ·2H <sub>2</sub> O + 1.5 mL/L H <sub>2</sub> O <sub>2</sub> + 7 g/L PVP
IL	IL (ChCl:urea 1:2 molar ratio) + 0.01M Zn(CH <sub>3</sub> COO) <sub>2</sub> ·2H <sub>2</sub> O + 1.5 mL/L H <sub>2</sub> O <sub>2</sub>

Choline chloride (denoted as ChCl, 99%), ethylene glycol (EG, 99.5%), urea (99.5%), tetrabutylammonium bromide (TBAB, ≥ 98%), ethanol (EtOH), hydrogen peroxide (H<sub>2</sub>O<sub>2</sub>) (30 wt. % in water), zinc acetate dihydrate (Zn(CH<sub>3</sub>COO)<sub>2</sub>·2H<sub>2</sub>O) (ZnAc) (98 %), poly (N-vinyl-pyrrolidone) with a molecular weight of 55000 (PVP), were used as received. The eutectic mixtures have been prepared by mixing and heating with gentle stirring ChCl with EG (symbolized ILEG) and ChCl with urea (symbolized IL) in 1:2 molar ratio at a temperature in the range 80°C-100°C, until a homogeneous, clear liquid was formed. The other compounds, according to the desired formulations were then introduced to prepare the electrolytes.

### 2.2. Electrochemical Synthesis

The electrochemical synthesis experiments were performed in stationary conditions and in an open system (with the electrolyte in contact with air and atmospheric humidity), using a DC power supply (0-5 A, 0-60 V). The cell has a two-electrode configuration and contains 400 mL ionic liquid as electrolyte. The ratio of anodic to cathodic area was 1:1.

To electrochemically prepare TiO<sub>2</sub>, pure titanium discs (4 mm thickness) of 38.46 cm<sup>2</sup> exposed surface area have been used as sacrificial anode and Ni strips (0.3 mm thickness) as cathode. Current densities between 20 and 70 mA cm<sup>-2</sup> were applied at temperatures in the range of 30-60°C for durations between 2 and 6 h. After Ti anode dissolution, 10 mL of water has been added to the electrolyte in the cell. Thus, a direct hydrolysis occurred with the formation of a white gel. The gel has been washed with ethanol and then subjected to centrifugation at 4000 rpm for 15 min. This sequence has been repeated for 4 times, followed by drying at 110°C for 1 h and calcination at temperatures between 400°C and 600°C for 1 h.

In order to synthesize ZnO, pure Zn strips have been used as sacrificial anode and a Pt sieve as cathode. Current densities between 15 and 50 mA cm<sup>-2</sup> were applied at electrolyte temperatures in the range of 20-30 °C for durations between 3 and 5 h. After Zn anode dissolution, 30-50 mL of water has been added to the electrolyte. The formed white precipitate has been washed with deionized water and ethanol and then subjected to centrifugation at 4000 rpm for 15 min. This sequence has been followed by drying at 105 °C for 3 h and calcination at 300 °C for 1 h to obtain nano-ZnO powder.

Faradaic efficiency was also determined, by the mass ratio between the practically to theoretically obtained metal oxide powder.

In other series of experiments, anodic behavior of Ti, respectively of Zn electrode in choline chloride based ionic liquids has been investigated by cyclic voltammetry, using a three electrode glass cell, either with a Ti working electrode (1 cm<sup>2</sup>) or a Zn working electrode (having an exposed constant geometrical area of 0.38 cm<sup>2</sup>), a platinum counterelectrode and a silver wire as quasi-reference electrode. The reference and counterelectrodes were immersed in the solutions without using a separate compartment. The working electrodes were polished with 0.3 μm alumina paste, rinsed and dried prior to all measurements. The voltammetric and chronoamperometric (I-t curves for different constant applied potentials) studies were performed using an Autolab PGSTAT 12 potentiostat controlled with GPES software.

### ***2.3. Characterization***

The composition and structure of the prepared nanosized oxide powders have been investigated using an X-ray diffractometer Rigaku Ultima IV instrument with graphite diffracted beam monochromator for CuK<sub>α</sub> radiation. The UV-VIS absorption spectra were recorded from 200 to 700 nm on dry nanopowder samples

using a JASCO 570 UV-VIS spectrophotometer with an integrating sphere. Raman spectroscopy was conducted at room temperature using a Horiba LabRam HR 800 equipment, in which excitation was made by 633 nm wavelength laser light (He-Ne laser). The nanopowder morphology was analyzed by scanning electron microscopy (SEM) associated with energy-dispersive X-ray (EDX) analysis (Zeiss EVO50 equipment provided with Bruker-EDX probe, SEM accelerating voltage of 2 kV, EDX accelerating voltage of 21 kV). X-Ray Photoelectron Spectroscopy (XPS) was carried out on a Quantera SXM equipment, with a base pressure in the analysis chamber of  $10^{-9}$  Torr. The X-ray source was Al  $K_{\alpha}$  radiation (1486.6 eV, monochromatized) and the overall energy resolution is estimated at 0.65 eV by the full width at half maximum (FWHM) of the Au4f<sub>7/2</sub> line. In order to take into account the charging effect on the measured Binding Energies (BEs), the spectra were calibrated using the C1s line (BE = 284.8 eV, C-C (CH)<sub>n</sub> bondings) of the adsorbed hydrocarbon on the sample surface. A dual beam neutralizing procedure ( $e^{-}$  and  $Ar^{+}$  ion beams) has been used to compensate the charging effect in insulating samples. The UV-VIS absorption spectra were recorded from 200 to 700 nm on dry nanopowder samples using a JASCO 570 UV-VIS spectrophotometer with an integrating sphere.

### 3. Results and Discussion

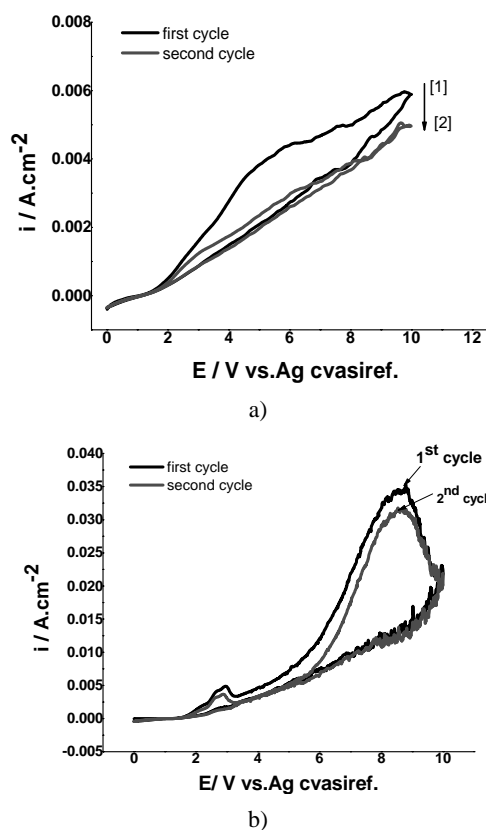
#### 3.1. *TiO<sub>2</sub> Electrochemical Synthesis*

Following the electrochemical synthesis process, white (sometimes with light grey tones) TiO<sub>2</sub> powders have been obtained. Faradaic efficiencies of 92-95% have been determined in ILEG based electrolyte whereas slightly higher values of efficiency, in the range of 95-98%, were calculated in the case of IL one. A slight increase of the anodic efficiency against the applied current density in the range of 20 - 70 mA cm<sup>-2</sup> has been also noticed.

In order to get more information on the anodic dissolution of Ti metal in ILEG based electrolytes, cyclic voltammograms in pure ILEG and in ILEG containing 1 mM TBAB at a constant temperature (25°C) and a constant scan rate (100 mV s<sup>-1</sup>) for two successive scans are presented in Fig.1.

As shown in Fig. 1a, the anodic current increased as the applied potential is shifted in anodic direction. Three potential domains may be evidenced, respectively: (i) a slight current increase between 0-2V that may be assigned to the anodic oxidation of chloride anion from choline chloride; (ii) between 2-5 V, an intensified anodic process is noticed, due to anodic oxide formation, followed by (iii) an oscillation of the current density between 5-10 V attributed to the anodic corrosion of TiO<sub>2</sub>/Ti interface under the presence of halide ions [20]. In addition, slightly lower anodic currents are evidenced during the second cycle. This behavior suggests the formation of a porous anodic oxide allowing electrolyte penetration at the metal/oxide interface with continuous metal dissolution. Visually, the detaching

of the oxihydroxide film from the metal surface was noticed, with formation of a precipitate within the electrolyte.

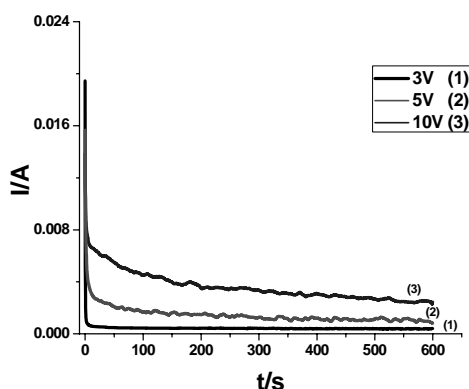


**Fig. 1.** Cyclic voltammograms for Ti working electrode ( $1 \text{ cm}^2$ ) in: (a) ILEG and (b) ILEG +1 mM TBAB (Scanning rate:  $100 \text{ mV s}^{-1}$ ).

The influence of TBAB addition on the voltammograms shape is exemplified in Fig. 1b. This compound facilitates the continuous anodic dissolution of Ti metal. Only a slight decrease of the amplitude of the current density with the number of cycles occurred, suggesting a continuous active dissolution of the Ti electrode in the electrolyte. A clear anodic peak is evidenced at about 8-9 V, followed by a current decrease during the reverse scan, suggesting the formation of an anodic film. In addition the small anodic peak at 2.5-2.7 V may be assigned to the supplementary oxidation of bromide ions from TBAB. The beneficial effect of TBAB addition consists in a significant increase of the anodic current from around  $5\text{-}6 \text{ mA.cm}^{-2}$  in the case of pure ILEG to  $35 \text{ mA.cm}^{-2}$  when TBAB was added.

Fig.2 presents typical I-t curves for Ti working electrode recorded at

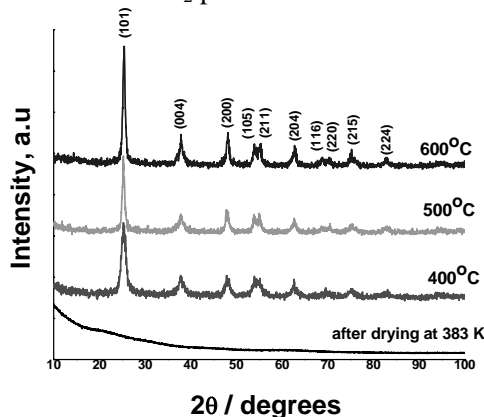
different applied potentials using ILEG ionic liquid containing 1mM TBAB. The anodic current had initially a relatively high value, but it decreased rapidly with time, up to a quasi-constant value which depends on the applied potential. The findings suggest that the anodic reaction during the initial polarization at 3–10 V removes the air-formed oxide from the electrode surface. Once the oxide layer is removed, the process seems to become a competition between the growth of oxide and its corrosion at the interface with the electrolyte.



**Fig. 2.** Current transients during the potentiostatic polarization of Ti electrode at different values of the applied potential in ILEG +1 mM TBAB.

Fig. 3 presents an example of the XRD patterns of  $\text{TiO}_2$  powder that was anodically synthesized in ILEG-EtOH system, after drying at  $110^\circ\text{C}$ , as well as after calcination at various temperatures between  $400^\circ\text{C}$  and  $600^\circ\text{C}$ . Similar results have been obtained when IL-EtOH system has been used during Ti metal anodic dissolution.

The synthesized and dried  $\text{TiO}_2$  powder showed an amorphous structure.



**Fig. 3.** XRD patterns of  $\text{TiO}_2$  nanopowders anodically synthesized in ILEG-EtOH system ( $40 \text{ mAcm}^{-2}$ ,  $40^\circ\text{C}$ , 2 h) after drying and after calcinations at different temperatures.



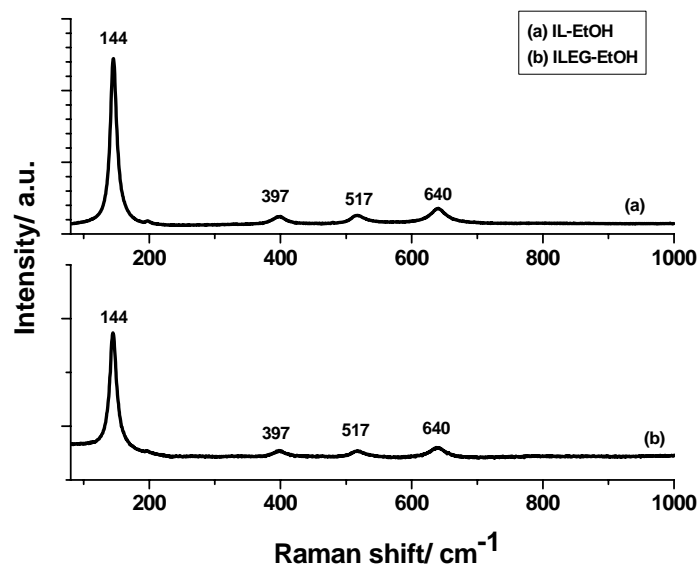
Calcination at 400°C determined a significant improvement in the crystallization of the anatase phase. The XRD peaks are narrow, suggesting the presence of very fine particles. The anatase phase is still stable at 600°C calcination (according to ICDD card No.03-065-5714). Moreover, it should be mentioned that no other peaks related to other titania phases or potential compounds resulting from thermal decomposition of ionic liquids were evidenced. Therefore, the anodically prepared anatase involving choline chloride based ionic liquids may be seen as a high thermal stability nanomaterial, giving rise to applications as a catalyst. The same behavior has been reported in [46], when titania anatase phase has been prepared from 1-butyl-1-methylpyrrolidinium bis(trifluoromethylsulphonyl)amide [Py14]TFSA ionic liquid. After calcination at 920°C, the anatase phase was subject to a phase transformation into a well crystallized rutile.

The crystallites average sizes ( $d$ ) of 8-18 nm have been determined (see Table 2) using the well-known Scherrer equation:

$$d = \frac{0.9 \lambda}{\beta \cos \theta} \quad (1)$$

where:  $\lambda$  is X-ray wavelength,  $\theta$  the diffraction angle and  $\beta$  the half width at half height for the diffraction peak. It should be noticed an increase of the crystallite size upon heat treating samples from 400°C to 600°C.

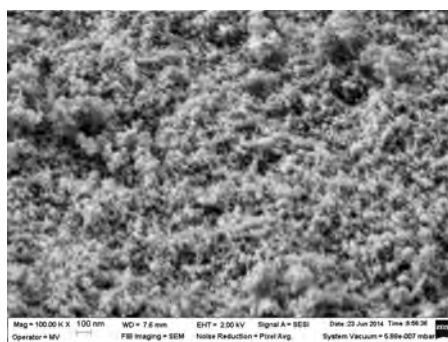
Raman spectroscopy has been also applied to characterize the obtained titania nanopowders, as shown in Fig. 4.



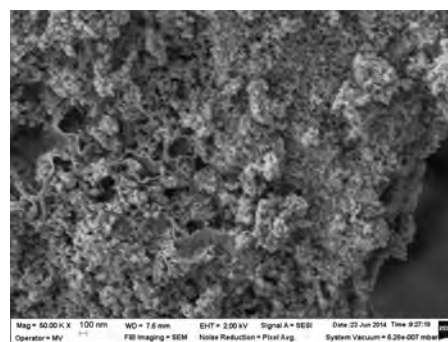
**Fig. 4.** Raman spectra of TiO<sub>2</sub> nanopowders anodically synthesized in: (a) IL-EtOH and (b) ILEG-EtOH systems after calcination at 500°C. The electrolysis conditions: 40 mA cm<sup>-2</sup>, 40°C, 2 h.

Anatase and rutile phases exhibit well distinct Raman fingerprints [17,53-55]. The anatase structure is tetragonal and its conventional cell is composed by two primitive cells, each with two  $\text{TiO}_2$  units. The six modes  $A_{1g}$ ( $517\text{ cm}^{-1}$ ),  $2B_{1g}$ ( $397\text{ cm}^{-1}$  and  $517\text{ cm}^{-1}$ ) and  $3E_g$ ( $144\text{ cm}^{-1}$ ,  $197\text{ cm}^{-1}$ , and  $640\text{ cm}^{-1}$ ) are Raman active [47, 56, 57]. As can be seen in Fig. 4, the Raman spectra of the electrochemically prepared  $\text{TiO}_2$  show four bands at  $144$ ,  $397$ ,  $517$  and  $640\text{ cm}^{-1}$  belonging to anatase phase, in agreement with previous reports of  $\text{TiO}_2$  structures prepared from ionic liquids [58]. The observation of Raman spectra indicating the presence of anatase phase is in accordance with XRD results shown in Fig. 3.

Examples of SEM micrographs of  $\text{TiO}_2$  powder calcined at  $600^\circ\text{C}$  are shown in Fig. 5. As can be seen, the samples contain very fine, spherical particles, with sizes between  $10\text{-}20\text{ nm}$ .



a)



b)

**Fig. 5.** SEM micrographs of  $\text{TiO}_2$  powder anodically prepared in: a) IL-EtOH and b) ILEG-EtOH electrolytes after calcination at  $600^\circ\text{C}$ .

It may be noticed a slight agglomeration state of the nanoparticles in the SEM images, due to their small size. Additionally, a more disordered wormlike morphology may be noticed when ILEG-EtOH electrolyte has been involved

during synthesis.

The elemental composition of the electrochemically prepared titania nanopowders after different applied thermal treatments has been determined by EDX analysis, as shown in Table 2.

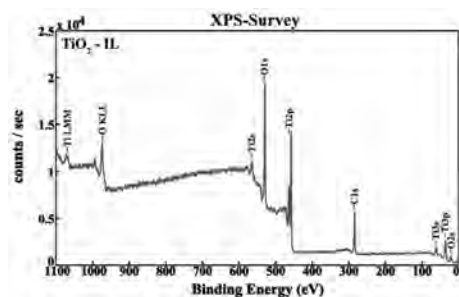
**Table 2.** The elemental composition (based on EDX spectra) and crystallite size of TiO<sub>2</sub> nanopowders after various thermal treatment regimes

Sample	Thermal treatment type	EDX content (wt.%)			XRD crystallite size, nm <sup>(a)</sup>
		O	Cl	Ti	
TiO <sub>2</sub> (ILEG-EtOH)	Drying 110°C	33.06	23.19	43.74	-
	Calcination at 400°C	44.25	1.24	54.51	7.9
	Calcination at 500°C	37.55	-	62.44	15.7
	Calcination at 600°C	36.38	-	63.61	16.6
TiO <sub>2</sub> (IL-EtOH)	Drying 110°C	32.76	27.47	39.77	-
	Calcination at 400°C	36.64	0.87	62.48	10.7
	Calcination at 600°C	32.69	-	67.30	15.8

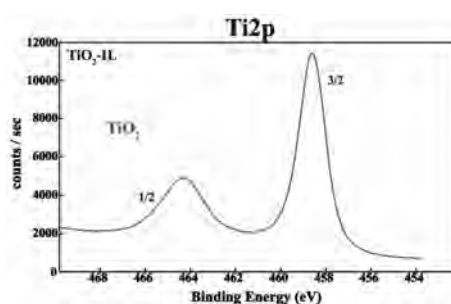
<sup>(a)</sup> Calculated by applying the Scherrer formula on the anatase (101) diffraction peak.

A significant amount of chlorine was detected in the case of dried powders, most probably originating from the anodic decomposition of choline chloride occurring at relatively high values of the applied anodic potential. The formed chlorine gas could be incorporated in the porous structure of the gel. In addition, the complexation of titanium ions with Cl<sup>-</sup> during anodic dissolution process is not excluded [18] that may contribute to its insertion in the titania structure. It should be noticed that the EDX signal related to Cl drastically decreased upon calcination at 400°C and then was entirely removed, at 500-600°C. Based on EDX investigations, oxygen rich titania nanopowders have been obtained, with O:Ti ratio between 2.11 and 3.88, depending on the calcination temperature and the initial electrolyte system.

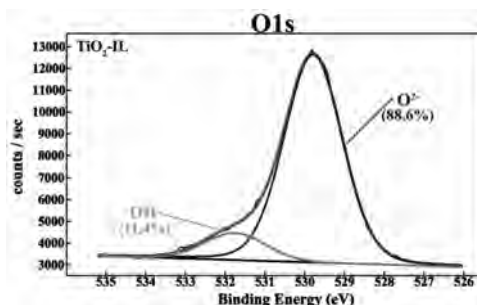
The composition of the electrochemically prepared titania nanopowder has been also investigated involving XPS. Fig. 6 presents the typical XPS survey spectra of the TiO<sub>2</sub> sample and the corresponding high resolution XPS spectra of Ti2p, O1s and C1s. It can be seen that the nano titania sample only contained Ti, O and C elements, with sharp photoelectron peaks appearing at binding energies of 459 (Ti 2p), 530 (O 1s) and 285 eV (C 1s), respectively.



a)



b)



c)

**Fig. 6.** XPS survey spectra of the  $\text{TiO}_2$  sample (a) and the corresponding high resolution XPS spectra of Ti2p (b) and O1s (c).

The carbon peak is attributed to the residual carbon from the sample and adventitious hydrocarbon from XPS instrument itself. High resolution spectrum of Ti 2p (see Fig.6b) clearly shows the two characteristic maxima of  $\text{Ti}^{4+}$  [59]. The core level XPS O 1s spectra are also analyzed, as presented in Fig.6c. The spectra specifies the presence of at least two kinds of chemical states that include the surface oxygen, probably in the form of surface hydroxyl groups and the lattice oxygen in  $\text{TiO}_2$ , at around 529.8 eV [59].

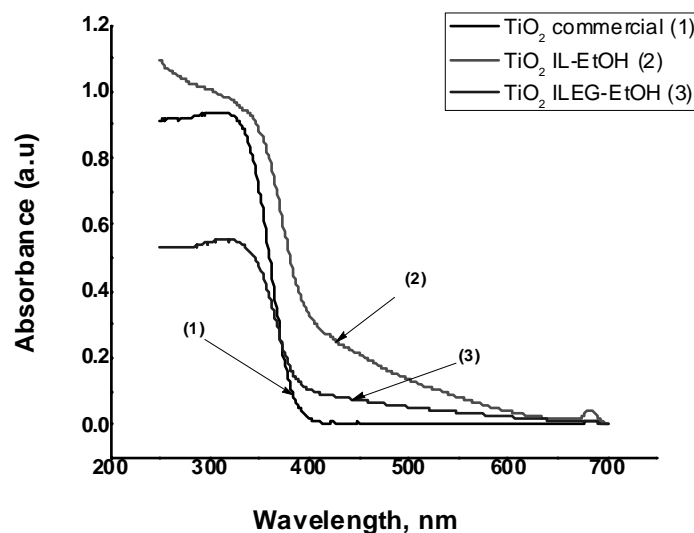
Fig. 7 shows the recorded UV-Vis diffuse reflectance spectra of  $\text{TiO}_2$  nanopowders obtained from different ChCl based ionic liquids systems compared

to commercial TiO<sub>2</sub>. It was perceived a noticeable shift of the optical absorption edges of the TiO<sub>2</sub> systems toward the visible regions of the solar spectrum, more pronounced in the case of the use of IL-EtOH system for electrochemical synthesis. It is evidenced an absorption band located in the range of 400–550 nm apart from the fundamental absorption edge of TiO<sub>2</sub>(in the UV region at about 350 nm) and the presence of a tail as well, suggesting a better photocatalytic activity (extended activity).

The band gap energy  $E_g$  [60] of the obtained nano-titania was determined from the graphs of  $(\alpha_0 \cdot h\nu)^{1/2}$  vs.  $h\nu$ , based on the relationship:

$$\alpha = \frac{[\alpha_0 (h\nu - E_g)^n]}{h\nu} \quad (2)$$

where  $\alpha$  is absorption of the TiO<sub>2</sub> powder and  $\alpha_0$  is absorption coefficient;  $h\nu$  is the photon energy and  $n$  is a constant. The value of  $n$  depends on the probability of transitions; it takes the values of 1/2, 3/2, 2 and 3 for direct allowed, direct forbidden, indirect allowed and indirect forbidden transition, respectively.



**Fig. 7.** UV-Vis diffuse reflectance spectra of TiO<sub>2</sub> nanopowders obtained from different choline chloride based ionic liquids systems compared to commercial TiO<sub>2</sub>.

The calculated  $E_g$  values for the electrochemically synthesized TiO<sub>2</sub> anatase nanopowders, considering the indirect type transition [61,62] were found to be 2.82 eV (IL-EtOH system) and 2.93 eV (ILEG – EtOH system) as compared to a value of 3.1 eV determined for commercial TiO<sub>2</sub> (TitanPE Technologies, Inc., China). These results suggest that these photocatalysts might be potentially adequate to operate under visible light illumination. Quite similar band gap energies values have been reported by Etacheri *et al.* [63] in the case of titania nanopowders

synthesized through a peroxo-titania route, characterized by the presence of high oxygen content. They considered that the oxygen excess defects present in the titania nanopowders could be responsible for the band gap narrowing. According to the previously presented results, oxygen rich titania nanopowders have been also obtained using anodic dissolution of Ti in different choline chloride based ionic liquids. Therefore, one may assume that the obtained lower values of the band gap energy may be ascribed to the higher content of oxygen.

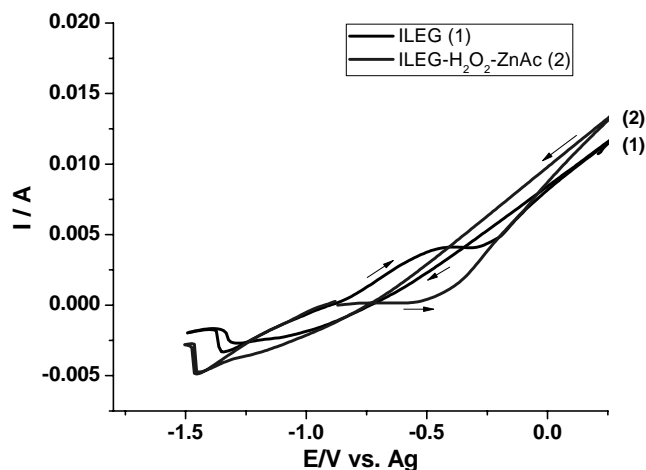
The electrochemically synthesized titania nanopowders involving choline chloride based ionic liquids exhibited relatively high photodegradation efficiency of Orange II as model dye, of about 95.5% under UV irradiation for 6 h. In addition, a two times higher photodegradation efficiency under visible light irradiation has been evidenced [51].

### ***3.2. ZnO electrochemical synthesis***

Usually, after anodic dissolution of Zn electrode in the above mentioned electrolytes from Table 1, some amounts of water were directly added to the choline chloride based ionic media to facilitate the formation of the white precipitate. The obtained ZnO powders after the applied thermal treatment were white. However, when ILEG-PVP system was involved, a dark grey tone was evidenced. Faradaic efficiencies of 85-92 % were determined in ILEG based electrolytes whereas slightly higher values, in the range of 90-95 % were calculated in the case of IL one. During electrochemical process, approx. 5-7 % of the anodically dissolved Zn was deposited onto the cathode, in the case of ILEG and IL systems. The addition of TBAB or PVP significantly diminished, respectively hindered the deposition phenomenon (up to 0.1-0.2 % of the dissolved Zn in the presence of TBAB, zero percentage when PVP was added).

In order to get information on the electrochemical behavior of Zn electrode in the proposed choline chloride based ionic liquids electrolytes, cyclic voltammograms have been recorded at 25 °C in the precursors (pure ILEG, ILEG-H<sub>2</sub>O<sub>2</sub>, ILEG\_ZnAc) and in the full electrolyte (ILEG-H<sub>2</sub>O<sub>2</sub>-ZnAc). For the sake of clarity, Fig.8 presents the CV curves in the case of pure ILEG and the full electrolyte, ILEG-H<sub>2</sub>O<sub>2</sub>-ZnAc.

As illustrated in Fig. 8 curve 1, a large oxidation peak on the anodic branch (or a plateau) is evidenced during scanning starting from the stationary potential. This peak is centered at around -0.5 V for pure ILEG and at approximately - 0.8 V for ILEG-ZnAc system (not shown here). The peak magnitude remained almost the same, regardless the applied scan rate or the number of cycles. By extending the anodic scan up to +2 V, a continuous increase of current was recorded, reaching the same maximum current values of 34-38 mA at any scan rate. By reversing the scan in cathodic direction, the current decreased on an identical route as in the forward scan.



**Fig. 8.** CV curves of Zn working electrode in different choline chloride based ionic liquids systems (scan rate:  $50 \text{ mV s}^{-1}$ ,  $25^\circ\text{C}$ ) ( $S_{\text{WE}} = 0.38 \text{ cm}^2$ ).

According to the literature [64,65], it is supposed that within the first part of potential scan, from  $-0.8 \text{ V}$  to  $-0.3 \text{ V}$ , Zn metal electrochemical dissolution takes place producing univalent  $\text{Zn}^+$  cations which are closely adsorbed onto the zinc anode surface, according to Eq(I):



In the next portion, along the linear portion of anodic branch and reversing scan, it is clear that a massive production of zinc ions occurs due to high polarization values. The processes taking place in this part of CVs may be described as both subsequent oxidation of  $\text{Zn}^+$  intermediate cations and electrochemical dissolution of Zn atoms from metallic anode, according to Eq(II) and Eq(III):



Oppositely, CV curves for ILEG +  $\text{H}_2\text{O}_2$  and ILEG +  $\text{H}_2\text{O}_2$  + ZnAc systems did not exhibit any anodic peak and the current increased continuously by scanning up  $+2 \text{ V}$  anodic potential limit and an exact route on reversing scan is recorded. An example is illustrated in Fig. 8 curve 2. This behavior suggests that the  $\text{H}_2\text{O}_2$  addition completely inhibits the processes (I) and (II) and only massive electrochemical dissolution of zinc anode takes place (process (III)).

It is worth to mention that at the end of cathodic branch of all voltammograms the small peak which appears within  $-1.35 \text{ V}$  to  $-1.45 \text{ V}$  potential range (see also Fig. 8) may be ascribed to the electroreduction of new formed  $\text{Zn}^{2+}$  cations, according to Eq(IV):



However, the position and amplitude of these cathodic peaks do not depend substantially on scan rate or cycling, but depend on the nature of the ionic liquid system, respectively on the H<sub>2</sub>O<sub>2</sub> content (1-2 mA in the absence and 4-5 mA in the presence of H<sub>2</sub>O<sub>2</sub>). This is another support for a favorable influence of H<sub>2</sub>O<sub>2</sub> to Zn<sup>2+</sup> production.

Based on the above observations, it can be supposed the mechanism for the reaction process in investigated H<sub>2</sub>O<sub>2</sub> containing ionic liquids involves a simultaneous oxidation of the peroxide ion (O<sub>2</sub><sup>2-</sup>) together with the electrodisolution of Zn metal. The new formed species, superoxide ion (O<sub>2</sub><sup>-</sup>) and Zn<sup>2+</sup> ion proceed to precipitate zinc oxide according to Eq(V), with zinc superoxide (ZnO<sub>4</sub>) as intermediate species [48]:

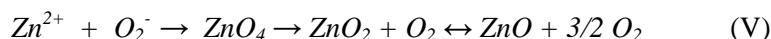
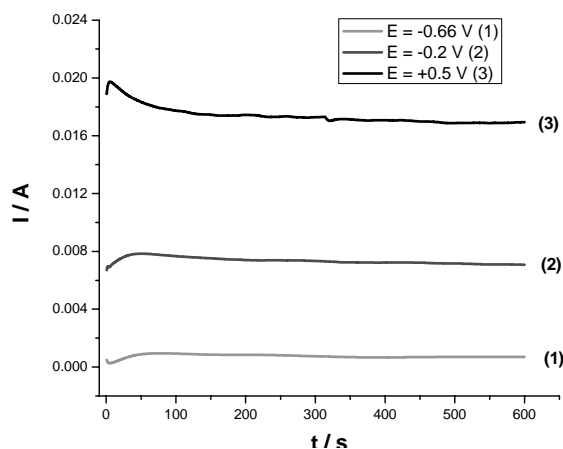


Figure 9 presents typical current versus time curves for Zn working electrode recorded at different applied potentials using ILEG-H<sub>2</sub>O<sub>2</sub>-ZnAc electrolyte. The anodic current had initially a maximum value, which is attained in the first 40-50 s when the applied potential belongs to the plateau region (E = -0.66V, E=-0.2V) and in the first 5 s when it is situated on the massive Zn dissolution zone (E = 0.5V). Then it attains a quasi-constant value which depends on the applied potential.



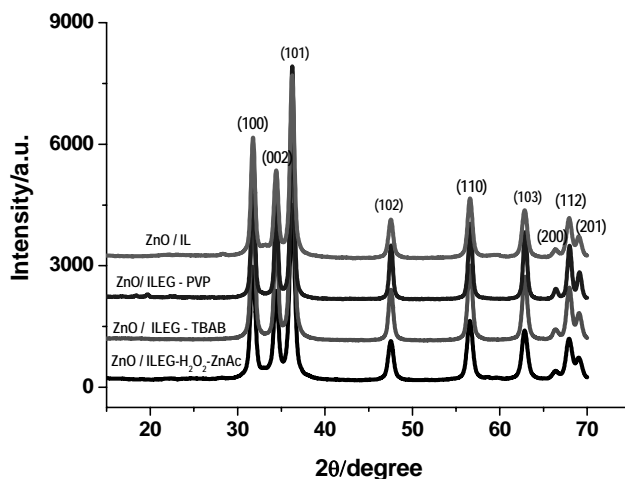
**Fig. 9.** I-t curves for Zn working electrode in ILEG-H<sub>2</sub>O<sub>2</sub>-ZnAc electrolyte for different values of the applied potential (t = 25 °C; S<sub>WE</sub> = 0.38 cm<sup>2</sup>).

Figure 10 presents the XRD patterns of ZnO powder anodically synthesized in different choline chloride based ionic liquids systems.

All observed peaks correspond to the hexagonal wurtzite structure of ZnO (according to the standard card JCPDS 00-036-1451), in agreement with other literature data [66]. No other peaks related to other potential impurities compounds resulting from decomposition of ionic liquids were evidenced. All the obtained

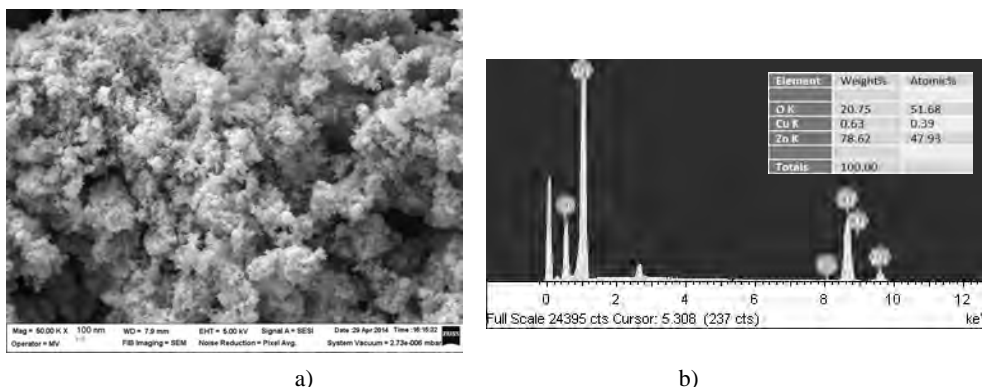


nanopowders exhibit the highest intensities of crystal growth orientation on the (101) plane, located at  $36.3^\circ$ . The crystallites average sizes of 12-18 nm have been determined using the Scherrer equation (1). The addition of either TBAB or PVP determines a slight increase of crystallites sizes, from around 12-13 nm towards about 18 nm.



**Fig. 10.** X-ray diffractograms for ZnO powder anodically synthesized in different choline chloride based ionic liquids systems.

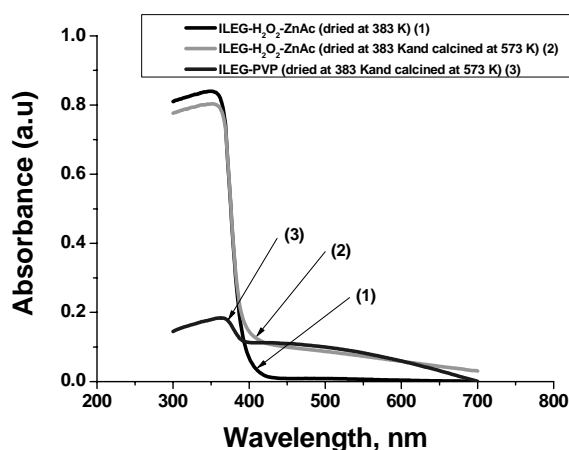
SEM micrographs, as exemplified in Fig. 11a, suggested that the nanoparticles are approaching spherical shape having crystallite sizes of about 15-31 nm, relatively similar to the calculated values from XRD patterns. It may be noticed a slight agglomeration state of the nanoparticles in the SEM images, due to their small size. EDX spectra of the anodically obtained ZnO nanopowder (see Fig. 11b) revealed the fact that oxygen is slightly higher than zinc.



**Fig. 11.** SEM micrograph (a) and (b) EDX spectrum of ZnO nanopowder anodically synthesized in ILEG electrolyte after the applied thermal treatments at  $105^\circ\text{C}$  for 3 h and  $300^\circ\text{C}$  for 1 h.

Figure 12 shows examples of the recorded UV–Vis diffuse reflectance spectra of ZnO nanopowders obtained from different ChCl based ionic liquids systems.

A new absorption band was observed in the visible range of 420–550 nm apart from the fundamental absorption edge of ZnO, which is located in the UV region at about 350 nm and the presence of a tail as well, suggesting a better photocatalytic activity, after the applied thermal treatment.



**Fig. 12.** UV–Vis diffuse reflectance spectra of ZnO nanopowders electrochemically prepared involving different choline chloride based ionic liquids.

#### 4. Conclusions

Based on the obtained experimental results, new electrochemical synthesis procedures to prepare TiO<sub>2</sub> and ZnO nanopowders from choline chloride based ionic liquids have been proposed.

This easy and efficient procedure allowed for TiO<sub>2</sub> preparation faradaic efficiencies of minimum 92% for applied current densities between 2-7 A/dm<sup>2</sup> and operating temperatures of 30-60°C. The obtained TiO<sub>2</sub> nanopowders showed a stable anatase structure after the thermal treatment at 400-600°C, with a narrow size distribution of 8-18 nm. Based on the recorded UV-Vis diffuse reflectance spectra for the electrochemically synthesized TiO<sub>2</sub> anatase nanopowders, band gap energies between 2.82-2.93 eV have been determined, that are lower as compared to those of the classical TiO<sub>2</sub>. It has been assumed that the oxygen excess present in the titania nanopowders may contribute to the band gap narrowing. These findings suggest that these photocatalysts are potentially adequate to operate under visible light illumination.

It has been also reported the successful electrochemical synthesis of ZnO nanopowders involving anodic dissolution of zinc electrode in choline

chloride-ethylene glycol or choline chloride-urea eutectic mixtures with additions of hydrogen peroxide. This is an efficient procedure allowing faradaic efficiencies of minimum 85 % for applied current densities between 15–50 mA cm<sup>-2</sup> and operating temperatures of 20-30°C .

The cyclic voltammetry investigations showed a continuous increase of current during anodic scan, assigned to a continuous dissolution of metallic Zn and simultaneous oxidation of the peroxide ion (O<sub>2</sub><sup>2-</sup>); both formed species precipitate as ZnO. XRD investigations showed the hexagonal wurtzite structure of ZnO, in agreement with other literature data.

Crystallites average sizes of 12-18 nm have been determined for the anodically synthesized ZnO nanopowders. The addition of either TBAB or PVP determined a slight increase of crystallites sizes, from around 12-13 nm towards about 18 nm. According to SEM micrographs, the nanoparticles are approaching spherical shape with a slight agglomeration state, due to their small size.

Some other important aspects such as a better understanding of the anodic processes occurring in the choline chloride based ionic liquid electrolyte and their influence of oxides nanopowders structure and photocatalytic behavior, as well as the possible increase of the performance through the addition of an appropriate doping element are suggested for further investigation.

**Acknowledgements.** The present work was financially supported by the Romanian Ministry of Education and Research, PNCDI II - PARTENERIATE, under Research Contract No.167/2012 – SELFPROPIEL and NANOCOATIL project (Contr.7-082/2013) under M ERA Net Program.

## References

- [1] H. FUKUYAMA and N. NAGAOSA, Editors, *Physics and Chemistry of Transition Metal Oxides*, Springer, Berlin, Germany, 1999.
- [2] A.N. BANERJEE, *The design, fabrication and photocatalytic utility of nanostructured semiconductors: focus on TiO<sub>2</sub>-based nanostructures*, Nanotechnology, Science and Applications, **4**, pp.35-65, 2011.
- [3] S.S. KUMAR, P. VENKATESWARLU, V.R. RAO and G.N. RAO, *Synthesis, characterization and optical properties of zinc oxide nanoparticles*, International Nano Letters, **3**, pp. 30-35, 2013.
- [4] P. ROY, S. BERGER and P. SCHMUKI, *TiO<sub>2</sub> Nanotubes: Synthesis and Applications*, Angew. Chem. Int. Ed., **50**, pp.2904 – 2939, 2011.
- [5] X.L. CHENG, H. ZHAO, L.H. HUO, S. GAO and J.G. ZHAO, *ZnO nanoparticulate thin film: preparation, characterization and gas-sensing properties*, Sens.Actuators B,102, pp. 248–252, 2004.
- [6] S.Y. LEE, E.S. SHIM, H.S. KANG and S.S. PANG, *Fabrication of ZnO thin film diode using laser annealing*, Thin Solid Films, **437**, pp. 31–34, 2005.
- [7] P. CHENG, C. DENG, M. GU and X. DAI, *Effect of urea on the photoactivity of titania powder prepared by sol–gel method*, Mater. Chem. Phys., **107**. pp. 77–81, 2008.

- [8] D-G. HUANG, S-J. LIAO, J-M. LIU, Z. DANG and L. PETRIK, *Preparation of visible-light responsive N-F-codoped TiO<sub>2</sub> photocatalyst by a sol-gel-solvothermal method*, J. Photochem. Photobiol. A **184** (2006) 282–288.
- [9] T. MORIKAWA, Y. IROKAWA and T. OHWAKI, *Enhanced photocatalytic activity of TiO<sub>2-x</sub>N<sub>x</sub> loaded with copper ions under visible light irradiation*, Appl. Catal., **A 314**, pp. 123–127, 2006.
- [10] M.K. SEERY, R. GEORGE, P. FLORIS and S.C. PILLAI, *Silver doped titanium dioxide nanomaterials for enhanced visible light photocatalysis*, J. Photochem. Photobiol., **A 189**, pp. 258–263, 2007.
- [11] V. STENGEL and S. BAKARDIEVA, *Molybdenum-doped anatase and its extraordinary photocatalytic activity in the degradation of Orange II in the UV and vis regions*, J. Phys. Chem., **C 114**, pp.19308–19317, 2010.
- [12] L. GAO and Q. ZHANG, *Effects of amorphous contents and particle size on the photocatalytic properties of TiO<sub>2</sub> nanoparticles*, Scr. Mater., **44**, pp. 1195-1198, 2001.
- [13] W. TANG, X. CHEN, J. XIA, J. GONG and X. ZENG, *Preparation of an Fe-doped visible-light-response TiO<sub>2</sub> film electrode and its photoelectrocatalytic activity*, Mater. Sci. Eng. B, **187**, pp. 39–45, 2014.
- [14] B.M. PIRZADA, N.A. MIR, N. QUTUB, O. MEHRAJ, S. SABIR and M. MUNEER, *Synthesis, characterization and optimization of photocatalytic activity of TiO<sub>2</sub>/ZrO<sub>2</sub> nanocomposite heterostructures*, Mater. Sci. Eng. B, **193**, pp. 137-145, 2015.
- [15] M.E. CONTRERAS-GARCIA, M. LORENA GARCIA-BENJUME, V.I. MACIAS-ANDRES, E. BARAJAS-LEDESMA, A. MEDINA-FLORES and M.I. ESPITIA-CABRERA, *Synergic effect of the TiO<sub>2</sub>-CeO<sub>2</sub> nanoconjugate system on the band-gap for visible light photocatalysis*, Mater. Sci. Eng. B, **183**, pp. 78–85, 2014.
- [16] M. GRATZEL, *Photoelectrochemical cells*, Nature (London), **414**, pp. 338-344, 2001.
- [17] S.K. GUPTA, R. DESAI, P.K. JHA, S. SAHOO and D. KIRIN, *Titanium dioxide synthesized using titanium chloride: size effect study using Raman spectroscopy and photoluminescence*, J. Raman Spectrosc., **41**, pp. 350-355, 2010.
- [18] POTTIER, S. CASSAIGNON, C. CHANEAC, F. VILLAIN, E. TRONC and J. JOLIVET, *Size tailoring of TiO<sub>2</sub> anatase nanoparticles in aqueous medium and synthesis of nanocomposites. Characterization by Raman spectroscopy*, J. Mater. Chem., **13**, pp. 877-882, 2003.
- [19] E.J. KIM and S.H. HAHN, *Microstructural changes of microemulsion-mediated TiO<sub>2</sub> particles during calcination*, Mater. Lett., **49**, pp. 244-249, 2001.
- [20] D. BRIDA, E. FORTUNATO, I. FERREIRA, H. AGUAS and R. MARTINS, *New insights on large area flexible position sensitive detectors*, J. Non-Cryst. Solids., **299**, pp. 1272–1276, 2002.
- [21] Z.L. WANG, *Zinc oxide nanostructures: growth properties and applications*, J.Phys. Condens. Matter., **16**, pp. R829–R858, 2004.
- [22] M. SUCHEA, S. CHRISTOULAKIS, K. MOSCHOVIS, N. KATSARAKIS and G. KIRIAKIDIS, *ZnO transparent thin films for gas sensor applications*, Thin Solid Films, **515**, pp. 551–554, 2006.
- [23] ASHOUR, M.A. KAID, N.Z. EL-SYED and A.A. IBRAHIM, *Physical properties of ZnO thin films deposited by spray pyrolysis technique*, Appl. Surf. Sci., **252**, pp. 7844–7848, 2006.
- [24] J.C. CHEN and C.T. TANG, *Preparation and application of granular ZnO/Al<sub>2</sub>O<sub>3</sub> catalyst for the removal of hazardous trichloroethylene*, J. Hazard. Mater., **142**, pp. 88–96, 2007.
- [25] N. SCARISOREANU, D.G. METAI, G. DINESCU, G. EPURESCU, C. GHICA, L.C. NISTOR and M. DINESCU, *Properties of ZnO thin films prepared by radio-frequency plasma beam assisted laser ablation*, Appl. Surf. Sci., **247**, pp. 518–525, 2005.
- [26] Y.H. NI, X.W. WEI, J.M. HONG and Y. YE, *Hydrothermal synthesis and optical properties of ZnO nanorods*, Mater. Sci. Eng., B, **121**, pp. 42–47, 2005.

- [27] S. CHANG, S.O. YOON, H.J. PARK and A. SAKAI, *Luminescence properties of Zn nanowires prepared by electrochemical etching*, Mater. Lett., **53**, pp. 432–436, 2002.
- [28] M. RISTIAC, S. MUSIAC, M. IVANDA and S. POPOVIAC, *Sol-gel synthesis and characterization of nanocrystalline ZnO powders*, J. Alloys Compd., **397**, pp. L1–L4, 2005.
- [29] J.J. WU and S.C. LIU, *Low-temperature growth of well-aligned ZnO nanorods by chemical vapor deposition*, Adv. Mater., **14**, pp. 215–218, 2002.
- [30] R.C. WANG and C.C. TSAI, *Efficient synthesis of ZnO nanoparticles, nanowalls, and nanowires by thermal decomposition of zinc acetate at a low temperature*, Appl. Phys. A., **94**, pp. 241–245, 2009.
- [31] Z. KHORSAND, A. ABID, W.H. MAJID, H.Z. WANG, R. YOUSEFI, M. GOLSHEIKH and Z.F. REN, *Sonochemical synthesis of hierarchical ZnO nanostructures*, Ultrasonic Sonochemistry, **20**, pp. 395–400, 2013.
- [32] SHETTY and K. NANDA, *Synthesis of zinc oxide porous structures by anodisation with water as an electrolyte*, Appl. Phys. A., **109**, pp. 151–157, 2012.
- [33] O. SINGH, N. KOHLI and R.C. SINGH, *Precursor controlled morphology of zinc oxide and its sensing behavior*, Sens. Actuators B., **178**, pp. 149–154, 2013.
- [34] A. VAZQUEZ, I.A. LOPEZ and I. GOMEZ, *Growth mechanism of one-dimensional zinc sulfide nanostructures through electrophoretic deposition*, J. Mater. Sci., **48**, pp. 2701–2704, 2013.
- [35] J. RODRIGUES-PAEZ, A.C. CABALLERO, M. VILLEGAS, C. MOURE, P. DURAN and J.F. FERNANDZ, *Controlled precipitation methods: formation mechanism of ZnO nanoparticles*, J. Eur. Ceram. Soc., **21**, pp. 925–930, 2001.
- [36] I. PARAMASIVAM, J.M. MACAK, T. SELVAM and P. SCHMUKI, *Electrochemical synthesis of self-organized TiO<sub>2</sub> nanotubular structures using an ionic liquid (BMIM-BF<sub>4</sub>)*, Electrochim. Acta, **54**, pp. 643–648, 2008.
- [37] E.P. GRISHINA, L.M. RAMENSKAYA and A.M. PIMENOVA, *Electrochemical oxidation of tantalum and niobium in 1-butyl-3-methylimidazolium bromide melt containing water admixtures*, Russ. J. Electrochem., **44**(2), pp. 213–217, 2008.
- [38] Z. LI, Z. JIA, Y. LUAN AND T. MU, *Ionic liquids for synthesis of inorganic nanomaterials*, Curr. Opin. Solid State Mater. Sci., **12**, pp. 1–8, 2008.
- [39] X.F. ZHOU, D.B. CHU and C.J. LIN, *Anodic dissolution of spongy titanium in ethanol solution for preparation of nano-sized TiO<sub>2</sub> powder*, Electrochim. Acta, **47**, pp. 2769–2773, 2002.
- [40] K. KAMADA, M. MUKAI and Y. MATSUMOTO, *Electrodeposition of titanium(IV) oxide film from sacrificial titanium anode in I<sub>2</sub>-added acetone bath*, Electrochim. Acta, **47**, pp. 3309–3313, 2002.
- [41] F. ENDRES, A.P. ABBOTT and D.R. MACFARLANE, *Electrodeposition from Ionic Liquids*, Wiley-VCH Verlag, Weinheim, 2008.
- [42] N. LIU, D. WU, H. WU, F. LUO and J. CHEN, *Controllable synthesis of metal hydroxide and oxide nanostructures by ionic liquids assisted electrochemical corrosion method*, Solid State Sci., **10**, pp. 1049, 2008.
- [43] A.P. ABBOTT, G. CAPPER, D.L. DAVIES, R.K. RASHEED and V. TAMBYRAJAH, *Novel solvent properties of choline chloride/urea mixtures*, Chem. Commun., **9**, pp. 70–71, 2003.
- [44] A.P. ABBOTT, D. BOOTHBY, G. CAPPER, D.L. DAVIES and R.K. RASHEED, *Deep eutectic solvents formed between choline chloride and carboxylic acids: versatile alternatives to ionic liquids*, J. Am. Chem. Soc., **126**, pp. 9142–9147, 2004.
- [45] H. MENG, X-W. CHEN and J-H. WANG, *Ionic liquid templated porous nano-TiO<sub>2</sub> particles for the selective isolation of cytochrome c*, Nanotechnology, **21**, pp. 385704, 2010.
- [46] H.K. FARAG, M. AL ZOUBI and F. ENDRES, *Sol-gel synthesis of alumina, titania and mixed alumina/titania in the ionic liquid 1-butyl-1-methylpyrrolidinium bis(trifluoromethylsulphonyl) amide*, J. Mater. Sci., **44**, pp. 122–128, 2009.

- [47] C. OUMAHI, J. LOMBARD, S. CASALE, C. CALERS, L. DELANNOY, C. LOUIS and X. CARRIER, *Heterogeneous catalyst preparation in ionic liquids: Titania supported gold nanoparticles*, *Catal. Today*, **235**, pp. 58–71, 2014.
- [48] E. AZACETA, R. TENA-ZAERA, R. MARCILLA, S. FANTINI, J. ECHEBERRIA, J.A. POMPOSO, H. GRANDE and D. MECERREYES, *Electrochemical deposition of ZnO in a room temperature ionic liquid: 1-Butyl-1- methylpyrrolidinium bis(trifluoromethane sulfonyl)imide*, *Electrochem. Commun.*, **11**, pp. 2184–2186, 2009.
- [49] E. AZACETA, J. IDIGORAS, J. ECHEBERRIA, A. ZUKAL, L. KAVAN, O. MIGUEL, H.-J. GRANDE, J.A. ANTA and R. TENA-ZAERA, *ZnO–ionic liquid hybrid films: electrochemical synthesis and application in dye-sensitized solar cells*, *J. Mater. Chem. A*, **1**, pp. 10173–10183, 2013.
- [50] M. HARATI, D. LOVE, W.M. LAU and Z. DING *Preparation of crystalline zinc oxide films by one-step electrodeposition in Reline*, *Mater. Lett.*, **89**, pp. 339–342, 2012.
- [51] L. ANICAI, A. PETICA, D. PATROI, V. MARINESCU, P. PRIOTEASA and S. COSTOVICI, *Electrochemical synthesis of nanosized TiO<sub>2</sub> nanopowder involving choline chloride based ionic liquids*, *Mater. Sci. Eng. B*, **199**, pp. 87–95, 2015.
- [52] S. COSTOVICI, A. PETICA, C.S. DUMITRU, A. COJOCARU and L. ANICAI, *Electrochemical synthesis on ZnO nanopowder involving choline chloride based ionic liquids*, *Chem. Eng. Trans.*, **41**, pp. 343–348, 2014.
- [53] LI BASSI, D. CATTANEO, V. RUSSO, C.E. BOTTANI, E. BARBORINI *et al.*, *Raman spectroscopy characterization of titania nanoparticles produced by flame pyrolysis: The influence of size and stoichiometry*, *J. Appl. Phys.*, **98**, pp. 074305, 2005.
- [54] F.D. HARDCASTLE, *Raman Spectroscopy of Titania (TiO<sub>2</sub>) Nanotubular water-splitting catalysts*, *J. Ark. Acad. Sci.*, **65**, pp. 43–48, 2011.
- [55] J.C. COLMENARES, M.A. ARAMENDIA, A. MARINAS, J.M. MARINAS and F.J. URBANO, *Synthesis, characterization and photocatalytic activity of different metal-doped titania systems*, *Appl. Catal. A*, **306**, pp. 120–127, 2006.
- [56] T. OHSAKA, F. IZUMI and Y. FUJIKI, *Raman spectrum of anatase, TiO<sub>2</sub>*, *J. Raman Spectrosc.*, **7**, pp. 321–324, 1978.
- [57] U. BALACHANDRAN and N.G. EROR, *Raman spectrum of titanium dioxide*, *J. Solid State Chem.*, **42**, pp. 276–82, 1982.
- [58] G. NAGARAJU, K. MANJUNATH, T. N. RAVISHANKAR, B. S. RAVIKUMAR, H. NAGABHUSHAN, G. EBELING and J. DUPONT, *Ionic liquid-assisted hydrothermal synthesis of TiO<sub>2</sub> nanoparticles and its application in photocatalysis*, *J. Mater. Sci.*, **48**, pp. 8420–8426, 2013.
- [59] H.JENSEN, A. SOLOVIEV, Z. LI and E.G. SØGAARD, *XPS and FTIR investigation of the surface properties of different prepared titania nano-powders*, *Appl.Surf.Sci.*, **246**(1-3), pp. 239–249, 2005.
- [60] S. SABALE, A. BANDGAR, H. WANG, K. GURAV, J. H. KIM and S. H. PAWAR, *Direct synthesis and characterization of high temperature stable anatase TiO<sub>2</sub> nanospheres from peroxo-titanium complex*, *Met. Mater. Int.*, **19**, pp. 483–488, 2013.
- [61] S. VALENCIA, J.M. MARIN and G. RESTREPO, *Study of the bandgap of synthesized titanium dioxide nanoparticules using the sol-gel method and a hydrothermal treatment*, *The Open Materials Science Journal*, **4**, pp. 9–14, 2010.
- [62] B. OHTANI, *Photocatalysis A to Z: What we know and what we do not know in a scientific sense*, *J. Photochem. Photobiol. C*, **11**, pp. 157–178, 2010.
- [63] V. ETACHERI, M.K. SEERY, S.J. HINDER and S.C. PILLAI, *Oxygen rich titania: A dopant free, high temperature stable, and visible-light active anatase photocatalyst* *Adv. Funct. Mater.*, **21**, pp. 3744–3752, 2011.
- [64] B. STYPULA, M. STAROWICZ, M. HAJOS and E. OLEJNIK, *Electrochemical synthesis of ZnO nanoparticles during anodic dissolution of zinc in alcohols solvents*, *Arch.Metall.Mater.*, **56**, pp. 287–292, 2011.

- [1] J. SWIATOWSKA-MROWIECKA and J. BANÀS, *Anodic behavior of zinc in methanol solutions of lithium perchlorate*, *Electrochim. Acta*, **50**, pp. 1829–1840, 2005.
- [2] S. FLICKYNGEROVA, K. SHTEREVA, V. STENOVA, D. HASKO, I. NOVOTNY, V. TVAROZEK, P. SUTTA and E. VAVRINSKY, *Structural and optical properties of sputtered ZnO thin films*, *Appl.Surf.Sci.*, 254, pp. 3643–3647, 2008.

## Zinc Oxide Thin Films for Radiation Hardened Devices by Materials Engineering

Rodica PLUGARU<sup>1</sup>, Iuliana MIHALACHE<sup>1</sup>, Raluca GAVRILA<sup>1</sup>,  
Anca Ionela DANCIU<sup>1</sup>, George BOLDEIU<sup>1</sup>, Oana Tatiana NEDELICU<sup>1</sup>,  
Neculai PLUGARU<sup>2</sup>, Valentin Adrian MARALOIU<sup>2</sup>, Daniela GHICA<sup>2</sup>,  
Mariana STEFAN<sup>2</sup>, Sergiu Vasile NISTOR<sup>2</sup>

<sup>1</sup>National Institute for R & D in Microtechnologies – IMT Bucharest,  
Erou Iancu Nicolae Str. 126A, Bucharest 077190, Romania

<sup>2</sup>National Institute of Materials Physics,  
P.O.Box MG07, Bucharest Magurele 077125, Romania

**Abstract.** Application of zinc oxide (ZnO) thin films in advanced optoelectronic devices designed to operate in space environment raises issues on material properties and device function modification under exposure to radiation. Colliding heavy charged particles may affect the structure as well as the optical and electrical properties of ZnO, by the accumulation of radiation induced defects. In this work we report results of a recent experiment performed with alpha particles at 3 MeV energy, 5.3 kGy/h dose rate, and various exposure periods between 100 s and 8 h, aiming to understand the atomic-level mechanisms of defects build-up in irradiated ZnO thin films. A plethora of characterization methods were used to analyse the material properties, before and after irradiation, including field emission scanning electron microscopy (FESEM), high resolution transmission electron microscopy (TEM-HRTEM), atomic force microscopy (AFM), x-ray diffraction (XRD), electron paramagnetic resonance (EPR), photoluminescence (PL). First principles calculations at the GGA+U level were performed to determine the electronic properties of ZnO, N:ZnO and Li:ZnO doped materials with local chemical and structural disorder. Numerical simulations of test devices whose structure includes defected ZnO thin films have also been performed in order to probe their electro-thermal and electrical behavior after irradiation. The ZnO, N:ZnO and Li:ZnO doped films investigated are polycrystalline, with wurtzite structure. The PL emission spectra reveal an increased intensity of the peaks corresponding to defects in the irradiated films. Our results evidence that a specific process of defect formation, hitherto unreported, may occur when a threshold exposure time is exceeded. Numerical modeling of electrical and coupled thermal-electrical response of ZnO FET transistors with various densities and areas of radiation-induced defects shows that the defect concentration, their distribution and the size of defected regions strongly affect the current density and the temperature distribution within the device.



## 1. Introduction

Recently, an increasing number of investigations have been undertaken on the evolution of the morphology, structure, optical and electrical properties of ZnO based materials irradiated with high energy electrons, heavy ions or gamma rays. Since these materials, including thin films, nano crystals, nano objects and powders, are relevant for advanced nanoelectronics, optoelectronics, transparent electronics, UV high performance photodetectors, solar cells and sensors, their performance when operating in harsh radiation conditions as existing in space is of utmost interest.

Thus, it was reported that the irradiation of ZnO and Al-doped ZnO thin films with high energy electron beams, at 0.8 MeV and a fluence of  $10^{16}$  electrons/cm<sup>2</sup>, is responsible for the increase in the electron mobility, but also for the decrease in carrier concentration by creating acceptor like defects, such as zinc vacancies ( $V_{Zn}$ ) and oxygen interstitials ( $O_i$ ). Besides the modifications of the optical and electrical characteristics, the structure and morphology of the films change by electron irradiation as well. The films showed larger grain size and rougher surfaces after irradiation, which was attributed to an irradiation induced annealing effect [1-3]. Also, it was observed that electrons with energies of 6, 12, 15 MeV at a fluence of  $1 \times 10^{12}$  electrons/cm<sup>2</sup> affect the structure of ZnO thin films, through a regrowth process activated by the electron beam-film interaction and the subsequent annealing effect [4]. Electron beams with higher energy/fluence characteristics can significantly affect the grain size, surface morphology, sheet resistance, optical constants, absorption edge, and the optical band gap of ZnO and Al-doped ZnO films. It was evidenced that after exposure to 8 MeV electrons at a fluence of  $6 \times 10^{13}$  electrons/cm<sup>2</sup> the grain size decreased, the absorption edge shifted to blue wavelength region, and the sheet resistance increased [5].

Irradiation of (0001) ZnO crystals with 500 keV  $^{129}\text{Xe}^+$  at fluences of  $5 \times 10^{14}$  and  $1.5 \times 10^{15}$  cm<sup>-2</sup> resulted in the formation of near-surface nanocavities, and stoichiometric imbalance [6]. Also, an increased surface roughness due to sputtering was observed in 1.2 MeV  $\text{Ar}^{8+}$ , fluence  $1-5 \times 10^{15}$  ions/cm<sup>2</sup> irradiated polycrystalline ZnO, along with an enhancement of the irradiated sample UV emission (~3.27 eV) and defect level emission (2–3 eV). The resistivity of the films exposed to higher fluence was reduced by four orders of magnitude compared to that of the unirradiated sample [7].

Gamma irradiation of ZnO nanoparticles at doses in the range 20-80 kGy significantly affects their absorption properties, the band gap ( $E_g$ ) and the electrical conductivity. UV-Visible spectroscopic studies showed that the band gap of ZnO nanoparticles increases as a result of gamma irradiation, which can be correlated with a decrease in the dc conductivity [8]. As well, it was reported that ZnO–CuO doped PVA nanocomposite thin films exposed to 60 Co  $\gamma$ -radiation source ranging from 0 to 30 kGy showed smoother surfaces for the highest gamma radiation dose.

Spectroscopy in the wavelength range 300–800 nm indicated that  $E_g$  increases from 2.70 to 3.80 eV as the  $\gamma$ -radiation dose increases [9].

The effect of alpha particles on the properties of ZnO thin films are scarcely reported. Some studies reported on the defects produced by irradiation, such as Zn interstitials ( $Zn_i$ ) resulted by 1.8 MeV proton irradiation of ZnO films, with fluences from  $1 \times 10^{13} \text{ cm}^{-2}$  to  $2.4 \times 10^{14} \text{ cm}^{-2}$  [10], or oxygen vacancies (OVs) produced in ZnO coatings and ZnO thin films or TFT devices [11]. It was reported that high-dose proton irradiation of indium-doped ZnO films changed their resistivity due to the formation of point defects and structure amorphization [12].

In this study we present the structural and photoluminescence properties of ZnO, N:ZnO and Li:ZnO thin films irradiated with 3 MeV alpha particles at 5.3 kGy/h and evaluate the effect of exposure time on the type and concentration of the radiation induced defects. The main features of the ab initio calculated electronic structure of the non-irradiated materials are highlighted. As well, we report results of numerical modeling of the electrical and coupled thermal-electrical behavior of ZnO FET transistors with defects. We evidence that the defect concentration, their distribution and the size of the defected regions strongly affect the current density and the temperature map in the FET channel.

## **2. Experimental**

### ***2.1. ZnO Films Preparation***

ZnO and Li or N doped ZnO (Li:ZnO, N:ZnO) thin films were deposited onto Si/SiO<sub>2</sub> and glass substrates by sol-gel method, spin coating technique. The precursor materials were zinc acetate dihydrate, Zn (CH<sub>3</sub>COO)<sub>2</sub>·2H<sub>2</sub>O (99.50% pure) (ZAD) and 2-methoxyethanol (2-ME). The solution was prepared by dissolution of ZAD in 2-ME, and then monoethanolamine (MEA) was added as stabilizer. This precursor solution was mixed at approximately 60°C for 1 h to yield a clear and homogeneous sol. Doping solutions were prepared from lithium acetate (Li (CH<sub>3</sub>CO<sub>2</sub>), LiAc (99.95%)) dopant source of Li, and ammonium acetate ((CH<sub>3</sub>COONH<sub>4</sub>) 99.99%) dopant source of N and were added to the sol. The concentration of doping elements in the solutions were 1, 3 and 5 at. % Li and 1, 3 and 5 at.% N. Also, some of the ZnO films were prepared in the presence of two doping elements Li, and N. The concentration of dopants in these films was 3 at. % Li and 5 at.% N.

The sol solutions were further spin-coated onto the substrates and stabilized by a pre-treatment as following: i) ZnO films were spin-coated onto the substrates at 1500 rpm for 30 s, then each layer was stabilized at 300°C for 10 min. The deposition process was repeated five times and led to the formation of ZnO films with thickness of about 100 nm. A final annealing of the films was performed at 500°C for 1 h in ambient atmosphere; ii) Li:ZnO films were spin coated onto substrates at 3000 rpm for 30 s and each layer stabilized at 130°C for 5 min. The

annealing was performed at 500°C for 1 h in ambient atmosphere. The thickness of the films was about 60 nm; iii) N:ZnO films were spin coated onto substrates at 3000 rpm for 30 s, then pre-treated at 130°C for 5 min to remove the organic compounds. The process was repeated five times, the films were annealed at 500°C for 1 h in ambient atmosphere. The thickness of the films was about 60 nm. vi) (Li, N) codoped films were deposited onto Si/SiO<sub>2</sub> and Si (FZ) substrates using the spin-coating process at 3000 rpm for 30 s, each layer was stabilized at 200 °C for 5 min and the thermal treatment after five layers deposition was performed at 500°C for 30 min in ambient atmosphere.

The electron paramagnetic resonance (EPR) investigations required thicker films, in order to have detectable amounts of unpaired spins in the samples, as well as substrates with high resistivity and very low content of paramagnetic impurities. Therefore four ZnO films were deposited on floating zone silicon substrates Si (FZ), using a ten layers spin-coating procedure, namely an undoped ZnO film, as reference, and three other ZnO films doped with 5 at. % N, 3 at. % Li and codoped with 3 at.% Li and 5 at. %N, respectively.

A detailed description of the thin films preparation by sol-gel process is presented in references [13, 14].

## ***2.2. Irradiation Conditions***

The films were irradiated with alpha particles at a dose rate of 5.3 kGy/h, the energy of 3MeV, and the irradiation time was varied from 100 s (~11 μC) to 500 s (~54 μC), 1000 s (~104 μC) and 8 h (~2100 μC).

The irradiations were performed at the U120 Cyclotron facility at the National Institute for R&D in Physics and Nuclear Engineering-“Horia Hulubei” (IFIN-HH), Bucharest.

## ***2.3. Characterization***

The surface morphology of the films was analyzed by using a Field Emission Scanning Electron Microscope (FESEM) - Nova NanoSEM 630 and Atomic Force Microscopy (AFM) by using a Scanning Probe Microscope NTEGRA Aura (NT-MDT Co). The structural characteristics were determined with a SmartLab X-ray thin film diffraction system from Rigaku, at grazing incidence (GIXRD). The photoluminescence (PL) emission spectra of the films were recorded with an Edinburgh FL920 fluorimeter, at 310 nm excitation wavelength.

The EPR experiments were performed on a Q-band (34 GHz) spectrometer model Bruker ELEXSYS E500Q equipped with variable temperature accessories, from the Center for advanced ESR/EPR techniques (CetRESav). Details about the equipment and magnetic field calibration procedures are described in ref. [15] and at <http://cetresav.infim.ro/>.

Transmission electron microscopy (TEM) investigations were performed by using a high resolution analytical electron microscope JEM ARM 200F. The microscope is equipped with a field emission gun (FEG) with a maximum acceleration voltage of 200 kV, CCD cameras for electronic recording of TEM / STEM images and electron diffractograms, an analytical unit EDS JEOL JED-2300T and a Gatan EELS Quantum SE unit. Microstructural investigations by TEM require the appropriate preparation of samples. The available preparation techniques allow obtaining samples with thicknesses below 50 nm, both in plan view and cross section. The samples were prepared by cutting and assembling the pieces (for the cross section specimens), mechanical polishing up to a thickness of approximately 20  $\mu\text{m}$  using the tripod technique, followed by thinning under an  $\text{Ar}^+$  ion beam up to electron transparency with the Gatan PIPS system.

#### ***2.4. First principles Calculations***

A study of the electronic structure in the Generalized Gradient Approximation (GGA) was performed using the FPLO14 code [16] in order to obtain accurate information at atomic scale on the effects of the dopant impurities. We used the Perdew-Burke-Ernzerhof (PBE) parametrization for the exchange and correlation potential [17] and a  $4 \times 4 \times 4$  k-points mesh (64 irreducible k-points) for the Brillouin zone integration. The substitutionally doped materials were simulated using  $3 \times 3 \times 2$  supercells built of ZnO unit cell at the equilibrium volume. All structural models were fully relaxed until a residual force less than  $5 \times 10^{-2}$  eV/Å on an atom was reached.

#### ***2.5. Numerical Simulations***

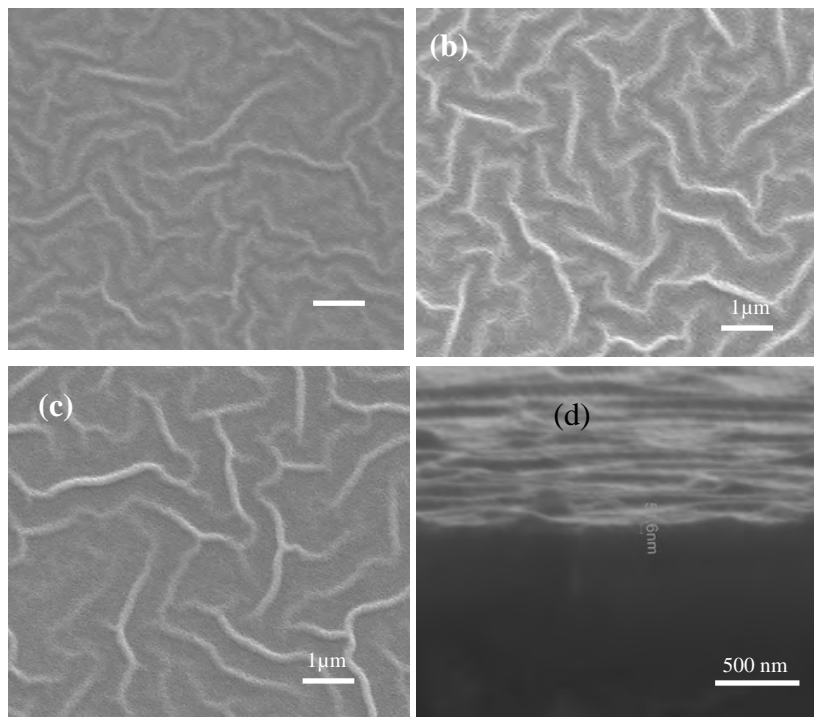
The effect of radiations - induced defects on the thermal and electrical properties of ZnO thin films used as active channel in thin film transistor devices has been simulated considering non-uniform resistivity of defective regions in the films volume. The resistivity variation was taken into account by discretization of the films thickness in several layers with different resistivity as function of defects density. Electro-thermal simulations were performed with CoventorWare 2012 design and simulation software tool, by applying a voltage to the electrodes of the test structure along with convection-thermal radiation boundary conditions on the external surfaces. Transient electric simulations were also performed with ANSYS Multiphysics 12.1 simulation tool for similar boundary conditions.

The electrical and thermal response of the test devices are simulated for various ZnO thin films geometries and defects distribution [18].

### 3. Results and Discussion

#### *a. As Prepared Films*

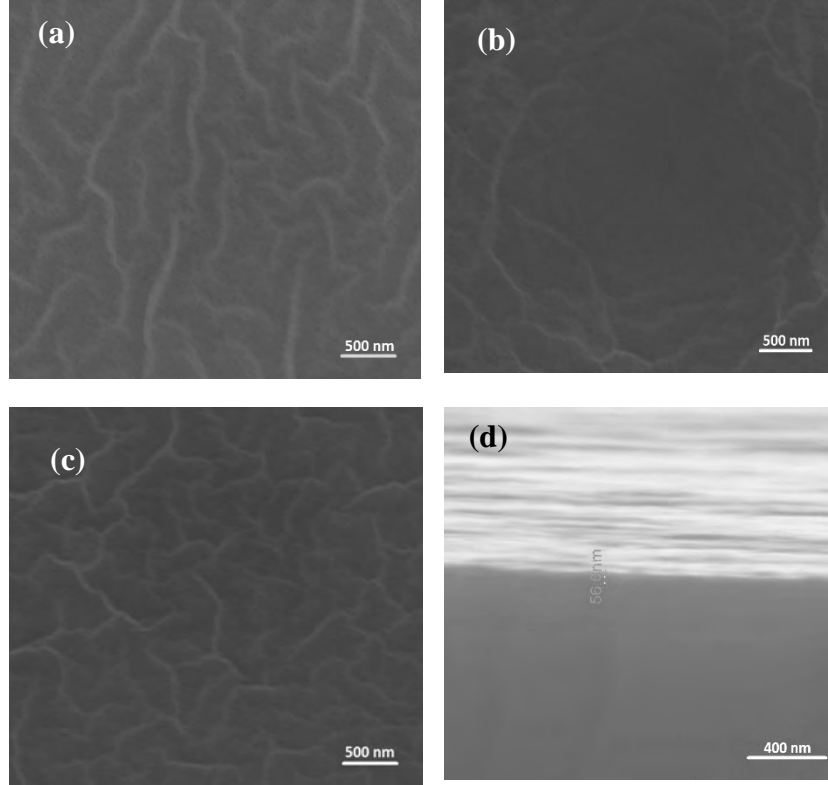
FESEM images of ZnO films doped with Li in various concentrations, 1-5 at. % are presented in Figs. 1 (a)-(d). The films have rough surfaces, with characteristic structural features, a network of fibers whose density decreases with increasing Li concentration from 1 at. %, 3 at. % and 5 at. %, Figs. 1(a), (b), (c). The cross section image presented in Fig. 1 (d) shows the cross section of a film doped with 5 % at. Li and the film thickness of 51.6 nm [14].



**Fig. 1.** Surface morphology of ZnO films doped with 1, 3 and 5 % at. Li: (a), (b), (c) FESEM images and cross section of a 5 % at. Li: ZnO film (d), [14].

Comparatively, the surface of the ZnO films doped with N, Figs. 2 (a)-(c), show a higher density of fibers, however the structures are less pronounced than those on the surface of the films doped with Li. FESEM images of Fig. 1 (a)-(c) emphasize a dense network of structures on the films surface. The cross section image of a film doped with 3 % at. N presented in Fig. 2 (d) shows that the film has a thickness of about 56 nm. Codoped films, with (3 at. % Li, 5 at. % N):ZnO present rough surfaces as well. XRD measurements demonstrate that all the films are polycrystalline, with wurtzite structure. The XRD patterns show main diffraction

peaks situated at  $2\theta=31.81^\circ$ ,  $34.44^\circ$ ,  $36.29^\circ$  which corresponds to (100), (002), (101) planes of ZnO wurtzite structure (standard JCPDS card No. 00-036-1451).



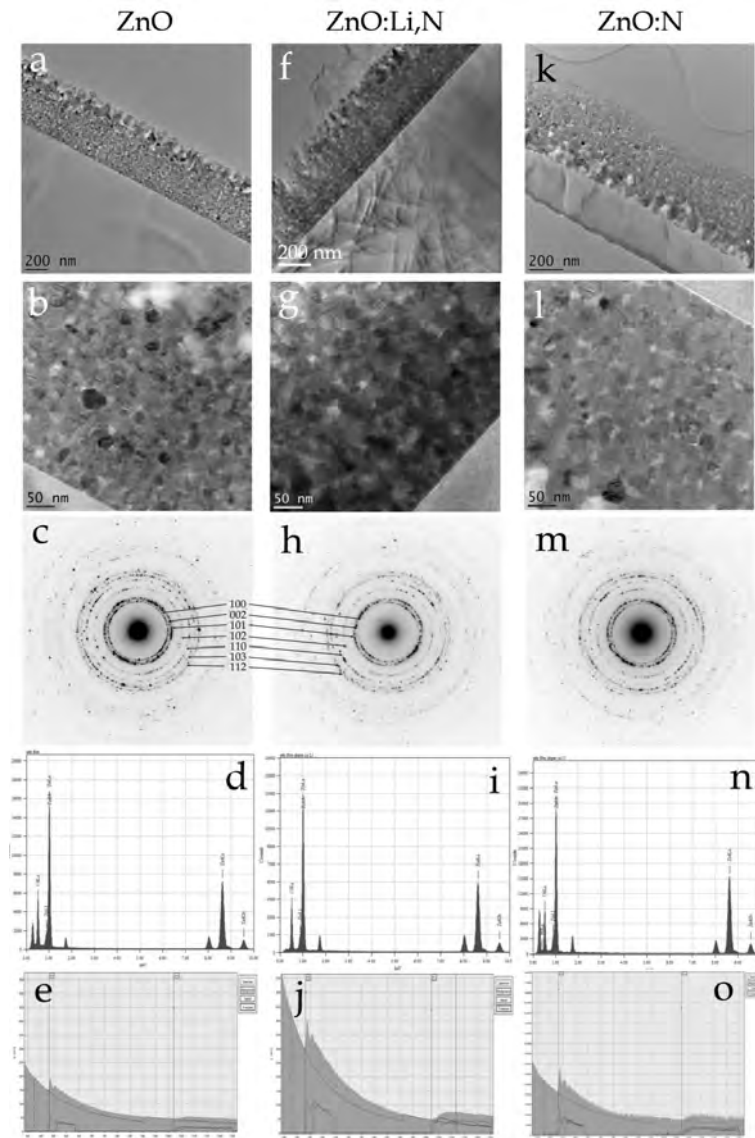
**Fig. 2.** Surface morphology of ZnO films doped with 1, 3 and 5 % at. N: (a), (b), (c) FESEM images and cross section of a 3% at. N: ZnO film (d), [14].

**Table 1.** The average crystallite size  $d_s$  (Scherrer),  $d_R$  (Rietveld),  $d_{W-H}$  (Williamson-Hall), lattice strain,  $\epsilon_R$ , residual stress,  $\sigma$ , for the Li:ZnO, N:ZnO and (Li,N):ZnO films.

Films	$d_s$ [nm]	$d_R$ [nm]	$d_{W-H}$ [nm]	$\epsilon_R$ [%]	$\sigma$ [GPa]
ZnO	13	16	15	0.23	0.18
3% Li:ZnO	14	13	16	0.11	0.18
5% N:ZnO	21	24	17	0.29	-0.31
(3%Li,5% N):ZnO	15	17	17	0.26	-0.31

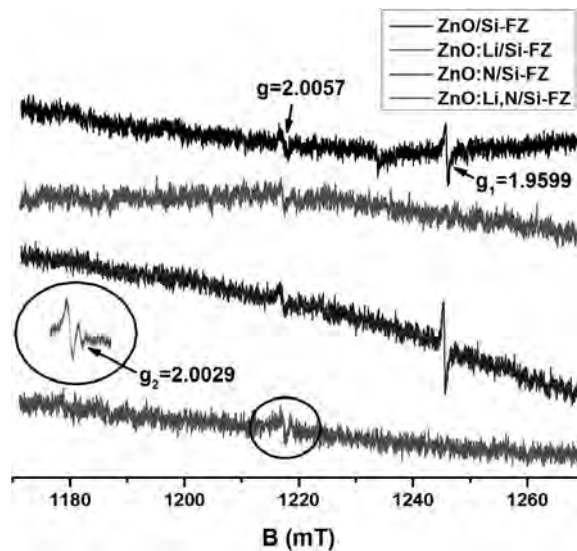
In Table 1 are listed the crystallites size in the films doped with 3 % at. Li and 5 % at. N and in the codoped films, calculated from the XRD data and refined with Rietveld and Williamson-Hall methods,  $d_s$  (Scherrer),  $d_R$  (Rietveld),  $d_{W-H}$

(Williamson-Hall), the lattice strain,  $\epsilon_R$ , and the residual stress,  $\sigma$ . One may observe the effect of N that causes an increase in crystallite size observed in the N:ZnO films and also in the codoped films. The lattice strain also increases in the films doped with N or codoped with Li and N. The residual stress in these films is compressive, which suggest that N substitute O in ZnO host lattice [14].



**Fig. 3** Morphological, structural and chemical properties of ZnO, (3 at.% Li, 5 at. %):ZnO and 5 at.% N respectively, determined by using transmission electron microscopy (a, b, f, g, k, l) electrons diffraction (c, h, m), EDS spectroscopy (d, i, n) and EELS spectroscopy (e, j, o).

TEM investigations were performed on the thicker ten layers ZnO films deposited on Si (FZ) for the EPR experiments. From the conventional transmission electron microscopy (CTEM) images of the undoped (Fig. 3 a), (Li, N) codoped (Fig. 3 f) and N doped (Fig. 3 k) ZnO films thicknesses of 440 nm, 520 nm and 440 nm, respectively, were determined for the three films. The high resolution transmission electron microscopy (HRTEM) images obtained at a higher magnification (Figs. 3 b), g) and l)) show that the films are composed of crystalline grains with different orientations, with a diameter ranging between 10 and 40 nm, their size increasing with the distance from the substrate. The electron diffraction patterns presented in Figs. 3 c), h) and m) demonstrate that the films are crystallized in a hexagonal structure with space group P63mc, with lattice parameters  $a = 3.2427 \text{ \AA}$  and  $c = 5.1948 \text{ \AA}$ , similar with the results of the XRD measurements. The chemical composition of the films is confirmed by the chemical analysis performed using energy dispersive X-ray spectroscopy (EDS). Figs. 3 d), i), n) indicate a composition of 49 at. % O and 51 at. % Zn for all three films. The films composition was determined also with the electron energy loss spectroscopy (EELS) technique. In the EELS spectra presented in Figs. 3 e), j), o), the O K line appears at 532 eV and the Zn L line at 1020 eV. The difference between the intensities of the O and Zn lines in the three spectra presented in Figs. e), j) and o) is due to the different thickness of the samples prepared for TEM. The signal-to-noise ratio is better for the thinner samples. The two doping elements, Li and N, could not be observed in the spectra, as they both are near the detection limit of these methods of analysis.



**Fig. 4.** Q-band EPR spectra of the ZnO, ZnO:Li, ZnO:N and ZnO:Li,N films deposited on floating zone silicon, measured at 90 K.



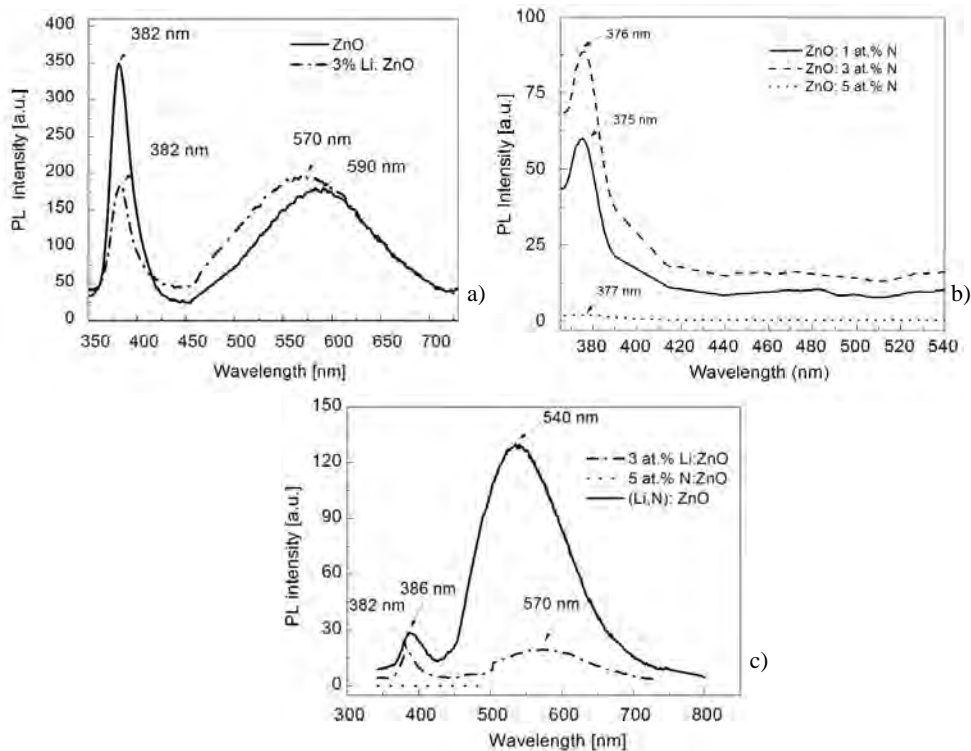
The electron paramagnetic resonance spectroscopy has been used as a very sensitive method to detect the presence of paramagnetic point defects in the films, being able to provide insightful information about their nature, structure, localization and ground state properties.

The EPR spectra of the films, recorded at 90 K, are displayed in Fig. 4. The EPR line with the  $g$ -factor value  $g = 2.0057$ , observed in all four samples, corresponds to the dangling bonds (DB) in the silicon substrate [19, 20]. Although no EPR spectrum, directly related to the presence of either N or Li dopants, could be observed at this temperature, the different doping has a visible effect on the defects formed in the films. The EPR spectrum of the film doped with N is similar with the spectrum of the undoped ZnO reference film, and contains, beside the DB signal, a strong line with  $g_1 = 1.9599$ , with similar intensity. This line corresponds to a shallow donor (SD) defect in ZnO, which has been previously associated with the presence of intrinsic defects like Zn in an interstitial position,  $Zn_i$  [21], or with the presence of impurities such as interstitial Na [22], substitutional Al [23] or Cl [24]. Given the impurity content of the starting materials, the origin of this defect could be assigned to either interstitial Zn or Na, which is present as native impurity in the ZAD precursor in concentrations of up to 50 ppm. The strong decrease of the SD signal intensity in the Li doped and (Li, N) codoped ZnO films could be an effect of the Li doping. The EPR spectrum of the codoped film shows the presence of another line at  $g_2 = 2.0029$ , which can be barely guessed in the other three samples. A survey of the existent literature shows that the only close  $g$ -values correspond to an acceptor center consisting of a substitutional  $Li^+$  ion, with a trapped hole at one of the four adjacent oxygen ligands. The reported values are  $g_{||} = 2.0026$ ,  $g_{\perp} = 2.0254$  in polycrystalline ZnO [24] and  $g_{||} = 2.0035$ ,  $g_{\perp} = 2.0254$  in a ZnO single crystal [25]. The  $g_2$  value would correspond, within experimental accuracy, to the reported  $g_{||}$  value. As the  $g_{||}$  signal is considerably weaker than the  $g_{\perp}$  one, the fact that we do not observe any feature corresponding to  $g_{\perp}$  makes this assignment debatable. Further investigations are needed in order to clearly assign this signal and to determine the presence of Li and N dopants in the films.

PL emission spectra of ZnO undoped, 3 at.% Li:ZnO, 5 at.% N:ZnO doped and (3 at.% Li, 5 at.%N):ZnO codoped films are presented in Figs. 5 (a), (b), (c). The PL spectrum of undoped ZnO film, Fig. 5 (a) shows two emission peaks, a sharp peak situated in ultraviolet (UV) region of the spectrum, at 382 nm (3.24 eV), and a broad and less intense emission maximum in the visible region (yellow-green), peaked at 590 nm (2.10 eV). The emission peak at 382 nm is attributed to direct band-band transitions (band edge emission) and gives the value of ZnO films band gap, Eg. PL emission peak located at 590 nm, is associated with the presence of intrinsic point defects in the film. Several type of defects, e.g. oxygen vacancies ( $OV_s$ ), oxygen interstitial ( $O_i$ ), zinc interstitial ( $Zn_i$ ), zinc vacancies ( $Zn_v$ ) or "antitsite" defects can act as radiative centers with emission bands in the visible region [26]. Previous PL spectroscopy studies suggested that

$Zn_i$  and  $Zn_v$  defects may contribute to blue and green emission, while  $O_i$  and  $O_v$  vacancies tend to produce yellow-orange and green-yellow emission, respectively. Extrinsic impurities, such as doping impurities can also contribute to the PL emission [27].

The PL emission spectrum of Li doped ZnO films, Fig. 5 a), shows a more intense emission peaked at 570 nm (2.17 eV) which suggests the presence of defects induced by Li doping. Contrary, the films doped with 1 at. % N and 3 at. % N exhibit an increased intensity of the UV emission peak, situated at 375 nm (3.30 eV) and 376 nm (3.29 eV) respectively, and quenching of the emission in the visible spectral region as can be observed in Fig. 5 b). Previously, PL peaks situated at 3.334 and 3.31 eV in the spectra of N doped ZnO films epitaxially grown n-type ZnO single crystal substrates were assigned to neutral acceptor-bound exciton (A0X) emission and a donor-acceptor pair (DAP) emission, respectively, [28]. In these films free exciton emission was observed at about 3.375 eV. The strong quenching of the emission peaks associated with intrinsic defects observed in Fig. 5 b) suggests that N annihilates the defect centers that yield luminescence emission at 570 nm. It can be observed that the PL emission is overall reduced in the films doped with 5 at.% N.



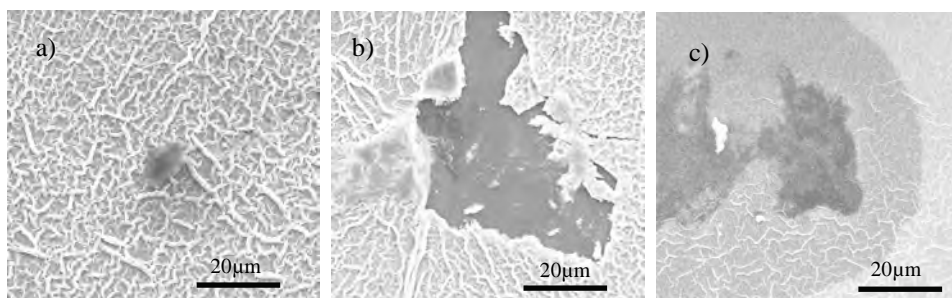
**Fig. 5.** PL emission spectra of the ZnO and 3 at.% Li: ZnO films (a), 1 at.%, 3 at.%, and 5 at.% N:ZnO films (b) and (3 at.% Li, 5 at.% N):ZnO films (c).

Fig. 5 c) shows the PL emission spectra of ZnO films doped with Li, N, or codoped with (Li, N). The PL emission spectrum of the codoped film shows a low intensity emission peak situated at 386 nm (3.21 eV) and a relatively broad and intense peak situated at 540 nm (2.30 eV). Therefore, PL spectra reveal the presence of dissimilar defects in Li and N doped films. The emission peak at 3.21 eV observed in the codoped films may be related to the presence of Li(Zn)-N(O) complex [29]. Previously, PL peak located at 3.24 eV in ZnO was attributed to radiative recombinations of donor-acceptor type and the PL peak located at 2.4 eV to recombination involving defect centers situated in the bandgap, such as  $OV_s$ ,  $Zn_i$ ,  $O(Zn)$  [30]. It was also reported that the PL peak situated at 3.21 eV is associated to the presence of acceptor complex defect involving Li and N, *e.g.* Li(Zn)-N(O) [31].

PL spectra of the films exposed to radiation should exhibit modifications in terms of intensity and peaks position due to radiation-induced defects, then a study of PL emission of ZnO and doped ZnO films has been performed to bring data on the mechanism of defects formation in ZnO films.

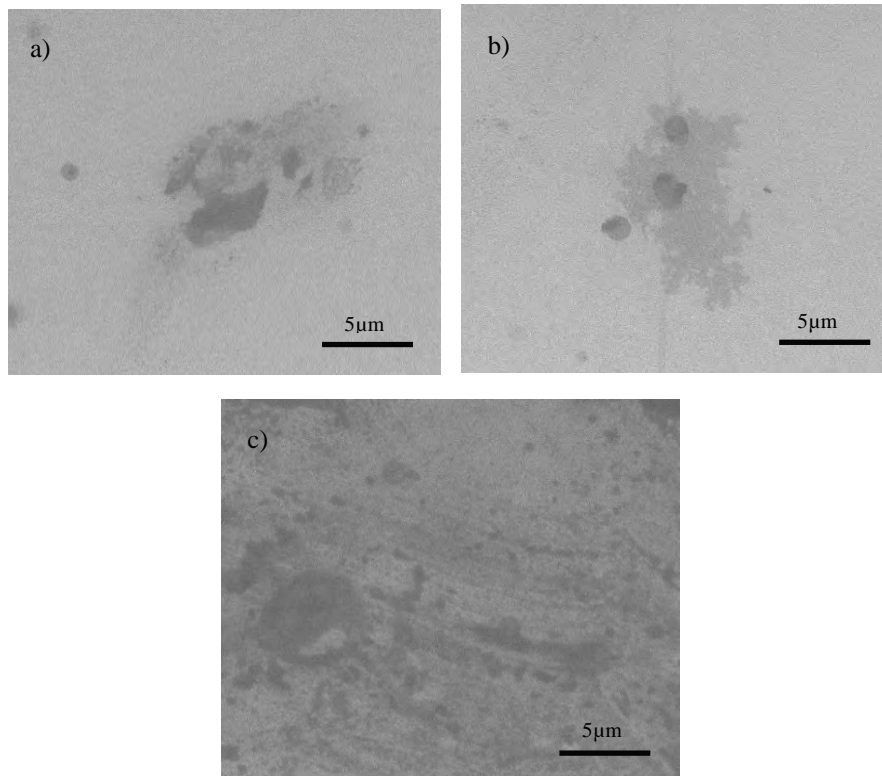
### 3.2. Irradiated Films

The FESEM images of ZnO films (Si(500  $\mu\text{m}$ )/SiO<sub>2</sub>(270 nm)/ZnO (100 nm), exposed to alpha particles with 3 MeV energy at a dose rate of 5.3 kGy/h, for various irradiation times are presented in the Figs. 6 a), b), c). After exposure to radiation for 100 s, the irradiated zone appears as a darker colored region in the centrum of the sample, Fig. 6 a). With increasing the exposure time to 500 s, irradiated dark region becomes larger. Also, some portions of the ZnO film appear as separated from the substrate, Fig. 6 b). The surface of the ZnO films exposed to radiation for 1000 s present two damaged regions, one with a darker color, surrounded by a more extended region which has a less pronounced color change, Fig. 6 c). It was previously reported that radiation induced coloration in ZnO is determined by OVs generated during irradiation, which create hydrogen like bound state with the nearby electrons. The defects created are F-centers or color centers [32]. The diameter of the affected region is about 10  $\mu\text{m}$  after exposure to radiation for 100 s, 20  $\mu\text{m}$  after 500 s and 100  $\mu\text{m}$  after 1000 s, respectively.



**Fig. 6.** FESEM images of ZnO films exposed to 3 MeV, 5.3 kGy/h alpha particles: a) 100 s (~ 11  $\mu\text{C}$ ), b) 500 s (~ 54  $\mu\text{C}$ ), c) 1000 s (~ 104  $\mu\text{C}$ ).

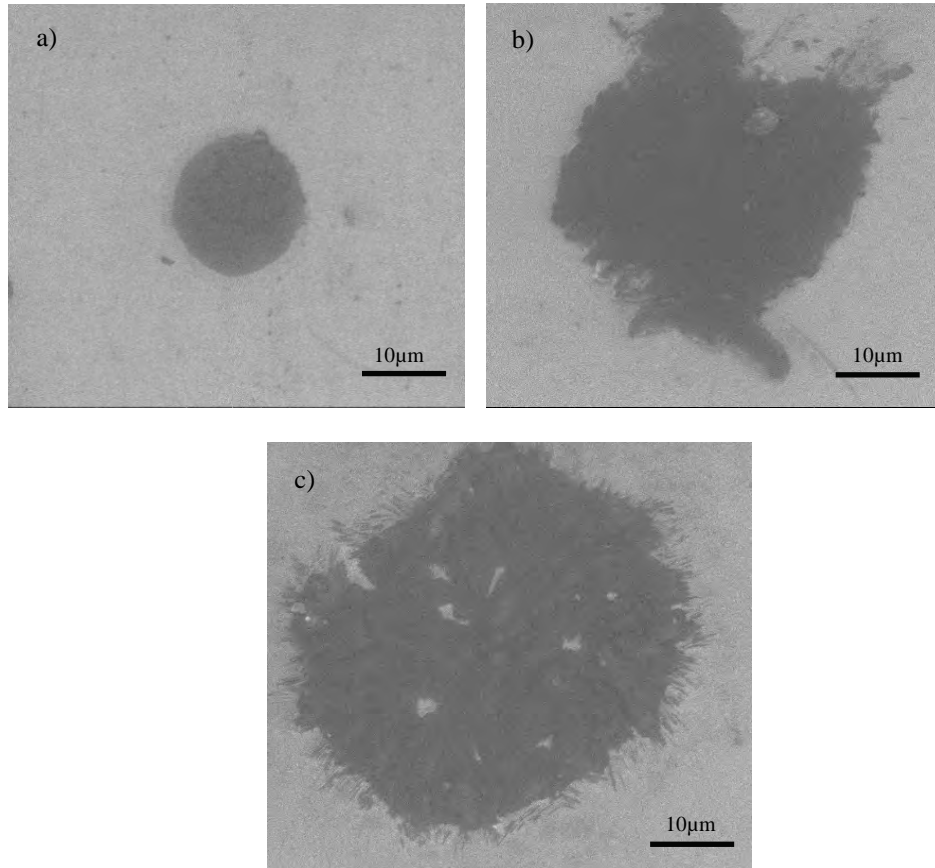
Figs. 7 a), b), c) show the FESEM images of the 1 at.% Li: ZnO films (Si (500  $\mu\text{m}$ )/SiO<sub>2</sub>(270 nm)/Li:ZnO (150 nm) irradiated with alpha particles in the same conditions as ZnO films. In this case the area affected by irradiation remains almost constant for short irradiation times and expands after increasing irradiation time to 1000 s. The films show a better stability comparatively with ZnO films. The surface of the damaged regions is  $\sim$  5-10  $\mu\text{m}$ , much smaller than in the case of ZnO films presented in Fig. 6. The increased stability of the Li doped films can be associated with the higher thickness of those films.



**Fig. 7.** FESEM images of 1 at.% Li: ZnO films exposed to 3 MeV, 5.3 kGy/h alpha particles: a) 100 s ( $\sim$  11  $\mu\text{C}$ ), b) 500 s ( $\sim$  54  $\mu\text{C}$ ), c) 1000 s exposure ( $\sim$  104  $\mu\text{C}$ ).

Figures. 8 a), b), c) present FESEM images of 3 at.% N: ZnO films (Si(500  $\mu\text{m}$ )/SiO<sub>2</sub>(270 nm)/N: ZnO (60 nm)), irradiated in the same conditions as ZnO and 1 at.% Li: ZnO films. The irradiated regions appear as dark zones whose area increases with the exposure time increases. The diameter of the dark regions is about 10  $\mu\text{m}$  after exposure for 100 s, 30  $\mu\text{m}$  after 500 s and 40  $\mu\text{m}$ , after 1000 s, respectively. It appears that 3 at.% N:ZnO films are more stable to the irradiation

with alpha particles comparatively to ZnO, which suggests that the chemical composition could influence their response to irradiation.

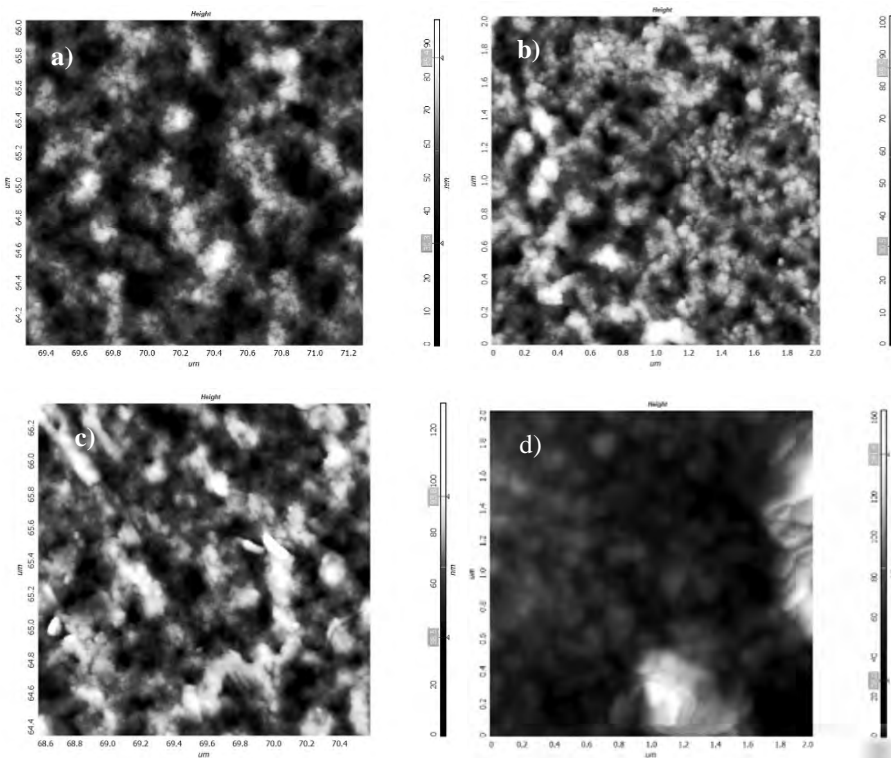


**Fig. 8.** FE-SEM images of 3 at. % N: ZnO films exposed to 3 MeV, 5.3 kGy/h alpha particles: a) 100 s (~ 11  $\mu\text{C}$ ), b) 500 s (~ 54  $\mu\text{C}$ ), c) 1000 s (~ 104  $\mu\text{C}$ ).

AFM images present the evolution of films surface roughness when the time of exposure to radiation increases. Figures 9 a), b), c), d) show the surface of ZnO films before and after radiation exposure for 500 s, 1000 s and 8 h, respectively. The surface roughness decreases after short time irradiation, 500 s, and increases after longer exposure to radiation, *e.g.* 1000 s, as can be observed in the diagram presented in the Fig. 10. The root mean square ( $R_{\text{rms}}$ ) value resulted from AFM measurements on  $2\mu\text{m} \times 2\mu\text{m}^2$  area, decreases from 12 nm in unirradiated films to 11 nm in the films exposed to radiations for 500 s, and slightly increases up to 13 nm in the films exposed for 1000 s. The films irradiated for 8 h show a transition region at the interface between the irradiated and non-irradiated zone where the  $R_{\text{rms}}$  value is 11-15 nm.  $R_{\text{rms}}$  value in the irradiated area presented in Fig.

9 c), is about 23 nm in the localized zones containing clusters or large grains, while in the smoother zones the value decreases to about 10 nm.

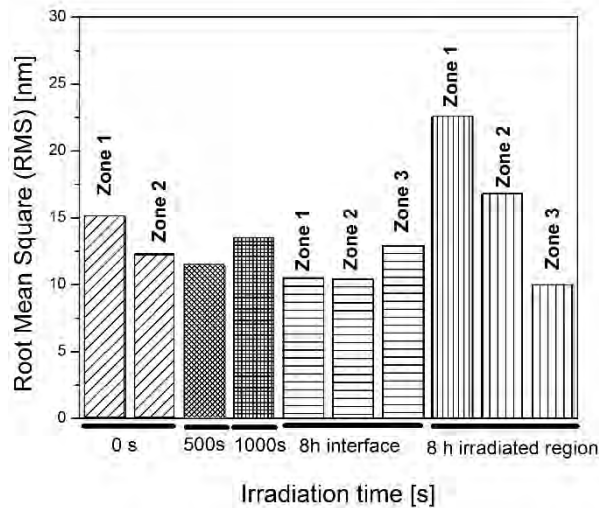
The results indicate a slight recrystallization of the surface caused by the heat generated during irradiation for 500 s, Fig. 9 b) and 1000 s, Fig. 9 c). The recrystallization process is stronger in the films exposed to radiation for 8 h and leads to formation of larger grains and clusters of grains, Fig. 9 d). It was previously reported that agglomeration of grains result as the effect of energy transfer from the accelerated particles to the materials and the irradiated regions had increased roughness [1-3].



**Fig. 9.** AFM images of the non-irradiated ZnO films a), and after exposure to 3 MeV, 5.3 kGy/h alpha radiation for 500 s b), 1000 s c) and 8 h d).

PL spectra of non-irradiated and irradiated ZnO films are presented in Fig. 11. Fig. 11 a) shows the PL emission spectra of non-irradiated ZnO films and after exposure to alpha particles for 100 s, 500 s and 1000 s respectively. The PL spectrum of non-irradiated films exhibit emission peaks situated at 3.26 eV (380 nm) and 2.75 eV (450 nm) and also a broad peak, with low intensity, in the region 2.60-2.25 eV (476 nm-551 nm). While the PL emission in the UV region is determined by free excitons band to band transitions, the emission peak in the

green-orange region is related to radiative transitions involving native point defects in ZnO [33-35]. The PL emission of the films irradiated for 100 s presents a slightly increased peak situated at 3.28 eV (378 nm) and decreased intensity of the peak at 2.75 eV. Low intensity and broad emission can also be observed in the region 2.59 - 2.23 eV (479 nm - 556 nm).

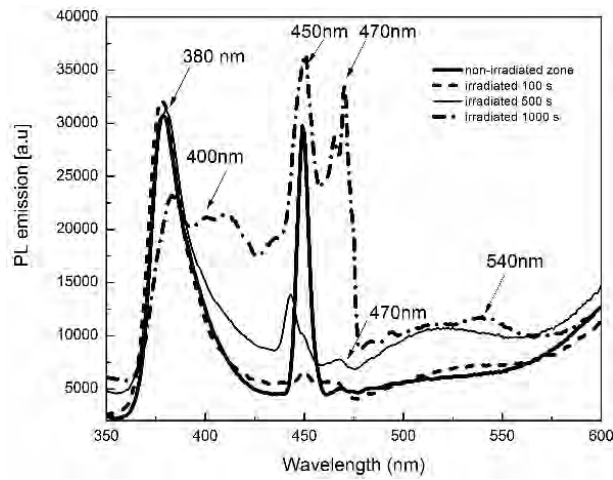


**Fig. 10.** Variation of surface roughness of ZnO films as function of irradiation time.

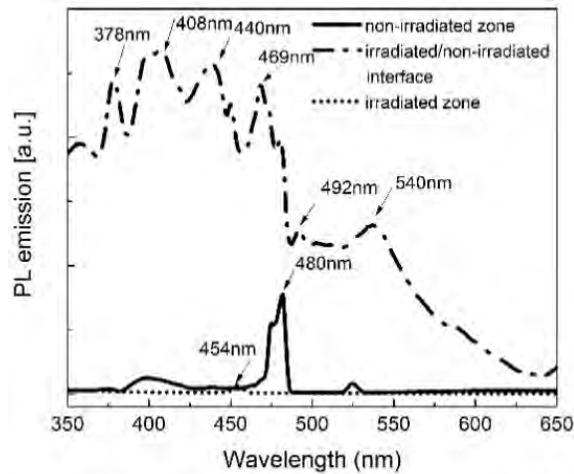
After exposure to irradiation for 500 s, PL spectrum shows that the emission peak at 380 nm (3.26 eV) remains intense, while the intensities of the peaks at 443 nm (2.80 eV), 468 nm (2.65 eV), 517 nm (2.40 eV) decrease significantly. The PL spectrum of the films irradiated for 1000 s exhibits new peaks situated at 400 nm (3.10 eV) and 470 nm (2.64 eV) which suggest the formation of  $Zn_i$  defects. The increased intensity of the peak situated at about 540 nm (2.30 eV) can be associated with the formation of oxygen vacancies (OVs).

The PL spectrum of ZnO films exposed to radiations for 8 h is presented in Fig. 11 b). The PL emission spectrum exhibit several peaks 384 nm (3.23 eV), 400 nm (3.10 eV), 410 nm (3.02 eV), 451 nm (2.75 eV), 473 nm (2.62 eV), 470 nm (2.64 eV), 540 nm (2.30 eV) observed at the interface between non-irradiated and irradiated regions. The PL emission is almost quenched in the irradiated region. The evolution of PL peaks suggest that the irradiation with alpha particles generates displacement defects such as  $Zn_i$  only for longer irradiation time (more than 1000 s), while the OVs are produced even after a short exposure time. The intensity of the PL peak corresponding to near band edge transitions decreases after long exposure time, while the intensities of the emission peaks associated with point defects increase, suggesting that both  $Zn_i$  and OVs act as efficient radiative centers [36].

Figures 12 a) and b) show the PL emission spectra of doped films, 1 at.% Li: ZnO and 3 at. % N: ZnO films, respectively, before and after exposure to alpha radiations for 100 s, 500 s and 1000 s. The PL emission of the films doped with Li increases after irradiation for 1000 s as is observed in Fig. 12 (a). Emission peaks are situated in the UV- visible region at 375 eV (3.30 eV), 410 nm (3.02eV), 440 nm (2.82 eV), 455 nm (2.72 eV) and 475 nm (2.61 eV). The emission could be associated with the presence of various type of defects induced by radiation, as these emission bands are observed only after long time exposure to alpha particles flux.



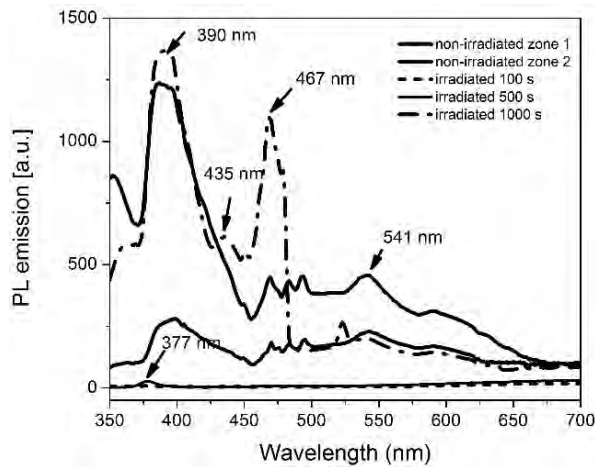
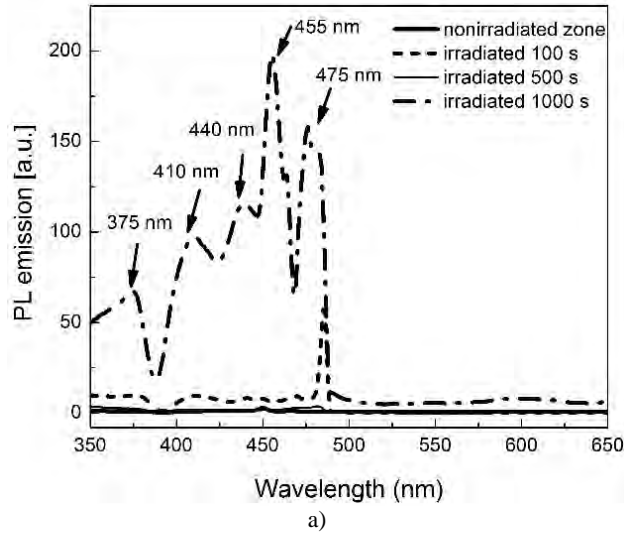
a)



b)

**Fig. 11.** PL emission of spectra of non-irradiated and of ZnO films irradiated with 3 MeV, 5.3 kGy/h alpha particles for: a) 100 s, 500 s, 1000 s and b) 8h.





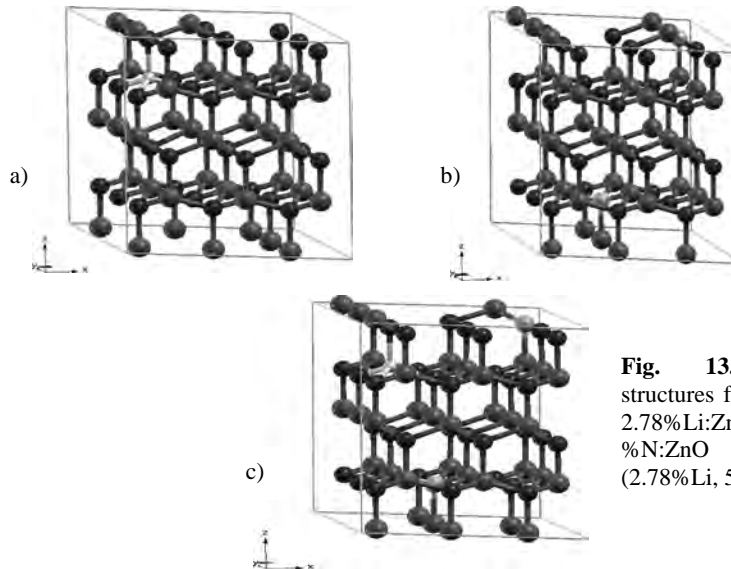
**Fig. 12.** PL emission of spectra of non-irradiated and of irradiated ZnO films:  
a) 1 at. % Li: ZnO films and b) 3 at. % N: ZnO films, irradiated with  
3 MeV, 5.3 kGy/h alpha particles for 100 s, 500 s, 1000 s.

The PL spectrum of the films doped with N are presented in Fig. 12 b). As in the case of the films doped with Li, the PL emission exhibits an increased intensity after irradiation for 1000 s. The emission peaks are situated at 380 nm (3.26 eV), 435 nm (2.85 eV), 467 nm (2.66 eV), 550 nm (2.25 eV). It appears that different radiation-induced defects acting as radiative centers form in 1 at. % Li: ZnO and 3 at. % N: ZnO films, respectively. The UV emission peak is situated at 3.30 eV in PL spectrum of Li:ZnO film and at 3.26 eV in the PL spectrum of N:ZnO films

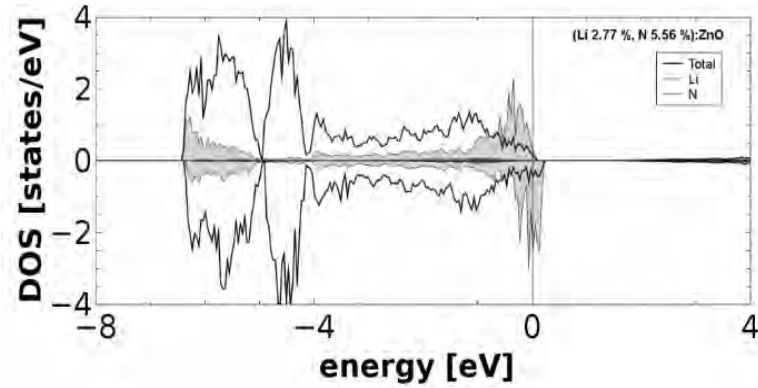
irradiated for 1000 s, suggest that Li and N doping strongly affect the band structure of the ZnO films which respond differently to radiation exposure. Several emission peaks situated at 3.02 eV to 2.61 eV in the PL spectrum of Li:ZnO films and at 2.85 eV to 2.25 eV in the spectrum of N:ZnO films may be related to various defects in the two type of films.

### 3.3. Electronic properties of 2.78 %Li:ZnO, (b) 5.56 %N:ZnO and (2.78 %Li,5.56%N):ZnO systems

Herein we discuss some results of DFT calculations for the 2.78 % Li:ZnO, 5.56 % N:ZnO and (2.78 % Li,5.56 % N):ZnO systems. Figs. 8 a), b), c), show the relaxed supercell structures for these systems. The density of states (DOS) plots reveal that Li substitution for Zn does not introduce an impurity level in the ZnO band gap. Instead, the N 2p states form a band almost completely filled at the Fermi energy which merges with the valence band maximum (VBM) dominated by O 2p states. At energies between -6.5 and -5 eV the N 2p orbitals hybridize strongly with Zn 3d ( $e_g$ ) orbitals and also with the O 2p orbitals between -4 and -0.5 eV. The fundamental state is paramagnetic with a magnetic moment of  $0.37 \mu_B$  localized at the N sites. A small polarization, of about  $0.06 \mu_B$  is found on the O near neighbors to N sites. The DOS plot of (2.78% Li, 5.56% N):ZnO, shown in Fig. 14, reveals that each dopant species produces its own characteristic effect, as that in the monodoped case. The N 2p states hybridize with O 2p and Li 2p states just below the Fermi level and also with Zn 3d ( $e_g$ ) states at lower energy. The results underline the contributions of Li and N impurities to electronic structure of ZnO [29].



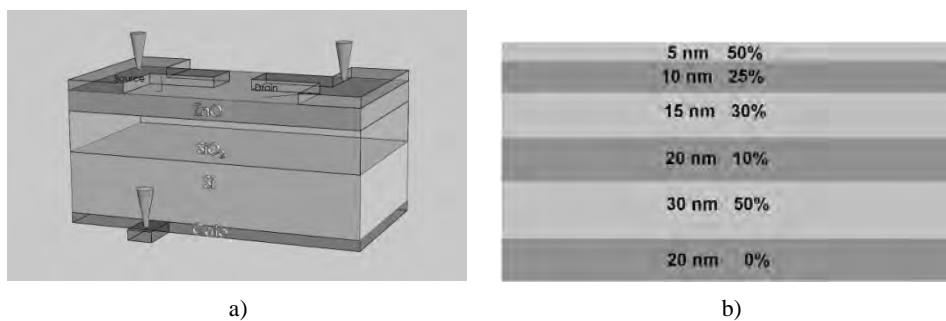
**Fig. 13.** Supercell structures for systems: a) 2.78%Li:ZnO, b) 5.56 %N:ZnO and c) (2.78%Li, 5.56%N):ZnO.



**Fig. 14.** Total DOS, per formula unit volume, and Li and N partial DOS in (2.78% Li, 5.56% N): ZnO.

### 3.4. Electro-Thermal and Electrical Simulation

Numerical simulations of the effect of radiation-induced defects on the electro-thermal and electric operation mode of a field effect transistor (FET) have been performed on a test structure with the layout presented in Fig. 15. FET devices were built in the bottom-gate configuration, with the channel parameters length  $L=10\text{-}50\ \mu\text{m}$  and width,  $W=100\text{-}600\ \mu\text{m}$ , Fig. 15 a). The device consists of a 100 nm thick ZnO film as active channel, deposited on  $\text{SiO}_2$  layer (270 nm) grown on Si substrate, with source (S), drain (D) and bottom gate (G) electrodes from Au. The presence of radiations-induced defects in ZnO thin films was simulated considering a nonuniform resistivity in the film volume. The resistivity variation was taken into account through discretization of the films thickness in several layers whose resistivities correspond to a certain concentration of defects as presented in Fig. 15 b).

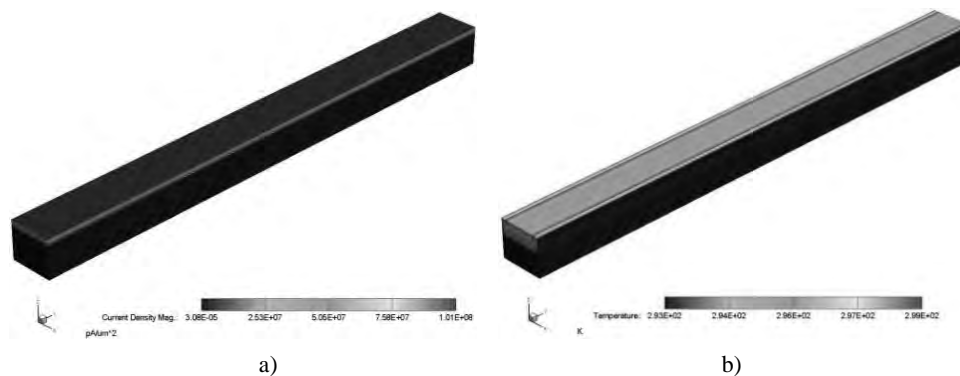


**Fig. 15.** FET device a) and ZnO film meshed in layers with variable thickness and density of defects % b).

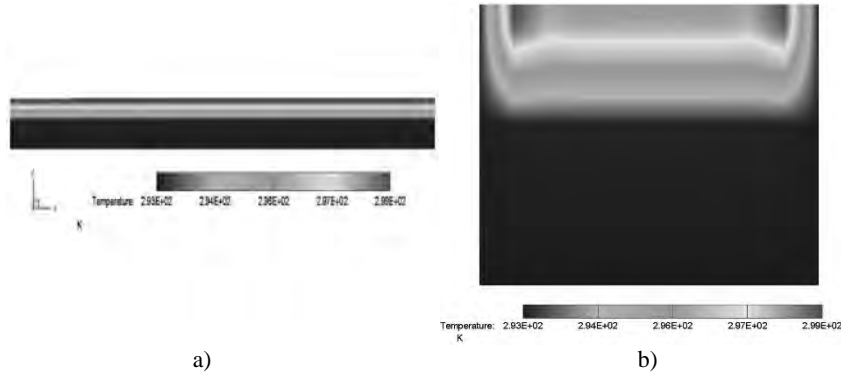
Electro-thermal simulations were performed with CoventorWare 2012 software package, by applying a voltage on the electrodes of the test structure and convection-thermal radiation boundary condition on the external surfaces. The voltage applied between the electrodes was 40 V, the convection-thermal radiation occurs on lateral and top surfaces, the top electrodes and the bottom surface were kept at room temperature (293 K). The electro-thermal simulations were carried out on a FET device with  $L=10\ \mu\text{m}$  and  $W=600\ \mu\text{m}$  [18].

The current density and temperature distribution in the test device with a defective ZnO film are presented in Figs. 16 a) and b). The current density for defect-free structure varies between  $3.08\times 10^{-5}$ - $2\times 10^8\ \text{pA}/\mu\text{m}^2$  whereas for the structure with defects the current density in the defective layers varies between  $3.08\times 10^{-5}$ - $1.01\times 10^8\ \text{pA}/\mu\text{m}^2$ . The maximum temperature in ZnO thin film is reached near the electrodes, and this value is higher in the defect-free structure, 312K, than in the structure with defects, 299 K. Temperature distribution along the FET channel and in the channel cross section is presented in Fig. 17. The temperature gradient show that the maximum value is obtained at the lateral contacts. As well, the temperature decreases in the film volume.

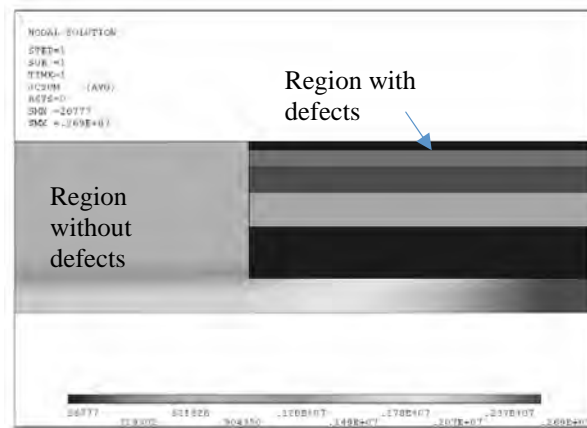
Transient electric simulations were performed with ANSYS Multiphysics 12.1 simulation tool, for similar boundary conditions, the voltage between the electrodes 1V, and the parameters of the FET device,  $L= 50\ \mu\text{m}$  and  $W = 500\ \mu\text{m}$ . Fig. 18 shows the current density distribution in the channel region of a FET device. The current density has a maxim value in the bottom region of the FET channel under the defected area. In the defected region the current density decreases with the concentration of defects, *e.g.* the degree of the defective region increases. The current density remains high in the region which correspond to the 4th layer, with the thickness of 20 nm and 10 % defects, as presented in Fig. 15 b).



**Fig. 16.** Electro-thermal simulation of FET device with defects: a) current density ( $\text{pA}/\mu\text{m}^2$ ) and b) temperature distribution (K) in the ZnO film 3D structure with defects.



**Fig. 17.** Temperature distribution (K): a) along the FET channel and in the cross-section of the FET channel.



**Fig. 18.** Current density distribution in the channel region of a ZnO FET: the interface between region without and region with defects.

#### 4. Conclusions

The morphology, structure and luminescence emission properties of ZnO and Li, N doped or (Li, N) codoped thin films prepared by sol-gel method, spin-coating technique have been investigated by FESEM, HRTEM, AFM and PL spectroscopy, with emphasis on the contributions arising from alpha radiation induced defects, and intrinsic defects and impurities, respectively. The presence of paramagnetic point defects in the films has been evidenced by electron paramagnetic resonance (EPR) spectroscopy and confirmed by the calculated electronic structure of the N doped and (Li, N) codoped systems.

The effect of irradiation with alpha particles on the structure and luminescence emission of ZnO and Li, N doped ZnO thin films has been investigated by FESEM, AFM and PL. Particularly, the PL emission of the films has been analyzed, aiming to evaluate the type and density of radiation-induced point defects as a function of the exposure time.

The AFM images point out changes in the morphology of ZnO films irradiated with alpha particles, showing that surface roughness decreases after short irradiation time, (500 s), and increases after several hours of exposure to radiation when crystalline grains with increased size and clusters of grains appear on the films surface.

The PL spectra of the films exposed to alpha particles beam reveal the variation of the peaks intensities, as well as the presence of new emission bands, suggesting that new radiative centers associated with point defects have been formed by irradiation. We suggest that the irradiation with alpha particles generates displacement defects such as Zn interstitials only for longer irradiation time (more than 1000 s), while the OV's are produced even after a short exposure time (100 s).

Numerical simulation of radiation-induced defects ZnO thin films materials electro-thermal and electrical behavior has been performed by using test FET devices with defective ZnO films as active channel. It was found that the concentration of defects and the size of the defected regions strongly affect the current density and the temperature in the FET channel.

**Acknowledgements.** This research was supported by STAR program, Project no. 94 MATSPACE, funded by Romanian Space Agency ROSA.

## References

- [1] E.-J. YUN, J.W. JUNG, Y.H. HAN, M.-W. KIM, B.C. LEE, *J. Appl. Phys.* **105**, 123509, 2009.
- [2] E.-J. YUN, J.W. JUNG, B.C. LEE, M. Jung, *Surf. Coat. Technol.* **205** (2011) pp. 5130–5134.
- [3] E.-J. YUN, J. W. JUNG, B.C. LEE, *J. Alloys Compd.* **496** (2010) 543–547.
- [4] E. GÜR, H. ASIL, C. COŞKUN, S. TÜZEMEN, K. MERAL, Y. ONGANER, K. ŞERİFOĞLU, *Nucl. Instrum. Methods Phys. Res. B* **266** (2008), pp. 2021–2026.
- [5] J.S. BHAT, A.S. PATIL, N. SWAMI, B.G. MULIMANI, B.R. GAYATHRI, N.G. DESHPANDE, G.H. KIM, M.S. SEO, AND Y.P. LEE, *J. Appl. Phys.* **108**, 043513 (2010).
- [6] M.T. MYERS, S. CHARNVANICHBORIKARN, M.A. MYERS, J.H. LEE, H. WANG, M.M. BIENER, L. SHAO, S.O. KUCHEYEV, *Appl. Surf. Sci.* **276** (2013) 129–132.
- [7] S. CHATTOPADHYAY, S. DUTTA, D. JANA, S. CHATTOPADHYAY, A. SARKAR, P. KUMAR, D. KANJILAL, D. K. MISHRA, S. K. RAY, *J. Appl. Phys.* **107** (2010) 113516.
- [8] K. SWAROOP, C.S. NAVEEN, H.S. JAYANNA, H.M. SOMASHEKARAPPA, *AIP Conference Proceedings* **1665**, 050100 (2015); doi: 10.1063/1.4917741.
- [9] N.A.N. AZMY, H. ABDULLAH, N.M. NAIM, A.A. HAMID, S. SHAARI, W.H.M.W. MOKHTAR, *Radiat. Phys. Chem.* **103** (2014), pp. 108–113.
- [10] M. HAYES, F.D. AURET, P.J. Janse van Rensburg, J.M. Nel, W. Wesch, E. Wendler, *Nucl. Instrum. Meth. B* **257** (2007), p. 311–314.

- [11] H. XIAO, M. SUN, C. LI, D. YANG, B. HAN, S. HE, Nucl. Instrum. Meth. B 266 (2008), pp. 3275–3280.
- [12] Y.-K. MOON, S. LEE, D.-Y. MOON, W.-S. KIM, B.-W. KANG, J.-W. PARK, Surf. Coat. Tech. 205 (2010), pp. S109–S114.
- [13] A. DANCIU, I. MIHALACHE, M. DANILA, B. BITA, R. PLUGARU, *2014 International Semiconductor Proc. (CAS)*, **1** 77 IEEE Catalog Number: CFP14CAS-PRT, ISBN: 978-1-4799-3916-9, ISSN: 1545-827X.
- [14] A. DANCIU, I. MIHALACHE, B. BITA, R. PLUGARU, *2014 14<sup>th</sup> International Balkan Workshop on Applied Physics, 2-4 July 2014, Constanta Romania*. To appear in: J. Optoelectron. Adv. Mater.
- [15] M. STEFAN, S.V. NISTOR, D. GHICA, C.D. MATEESCU, M. NIKL, R. KUCERKOVA, Phys. Rev. B **83**, 045301 (2011).
- [16] K. KOEPERNIK, H. ESCHRIG, Phys. Rev. B **59**, (1999) 1743; I. OPAHLE, *et al.*, Phys. Rev. B **60**, (1999) 14035; H. ESCHRIG, *et al.*, J. Solid State Chemistry **176**, (2003) 482.
- [17] J.P. PERDEW, K. BURKE, M. ERNZERHOF, Phys. Rev. Lett. **77**, (1996) 3865.
- [18] O. NEDELICU, G. BOLDEIU, R. PLUGARU, *2014 18th International School on Condensed Matter Physics (ISCOMP) September 1-6, 2014, Varna, Bulgaria*.
- [19] C. GHICA, L.C. NISTOR, M. STEFAN, D. GHICA, B. MIRONOV, S. VIZIREANU, A. MOLDOVAN, M. DINESCU, Appl. Phys. A **98** (2010) 777.
- [20] S.V. NISTOR, D. GHICA, I. PINTILIE, E. MANAILA, Rom. Rep. Phys. **65** (2013) 812.
- [21] S.B. ORLINSKII, J. SCHMIDT, P.G. BARANOV, D.M. HOFMANN, C. DE MELLO DONEGA, A. MEIJERINK, Phys. Rev. Lett. **92** (2004) 047603.
- [22] S.B. ORLINSKII, J. SCHMIDT, P.G. BARANOV, V. LORRMANN, I. RIEDEL, D. RAUH, V. DYAKONOV, Phys. Rev. B **77** (2008) 115334.
- [23] L.S. VLASENKO, G.D. WATKINS, Phys. Rev. B **72** (2005) 035203.
- [24] P.H. KASAI, Phys. Rev. **130** (1963) 989.
- [25] J. SCHNEIDER, O. SCHIRMER, Z. Naturforsch. **18a** (1963) 20.
- [26] S.S. SHINDE, C.H. BHOSALE, K.Y. RAJPURE, J Photoch. Photobio. B **120** (2013), pp. 1–9.
- [27] L. KE, S.C. LAI, J.D. YE, V.L. KAIXIN, S.J. CHUA, J. Appl. Phys. **108**, (2010) 084502.
- [28] A. NAKAGAWA, F. MASUOKA, S. CHIBA, H. ENDO, K. MEGRO, Y. KASHIWABA, T. OJIMA, K. AOTA, I. NIKURA, Y. KASHIWABA, Appl. Surf. Sci. **254** (2007), pp. 164–166
- [29] R. PLUGARU, N. PLUGARU, accepted in J. Phys.: Condens. Matter.
- [30] J. KWONET, *et al.*, Appl. Phys. Lett. **91**, 061903 (2007).
- [31] Y.Z. Zhang, J.G. Lu, Z.Z. Ye, H.P. He, L.P. Zhu, B.H. Zhao, L. Wang, Appl. Surf. Sci. **254** (2008), pp. 1993–1996.
- [32] S. CHATTOPADHYAY, S. DUTTA, D. JANA, S. CHATTOPADHYAY, A. SARKAR, P. KUMAR, D. KANJILAL, D. K. MISHRA, S.K. RAY, J. Appl. Phys. **107** (2010), 113516.
- [33] H. ZANG, Z.G. WANG, X.P. PENG, Y. SONGA, C.B. LIU, K.F. WEI, C.H. ZHANG, C.F. YAO, Y.Z. MA, L.H. ZHOU, Y.B. SHENG, J. GOU, Nucl. Instrum. Meth. B **266** (2008), pp. 2863–2867.
- [34] E. GÜR , H. ASIL, C. COŞKUN, S. TÜZEMEN, K. MERAL, Y. ONGANER, K. ŞERİFOĞLU, Nucl. Instrum. Meth. B **266** (2008) 2021–2026.
- [35] V. KUMAR, V. KUMAR, S. SOM, L.P. PUROHIT, O.M. NTWAEABORWA, H.C. SWART, J. Alloys Compd. **594** (2014) 32–38.
- [36] R. PLUGARU, A. ISTRATE, I. MIHALACHE, R. GAVRILA, 2015 28th International Conference on Defects in Semiconductors (ICDS), July 27 – 31, 2015, Espoo, Finland.

# **Current and Future Trends to Elaborate Nanostructured Materials by the Powder Metallurgy Technology. Education and Research Management**

Oana GINGU, Cristina TEISANU, Gabriela SIMA, Daniela COMAN,  
Anca DIDU, Mihail MANGRA

University of Craiova, Faculty of Mechanics,  
107 Calea Bucuresti, 200512, Craiova, Dolj, Romania  
E-mail: oanagingu@yahoo.com

**Abstract.** The paper presents the state of art of the most recent research developed at the University of Craiova (Romania) in the field of nano and microstructured structured materials by the powder metallurgy (PM) technology. High performing applications in the field of tissue engineering and optic-electronic are envisaged: Romanian patented hydroxyapatite-based biocomposite foams, respectively AgCu bimetallic matrix in-situ reinforced by ceramic nanoparticles. Another Romanian patent concerns the PM elaboration of new composite material for tennis table racket. Future PM trends focus on the nanostructured materials elaboration by advanced technologies as well on the education and research management

## **1 Introduction**

The advanced materials' outlook in designing, elaboration, characterization and application presents a great attraction especially for engineers. The possibility to improve the life style and conditions is basically supported by the evolution of the products quality respectively high performing materials and processing technologies.

The powder metallurgy (PM) technology started almost 20.000 years ago as forming technology in clay crockery, as some archaeological sources mention. Nowadays, the miniaturized parts for several microns up to nanorobots represent the majority of the high-tech products processed by advanced PM routes or complex combinations between classic and modern fabrication technologies. The flexibility to combine more or less any material (ceramic, metallic, metalloid, polymeric) as powder particles in different size and shape, for specific mixing rate



represent ones of the main PM challenges for the researchers and engineers in materials science and engineering field. On the other hand, the possibility to obtain high performing materials (cermets, composites) which are difficult to elaborate by conventional technologies simultaneously with the near-net shape products stand for ones of the best references to produce high quality parts in technical-economical terms.

These are the reasons we selected PM as research area for more than 20 years ago, considering the large spectrum of developments able to be performed in the next future. This decision was accompanied by the national and international support in the Romanian and ERA (European Research Area) spaces, providing special research programs for nanotechnologies and nanosciences, knowledge-based multifunctional materials and new production processes and devices, advanced materials, advanced manufacturing and processing for a lot of economic sectors (industry, medicine, agriculture, space, security). Here are some examples of competition research programs: Romanian (ANSTI, CNCSIS, CEEX, PNCDI - I, II) and European (ESF, COST, FP6, FP7, H2020).

The applicative research is the main driven force of the present research programs and the SMEs partnerships get a tremendous support from specific European programs, such as EUREKA - EUROSTARS and COSME.

Another core element of the present research programs is the innovation. This component should significantly contribute, by excellent science, industrial leadership and tackling societal challenges, to create high-class science and eliminate walls to simpler sharing innovation.

## **2. PM Nanoparticles For Joining Applications**

### **2.1. Preamble**

The main applications are represented by (the whole name should be given, when first ICT abbreviation is introduced) ICT micro-joints [1, 2]. As far as the optoelectronics applications concern, Ag and Cu, as individual metals are well known from this point of view [3], as well as their alloys [4-6]. That is why they are used, for instance, for sharp tips fabrication of Ag<sub>50</sub>Cu<sub>50</sub> by cryo-milling [7]. Also, the eutectic Ag-Cu alloys used to be applied in the dentistry sector for amalgam preparation [8].

The Ag-Cu alloys processing technologies developed as their applications upgraded in time. Cast or wrought, the improvement of AgCu properties has mainly developed by work hardening effects more than by age hardening ones, related, also, to the chemical composition of the alloys. Thus, Frommeyer et al. synthesized high tensile strength eutectic Ag-28%wt. Cu cast alloys by reinforcing Cu matrix with 50 nm Ag fibers [9] while Hodge *et al.* developed AgCu hypereutectic alloys (28...94 wt.% Cu) with tensile strength higher than 1 GPa, all by cold working technology [10]. On the other hand, Zhang et al. obtained high

hardness values, closed to 6 GPa, for Ag - 50%wt. Cu alloys. Actually, AgCu nanocomposites have been processed with a decomposition scale ranging of 30 nm after dynamic recrystallization (by milling at 230°C) respectively 75 nm after static recrystallization (by annealing at 230°C for 10 h) [11]. Also, ultrafine or nanocrystalline structures of AgCu alloys have been fabricated by different plastic deformation routes: high pressure torsion [12], cold rolling [13] or accumulative roll-bonding [14]. These research pointed out the increasing of microhardness values up to 350...400 units respectively the tensile strength to 1420 MPa after 20 revolutions of the alloy samples [12].

As far the microstructural evolution of Ag and Cu phases concern, Sheng *et al.* mentioned that nano-grained phases occurs after the annealing treatment at 260°C of the cold-rolled of 50 passes of the Cu-Ag foils [15] or at ambient temperature after a certain passes of accumulative roll-bonding process as Ohsaki pointed out [14]. This improvement of the mechanical properties is based on the eutectic component of the alloys, which is more deformable than other phases as Tian *et al.* mentioned [12]. Thus, the strengthening mechanism of the processed alloys is due to the continual deformation-recovery-recrystallization cycle developing during the plastic deformation processes, that characterizes the mechanical alloying (MA) process at low or elevated temperatures.

This was the reason to develop the processing of Ag-Cu alloys by MA route, starting from elemental powder particles mixtures. Qin *et al.* synthesized Ag<sub>37</sub>Cu<sub>63</sub> nanocrystalline powders less than 10 nm grain sized by ambient temperature ball milling, in dry argon atmosphere, reaching amorphous phases as well as crystalline (fcc) ones [16].

More detailed study, developed by Wu *et al.*, underlined that cryo-milling (at -180°C) provides a near random mixing of 100% Ag and Cu atoms whereas higher temperature milling (at +420C) affords only 70% level [7]. The nanometer scale information obtained from the atomic probe field ion microscopy analysis of Ag-50%Cu powder mixture processed by MA route pointed out the heterogeneous plastic deformation taking place at micro- and nano-scale.

Notwithstanding, some technical issues are reported such as: possible cracks/microcracks occurring inside the micro-joints because of Ag-rich and Cu-rich eutectic phases coarsening during the artificial aging treatment [17] and the delaminating of the micro-joint due to the Kirkendall effect that generates micropores at the interface between the electronic components to be assembled [18].

On the other hand, AgCu alloys are suitable, too, for fabrication of optoelectronic/electrical parts operating at elevated temperature rather than under heavy loads or exposed to temperature changes [19]. Thus, Gluchowski and Rdzawski pointed out the improvement of the stability of the properties for Ag+7.5% wt. Cu (and Ag-mishmetal alloys) above 300°C. This improvement is based on ultrafine structure of those alloys (200...400 nm crystalline grains size) obtained by (the whole name should be introduced) KOBOL extrusion process.

The eutectic alloy, 72% Ag + 28% Cu (wt.) has been selected for the study concerning the properties improvement of at high temperatures, namely higher than the eutectic melting point (778.1°C). This materials system is characterized by the positive mixing enthalpy ( $\Delta H = 6-10$  kJ/mol) which means it is difficult to mix in liquid state, but it is easy to be done in solid state. Using high energy techniques, like high pressure torsion (HPT), severe plastic deformation (SPD) and MA, the density of the crystalline defects increases by rapid atomic diffusion [20-22] and the alloying effect occurs at the interface between the two different metal powders even at low strain level [23, 24]. Thus, the solid-state reactions generate super-saturated solid solutions leading to non-equilibrium alloys that decompose to fine Ag and Cu rich phases on heating [25].

## **2.2. Research Goals**

The main research goal was to elaborate AgCu-based composite nanoparticles reinforced by in-situ processed oxides type  $\text{Cu}_2\text{O}$  nanoparticles for the following reasons: (i) to decrease the intensity of the decomposing reaction of the super-saturated solid solutions that usual forms during the MA process; this goal could be fulfilled by the means of in-situ  $\text{Cu}_2\text{O}$  nanoparticles synthesis which will reinforce the AgCu nanostructured matrix; (ii) to increase the melting point of AgCu nanoparticles by in-situ reinforcing with  $\text{Cu}_2\text{O}$  nanoparticles and (iii) to obtain a composite precursor for some advanced fillers used for special joining applications [26-28].

Our research use powder particles of silver (Sigma Aldrich,  $\geq 99.9\%$ , flakes, 10  $\mu\text{m}$  average) and cooper (Sigma Aldrich, 99%, irregular shape, 75  $\mu\text{m}$  average). The chemical composition of the Ag + Cu powder mixture corresponds to the eutectic one respectively Ag-28 Cu (% wt.).

The wet mechanical alloying (WMA) process is applied in order to get Ag and Cu powders in intimate contact by this mechanic-chemical route. The WMA takes place for 80 hours in a planetary ball mill Pulverisette 6 (Fritsch, Germany) with agate balls in agate vial, working in ethylene glycol (EG) aqueous solution (1:1 ratio respectively water: EG) to prevent the powder mixture's agglomeration as well as its contamination.

## **2.3. Research Developments**

The technological developments consist in using the mechanical alloying (MA) process developed in wet conditions [29] in order to elaborate the AgCu-based composite nanoparticles. The technological parameters of the MA process are: the milling bowl and balls are in agate in order to avoid the contamination of the processed powders; the milling bowl is 80 ml and the milling balls are 5, 10 and 20 mm diameter; the ratio between (Ag + Cu) powder mixture and milling balls is 1:5; the rotation speed  $n = 200$  rpm; the milling time is up to 80 hours.

Table 1 presents the samples quotations.

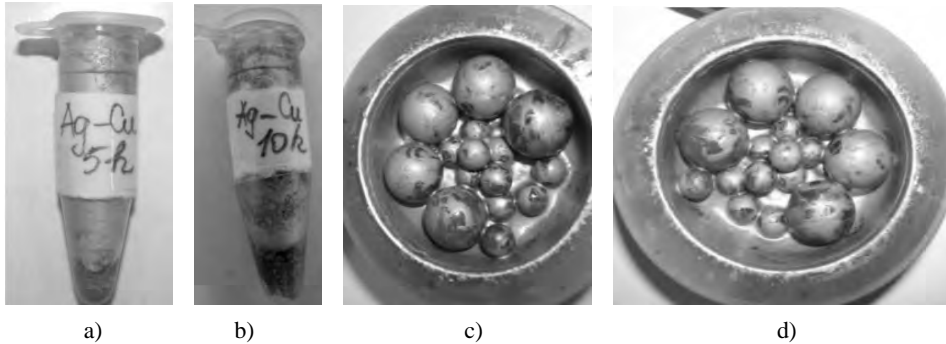
**Table 1.** The quotations for Ag-28% Cu (wt.) samples prepared by the WMA route

Sample code	WMA [h]
WMA-5	5
WMA-10	10
WMA-20	20
WMA-45	45
WMA-80	80

### Scientific developments

Along the MA time process, the powder mixture improves its homogeneity, Fig. 1. Simultaneously, the powder particle size changes from micrometric range up to nanometric scale, Table.2.

The scientific progress is based on the knowledge development regarding the influence of the MA time as far as concern the following characteristics of AgCu-based composite nanoparticles: the particle size, morphology, crystallite size, chemical composition, reactivity between the powder particles and the inert gases and melting point.

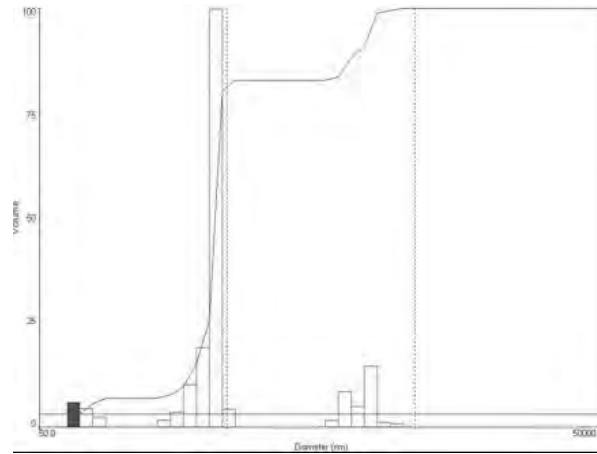


**Fig. 1.** Macroscopic changes of AgCu powder particles vs. the MA time process: a)5h; b) 10 h; c) 45 h; d) 80 h.

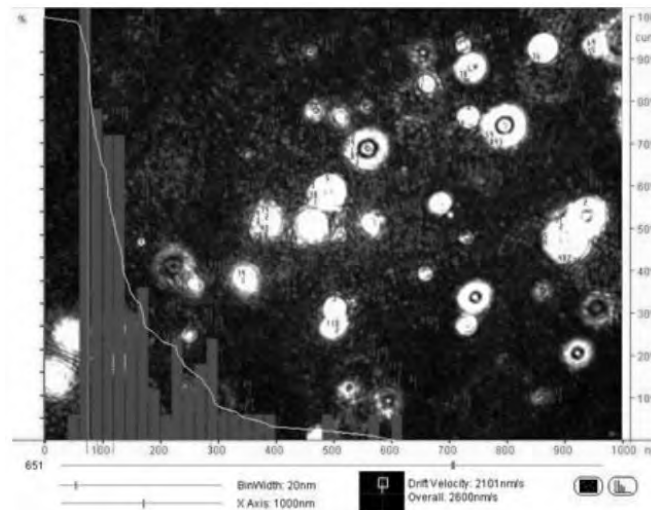
**Table 2.** Powder particle size changes vs. the MA time

Property	AgCu samples at different MA time					Remarks on Ag28Cu mixture
	0 h (initial)	5 h	20 h	45 h	80 h	
Powder particle size	Ag, 10 $\mu\text{m}$	6 $\mu\text{m}$	4-7 $\mu\text{m}$	2-3 $\mu\text{m}$	565-690 $\mu\text{m}$	Agglomerates
	Cu, 75 $\mu\text{m}$	800-900 nm	758-863 nm	350-470 nm	60-80 nm	Dispersion

The powder particles' size is determined by BROOKHAVEN 90 PLUS BI-MAS, Fig. 2 [29], and NANOSIGHT LM 10, Fig. 3 [30].



**Fig. 2.** Volumetric particle size distribution of AgCu-based powder particles after 80h of MA provided by BROOKHAVEN 90 PLUS BI-MAS [29].



**Fig. 3.** Numerical particle size distribution of AgCu-based powder particles after 80h of MA provided by NANOSIGHT LM 10 after the third dilution [30].

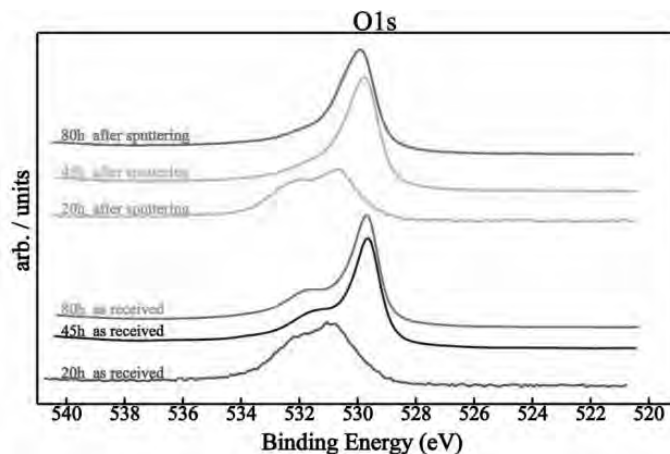
Both equipments assess this morphological parameter on the base light scattering by the 15 mW solid laser,  $\pm(1-2)\%$  accuracy for the mono-dispersed samples and the measurement range is 2nm...3 $\mu$ m. Furthermore, the NANOSIGHT LM 10 equipment provides on-line visual image of the studied powders as accurate as higher the dilution of the solution incorporating the powder a particle is. According to the experimental results, the longer the MA process, the smaller the powder particle size are up to the nanometric range.

The *chemical composition* (quantitative – whole name - RIR analysis) of the AgCu-based submicronic and nanometric powder particles and their crystallite size (by William-Hall method) are detected by XRD analysis. The experimental results confirm the nanometric range of the crystalline grains and a partial oxidation of Cu, up to 25% [wt.] average?, after 45h of MA process, Table 3, [30]. By consequence, composite nanoparticles with AgCu nanostructured matrix reinforced by nanometric Cu<sub>2</sub>O particles are elaborated by MA process described above.

**Table 3.** Crystallite size and chemical composition of AgCu-based nanoparticles [by courtesy of Dr. Speranta TANASESCU, “Ilie Murgulescu” Physical Chemistry Institute of the Romanian Academy, Bucharest, Romania]

Chemical composition	Ag28Cu samples along MA process			
	After 45 h		After 80 h	
	Crystallite size [Å]	Content [%]	Crystallite size [Å]	Content [%]
Ag	209.2	67.5	160.58	687.2
Cu	394	6.1	49.83	7.2
Cu <sub>2</sub> O	174	26.5	72	24

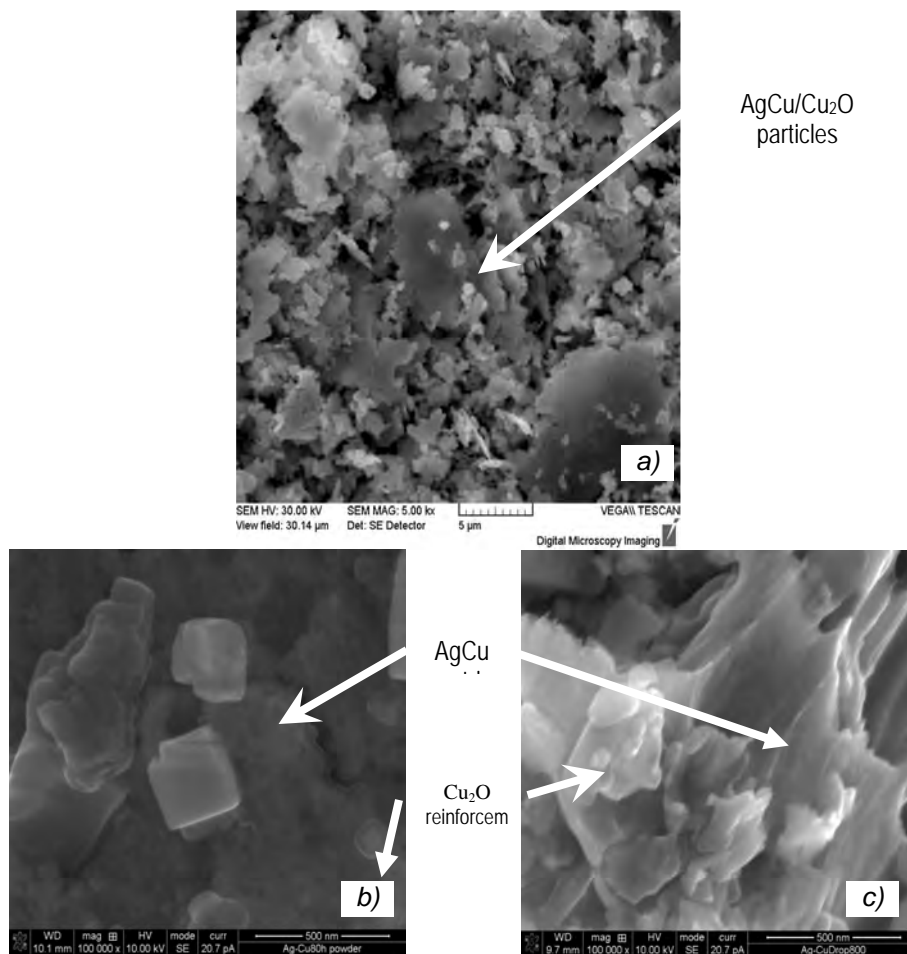
The X-ray photoelectron spectroscopy (XPS) is used to determine the chemical composition respectively the chemical states of the Ag and Cu elements present on the very top surface (less than 110Å depth) of the powder particles. The experimental data show that after 45 h milling time, the Ag content drop up to 5% respectively Cu content increases up to 90% on the surface of the powder particles [30]. In the meantime, the oxygen binding energy increases along the milling time, Fig. 4, which confirms the Cu<sub>2</sub>O presence in the AgCu nanoparticles.



**Fig. 4.** The superimposed XPS spectra of O1s of the AgCu-based nanoparticles processed after 20h, 45h and 80h (by courtesy of Dr. Petre OSICEANU, “Ilie Murgulescu” Physical Chemistry Institute of the Romanian Academy, Bucharest, Romania).

In the same time, the AgCu/Cu<sub>2</sub>O composite submicronic powders change their morphology along the MA process from initial irregular shapes to lamellar geometry much thinner as the milling time is longer, Fig. 5.

The information provided by Fig. 5 and the thermal analysis developed in [30] confirms the in-situ formation of the ceramic reinforcements type Cu<sub>2</sub>O by the induced oxidation of the Cu matrix [31].



**Fig. 5.** AgCu-based nanoparticles after 80 h of MA a) flakes-like morphology (by courtesy of Dr. Dan COJOCARU, Politehnica University, Bucharest, Romania); b) components of the composite after synthesis and c) components of the composite after heating at 8000C (by courtesy of Dr. Speranta TANASESCU, “Ilie Murgulescu” Physical Chemistry Institute of the Romanian Academy, Bucharest, Romania Bucharest, Romania)

The *reactivity* of the AgCu nanopowders to the inert gases highlighted the following main results [30]:

- the increasing of the powders specific surface along the MA process determines the ignition of adsorption chemical reactions between the AgCu/Cu<sub>2</sub>O nanoparticles and the argon gas;
- the analysis of these reactions was studied by the thermal analysis and the important outcomes are:
  - the reactions develop with different intensity which is measured by the powders mass variation, respectively the quantity of the entrapped argon on the nanopowders' surface. Thus, the mass increasing belongs to 1...4,5 % once the milling time increases from 20 to 80 hours. The mass decreasing is registered between 1...2,5 %. This phenomenon means the composite nanoparticles processed for 80h by MA gain 2% of entrapped Ar due to the highest specific surface in comparison with the powders elaborated after 20 hours whose mass variation is zero.
  - the inert gas (Ar) is entrapped on the nanopowders' surface by chemisorbtive reactions. The bonding energy between Ar and Ag<sub>28</sub>Cu nanoparticles belongs to 0,9...1,5 eV and it corresponds to chemical adsorption reactions type [32].

#### **2.4. Results**

The research of Ag-Cu system brings the following contributions to the state of the art:

- the elaboration of AgCu/Cu<sub>2</sub>O composite nanoparticles of 60...80 nm by the MA process. The nanostructured metallic matrix is characterized by nanometric crystallite size: Cu-49,83Å and Ag-160,58Å respectively the ceramic reinforcements of Cu<sub>2</sub>O-72Å. The reinforcing level is in range of 24...26,4 % [wt.].
- the increasing of the melting point. The nanostructured metallic matrix starts to melt more than 200C over the conventional AgCu eutectic alloy, namely 800C. This advantage could enlarge the spectrum of these nanocomposites' applications.
- the identification of the chemisorbtive reactions between the nanopowders' surface and the argon gas along the TA. The desorption energy varies between 0,95...1,99 eV/molecule depending on the milling time (20...80 hours). This reaction may lead to the potential elaboration of AgCu nanofoams due to the gas entrapping inside the nanopowders, also reported by the literature [33];
- the improvement of the thermomechanical behavior of this composite filler for joining application. The linear and smooth variation of the AgCu/Cu<sub>2</sub>O coefficient of thermal expansion (CTE) along the composite heating proves the underpinning effect of the oxides nano-reinforcements on the metallic matrix [30, 34].



### 3 PM biocomposites for bone reconstruction

#### 3.1. Preamble

Last decades point out the increasing of the crania-facial and vertebrae trauma. For most of the cases, the cause of these problems is represented by the fractures of the skull, fractures-compaction of the vertebrae body and tumors (primary or, more frequently, metastatic). The reconstruction can be processed using the patient's native bone or harvested from another donor. But these solutions bring a lot of disadvantages such as: long time surgery procedure, high risk for implant rejection, low supply from the bone banks, different anatomic and structural problems [35-37]. Advanced surgical procedures require the bone reconstruction by the substitution of the patient's native affected bone tissue with special materials. The market customers are the bone banks and hospitals (civil, military, veterans and veterinary). This is a growing market due to accidents high frequency like in sports (football, winter sports), transportation, wars theaters and animal welfare (pets and trained animals for special purposes).

Nowadays, the bone reconstruction procedure claims the most advanced synthetic materials. For skull and vertebrae reconstruction, polymeric, metallic and composite materials are used for the implants manufactured through highly developed technologies, as follow: *polymeric implants* respectively the *polymeric composites* ones (PLLA, PMMA, PEEK, PEEK-OPTIMA<sup>®</sup>, OXPEEK OsteoFab<sup>™</sup> by selective laser sintering (SLS) [38] and high speed milling (HSM) [39]; Ti-based metallic implants, as compact sheets or meshes using HSM, selective laser melting (SLM) [40], electron beam melting (EBM) [41] or laser engineered net shaping (LENS) [42], respectively bioceramic implants based on  $\beta$ -tricalcic phosphate [43] and synthetic hydroxyapatite  $\text{Ca}_{10}(\text{PO}_4)_6(\text{OH})_2$  (hereinafter named HAP) [44, 45]. However, the polymers' non-resorbability [46, 47], metals' radiation opacity and stress shielding [48, 49] as well as ceramics' dimensional instability and low mechanical strength [50-52] represent important structural drawbacks.

As far as concern the functional properties, the osseointegration process of the bone implants into the native bone tissue may be accelerated by the HAP presence. As macroscopic product or nanometric coatings (50...500nm thickness) on Ti substrates for skull reconstruction, HAP provides the advantage of osteoblasts proliferation [53, 54]. Yet, HAP cracking occurs due to its geometrical instability and the large difference between the physical and mechanical properties of the ceramic coating and the metallic substrate. Thus, low in-vitro toxicity and in-vivo inflammation of the adjacent native bone are claimed [55-57]. On the other hand, for the vertebrae reconstruction, usually the Ti mesh is filled with proteins and debris of native bone tissue mixture [58]. These procedures are equivalent to the alloplastic or autologous grafts, leading to an increased risk of the implant rejection, spine instability and, generally, to the patient's discomfort [50, 59, 60].

### 3.2. Research goals

Our research purposes envisaged the elaboration of HAP-based biocomposites (hereinafter named BONY) for cortical and trabecular bone tissue grafting with performing structural and functional respectively biocompatibility characteristics. Advanced PM routes were used to fulfill these goals. Micronic HAP powders (Sigma-Aldrich, 30-50  $\mu\text{m}$ , >90% purity), respectively submicronic particles (Sigma-Aldrich; <200 nm; 99,99% purity) were used as biocomposite matrix. Titanium hydride ( $\text{TiH}_2$ ) powders (Merck; 100-150  $\mu\text{m}$ ; >98% purity) were used as Ti reinforcement precursor as well as blowing agent for the foaming process. Calcium bicarbonate ( $\text{CaCO}_3$ ) powders (2,93  $\text{g}/\text{cm}^3$ ; melting point 800°C; Merck) were used as space holder agent for the foaming process. The PM routes as well as the processing technological parameters are presented in Table 4.

**Table 4.** Synthetic presentation of the biocomposites composition and processing technologies

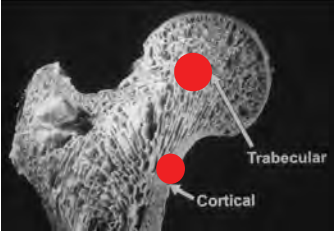
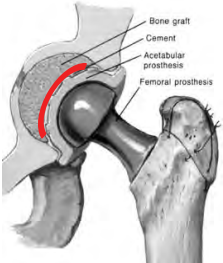

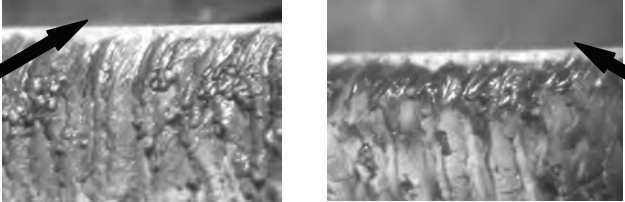
BONY chemical composition [% mass]			PM routes processing		Applications
HAP	TiH <sub>2</sub>	CaCO <sub>3</sub>	Technology 1		Trabecular bone reconstruction
75	15-25	0-10	Cold die compaction	Two steps sintering (TSS)	
			P = 120-150 MPa	Step 1: 900 <sup>0</sup> C / 1-5 min. Step 2: (750-850) <sup>0</sup> C / 5-10 hours	
			Technology 2		Cortical bone reconstruction
			Spark plasma sintering (SPS): 1000-1100 <sup>0</sup> C / 10-30 min.		

### 3.3. Research Developments


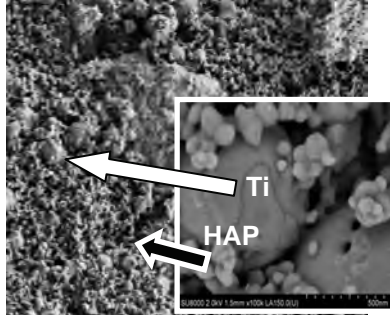
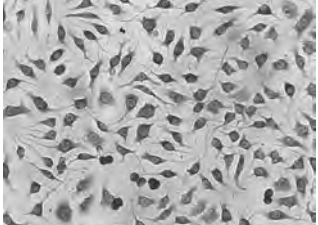
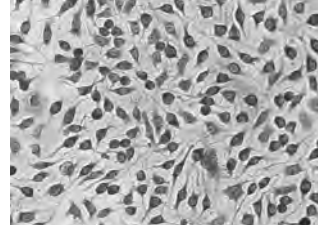
The applicative developments, Table 5, were requested by the necessity to design advanced grafts for cortical and trabecular bone tissues, which present different physical and mechanical respectively functional properties. The BONY biocomposites had to match the grafting placement demands, meaning to provide the most important required properties: physical (density/porosity), chemical composition, reliability (wear behavior) and geometrical adaptability (micro-machinability).

The scientific developments consist in upgrading the biocomposites design by the means of their internal structure, Table 6, respectively ceramic HAP nanostructured matrix (<200 nm grain size, black arrows) reinforced by Ti micrometric metallic particles (<150  $\mu\text{m}$ , white arrows). The hybrid structure of the BONY biocomposites provides: the Young modulus improvement matching the natural bone one (5...40 GPa) [67] and comparable biocompatibility (97...98 %) [68, 69] with standard biomaterials (100%), Table 7, especially due to the nanostructured ceramic matrix [45]. Over 80% viability provides the quality of biocompatible material [69] and the experimental results show that BONY biocomposites are biocompatible and comparable with pure HAP, Table 7 [68].

**Table 5.** Applicative developments by BONY biocomposites

Applicative developments of HAP/Ti biocomposites	CORTICAL BONE RECONSTRUCTION		TRABECULAR BONE RECONSTRUCTION			
Applications						
Know-how	BONY [61]	Natural cortical bone	BONY [62]	Natural trabecular bone		
Density, $\rho$ [g/cm <sup>3</sup> ]	1,9 ... 2,5	2,1 ... 2,2.	1,2 ... 1,6	1,3 ... 1,5		
Porosity, P [%]	5 ... 12	5 ... 10	50 ... 65	50 ... 90		
Benefits	<p>High precision for grafting placement with specific structure</p> <ul style="list-style-type: none"> <li>High wear strength of BONY in contact (red area contact) with:           <table style="width: 100%; border: none;"> <tr> <td style="width: 50%; text-align: center;">ceramic implant</td> <td style="width: 50%; text-align: center;">metallic implant</td> </tr> </table> </li> </ul>				ceramic implant	metallic implant
ceramic implant	metallic implant					
						
	BONY [63]	Others biomaterials [64]	BONY [65]	Other biomaterials [64]		
Wear rate [mm <sup>3</sup> /Nm]	2,2...3,4 × 10 <sup>-4</sup>	2 ... 3 × 10 <sup>-4</sup>	0,9×10 <sup>-4</sup> ...1,5×10 <sup>-3</sup>	2 ... 3 × 10 <sup>-4</sup>		
	<p>Accurate laser micro-machining in case of post-sintering operations for bone grafts finishing (smooth surfaces pointed out by the black arrows in the below figures)</p>					
						
Ra [μm]	7,8 ... 34,4 [66]					

**Table 6.** Scientific developments by BONY biocomposites

Scientific developments	CORTICAL BONE RECONSTRUCTION		TRABECULAR BONE RECONSTRUCTION	
Applications				
Know-how	BONY [67]	Natural cortical bone	BONY [67]	Natural trabecular bone
Young modulus, E [GPa]	25 ... 30	15 ... 40	7 ... 15	5 ... 25
Benefits	Comparable biocompatibility* of BONY with standard biomaterials characterized by lower mechanical properties			
				
	**Mouse fibroblast-like cells on BONY [68]		**Mouse fibroblast-like cells on standard sample [68]	
Cellular viability in case of BONY biocomposites	97,1 ... 98,7 [%]		100 [%]	

\*The biocompatibility tests were developed with mouse fibroblast-like cells in a specific cultivation environment. The biocompatibility evaluation was performed qualitatively (Giemsa etching\*\*) and quantitatively (MTT test - cellular viability\*\*).

**Table 7.** Biocompatibility evaluation of BONY biocomposites [68]

Cultivation solution concentration [mg/l]	Samples viability [%]	
	HAP calcinated	BONY
12,5	98,9	95,6...98,7
25	103,7	93,2...98,6
50	102,9	85,5...97,1

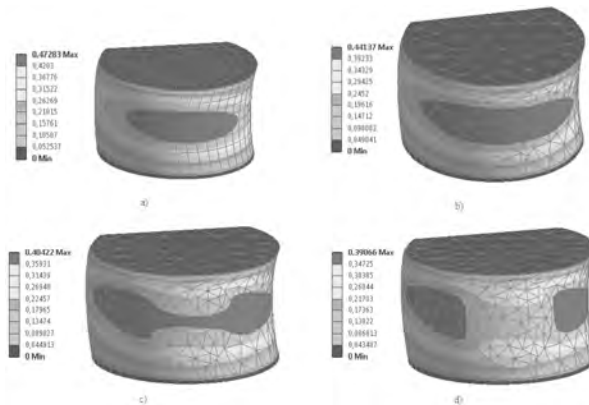
The technological developments, Table 8, represent the key-tool for BONY processing. The Spark Plasma Sintering (SPS) technology proved its adaptability and efficiency to Ti processing [71] as well as for nanostructured biocomposites [61]. The Two Steps Sintering (TSS) technology input is based on the “kinetic window” concept respectively the ratio between the second step temperature and dwell time for nanostructured materials processing [72].

**Table 8.** Technological developments by BONY biocomposites

Technological developments	Advanced PM routes to produce BONY biocomposites	Know-how	Economic benefits
CORTICAL BONE RECONSTRUCTION	<p><b>Spark Plasma Sintering (SPS)</b></p>	<p>The adjustment of the SPS technological parameters for biomaterials elaboration [71].</p>	<p>Quite expensive route (max. 300.000,00 \$ investment in equipments) but very short time production (20...30 min.), with large possibilities for productivity improvement.</p>
TRABECULAR BONE RECONSTRUCTION	<p><b>Two Steps Sintering (TSS)</b></p>	<p>The development of the TSS “kinetic window” concept tailoring the internal architecture of BONY biocomposites [72].</p>	<p>The use of conventional furnaces (low investments), with high productivity (x107 samples / batch) but time consuming (10 hours). Low production costs.</p>

The future technological developments envisage the PM foaming technology to elaborate biocomposite foams with specific structural and functional characteristics and high matching level to the natural bone tissue. Blowing and space holder techniques will be combined with different sintering technologies in order to facilitate the foaming reactions along the ongoing heat treatment [73-77]. Based on the experimental results, predictive modeling and simulation of the BONY grafts’ mechanical behavior will be developed by the finite element method. First approaches has been already done and mechanical shielding of the

vertebrae body grafted with the BONY biocomposites may be stated, in the case of frontal collision, using an empty car with two anthropomorphic test devices and afferent luggage [78]. Fig. 6 show a comparative displacement of the total deformation of the lumbar L5 vertebra model (a) simulated at the frontal collision with 44 kN and the respective response in case of different BONY biocomposites used as grafts (b-d).



**Fig. 6.** Total deformation  $\Delta l$  [mm] of the lumbar L5 model vertebra in case of frontal collision with simulated 44 kN impact force: a) genuine vertebra (0,47 mm); b-d) grafted vertebrae with tronconic BONY graft. The total deformation varies from 0,44 mm (b) up to 0,39 mm (d) depending on the BONY grafts manufacturing technology [78].

In the frame of BONY project [79], the BONY biocomposites research will focus on three new research areas: (1) the innovative biocomposite material as bulk product for vertebral implant processed by micro-injection moulding technique; (2) the innovative biocomposite materials as coating for skull implant processed by MAPLE technique on Titanium substrate; (3) the acceleration of the osseointegration process by the natural organic esters of bor.

### 3.4. Results

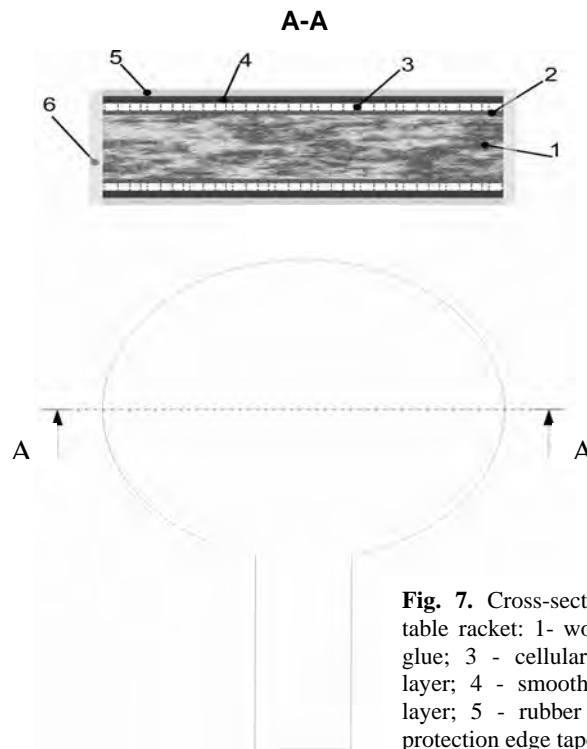
The research of HAP-based biocomposites brings the following contributions to the state of the art:

- The PM technology provides the flexibility to select the proper matrix to fulfill the biocompatibility demands;
- The PM technology provides the flexibility to select the proper reinforcing elements to ensure the structural and functional matching to the natural human bone tissues;
- The correlation of the conventional foaming techniques and advanced sintering techniques in order to optimize the foaming process to elaborate specific bone grafts for cortical/trabecular tissue.

## 4. PM Composites for Sports

### 4.1. Preamble

From the technological point of view, the table tennis racket is an assembly comprising different layers of wooden, polymeric and textile materials, in a specific geometrical displacement, Fig. 7.



**Fig. 7.** Cross-section of a tennis table racket: 1- wooden blade; 2 - glue; 3 - cellular sponge rubber layer; 4 - smooth, grippy rubber layer; 5 - rubber protection; 6 - protection edge tape.

The performing functionalities of this sports article are evaluated by the following parameters, Table 9.

**Table 9.** Performing parameters of the tennis table racket

<b>BLADE</b>	<b>RUBBER</b>
Speed	Speed
Control*	Spin
Weight	Control*
Price	

\* This parameter should be probably how easy is to block, to return a serve or, generally, to move the ball wherever you want [80] = this sentence is not clear; it should be improved.

There are different scales to evaluate these parameters, used by the manufacturers: ANDRO (0...110), JOOLA (words), DONIC (0...10), STIGA (0...160) etc. In other terms, there is no unique range to compare the performance of one tennis table racket. The state of the art concerning the materials performances is presented in Table 10 for the blades respectively Table 11 for the rubbers.

**Table 10.** Tennis table blades - state of the art [81]

BLADES performing parameters	Parameter scales	
	Min. / Product / Performing features	Max. / Product / Performing features
<b>SPEED</b>	60 / <i>YinHe 980; YinHe DE-1</i> / 5-ply wood for blocks and hits	107 / <i>Donic Ovtcharov Carbospeed</i> / 5-ply carbon blade; great stiffness; nearly impossible to fracture  110 / <i>Yasaka Hinoki Leo 11</i> / 11-ply Hinoki wood; very light blade providing very high speed
<b>Control</b>	69 / <i>Butterfly Senkoh Special 90</i> / 1-ply Hinoki wood for steady topspins and precise blocks  72 / <i>Butterfly Innerforce T500</i> / 2-ply carbon close to the wooden core which increase the dwell time and control	100 / <i>729 Friendship</i> / 5-ply from hard (outer layer, very thin) to high-grade soft (core) wood that give increased spin and dwell time  104 / <i>Joola Chen Defender</i> / 7-ply Samba wood bonded with Enzo glue layer that provides big control and great feel of the ball
<b>Weight</b>	68 / <i>Yasaka Balsa Plus</i> / 5-ply Balsa and Scandinavian woods providing a faster blade than traditional Balsa  70 / <i>Joola Chen Weixing Jr</i> / 5-ply composite woods	90 / <i>Yasaka Silverline Carbon</i> / the 2 hard outer wooden veneers, sticked on the 2 thin carbon layers by an advanced gluing technology, maximize the sweet spot size  102 / <i>Stiga CarboKev</i> / 7-ply wood (stiff), carbon fiber (speed) and Kevlar (soft) significantly increase the sweet spot (hitting area with maximum control) and maximize the speed of the blade
<b>Price [\$]</b>	17.95 / <i>729 Friendship Bomb Penhold</i> / for 5-ply, <b>control-100, speed-90</b> , thickness 6.2 mm, <b>weight 82 g</b> , offensive style  32.95 / <i>Donic Applegren Exclusive AR</i> / for 5-ply, <b>control-85, speed-60, weight 80 g</b>	317.99 / <i>Butterfly Ryu Seung Ming G Max</i> / for 1-ply, <b>weight 90 g</b> , thickness 10 mm, fast attack style  283.99 / <i>Butterfly Cypress Wood</i> / for 1-ply wood and carbon, <b>control-88, weight 93 g</b> , thickness 10 mm, top-spin style



**Table 11.** Tennis table rubbers - state of the art [81]

RUBBERS performing parameters	Parameter scales	
	Min. / Product / Performing features	Max. / Product / Performing features
<b>SPEED</b>	70 / 729 <i>Friendship</i> / slight ability to generate spin, strange effect of the ball, recommended for attack style  90 / <i>Andro Rasant Powersponge</i> / the soft sponge absorbs the energy of the arriving stroke and converts it into considerable power	120 / <i>DHS Hurricane 2 Neo</i> / the sponged rubber (hardness 39) offer an extra pace and rebound without losing the spin and control  140 / <i>Butterfly Bryce Speed FX</i> / the soft (hardness 32) and flexible sponge provide great control
<b>CONTROL</b>	34 / <i>Butterfly Feint Long II – OX</i> / no sponge  38 / <i>Butterfly Feint Long II</i> / the thinner and taller the pimple rubber is, the more effective the pimples are for ball control. <b>Regluing rubber is not recommended.</b>	120 / <i>RITC 729 Friendship</i> / the medium hardness sponge in combination with high degree of friction and power making convert this rubber in an energy storing highly elastic top sheet.
<b>SPIN</b>	0 / <i>RITC 804 Anti-Spin Rubber</i> / for precision placements due to the sinking ball effect  32 / <i>Butterfly Feint Long II</i> / the spin effect is maximized when the pimples (hardness 38) are easily bent and deformed	120 / <i>Xiom Omega IV Pro</i> / the new top sheet (hardness 47.5) matched with upgraded carbo sponge offers extra-ordinary playing properties: ball contact + clicking sensation generated by speed glues
<b>PRICE [\$]</b>	5.95 / <i>RITC 837 Long Pips No Sponge</i> / the hard bat (no sponge) ensures long range heavy chopping strokes; <b>control-110; speed -110; spin-70</b>	69.95 / <i>Donic Traction MS Pro</i> / the innovative TRACTION rubber technology provides better adhesion and stronger friction; <b>spin-107; speed-103; control-50</b>

The known technique for the rubbers attaching to the sandwich composite blades is to use special glues [82, 83]. The presence of VOCs in the chemical composition of the glues has negative effects on the human health and environment, so the International Tennis Table Federation (ITTF) did not allow the using of such chemicals since 2009, January, 1. By consequence, one of the improving trends to fabricate tennis table racket is to design new attaching

technologies of the rubber to the blade. One processing route is developed by [84], the attaching technique is based on the magnetic film between the rubber coating and the blade. The innovative solution provided by the author and the research team [85] is described below.

#### ***4.2. Research goals***

The International Tennis Table Federation's (ITTF) mentions, in June 2007, on the volatile organic compounds (V.O.C.) - free glue using rules, have been refined, in 1 January 2009, up to higher standards due to the human health protection. In this respect, the research on the materials and technologies related to coatings processing and bonding to the wooden support of the table tennis rackets have been developed. According to the new specifications of ITTF on using the VOC-free glues, magnetic bonding of the coverings subscribes to this demand [84].

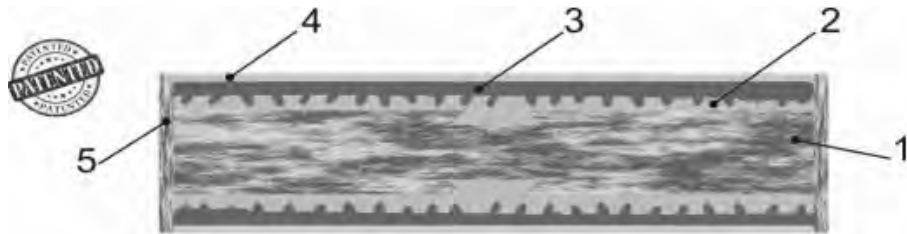
The experimental results presented in our research concern the processing of a new table tennis racket made of Al alloy foams and rubber coating bonded to the foam by a thermo-mechanical technique. The rubber/Al composite is attached to the wooden support of the racket by a mechanical procedure.

The PM technology has been used in order to process Al-based foams using 40% mass of Al alloy powder particles (200  $\mu\text{m}$  average particle size) and 60% mass NaCl granules (3 mm and 4 mm average size) as a spacer component. The conventional PM technology is developed: the homogenization step is followed by the cold compaction at 500 MPa, respectively the sintering in argon atmosphere at 630...6500C for 20...40 min. As the final operation, the lightweight metallic structure is water washed and the Al alloy metallic foam gets lighter due to the NaCl dissolution in water. The novelty of the rubber and carbon black mixture coating on the metallic foam is the injection molding (IM), process developed at 30-70 bar pressure and 130-1500C. For 1...4 mm thickness of the rubber coating, the Shore hardness is 40...80 respectively 0,9...1,4 g/cm<sup>3</sup> as density.

Thus, a new composite blade, hereinafter named MIGGO, has been processed. Another innovation element is represented by the mechanical technique to attach MIGGO to the wooden blade. The research developed on this topic is patented at the Romanian State Office for the Inventions and Trademarks [85].

#### ***4.3. Research developments***

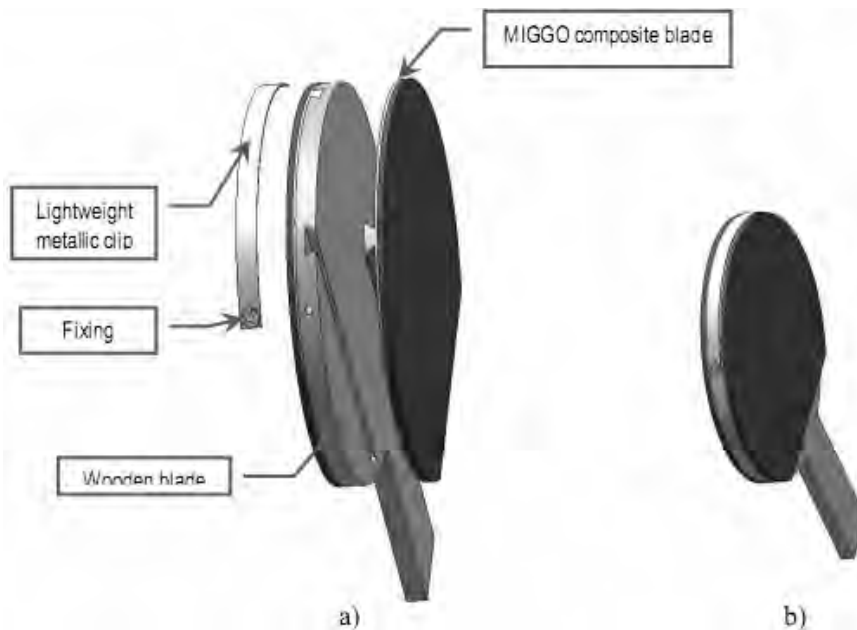
The technical problem solved by the patent [85], Fig. 8, is the fabrication of the MIGGO composite blade (2 and 3), which is mechanically attached to the wooden blade (1). The lightweight metallic clip (5) fastens the composite blade on the wood. The lightweight metallic foam on Al alloy – based is one side injected by the rubber and the opposite side is mechanically milled as dovetail shape for the mechanical attaching on the wooden blade.



**Fig. 8.** Cross-section of the new tennis table racket: 1-wooden blade; 2 – lightweight metallic foam injected by 3 – rubber that is MIGGO composite blade; 4 - rubber protection; 5 – lightweight metallic clip [85].

The *innovative technological developments* are represented by the followings, Fig. 9.:

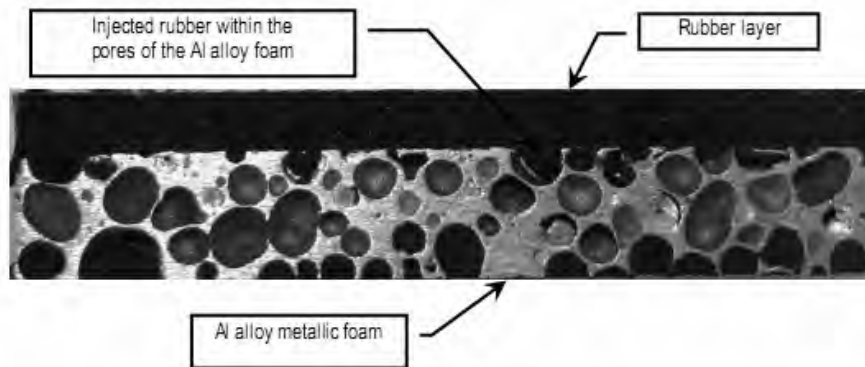
- the powder metallurgy (PM) technology to elaborate the Al alloy foam using NaCl as space holders for the foaming technique;
- the thermomechanical attachment by rubber injection to one-side coating the metallic foam;
- the milling processing for MIGGO composite blade placement on the wooden blade;
- the mechanical fixing of the MIGGO composite blade by the lightweight metallic clip.



**Fig. 9.** New tennis table racket: a) by components; b) assembly.

The *innovative scientific* developments are represented by the followings, Fig. 10:

- the porous structure of the Al alloy foam (pore size, Plateau border thickness, functional graded porosity) is tailored in order to monitor the blade functional parameters (speed, spin, weight and control);
- the rubber chemical composition, thickness and hardness are adapted to the functional parameters (speed, control and spin).



**Fig. 10.** Macrostructure of the MIGGO composite blade.

The main properties of the MIGGO composite blade are presented in Table 12.

**Table 12.** Properties of the MIGGO composite blade [86]

<b>METALLIC FOAM</b>		
<b>Property</b>	<b>with 3 mm NaCl granules</b>	<b>with 4 mm NaCl granules</b>
Density [g/cm <sup>3</sup> ]	0,2 – 0,35	0,15 – 0,25
Porosity [%]	60 - 70	65 - 75
Pores diameter, average [mm]	2,15	2,65
Pore wall thickness [µm]	80 - 150	
<b>RUBBER COATING</b>		
Density [g/cm <sup>3</sup> ]	0,9 – 1,4	
Thickness [mm]	1 - 4	
Shore hardness	40 - 80	

#### **4.4. Results**

Beyond the state of the art, the following assessments may be stated:

- the elimination of the gluing step from the technological chain due to the rubber injection operation on one side of the Al alloy foam;
- the improvement of the rubber adhesion by the injection operation due to its impregnation within the superficial pores of the Al alloy foam;

- the elimination of the rubber regluing, which is an usual operation to fix the rubber outer layers on the blade. For those brands that don't recommend the rubber regluing (see Table 11, Butterfly Feint Long II tennis table racket), the rubber injection could be the most appropriate solution in the case of pimpled rubber outer layer.
- the preservation of the racket weight because of the low density of the metallic foam (0,2...0,35) g/cm<sup>3</sup> respectively low weight (35...50) g, considering the 15 cm diameter and 1 mm thickness of the metallic foam, including the dovetail profile.
- the development of a new robust and stable tennis table racket by the means of the mechanical adjustment of the MIGGO blade on the wooden one and their fastening with the lightweight metallic clip and screws;
- the reliability of the technological solution. In the case of random spoilage, the MIGGO blade can be easily and quickly replaced.

## **5. Future Trends in PM Technology by Education and Research Management**

### **5.1. Preamble**

The materials science and engineering field may significantly contribute to the society development. From the common goods industry up to the miniaturized ICT technology or space and defense sectors, the smart designing of materials and high technological progress have to be the driving force for the next future.

For the particular case of the PM materials and technologies, the first step of our efforts towards their development will be focused on the following *selected topics*, but not only:

- *The societal needs.* The R&D must be always in contact with the society because it serves it. For example, the bone banks providing hard tissue implants complain for the low level supplies for such products (that are depending on the donors) as well as for their quality (especially from the structural point of view). In this case, we propose to promote the parametric design of bone implants to accelerate the supplying effort and high processing technologies for quality improvement. This would mean to design implants selected by gender and age, for a specific bones category, capable for final geometrical adjustments and with tailored properties according to the native hard tissue to be grafted.
- *Powders' multi-functionality.* In addition to the smart materials, our proposal targets the designing, elaboration and characterization of multifunctional powder particles for specific applications (bulk or coatings) that differently behave according to the functioning conditions.
- *Environmental friendly miniaturization by micro-injection molding.* We propose two concepts regarding the binders designing:

- to avoid the residual gases/emissions exhausting during the de-binding operation by using special binders that soften below 100°C
- to bypass the de-binding operation by using special binders from natural lubricant substances and contributing to the materials systems sinterability.
- *Environmental friendly heat treatments.* Fast heat treatments for sintering purposes, enabling any microstructural features of the final products (micro- and nanostructures) may be designed on the basis of the microwave heating.

The **second step** of our strategy looks on the “near-to-the-market” stage of the developed materials / products. This would include:

I. **Researcher’s preparation for the intellectual property rights (IPR)** by basic courses and patenting. The key-role of innovation is highlighted in present Romanian (PNCDI - II) and European (H2020, ESF etc.) programs. This training will bring benefits regarding the research management skills that are highly requested to face the competition for the world-wide platforms/programs.

II. Application for the **specific programs/platforms** to bring the innovative products to the international markets.

III. Applications for **consortia** coordinated by special entities able to manage the market transfer.

IV. Applications for the **European SMEs’ programs** [87, 88].

We conclude that there is mandatory to train, as student in license, Master and Ph.D. programs and after that, as a researcher, to acquire the best skills in research management. By consequence, we propose a strategy for the academic business.

### ***5.2. Research Development by Education and Academic Management***

Our proposal to improve the students’ and researchers’ proficiency in IPR and research management is represented in Fig. 11.

The model of the **metallic chemical bond** is used to design this new concept. This selection is based on the main properties of the metallic bond, which may fit the academic environment behavior, too:

- It operates inside a crystalline structure (Fig. 11a) characterized by the large distance 3D atomic order (in crystallography). Each cubic entity corresponds to the university structure (primitive cell, in crystallography).
- It operates by means of the electronic gas (Fig. 11b), to transfer the heat and electricity (in physics). This corresponds to the society always in contact with the academic environment.

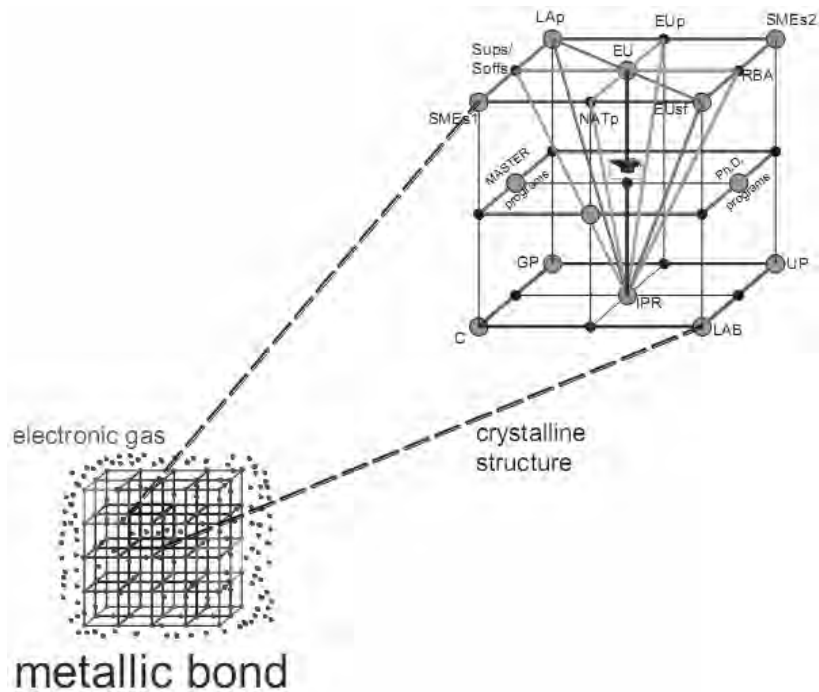


Fig. 11. New concept for the academic business.

The university structure is similar to the body centered one (in crystallography) in its central atom called **UNI**. There are two textures:

- The organizational structure (horizontal) layered on three levels:
  - The 1<sup>st</sup> level: the license (courses-C, training in laboratories-LAB, inter-universities programs-UP, good practice-GP). The IPR atom plays an important role, representing the special training of the undergraduate students in the field of IPR basics.
  - The 2<sup>nd</sup> level: the postgraduate (Master and Ph.D. programs) that is the interface between the first and the last level and provides the strong connections between them.
  - The 3<sup>rd</sup> level: the **academic business** level. The atoms represent the local/regional, national and European contact points acting on behalf of the university interests. The **EU** atom represents the contact point for all the connections that **UNI** has with the European Commission and reverse, such as: European programs (**EUp**), European structural funds (**EUsf**), national programs (**NATp**), local administration programs (**LAp**), and private business environment represented by the **SMEs** clusters (**SMEs1, 2**). Belonging directly to the **UNI**, there are the research and

business administration office (**RBA**) and the start-ups (**Sups**) and/or spin-offs (**Soffs**).

- The **BUSINESS STRUCTURE** (transversal) organized in three plans:
  - The 1<sup>st</sup> plan, **research management**, containing the following “atoms”: **IPR – RBA – Sups/Soffs**;
  - The 2<sup>nd</sup> plan, **infrastructure development** plan: **IPR – Eusf – Lap**;
  - The 3<sup>rd</sup> plan, R&D: **IPR – NATp – EUp**.

The intersection of these three plans gives the main line to follow for benefic academic management and business: **IPR – UNI – EU**. In other words, this line is defined by the key-role players able to promote the university research and innovation capacity on its behalf and the society's, in the national space and the European Research Area.

**Acknowledgements.** We hereby acknowledge for the financial support respectively research and academic development to:

- the research project PN-II-PT-PCCA-2013-4-2094, “Research on the bone substitution with biocomposite materials processed by powder metallurgy specific techniques”, acronym BONY.
- the research project COST - MPNS Action MP0903, “Nanoalloys as Advanced Materials: From Structure to Properties and Applications”, acronym NANOALLOY.

## References

- [1] H. JIANG “Synthesis of tin, silver and their alloy nanoparticles for lead-free interconnect applications”, PhD thesis, Georgia Institute of Technology, U.S.A., pp: 8-9, 2008;
- [2] S.J. KIM, E.A. STACH, C.A HANDWERKER, Fabrication of conductive interconnects by Ag migration in Cu–Ag core-shell nanoparticles, Applied Physics Letters 96(144101), 2010;
- [3] H. EHRENREICH, H.R. PHILIPP, Optical properties of Ag and Cu, Phys. Rev., 128(4), pp.1622-1629, 1962;
- [4] R.H. MAGRUDER III, D.H. OSBORNE Jr., R.A. ZUHR, Non-linear optical properties of nanometer dimension of Ag-Cu particles in silica formed by sequential ion implantation, J. Non-Cryst. Solids, 176, pp.299-303, 1994;
- [5] P. PREM KIRAN, B. N. SHIVAKIRAN BHAKTHA, D. NARAYANA RAO, Nonlinear optical properties and surface-plasmon enhanced optical limiting in Ag–Cu nanoclusters co-doped in SiO<sub>2</sub> Sol-Gel films, J. Appl. Phys. 96(11) pp.6717-6723, 2004;
- [6] P. NARAYANA REDDY, A. SREEDHAR, M. HARI PRASAD REDDY, S. UTHANNA, J.F. PIERSON, Process-parameter-dependent structural, electrical and optical properties of reactive magnetron sputtered Ag-Cu-O films, J. of Nanotechnology, artic. ID 986021, pp.1-8, 2011;
- [7] F. WU, P. BELLON, A.J. MELMED, T.A. LUSBY, Forced mixed and nanoscale decomposition in ball-milled Cu-Ag characterized by APFIM, Acta mater. 49, pp.453-461, 2001;
- [8] R.W. BRYANT, Microprobe analysis of dental amalgam alloy particles of Ag-Cu eutectic composition, J. Oral Rehabilitation, 11, p. 571-578, 1984;



- [9] G. FROMMEYER, G. WASSERMANN, *Acta metall.* 23, pp. 1353, 1975;
- [10] W. Hodge, R. I. Jaffee, J. G. Dunleavy and H. R. Ogden, *Metals Technology*, pp. 15, June, 1948;
- [11] S. ZGHAL, R. TWESTEN, FANG WU, P. BELLON, Electron microscopy nanoscale characterization of ball-milled Cu-Ag powders. Part II: Nanocomposites synthesized by elevated temperature milling or annealing, *Acta Materialia* 50, pp. 4711–4726, 2002;
- [12] Y.Z. TIAN, S.D. WU, Z.F. ZHANG, R.B. FIGUEIREDO, N. GAO, T.G. LANGDON, Microstructural evolution and mechanical properties of a two-phase C-Ag alloy processed by high-pressure torsion to ultrahigh strains, *Acta Mater.* 50, pp. 2783-2796, 2011;
- [13] S.I. HONG, M.A. HILL, Microstructural stability and mechanical response of Cu-Ag microwires composites, *Acta Mater.*, 46(12), pp. 4111-4122, 1998;
- [14] S. OHSAKI, S. KATO, N. TSUJI, T. OHKUBO, K. HONO, Bulk mechanical alloying of Cu-Ag and Cu/Zr two-phases microstructures by accumulative roll-bonding process, *Acta Mater.* 55, pp.2885-2895, 2007;
- [15] H.W. SHENG, G. WILDE, E. MA, The competing crystalline and amorphous solid solutions in the Ag-Cu system, *Acta Mater.* 50, pp.475-488, 2002;
- [16] Y. QIN, L. CHEN, H. SHEN, In-situ X-ray diffraction examination of nanocrystalline Ag<sub>37</sub>Cu<sub>63</sub> powders synthesized by mechanical alloying, *J. Alloys and Comp.* 256, pp.230-233, 1997;
- [17] D. ANDERS, K. WEINBERG, Numerical investigation of diffusion induced coarsening processes in binary alloys, *IOP Conf. Series: Materials Science and Engineering* 10, 2010;
- [18] Intel Technology Journal, “Featuring Intel’s recent research and development: Intel’s 45 nm CMOS Technology”, 12(2), 2008;
- [19] W. GLUCHOWSKI, Z. RDZAWSKI, Silver-mishmetal alloy for application at elevated temperature, *Journal of Achievements in Materials and manufacturing engineering*, 26(2), pp. 123-126, Febr, 2008;
- [20] Y.F. SUN, T. NAKAMURA, Y. TODAKA, M. UMEMOTO, N. TSUJI, *Intermetallics* 17, pp.256, 2009;
- [21] H.W. SHENG, G. WILDE, E. MA, *Acta Mater.* 50, pp. 475, 2002;
- [22] H.W. SHENG, E. MA, *Phys. Rev.* 63, pp.224205, 2001;
- [23] Y. F. SUN, N. TSUJII, H. FUJII, F.S. LI, *J. Alloys Compd.* 504S, S 443, 2010;
- [24] S. OHSAKI, S. KATO, N. TSUJII, T. OHKUBO, K. HONO, *Acta mater.* 55, pp.2885, 2007;
- [25] H. SHEN, Z. LI, B. GÜNTHER, A.V. KORZNIKOV, R.Z. VALIEV, Influence of powder consolidation methods on the structural and thermal properties of a nanophase Cu-50wt%Ag alloy, *Nanostructured Materials*, 6(1-4), pp. 385-388, 1995;
- [26] R. ARROYAVE, T.W. EAGAR, Thermodynamic assessment of the Ag-Cu-Ti system, *TMS Letters*, 1(5), pp. 887-896, 2003;
- [27] S. HIRNYJ, J.E. INDACOCHEA, Phase transformation in Ag<sub>70.5</sub>Cu<sub>26.5</sub>Ti<sub>3</sub> filler alloy during brazing processes, *Chem. Met. Alloys* 1, pp. 323-332, 2008;
- [28] A. LAIK, A.A. SHIRZADI, R. TEWARI, A. KUMAR, T. JAYAKUMAR, G.K. DEY, Microstructure and interfacial reactions during active metal brazing of stainless steel to titanium. *Metallurgical and Materials; Transactions A*, 44(5) pp. 2212–2225, 2013;
- [29] O. GINGU, C. NICOLICESCU, G. SIMA, Research of the milling time influence on Ag-Cu powder particles size processed by mechanical alloying route, *Solid State Phenomena* 188 (2012) pp. 382-387, 2012;
- [30] O. GINGU, P. ROTARU P, A. MARIN, A. MILEA, C. NICOLICESCU, G. SIMA, S. TANASESCU, In-situ synthesis of AgCu/Cu<sub>2</sub>O nanocomposite by mechanical alloying: The effect of the processing on the thermal behavior, *Thermochimica Acta* 606, pp.1–11, 2015;
- [31] Y. WU, X. LIU, J. ZHANG, J. QIN, C. LI, In situ formation of nano-scale Cu–Cu<sub>2</sub>O composites, *Materials Science and Engineering A* 527, pp.1544–1547, 2010;
- [32] TH, WOLKENSTEIN, *Physico-chimie de la surface des semi-conducteurs*. Editions Mir, Moscou, 1977;

- [33] K.B. VANLEEUEWEN, K.A. DARLING, C.C. KOCH, R.O. SCATTERGOOD, Novel technique for the synthesis of ultra-fine porosity metal foam via the inclusion of condensed argon through cryogenic mechanical alloying, *Materials Science and Engineering A* 528, pp. 2192–2195, 2011;
- [34] A. MILEA, O. GINGU, S. PREDA, G. SIMA, C. NICOLICESCU, S. TANASESCU, Thermodynamic measurements on Ag-28% Cu nanopowders processed by mechanical alloying route, *Journal of Alloys and Compounds*, Accepted manuscript (unedited version) available online: 9-JAN-2015, Reference: JALCOM33015;
- [35] C. SCHILLER, C. RASCGE, M. WEHMOLLER et al, *Biomaterials* 25, pp. 1239-1247, 2004;
- [36] B. KLONGNOI, S. RUPPRECHT, P. KESSLER, M. THORWARTH, J. WILTFANG, *Clin Oral Implants Res.* 17, pp. 312-320, 2006;
- [37] C. VON WILMONSKY, E. VAIRAKTARIS, D. POHLE, T. RECHENWALD, LTZ.R.H. MUNSTADT, G. KOLLER, M. SCHMIDT, FH. NEUKAM, KA SCHLEGEL, E. NKENKE, *J. Biomed. Mater. Res. A* 87A(4), pp. 896-903, 2008;
- [38] C. APARICIO, F.Y. GIL, C. FONSECA, M. BARBOSA, Planell JA, *Biomaterials* 24, pp. 263-273, 2003;
- [39] <http://phys.org/news/2010-12-medical-implants-high.html>;
- [40] M. LINDER, S. HOEGES, W. MEINES, K. WISSENBACH, R. SMEETS, R. TELLE, R. POPRAWE, H. FISCHER, *J. Biomed Mater. Res. A* 97(4), pp. 466-471, 2011;
- [41] L. JIA PING, *Biomaterials* 28, pp. 2810-2820, 2007;
- [42] D. ESPALIN, K. ARCANTE, D. RODRIGUEZ, F. MEDINA, *Rapid prototyping Journal* 16(3), pp. 164-173, 2010;
- [43] J.O. HOLLINGEN, G.C. BATTISTONE, *Clin. Orthop. Relat. Res.* 207, pp. 290-305, 1986;
- [44] S.F. HULBERT, S.J. MORISSON, J.J. KLANITTER, *J. Biomed.Mater.Res.* 6, 347-374, 1972;
- [45] J. ZHANG, C. HUANG, Q. XU, A. MO, J. LI, Y. ZUO, *Clin.Oral Implants Res.* 21, pp. 392-397(2010);
- [46] E. NEOVIUS, T. ENGSTRAND, *J. Plast. Reconstr. Aesthet. Surg.* 63(10), pp. 1615-1623, 2010;
- [47] W.T. COULDWELL, C.B. STILLERMAN, W. DOUGHERTY, *Skull Base Surg.* 7(2), pp. 57-63, 1997;
- [48] C.H. SODERLUND, V. POINTILLART, M. PEDRAM, G. ANDRAULT, M. VITAL, *European Spine Journal* 13(8), pp. 685-690, 2008;
- [49] D. BUSER, R. SCHENK, S. STEINMANN, J. FIORELLINI, C. FOX, A. STICH, *J. Biomed. Mater. Res.* 25, pp. 889-902, 1991;
- [50] F.X. HUBER et al. *J. Mater. Sci. Mater. Med.* 19, pp. 33-38, 2008;
- [51] Y.H. MENG et al. *J. Mater.Sci.Mater.Med* 19, 75-81, 2008;
- [52] [http://www.spine.org/Documents/bone\\_grafts\\_2006.pdf](http://www.spine.org/Documents/bone_grafts_2006.pdf)
- [53] F.D. BURSTEIN, *Cleft Palate Craniofac. J.* 37, 2000;
- [54] R. SCHNETTLER et al. *Eur.J.Trauma* 30(4), pp. 219, 2004;
- [55] HUANG S. et al. *J.Mater.Sci.Med* 19, pp. 437-442, 2008;
- [56] J.A. JANSEN et al. *J.Biomed.Mater.Res.* 25, pp. 973-989, 1991;
- [57] K. SOBALLE, *Acta Orthop.Scand.* 255 (Suppl), pp. 1-58, 1993;
- [58] [www.neurosurgerydallas.com/2\\_2\\_3\\_3.php](http://www.neurosurgerydallas.com/2_2_3_3.php);
- [59] N FRANCAVIGLIA. et al. *Argos Spine News* 9, 2004;
- [60] J.G. SEILER III et al., *J.South Orthop Assoc.* 9(2), pp. 91-97, 2000;
- [61] O. GINGU, I.C. PASCU, N. LUPU, G.C. BENGA (125713/2015), Derwent Primary Accession Number: 2010-M69278 [69];
- [62] I.C. PASCU, O. GINGU, I. CIUPITU, P. ROTARU (125714/2015), Derwent Primary Accession Number: 2010-M69276 [79];

- [63] B.A. OLEI, O. GINGU, G. BENGA., Study of the surface response at dry friction tests of nanostructured ceramic PM biocomposites, The 8th International Conference on Materials Science and Engineering BRAMAT 2013, Brasov, Febr. 2013
- [64] M. MASMOUDI *et al.*, Applied Surface Science, 253, pp. 2237-2243, 2006;
- [65] O. GINGU, G. BENGA, A. OLEI, N. LUPU, P. ROTARU, S. TANASESCU, M. MANGRA, I. CIUPITU, I. PASCU, G. SIMA, J. Proc. Mech. Eng., Part E, 225(1), pp. 62-71, 2011;
- [66] G. BENGA, O. GINGU, I. CIUPITU, L. GRUIONU, I. PASCU, M.J. CALDERON., 20100) Processing and laser micromachining of HAP based biocomposites, in Engineering the Future, edit. by Laszlo Dudas, Sciyo Ed.; <http://www.intechopen.com/books/engineering-the-future>;
- [67] Ongoing research development on advanced biocomposites between University of Craiova (Romania) and University Carlos III of Madrid (Spain), European "Erasmus+" program;
- [68] A.M. SOFRONIA, Thermochemical study of some micro and nanostructured biomaterials, Ph.D. thesis, "Ilie Murgulescu" Institute of Physical Chemistry of the Romanian Academy, Bucharest, nov. 2013;
- [69] K. GEETHALAKSHMI, T. PRABHAKARAN, J. HEMALATHA, Dielectric studies on nano zirconium dioxide synthesized by co-precipitation process, World Academy of Science, Engineering and Technology 64, 2012;
- [70] Y. ESTRIN., Nanostructured materials for permanent and bioresorbable medical implants, AzoNano.com, June 2011
- [71] C.I. PASCU, O. GINGU, P. ROTARU, I. VIDA-SIMITI, A. HARABOR, N. LUPU, Bulk titanium for structural and biomedical applications obtaining by Spark Plasma Sintering (SPS) from titanium hydride powder, Journal of Thermal Analysis and Calorimetry, doi: 10.1007/s10973-012-2824, 2012;
- [72] A.J. RUYTS, O. GINGU, SIMA G.S. MALEKSAEEDI, Handbook of Manufacturing Engineering and Technology, Chapter 7: Powder processing of bulk components in manufacturing, Springer Ed., <http://www.springerreference.com/docs/html/chapterdbid/331461.html>, 2013;
- [73] I.G. BUCSE, C. RISTOSCU, B. A. OLEI, Structural analysis of PM hydroxyapatite-based biocomposites elaborated by two-step sintering, Proceedings of the 9th International Conference on Materials Science & Engineering BRAMAT 2015, pp. 119, Journal of Optoelectronics and Advanced Materials JOAM 2015 (in due evaluation);
- [74] O. GINGU, D. COJOCARU, C.G. RISTOSCU, G. SIMA, C. TEISANU, M. MANGRA, The influence of the foaming agent on the mechanical properties of the PM hydroxyapatite-based biocomposites processed by two-step sintering route, Proceedings of the 9th International Conference on Materials Science & Engineering BRAMAT 2015, pp. 62, Journal of Optoelectronics and Advanced Materials JOAM 2015 (in due evaluation);
- [75] B.A. OLEI, I.G. BUCSE, The wear behavior of PM hydroxyapatite-based biocomposites processed by two-step sintering, Proceedings of the 9th International Conference on Materials Science & Engineering BRAMAT 2015, pp. 153, Advanced Engineering Forum, Trans Tech Publications 2015 (in due evaluation);
- [76] G. SIMA S, I. CINCA, C. TEISANU, O. GINGU, Mechanical characterization of the PM hydroxyapatite-based biocomposites elaborated by two-step sintering, Proceedings of the 9th International Conference on Materials Science & Engineering BRAMAT 2015, pp. 182, Advanced Engineering Forum, Trans Tech Publications 2015 (in due evaluation);
- [77] C. TEISANU, C. RISTOSCU, G. SIMA, I.G. BUCSE, B.A. OLEI, O. GINGU, The influence of the foaming agents on the porosity of the PM hydroxyapatite-based biocomposites processed by two step sintering, Proceedings of the 9th International Conference on Materials Science & Engineering BRAMAT 2015, pp. 195, Advanced Engineering Forum, Trans Tech Publications 2015 (in due evaluation);

- [78] D. COMAN, M.R. GORGAN, F. BREHAR, O. GINGU, Biomechanics study of the vertebral body/biocomposite graft interface by computational methods, Proceedings of the 9th International Conference on Materials Science & Engineering BRAMAT 2015, pp. 292, Advanced Engineering Forum, Journal of Applied Surface Science 2015 (in due evaluation);
- [79] Research grant PN-II-PT-PCCA-2013-4-2094, no. 244/2014; beneficiary: UEFISCDI; coordinator: University of Craiova, Romania / Prof. Gingu O.; title: Research of the bone substitution with biocomposite materials processed by powder metallurgy specific techniques, acronym BONY; funding course: 2014-2016; <http://www.mecanica.ucv.ro/Cercetare/BONY/index.html>;
- [80] [www.pingpongdepot.com](http://www.pingpongdepot.com)
- [81] <http://www.megaspin.net>
- [82] US Patent 4324400, Table tennis bat blade, 1982
- [83] US Patent 7204770B2, Table tennis racket, 2007
- [84] US Patent 7559861, Racket, blade and rubber for table tennis, July 14, 2009;
- [85] G.I. MANGRA, O. GINGU, RO Patent 125890/2014, Derwent Primary Accession Number: 2011-A29765 [42], Plate of metallic foam-rubber composite material mechanically attached to the table tennis bat and process for making the same,
- [86] G.I. MANGRA, O. GINGU, Processing of the metallic foam coverings for the tennis table rackets, The 8th Conference of the International Sports Engineering Association, ISEA 2010, Vienna, Austria, pp.12-16, July, 2010, Proceedia Engineering, The Engineering of Sports, 2(2), pp. 3447, 2010, ISSN 1887-7058, available online at Science Direct ([www.sciencedirect.com](http://www.sciencedirect.com))
- [87] <https://www.eurostars-eureka.eu/>;
- [88] [http://ec.europa.eu/enterprise/initiatives/cosme/index\\_en.htm](http://ec.europa.eu/enterprise/initiatives/cosme/index_en.htm)